DOE-ER-0313/52
Distribution
Categories
UC-423, -424

FUSION MATERIALS
SEMIANNUAL PROGRESS REPORT
FOR THE PERIOD ENDING

June 30, 2012

Prepared for
DOE Office of Fusion Energy Sciences
(AT 60 20 10 0)

DATE PUBLISHED: September 2012

Prepared by
OAK RIDGE NATIONAL LABORATORY
Oak Ridge, Tennessee 37831
Managed by
UT-Battelle, LLC
For the
U.S. DEPARTMENT OF ENERGY

FOREWORD

This is the fifty-second in a series of semiannual technical progress reports on fusion materials science activity supported by the Fusion Energy Sciences Program of the U.S. Department of Energy. It covers the period ending June 30, 2012. This report focuses on research addressing the effects on materials properties and performance of exposure to the neutronic, thermal and chemical environments anticipated in the chambers of fusion experiments and energy systems. This research is a major element of the national effort to establish the materials knowledge base for an economically and environmentally attractive fusion energy source. Research activities on issues related to the interaction of materials with plasmas are reported separately.

The results reported are the products of a national effort involving a number of national laboratories and universities. A large fraction of this work, particularly in relation to fission reactor irradiations, is carried out collaboratively with partners in Japan, Russia, and the European Union. The purpose of this series of reports is to provide a working technical record for the use of program participants, and to provide a means of communicating the efforts of fusion materials scientists to the broader fusion community, both nationally and worldwide.

This report has been compiled under the guidance of F. W. (Bill) Wiffen and Betty Waddell, Oak Ridge National Laboratory. Their efforts, and the efforts of the many persons who made technical contributions, are gratefully acknowledged.

Peter J. Pappano
Research Division
Office of Fusion Energy Sciences

TABLE OF CONTENTS

TABLE OF CONTENTS

TABLE OF CONTENTS

TABLE OF CONTENTS

TABLE OF CONTENTS

TABLE OF CONTENTS

TABLE OF CONTENTS

In a fusion reactor environment He is produced at high rates in steels by nuclear (n, α) transmutation reactions. Understanding the deleterious effects of He, especially the nucleation of He bubbles at GBs in steels, is one of the most important issues in nuclear fusion technology. The accumulation of He atoms and nucleation of He bubbles in the Σ3 <110> {112} GB in α-Fe have been previously studied [1] using molecular dynamics with our newly developed Fe-He potential [2]. It was found that the accumulation of He atoms, the formation of He bubbles, and the evolution of the GB structure all depend on the local He concentration and temperature. In order to broaden understanding of the effects of GB structure on the accumulation of He atoms and the nucleation of He bubbles in α-Fe the interaction of He with the ∑73b<110>{661} GB in α-Fe is currently being investigated using the same methodology as that used for our earlier studies of He in the Σ3 GB. It is found that in the ∑73b GB at low He concentrations most He atoms migrate to the GB dislocations in a very short time, and they can move along the GB dislocation lines at high temperatures. He atoms seldom congregate to form clusters in the ∑73b GB, even at 800 K, compared to clustering in the Σ3 GB. Emission of an Fe self-interstitial atom (SIA) caused by a single He is observed at 300 K, while it occurs for the clusters containing at least four He atoms at 600 K in the Σ3 GB and higher temperatures. At a local He concentration of 5 % (as defined within 20 Å from the GB), a large number of He clusters are formed. The nucleation of He bubbles is more significant at higher temperatures in the ∑73b GB, while it depends only slightly on the temperature in the Σ3 GB. Most of the He clusters are distributed along the GB dislocation lines in the ∑73b GB at low temperatures, forming platelet like configurations. At a 10 % local He concentration, a large number of SIAs are created, which results in the propagation of GB dislocations along the <112-1> direction.

A large series of molecular dynamics simulations are underway to provide the detailed atomistic data, which will enable final fitting of a new equation of state for helium in iron. This potential will be based on the behavior of helium as described by the three-body Fe-He potential developed at ORNL under the fusion program.

Due to its advantageous physical properties, tungsten (W) is being considered as a candidate structural material in fusion applications. In this paper, we perform stochastic cluster dynamics calculations of irradiation damage accumulation in pure W under fast neutron spectra up to doses of 1.5 dpa in the 400–600°C interval. Our calculations suggest that He bubbles and dislocation loops accumulate under fusion conditions, but

TABLE OF CONTENTS

1.1 STABILITY OF STRENGTHENING PRECIPITATES IN MODEL FERRITIC STEELS —

L. Tan (Oak Ridge National Laboratory)

OBJECTIVE

Evaluate the stability of a variety of candidate strengthening precipitates in RAFM steels under thermal, stress, and radiation conditions, based on experimental observation coupled with computational thermodynamics and kinetics simulations.

SUMMARY

The effect of thermal aging, creep, and irradiation on the stability of strengthening precipitates including VN, TaN, and TaC are being systematically evaluated. Three model alloys, Fe-1WVN, Fe-1WTaN, and Fe-1WTaC, have been designed and fabricated. Nano-precipitates of VN, TaN, and TaC with sizes ~9 – ~19 nm and densities in the orders of 10^{20} – 10^{22} m^{-3} were developed in these alloys. These nano-precipitates will serve as good initial point for investigating their stabilities under different tests. Free dislocation densities were characterized in the order of 10^{13} – 10^{14} m^{-2}. Tensile tests of the control samples have been completed, which results will be used as benchmarks for the aging and irradiation experiments. Thermal aging of the alloys at 600°C and 700°C for 100 h has been completed. Creep testing of a Fe-1WTaC sample at 600°C and 170 MPa (~70% yield strength) has been completed. The microstructures of the tested samples are being characterized. Longer time thermal aging and creep tests of the other samples are in progress. Self-ion (Fe^{2+}) irradiation of the samples has been planned at 500°C and 700°C for 20 dpa and 200 dpa. Tensile samples of the alloys have been prepared for neutron irradiation at 300°C, 500°C, and 650°C for up to ~20 dpa.

PROGRESS AND STATUS

Introduction

High-temperature aging-induced softening is one of the issues of ferritic-martensitic (FM) steels. It has been observed that reduced activation ferritic-martensitic (RAFM) steel F82H suffered aging-induced softening at temperatures above ~550°C, which was more than 30% after aging at 650°C for more than ~10,000 h [1]. The softening is primarily a result of the weakened pinning effect of coarsened or disappeared precipitates leading to recovery of dislocation substructures. Similar to conventional FM steels, there are three major types of precipitates in F82H. $M_{23}C_6$ and Laves phase are two types of predominant precipitates. Extensive studies have been pursued on the stability of these two types of precipitates. Significant coarsening occurs in both $M_{23}C_6$ and Laves phase, reaching a size greater than ~300 nm, despite the usually delayed appearance of Laves phase. The third type precipitates, MX with M = metals and X = C/N, are excellent strengthening phase due to their ultrafine size in tens of nanometers or smaller. Limited literature data suggested superior stability of TaC followed by TaN and VN under thermal and/or stress conditions [2,3]. Preliminary heavy ion irradiation experiments, however, suggested instability of TaC under Fe^{3+} ion irradiation at 500°C for 20 dpa (displacement per atom) [4]. This study is to screening the stability of candidate strengthening precipitates in RAFM steels under thermal, stress, and radiation conditions. The outcome of this study will help understanding the degradation mechanisms of RAFM steels induced by precipitates evolution, and more importantly provide invaluable insights for developing advanced RAFM steels.

Experimental Procedure

Model Alloy Design and Fabrication

Three model alloys, i.e., Fe-1WVN, Fe-1WTaN, and Fe-1WTaC, have been designed using computational thermodynamics to favor the formation of VN, TaN, and TaC in respective alloys. The calculated phase fraction as a function of temperature for the model alloys is shown in Fig. 1. Two types of precipitates, i.e., Laves phase Fe_2W and MX (VN, TaN, and TaC), exist in the model alloys. Chromium is not added in the model alloys to prevent the difficulty during microstructural characterization during transmission electron microscopy (TEM) because of the similar size between $M_{23}C_6$ and Fe_2W. It is assumed that the nonexistence of chromium will not influence the stability of MX because chromium is the primary element forming $M_{23}C_6$ and may promote the coarsening of $M_{23}C_6$ and Fe_2W.

One ingot (~4.5 kg) was casted using vacuum induction melting (VIM) for each model alloy. A ~19 mm thick plate was obtained from each ingot by hot forging, hot rolling, normalization, and tempering. The same normalization and tempering temperatures, 1200°C and 750°C, respectively, were applied to the plates.

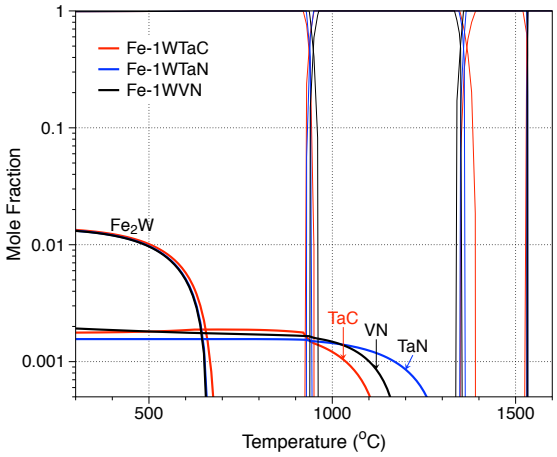

Fig. 1. Calculated phase fraction as a function of temperature for the three model alloys.

Stability Screening

Three types of testing conditions, i.e., thermal aging, creep, and irradiation, are planned for screening the stability of the strengthening precipitates. Thermal aging experiments have been started at 600°C and 700°C with times from 100 h to 5000 h. Possible effect of Laves phase on MX stability will be assessed at the 600°C aging condition. Creep tests will be conducted at two levels of loading stress, e.g., ~70% and ~40% yield strength. Both neutron irradiation and heavy ion irradiation experiments are planned for the model alloys.

Microstructure Characterization

The microstructures of the samples prior to and after the screening experiments are primarily characterized using TEM. Other supplementary techniques such as energy dispersive X-ray

spectroscopy (EDS), scanning electron microscopy (SEM) and optical microscopy are also employed.

Results

Alloys in the Control Condition

Optical micrographs in Fig. 2 indicate that the Fe-1WTaN alloy has slightly smaller grain size than the other two alloys. Many nano-precipitates were observed in the alloy as shown in the bright-field TEM images of Fig. 2. Very few free dislocations were observed within the grains of these alloys. The statistical results of the size and volume number densities of these nano-precipitates and the density of free dislocations are listed in Table 1. The size of VN precipitates was about twice of the TaN and TaC precipitates. The density of TaN was in the order of 10^{22} m^{-3}, one order of magnitude greater than that of TaC and two orders of magnitude greater than that of VN. The large deviation of the VN density was a result of the non-uniform distribution of the particles with Fig. 3 as an example. Similar free dislocation density in the order of 10^{14} m^{-2} was observed in the Fe-1WTaN and Fe-1WTaC alloys, which is comparable to tempered P91 of ~5×10^{14} m^{-2}. The dislocation density in the Fe-1WVN alloy was about one order of magnitude lower than the other two alloys.

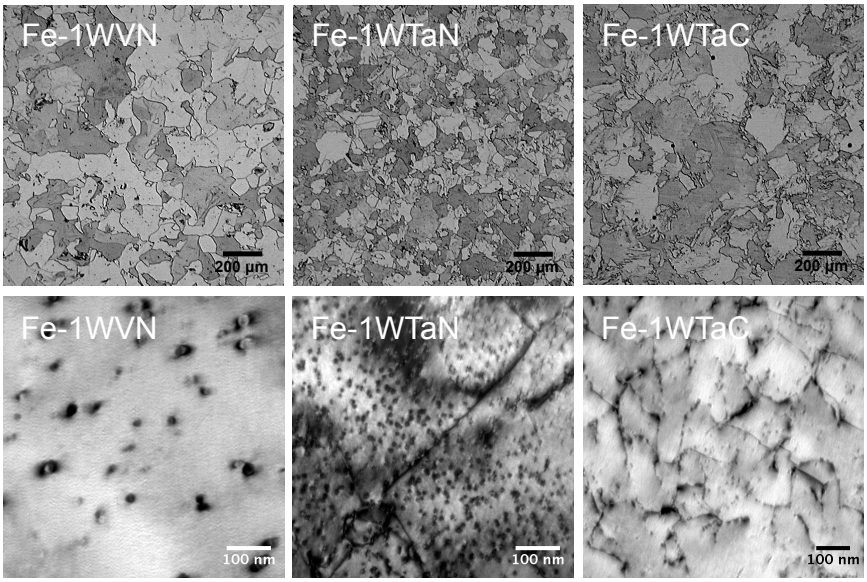

Fig. 2. Optical micrographs (first row) and bright-field TEM images (second row) of the model alloys.

Table 1. Statistical results of the precipitates and free dislocations in the model alloys.

Microstructural Feature		Fe-1WVN	Fe-1WTaN	Fe-1WTaC
Particle	Type	VN	TaN	TaC
	Size (nm)	18.6±3.1	9.1±2.3	9.7±1.9
	Density ($\times10^{21}$ m^{-3})	0.396±0.290	19.3±4.56	3.41±0.76
Dislocation	Density ($\times10^{14}$ m^{-2})	0.22±0.04	1.30±0.26	1.80±0.31

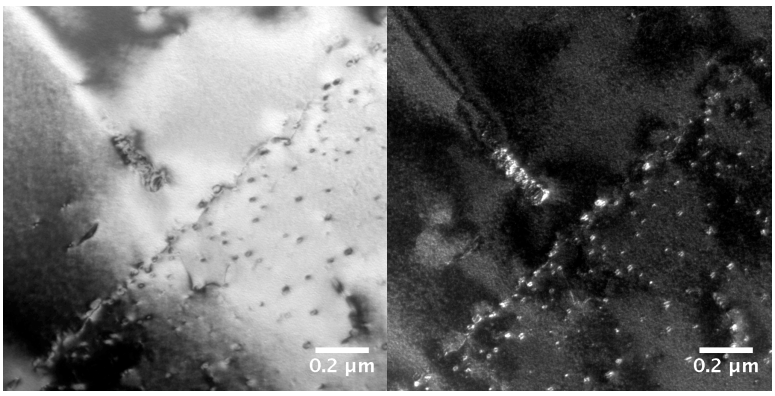

Fig. 3. Bright-field and dark-field TEM images showing non-uniform distribution of VN in alloy Fe-1WVN.

The yield strength data of the three model alloys at temperatures up to 700°C are plotted in Fig. 4. The data of RAFM steel F82H from Ref. [5] are included for comparison. The model alloys exhibited lower yield strength than F82H because of their fewer strengthening elements such as sub-boundary strengthening and solution strengthening from W, Cr, etc. However, Fe-1WTaC and Fe-1WTaN showed yield strength comparable to F82H at temperatures above 600°C. Alloy Fe-1WVN had the lowest strength due to the smaller densities of both strengthening particles VN and dislocations. The particle strengthening and dislocation strengthening were estimated using the equations of σ_P (GPa) = $1.1Gb(r \times n)^{1/2}$ and σ_D (GPa) = $0.5Gb\rho^{1/2}$, respectively, where G is shear modulus (80.2 GPa for iron), b the magnitude of Burger's vector (2.49×10^{-10} m for iron), r the radium of particles, n the density of particles, and ρ the density of free dislocations. The calculated results are summarized in Table 2. The particle and dislocation strengthening contributed ~38%, ~66%, and ~56% to the yield strength of Fe-1WVN, Fe-1WTaN, and Fe-1WTaC, respectively.

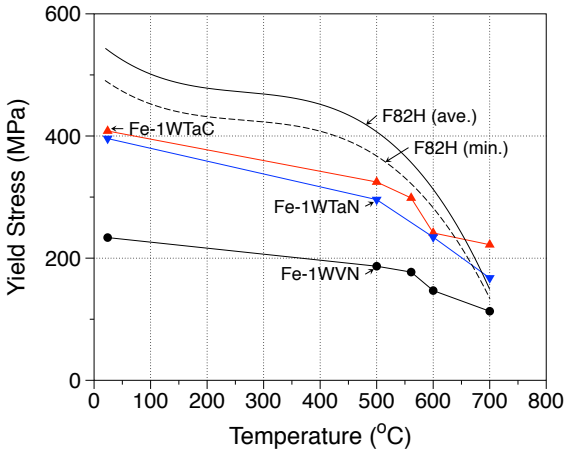

Fig. 4. Yield strength of the model alloys at temperatures up to 700°C.

Table 2. Calculated strength contributions from particles and free dislocations.

Stress (MPa)	Fe-1WVN	Fe-1WTaN	Fe-1WTaC
σ_P (particle)	42	157	89
σ_D (dislocation)	47	114	134

Thermal Aging

Thermal aging experiments on the model alloys at 600°C and 700°C have completed 100 h. The aging effect on yield strength of the alloys is shown in Fig. 5. Some variation in yield strength occurred in the alloys. Microstructural evolution induced by the aging is being characterized. The aging for 1,000 h and 5,000 h is in progress.

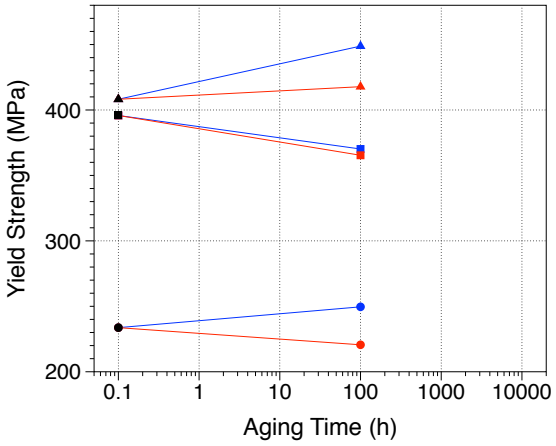

Fig. 5. Effect of thermal aging at 600°C (blue) and 700°C (red) on yield strength of Fe-1WVN (circles), Fe-1WTaN (squares), and Fe-1WTaC (triangles).

Creep Testing

A creep test of a Fe-1WTaC sample was conducted at 600°C and 170 MPa (~70% yield strength). Its creep life (371 h) is comparable to F82H [6] as shown in Fig. 6. The microstructural of the crept sample is being characterized. Creep tests of the other alloys are in progress.

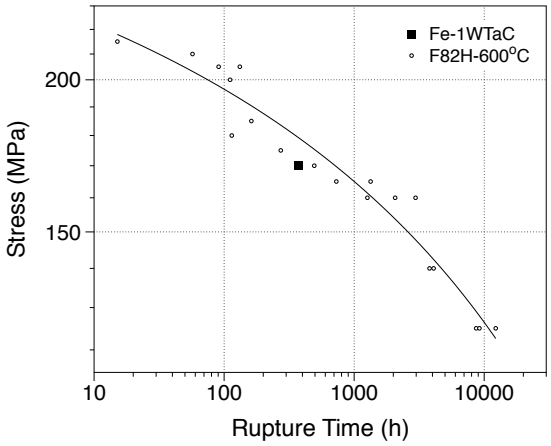

Fig. 6. Creep rupture time of Fe-1WTaC at 170 MPa load.

Heavy Ion and Neutron Irradiation

Self-ion (Fe^{2+}) irradiation of the samples is planned at 500°C and 700°C for 20 dpa and 200 dpa, using the ion beam facility at University of Michigan through ATR National Science User Facility (ATR-NSUF).

Type SS-J2 tensile samples of the alloys had been prepared and incorporated into the US-Japan irradiation campaign, which will be irradiated in the High Flux Isotope Reactor (HFIR) at 300°C, 500°C, and 650°C for up to ~20 dpa. The irradiation conditions and number of samples are listed in Table 3.

Table 3. Number of type SS-J2 samples planned for neutron irradiation in HFIR.

Capsule ID	Temperature (°C)	Fluence ($\times 10^{25}$ n/m^2)	Fe-1WVN	Fe-1WTaN	Fe-1WTaC
TB-300-2	300	0.1	1	1	1
TB-300-3		0.5	1	1	1
TB-300-4		7	1	1	1
TB-500-1	500	0.1	1	1	1
TB-500-2		0.5	1	1	1
TB-500-3		7	1	1	1
TB-650-1	650	0.1	1	1	1
TB-650-2		0.5	1	1	1
TB-650-3		7	1	1	1
TB-650-4		20	1	1	1

REFERENCES

[1] H. Tanigawa, K. Shiba, A. Möslang, R. E. Stoller, R. Lindau, M. A. Sokolov, G. R. Odette, R. J. Kurtz, and S. Jitsukawa, *J. Nucl. Mater.* **417** (2011) 9-15.
[2] M. Tamura, H. Sakasegawa, A. Kohyama, H. Esaka, and K. Shinozuka, *J. Nucl. Mater.* **329** (2004) 328.
[3] A. Kabadwal, M. Tamura, K. Shinozuka, and H. Esaka, *Metall. Mater. Trans. A* **41** (2010) 364.
[4] H. Sakasegawa, et. al., "Microstructural changes of finely dispersed MX precipitates in ion-irradiated ferritic heat –resistant steels," presented in the Conference of Japan Institute of Metals, Sept. 22-24, 2001.
[5] A.-A. F. Tavassoli, J.-W. Rensman, M. Schirra, and K. Shiba, *Fusion Eng. Des.* **61** (2002) 617.
[6] N. Yamanouchi, M. Tamura, H. Hayakawa, A. Hishinuma, and T. Kondo, *J. Nucl. Mater.* **191** (1992) 822.

1.2 DUAL ION BEAM IRRADIATION STUDIES OF CAVITY EVOLUTION IN A TEMPERED MARTENSITIC STEEL AND NANOSTRUCTURE FERRITIC ALLOYS — T. Yamamoto, Y. Wu, G. R. Odette (University of California, Santa Barbara), K. Yabuuchi, S. Kondo, A. Kimura (Kyoto University)

OBJECTIVE

The objective of this work is to characterize cavity evolution under Fe^{3+} and He^{+} dual ion beam irradiation in a normalized and tempered martensitic steel (TMS) F82H mod.3 and two nanostructured ferritic alloys (NFA), MA957 and 14YWT-PM2.

SUMMARY

Dual ion (Fe^{3+} and He^{+}) irradiations (DII) were performed at 500°C and 650°C, to nominal dpa and He levels of ≈ 10 to 47 dpa and ≈ 400 to 2000 appm, respectively. The irradiations were performed at dual ion beam facility, DuET, located at Kyoto University in Japan. The actual dpa, He and He/dpa vary with depth. The alloys studied include normalized and tempered martensitic steel, (TMS) F82H mod.3 (at 500°C), and two nanostructured ferritic alloys (NFAs), MA957 (at 500 and 650°C) and 14YWT-PM2 (at 650°C). The dual ion results are compared to in situ He injection (ISHI) irradiations in HFIR at a much lower dpa rate. The cavity microstructures were characterized by TEM. Cavities in the DII were observed at depths up to ≈ 1600 nm. The TMS F82H irradiated at 500°C contains a moderate density of non-uniformly distributed cavities with sizes ranging from ≈ 1 nm up to ≈ 20 nm, including large faceted voids along with small bubbles. In contrast, the MA957 contains a uniform distribution of small ≈ 1.3 nm diameter bubbles. Notably a similar bubble distribution is observed up to ≈ 80 dpa and ≈ 3900 appm He at 650°C, demonstrating the outstanding He management capability of nm-scale features in MA957 and 14YWT. The net swelling in F82H at 500°C reaches ≈ 0.29% at 45 dpa, with a well-established post-incubation population of growing voids. Swelling is also observed in the ISHI irradiations, which manifest even more pronounced bimodal cavity size distributions compared to those for DII conditions. Notably, the incubation dose (He and dpa) for swelling appears to be shifted too much lower dpa in the ISHI case, and the swelling rate appears to be higher. While the absolute swelling and swelling rates are low in both cases, it is important to emphasize that it is likely that the cavity volume fraction will continue to increase, and even accelerate, at higher dpa, perhaps reaching the nominal 0.2%/dpa proposed by Garner. In contrast the bubbles in the NFA are very similar in all cases, even for the DII at 650°C.

PROGRESS AND STATUS

Introduction

Predicting and mitigating the effects of a combination of large levels of transmutant He and displacement damage (dpa), produced by high energy neutrons, on the dimensional stability

and mechanical properties of structural materials is one of the key challenges in the development of fusion energy [1]. The fundamental overriding questions about He-dpa synergisms include: a) what are the basic interacting mechanisms controlling He and defect transport, fate and consequences, and how are they influenced by the starting microstructure and irradiation variables (dpa rate, He/dpa ratio, temperature and applied stress)? and, b) how can the detrimental effects of He-dpa synergisms be mitigated and managed by proper microstructural design?

We have previously demonstrated that in situ He implantation (ISHI) in mixed spectrum fission reactor irradiations provides a very attractive approach to assessing the effects of He-dpa synergisms, while avoiding most of the confounding effects associated with Ni- or B-alloy doping type experiments [1-8]. Another approach is to use multiple ion beams to simultaneously implant He and create displacement damage with heavy ions [1,9-12]. In spite of an apparent similarity, however, the two techniques manifest many differences that include the dpa rates, the spatial distribution of dpa and He and the proximity of a free surface in the case of DII. Thus comparing the microstructural evolutions in the same alloys for the two different irradiation techniques is an important objective, and provides a basis to inform, calibrate and validate predictive models.

Experimental Procedure

The alloys studied here are a TMS F82H mod.3 and two NFAs, MA957 and 14YWT-PM2. The F82H series is a TMS alloy widely used for variety of studies, including characterizing He effects [1,3,7,11-17]. In the case of F82H mod.3, the base composition of F82H-IEA (nominally wt.%, 7.5%Cr 2%W 0.2%V 0.1%C 0.1%Si 0.02%Ta, 60ppm N, bal. Fe) was modified to reduce N and Ti to 14 ppm and 0.001%, respectively, while adding 0.1% Ta [13]. The steel was austenitized at 1040°C for 30 min, normalized (air-cooled), and tempered at 740°C for 1.5 h. F82H mod.3 has a fine prior-austenite grain size (ASTM 9.5) containing packets of finer scale lath structures formed during the martensitic transformation [13]. It also contains carbide precipitates over a wide range of sizes. MA957 is a representative of the 14YWT NFA (nominally Fe-14%Cr, 1%Ti, 0.3%Mo, 0.25Y_2O_3, bal. Fe) ferritic stainless steel that was produced by INCO in the late 1970s and 1980s. NFA are of growing interest due to their radiation damage resistance, and especially good He management capabilities; NFAs also have outstanding high temperature mechanical properties [1,5,8,18,19]. As-extruded MA957 has a fine scale elongated grain structure containing nm-scale oxide nanofeatures (NFs) dispersed in the matrix; the NFs act as obstacles to dislocation glide and climb. The average grain size (d_g) in MA 957 is about 1 and 5 mm in the transverse and axial directions, respectively. The number densities (N) and average diameter (<d>) of the NFs in MA957 are ≈ $5.3x10^{23}/m^3$ and 2.7 nm, respectively. The corresponding dislocation densities (r) are ≈ $0.8x10^{15}/m^2$. The PM2 14YWT NFA heat (nominally Fe-14%Cr, 3%W, 0.35%Ti, 0.3%Y_2O_3 wt.%, bal. Fe) was produced at ORNL by D. Hoelzer as part of a LANL-ORNL-UCSB collaboration to develop a larger, best practice heat of 14YWT. The N, d, d_g and r in PM2 are ≈ $8x10^{23}/m^3$, 1.8 nm, 425 nm and $1.2x10^{15}/m^2$, respectively. More details about these materials, including processing paths, micro-nanostructures and properties, are given elsewhere [5,13,18,19].

The specimens used in the 500°C irradiations were 3 mm diameter disks mechanically ground to a nominal thickness of 200 mm, while 4 x 8 (mm) coupons with a nominal thickness of 500 mm were used for the 650°C irradiation. The specimen surfaces were electro-polished before irradiation. The DII was performed in DuET facility in the Institute of Advanced Energy, Kyoto University (Kyoto, Japan), where Fe^{3+} ions are accelerated to 6.4MeV by a tandem accelerator and He^{+} ions are accelerated to 1MeV by a single end accelerator. The specimens were positioned in a temperature-monitored/controlled stage [20]. The He^{+} ion beam was passed through a rotating beam energy degrader creating four ion implantation energy bands, that result in a broader and more uniform He deposition profile up to a maximum depth of ≈ 1500 nm.

The 500°C irradiations targeted nominal conditions at 600 nm from the specimen surface of 10 dpa/400 appm He and 25 dpa/1000 appm He. The 650°C DII targeted a nominal condition at 600 nm of 48 dpa and 2200 appm. Table 1 summarizes the irradiation conditions, while Figure 1 shows depth profile of the dpa damage and He deposition calculated with SRIM 2006 code for the 650°C case. As can be seen in the profile the implantation covers a wide range of He, He/dpa ratios, dpa and dpa rates. The region between ≈ 400 to 1100 nm has an approximately constant He/dpa ratio of ≈ 48±5 appm/dpa. Near the He peak at ≈ 1050 nm, the displacement dose is ≈ 83 dpa and the He concentration is ≈ 3900 appm. The corresponding dpa rates are ≈ 1 and 1.7 $x10^{-3}$ dpa/s for 650 °C, and ≈ 5 and 9 $x10^{-4}$ dpa/s for the 500°C irradiations. More generally, the dpa increases to a peak at ≈ 3 times the nominal dose at 1600 nm, while the He and He/dpa decrease with increasing depths greater than 1100 nm, approaching 0 at ≈1500 nm. Thus, in principle, a DuET irradiation provides a basis to evaluate the effects of a wide range of irradiation dose variables, including high dpa with no He, as well as undamaged regions. The target specimen temperature was maintained by resistive heating of the stage that adjusts for the ion beam heating.

Table 1. Summary of DuET experimental conditions.

Exp ID	Materials	T (°C)	Nominal Condition (@550-650nm)				Peak He (@1000-1100nm)		
			dpa	He (appm)	He/dpa	dpa/s	dpa	He (appm)	He/dpa
DI10B1	F82H mod.3, MA957	500	25	1010	40	5.0×10^{-4}	43	1750	40
DI10B3			10.1	406	40	5.1×10^{-4}	17	700	40
DI12A1	MA957, 14YWT(PM2)	650	48	2230	47	1.1×10^{-3}	83	3860	47

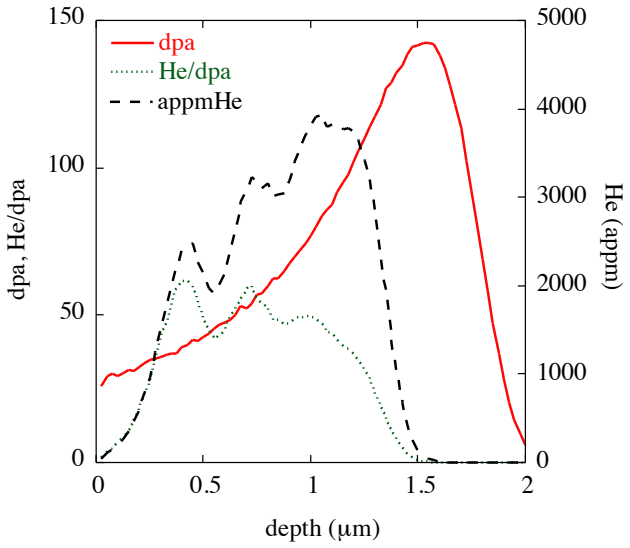

Figure 1. Depth profile of displacement damage and He deposition in the specimens in the DuET dual ion beam irradiation calculated with SRIM 2006 code for the case of nominal 47 dpa irradiation.

A FEI HELIOS Focused Ion Beam (FIB) tool was used to micro-machine < 100 nm thick electron transparent ≈ 5 mm wide and 5 mm deep lift-outs that included both damaged-implanted and undamaged regions. TEM was performed on the FEI 200 keV Technai T20 and 300 KeV Titan instruments in the UCSB Microstructure and Microanalysis Facility. Through focus bright field imaging was used to characterize the cavities. The cavity images were manually marked for location and size, and the image analysis software package Image-J was used to determine their area number densities and size distributions. The foil thickness, needed to compute volume number densities, was measured by convergent beam electron diffraction.

RESULTS

Cavity formation in TMS F82H and NFA MA957 after nominal 25dpa/1000appm He irradiation at 500°C

Figures 2a-b show the TEM images for irradiated (a) F82H mod.3 and (b) MA957 around 1000 nm from the surface, at an estimated 43 dpa and 1750 appm He. Note that the magnification is adjusted to provide the best visibility for each alloy. The F82H mod 3 contains a moderate number density (N) of cavities over a wide range of diameters (d), from ≈ 1 to ≈ 20 nm. In this case the cavities are non-uniformly distributed, in a way that depends on the local microstructure. In contrast, the size and spatial distributions of He bubbles in MA957 are more uniform, with larger N and smaller d. The average diameter (<d>) of the cavities in F82H mod3 varies with depth and ranges up to <d> ≈ 5.0 nm, while in MA957 <d> ≈1.3 nm.

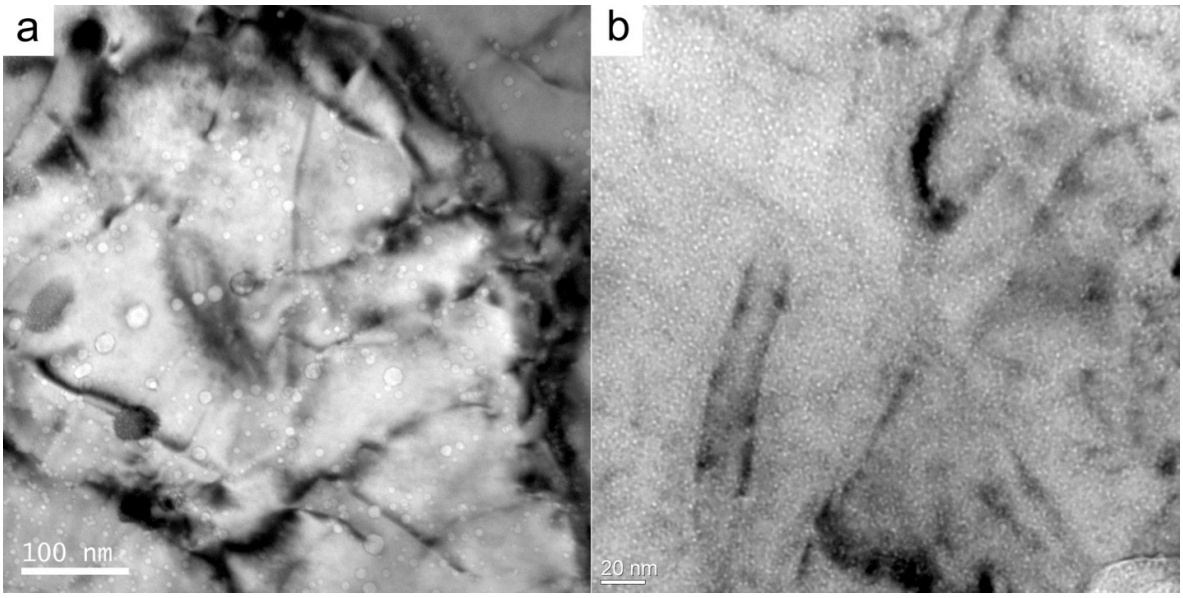

Figure 2. Under-focused bright field TEM images of the DII cavity structures in nominal 25 dpa, 500°C condition in (a) F82H mod3 and (b) MA957 that produced ≈ 43 dpa and 1750 appm He at ≈1000 nm from the surface.

Figure 3 shows N and <d> as a function of the depth greater than 600 nm. The N ranges from < 1 to ≈ $5x10^{22}/m^3$ in F82H; the corresponding <d> ranges from ≈ 3 to ≈ 5 nm, and systematically increases with the amount of implanted He and dpa. The <d> in MA957 is almost constant at ≈ 1.3 nm, while N ranges from ≈ 2.5 to $5x10^{23}/m^3$. These results clearly demonstrate the superior He management capability of the NFA compared to TMS. Note the spatial variations in N are not systematic, especially in F82H; again this is believed to be largely due to the effects of locally non-uniform microstructures that act as the bubble formation sites.

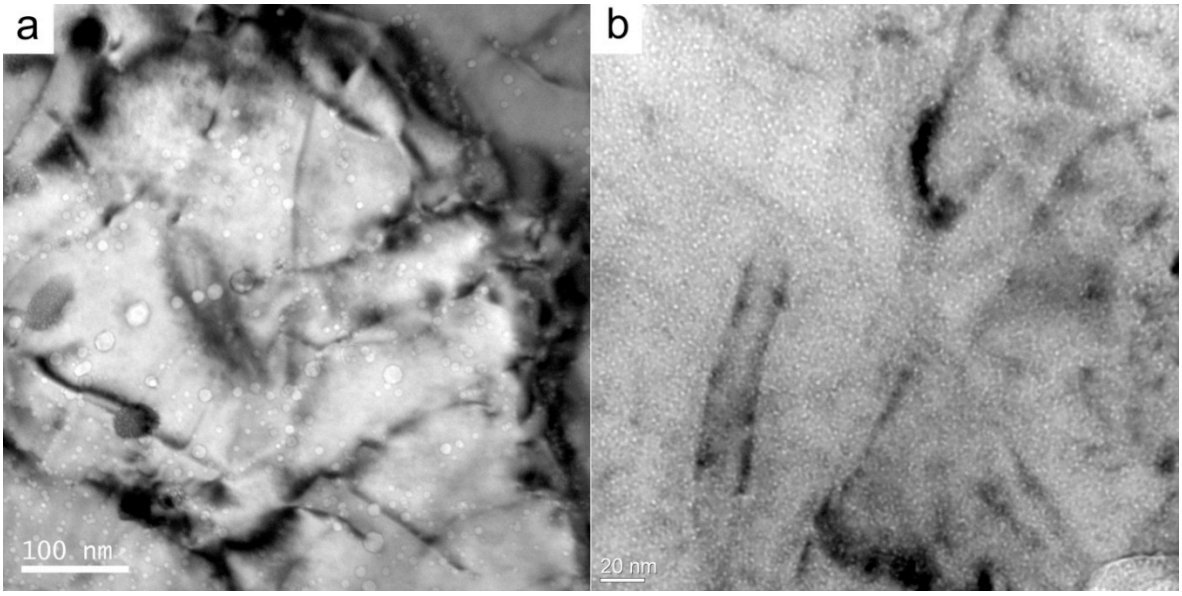

Figure 3. Average size and number density of cavities as a function of depth for the DII at 500°C in the nominal 10 dpa and 400 appm He condition in: (a) F82H mod.3; and, (b) MA957.

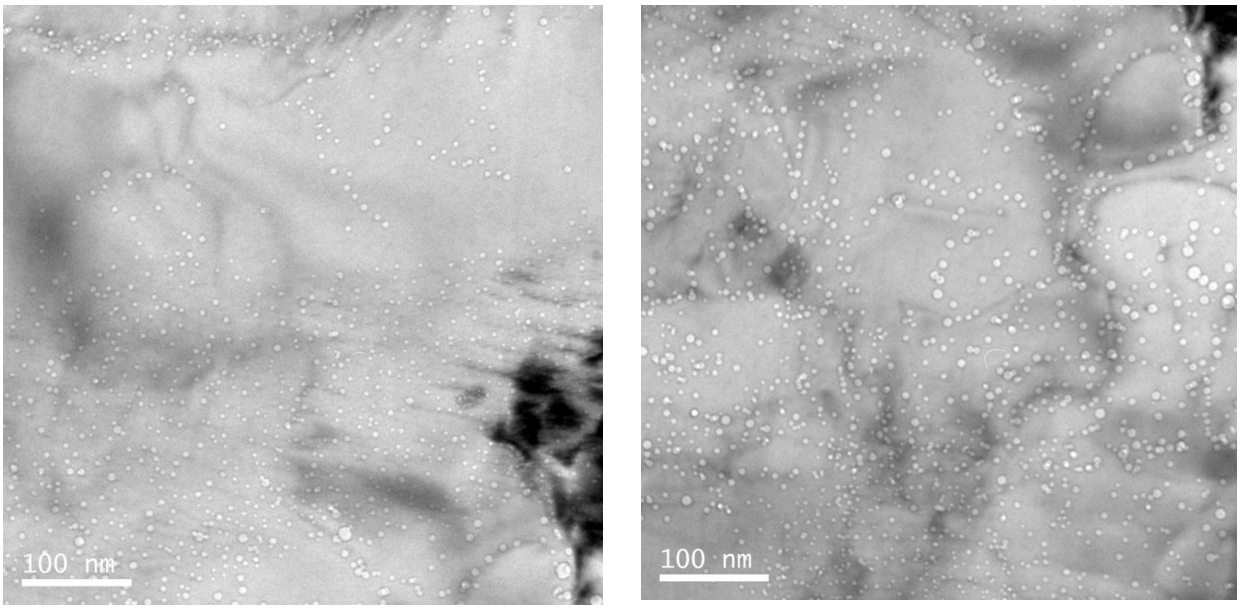

Figure 4. Cavity microstructures in F82H mod.3 irradiated to nominal 25 dpa at 500°C at two depths, (a) 0.5 to 1.0mm and (b) 0.9 to 1.4 mm. The dpa and He at the vertical center of the picture are ≈ 30 and ≈ 50 dpa, and ≈ 1200 and 2000 appm, respectively.

Figure 4a and b illustrate the cavity microstructure in F82H mod.3 irradiated to nominal 25 dpa at two depths, from the top edge to the bottom of the micrographs of: (a) 500 to 1000 nm and (b) 900 to 1400 nm. The dpa and He at the vertical center of the micrographs are ≈ 30 dpa/1200 appm and ≈ 50 dpa/2000 appm, respectively. The higher dpa and He leads to increased average cavity size <d> and especially more numerous larger faceted voids.

Figure 5 plots of the corresponding variations of N, <d> and the volume fraction (f) of cavities as a function of the He (a,d,g) and dpa (b,e,h). He/dpa (c,f,i) and He*dpa (j,k,l) for depths between 650 and 1250 nm. The various measures of damage were derived from the profiles shown in Figure 1, scaled to the actual He and dpa for each data set. The dependence of N on He, dpa and He/dpa is weak. The <d> and f do not vary systematically with He/dpa, but tend to increase with He and dpa. Here we focus on the cavity trends as a function of He(appm)*dpa, which provides the best correlation of the swelling (f) trends (Fig. 5j-l). Note, there is no special significance in the use of this damage parameter, except that both He and dpa are needed for void formation. The variation of N in F82H with He*dpa is not systematic but appears to decrease slightly at higher He*dpa. However, the overall trends of increasing <d> and f are very clear. Bubbles in the 10 dpa and 400 appm He data set dominate the cavity microstructure, but the small increases in <d> and f indicate the slow conversion of some bubbles to voids. The increases in the <d> and f with He*dpa are clear in the higher 25 dpa and 1000 appm He data set. The trend in f is approximately linear beyond a threshold He*dpa, except for the highest combined damage points, which have the highest dpa but a lower and He and He/dpa ratio. These figures also include 500°C data (open symbols) for several TMS alloys from in situ helium injection (ISHI) irradiation experiment for the data sets at 9 dpa/380 appm He and 21.2 /1230 appm He. The transition to void swelling is much faster in the ISHI case, perhaps due to the much lower fusion relevant damage rates. The swelling rates are also higher.

Figure 6a and b plot the cavity size distribution for the peak He in the DII irradiation and for a 500°C ISHI to 530 appm He/21.2 dpa [21]. Clearly the formation and evolution of larger voids occurs at lower He and dpa levels in the ISHI case.

Figure 7 shows the same plots as in Figure 5 but for MA957. Clearly the trends are very different than in the F82H. In MA957 the <d> are remarkably constant, while the N and f appear to decrease with He*dpa. The N in MA957 are much higher and the <d> much smaller than in F82H. These results clearly indicate the ability of NFs in NFA to manage high concentrations of He.

Cavity formation in NFA MA957 and 14YWT(PM2) after nominal 48 dpa irradiation at 650°C

Figures 8 a-b show the under- and over-focus images of MA957 for the 650°C DII at around 600 nm, with 48 dpa/2200 appm He. Figure 8c-d show the corresponding images for 14YWT-PM2. Figure 9a-d show the corresponding set of images near 1050 nm with ≈ 83 dpa/3800 appm He. The red lines mark increasing depth in 100 nm increments. In spite of these extremely severe damage conditions, the high N is generally similar to those shown in Figure 2 that are at much lower dpa and He levels. The <d> of the bubbles is nearly the same in both locations, while number density depends strongly on the amount of injected He. There is no evidence of void formation. He bubbles are observed on a grain boundary in the region with 83 dpa/3800 appm. These bubbles appear to be larger than those in the matrix. However it is not clear if the individual bubbles themselves are larger, or if this is the result of the larger grain boundary NFs that the bubbles are associated with. Indeed, a number of bubbles are observed to decorate

larger precipitates. Thus it is possible that small bubbles may coalesce on the interface forming a larger NF cavity.

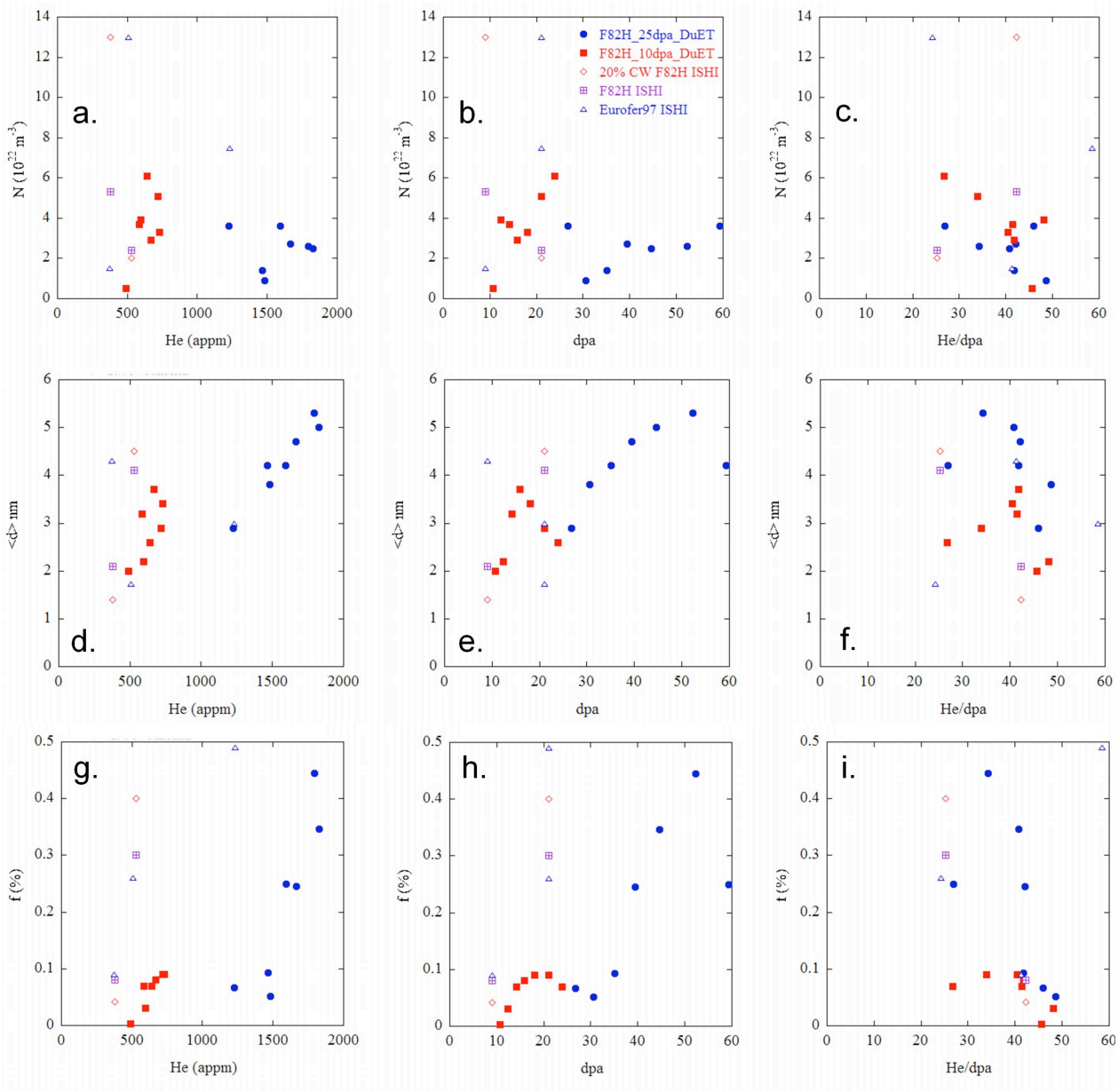

Figure 5a-i. The N, <d> and f of cavities as a function of the He (a,d,g), dpa (b,e,h) and He/dpa (c,f,i) for DII at depths between 650 and 1250 nm in F82H mod.3 irradiated at 500°C to a nominal 10 and 25 dpa (filled symbols). The DII results are compared with three ISHI irradiated TMS alloys, F82H mod.3 (as tempered and 20% cold worked conditions) and Eurofer97 ISHI experiments (unfilled symbols).

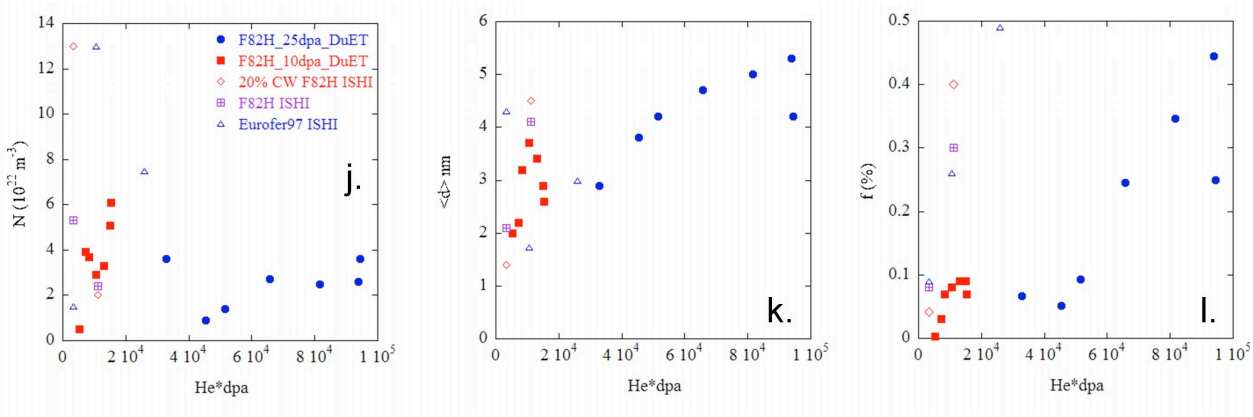

Figure 5j-l. The N, <d> and f of cavities as a function of the He(appm)*dpa at depths between 650 and 1250 nm nm in F82H mod.3 DII at 500°C to a nominal 10 and 25 dpa, compared with three ISHI irradiated TMS alloys, F82H mod.3 (as tempered and 20% cold worked conditions) and Eurofer97.

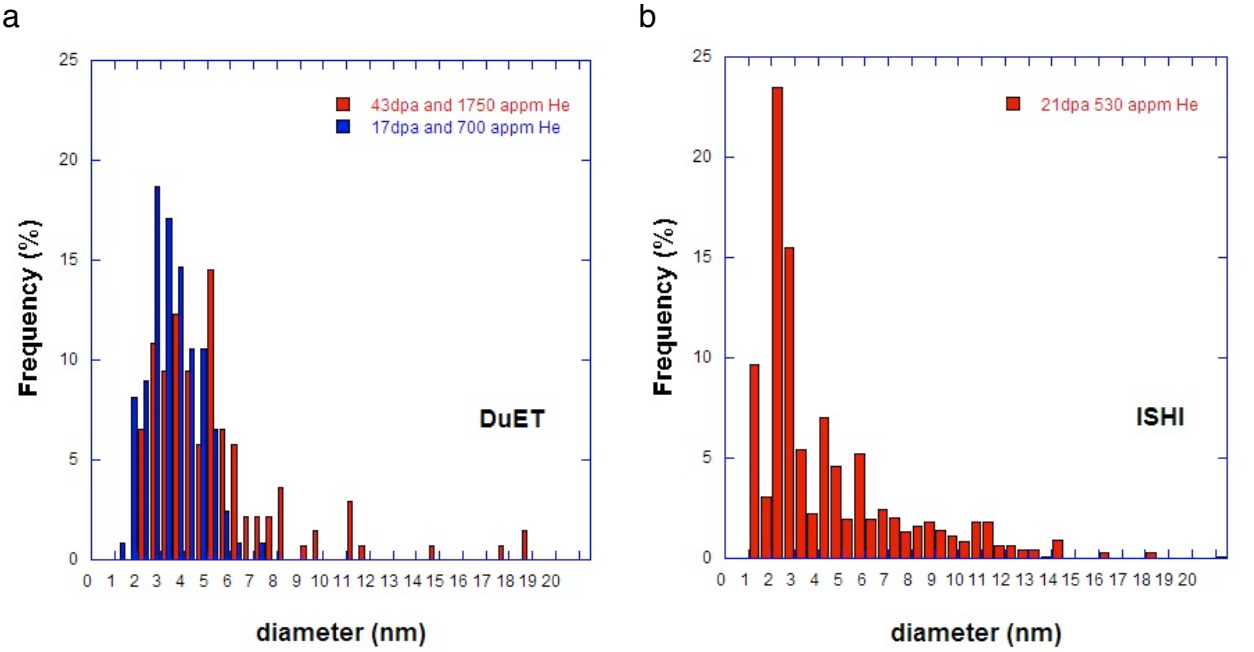

Figure 6. Cavity size distributions in F82H mod. 3 irradiated at 500°C in (a) in DuET and (b) in HFIR ISHI experiments to the indicated dpa and He levels.

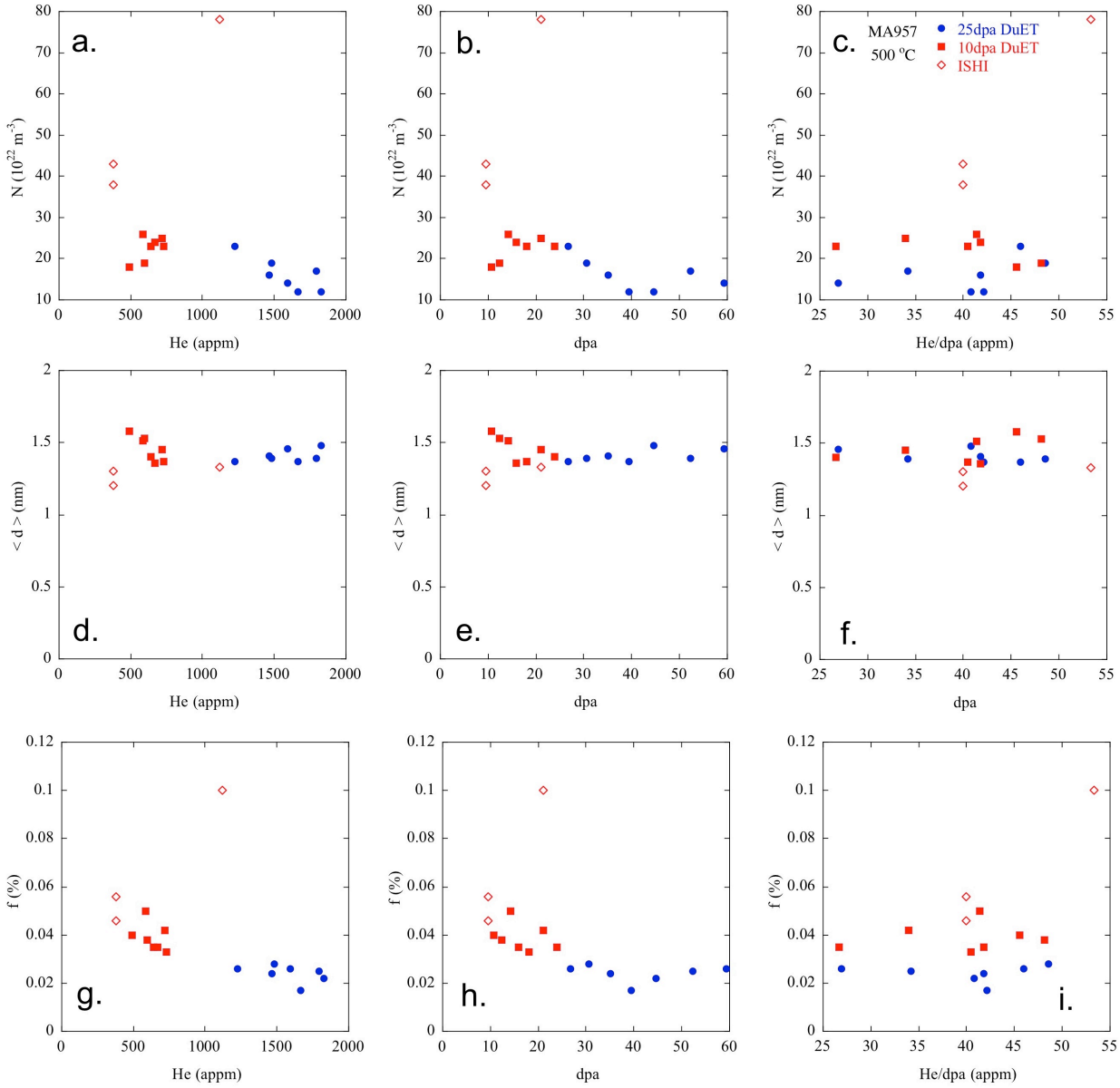

Figure 7a-i. The N, <d> and f of cavities as a function of the He (a,d,g), dpa (b,e,h) and He/dpa (c,f,i) for DII at depths between 650 and 1250 nm in MA957 irradiated at 500°C to a nominal 10 and 25 dpa (filled symbols) compared ISHI irradiated MA957 (unfilled symbols).

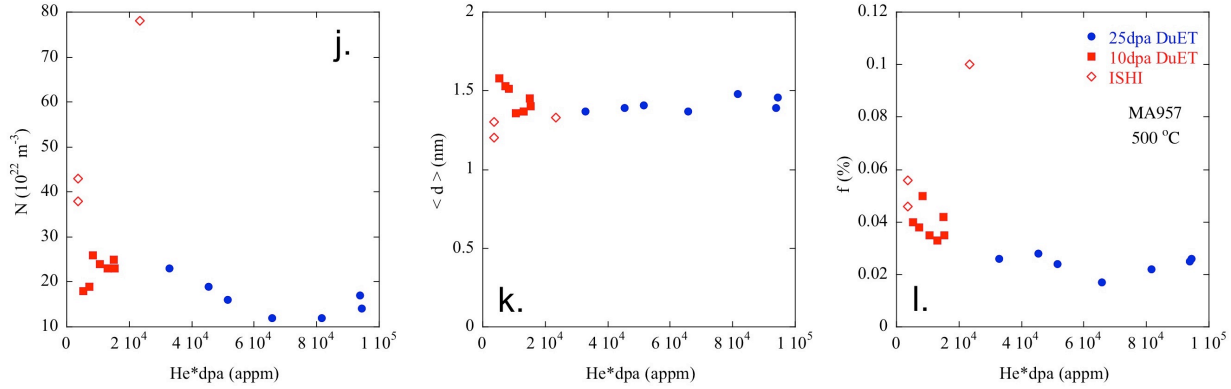

Figure 7 j-l. The N, (b), <d> and f of cavities as a function of the He(appm)*dpa at depths between 600 and 1200 nm in MA957 DII at 500°C to a nominal 10 and 25 dpa, compared ISHI irradiated MA957 (open symbols).

Cavity formation in NFA MA957 and 14YWT(PM2) after nominal 48 dpa irradiation at 650 °C

Figure 10a-b summarizes the average cavity size and number density as a function of depth in (a) MA957 and (b) 14YWT-PM2, respectively. Figure 11 compares the estimated amount of He that can be accounted for in the bubbles based on the observed size distributions and number densities compared to TRIM estimates of the total injected He. There is a large discrepancy that is not understood. Potential reasons include underestimating the size of small bubbles, unaccounted for He that contained in even smaller unresolved bubbles, or those that are hidden by the associated NFs, uncertainties in the bubble surface energy and the He equation-of-state (EOS), although in the latter case the He is probably underestimated. The reasons for these differences continue to be under active investigation. Figure 12 shows the narrow size distribution of matrix bubbles in both NFA at the nominal and peak He regions. Figure 13 plots the N, <d>and f for the DII of the NFA at 650°C as a function of He, dpa, He/dpa and He*dpa, similar to those shown previously. The most notable results are that <d> is independent of He*dpa, while the corresponding N and, especially, f increase. The observed bubble f is higher in MA957 than in 14YWT-PM2.

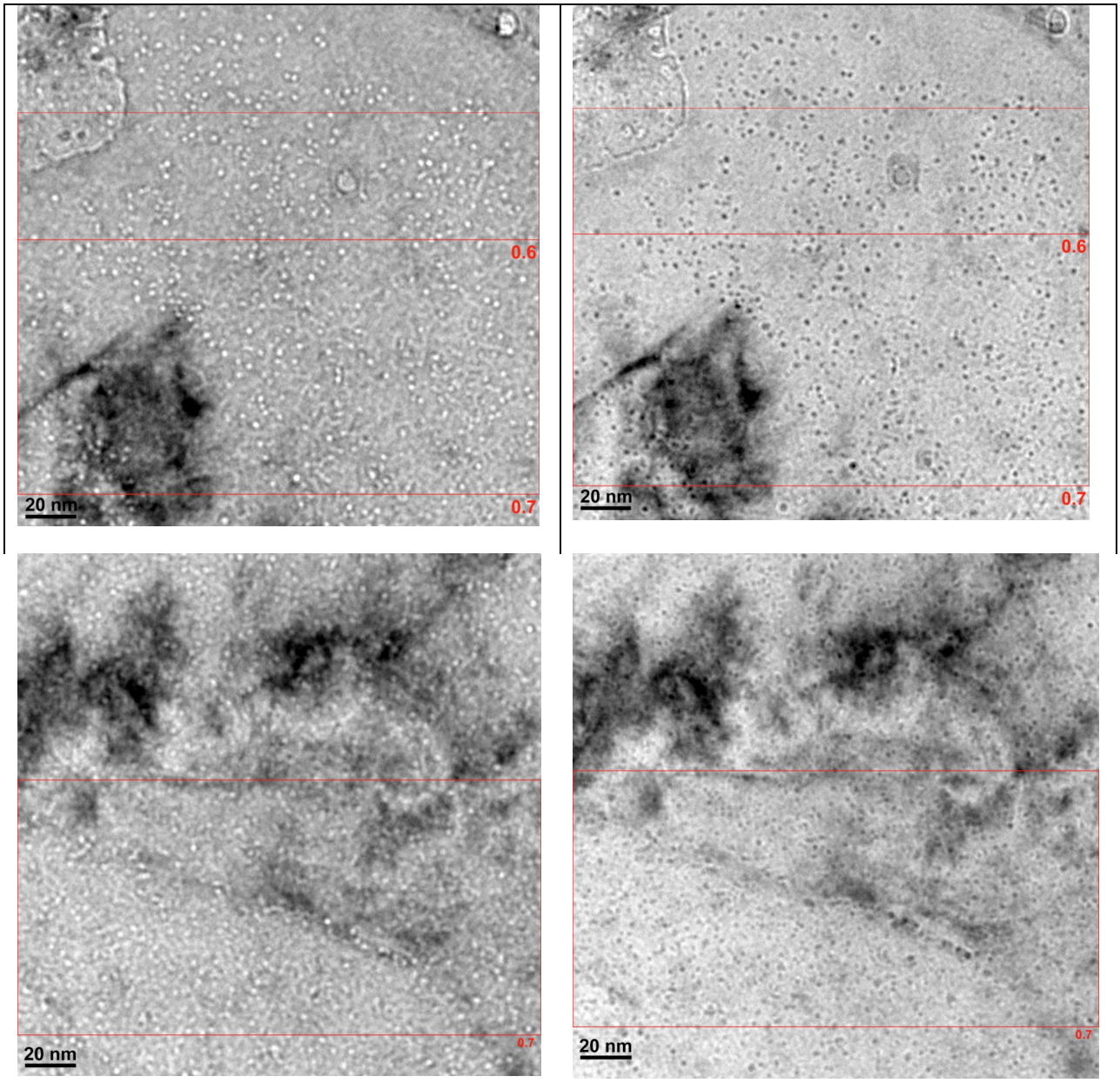

Figure 8. Under- and over-focus images of MA957 and 14YWT PM2 DII at 650°C to ≈ 48 dpa/2200 appm He.

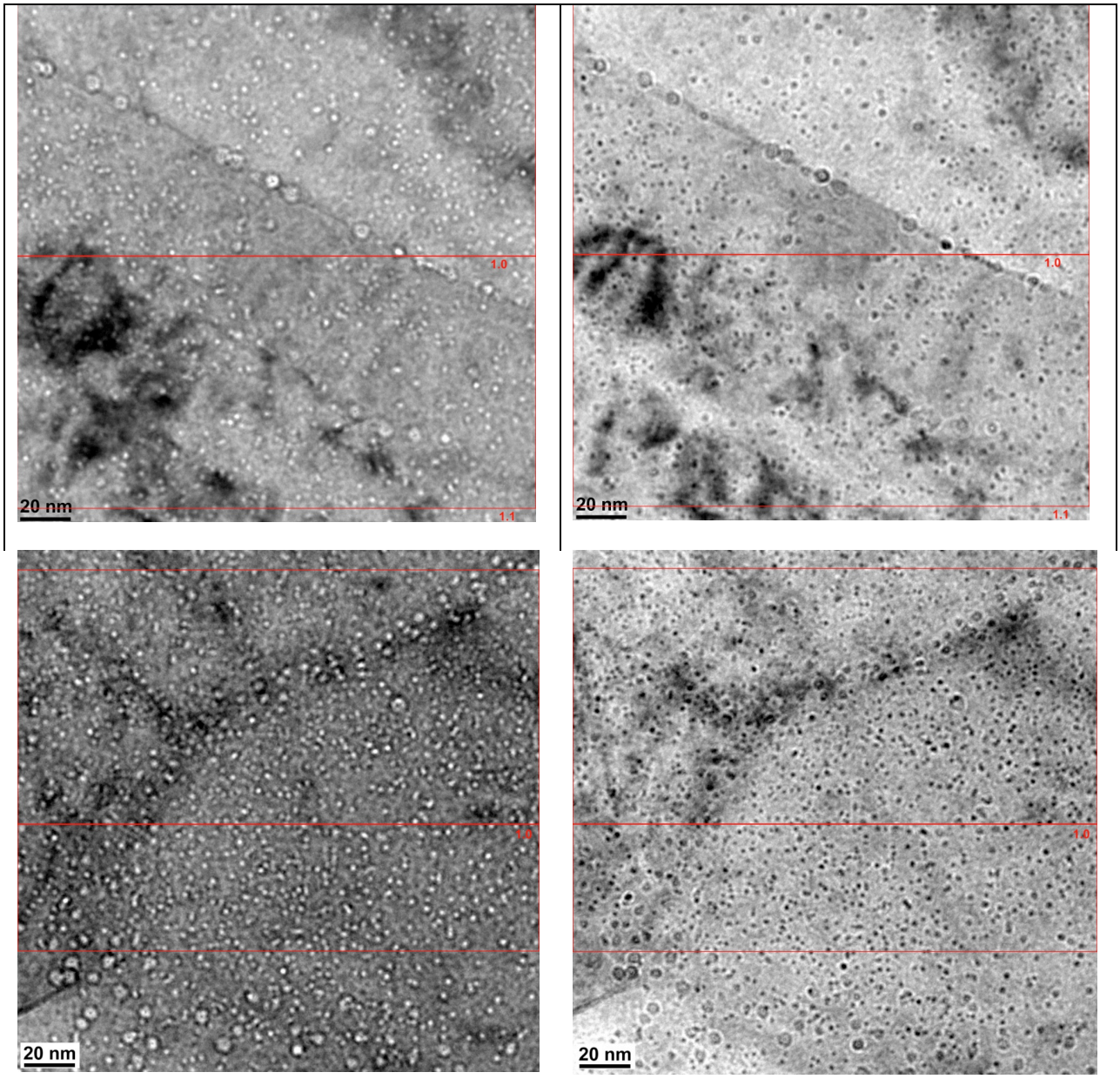

Figure 9. a) Under- and b) over-focus images of MA957 and 14YWT PM2 DII at 650 ^{o}C,to ≈ 83 dpa/3800 appm He.

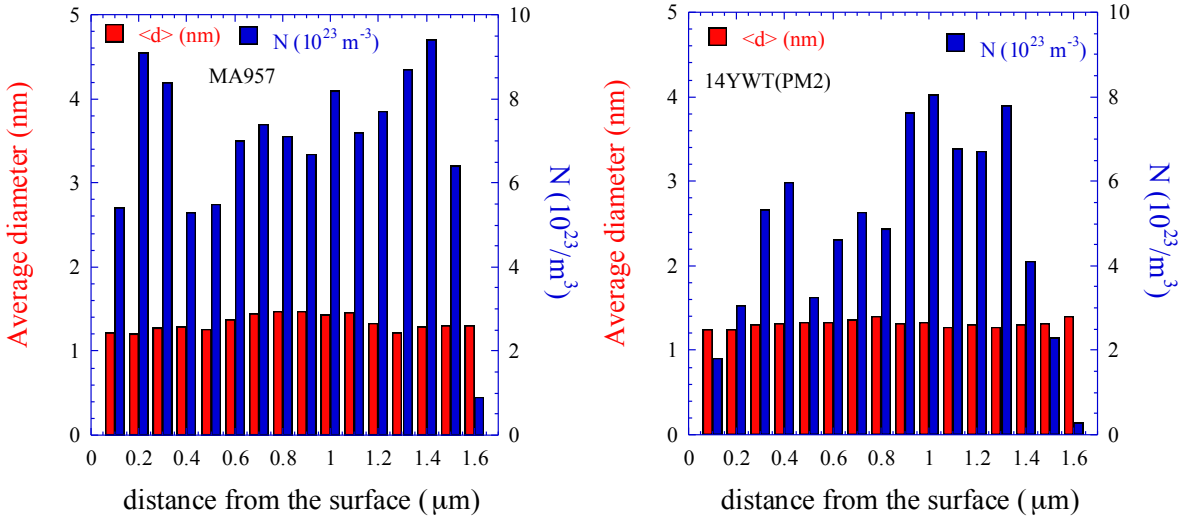

Figure 10. Average cavity size and number density as function of depth in the MA957 and 14YWT PM2 DII at 650°C.

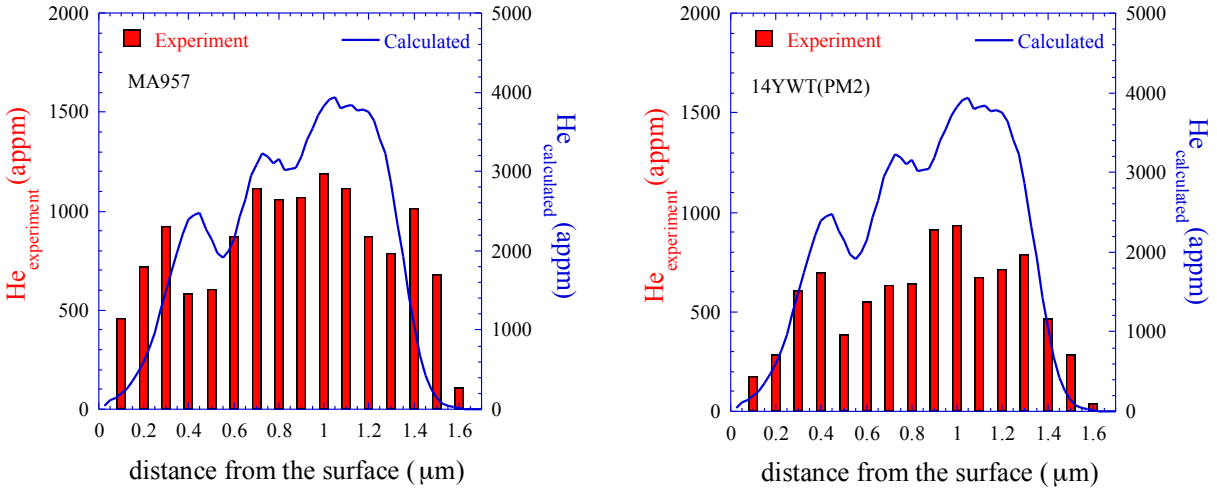

Figure 11. The estimated He in bubbles as a function of depth compared to the injected amount as calculated by TRIM for the 650°C DII.

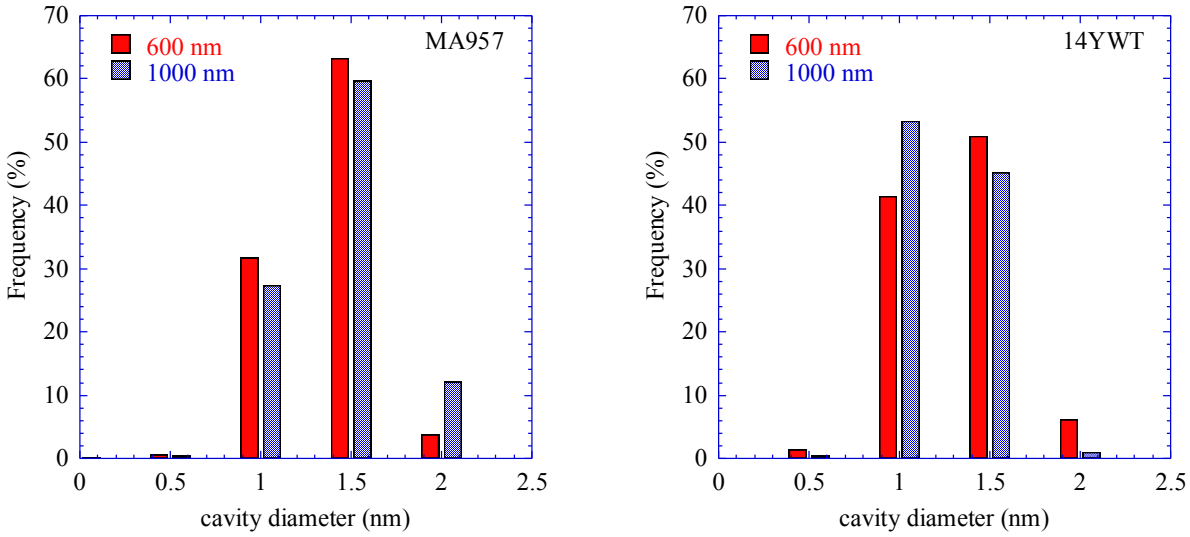

Figure 12. Cavity size distribution at nominal and peak He locations in the DII at 650°C.

DISCUSSION AND FUTURE RESEARCH

Figure 14 cross-compares plots of N, <d> and f versus He*dpa for the different irradiation conditions, illustrating the basic differences between cavity evolution in TMS F82H mod.3 and NFA MA957 and 14YWT PM2, including at 650°C in the case of MA957 and 14YWT PM2. The key observations include:

The N are generally weakly dependent on He*dpa.

The NFA contain a much higher N and smaller <d> and f, since the cavities in this case are all bubbles, compared to the TMS, which contain a mixture of small bubbles and larger voids.

The bubbles in NFA are associated with the large number of NFs.

A small but systematic increase in f (swelling) begins in the TMS beyond He*dpa ≈ $5x10^4$ appm He-dpa due to the presence of growing voids, as signaled by a corresponding trend in <d>.

The <d> in the NFA are essentially independent of He*dpa and the DII temperature.

The N and f in the NFA increase with He*dpa and the DII temperature.

The objective of this report was to summarize the DII results and to crudely assess trends in the cavity microstructures with various measures of irradiation dose. However, this significant and growing database, and the corresponding results for the ISHI, will provide a very rich knowledge base for more detailed analysis and modeling studies in the future.

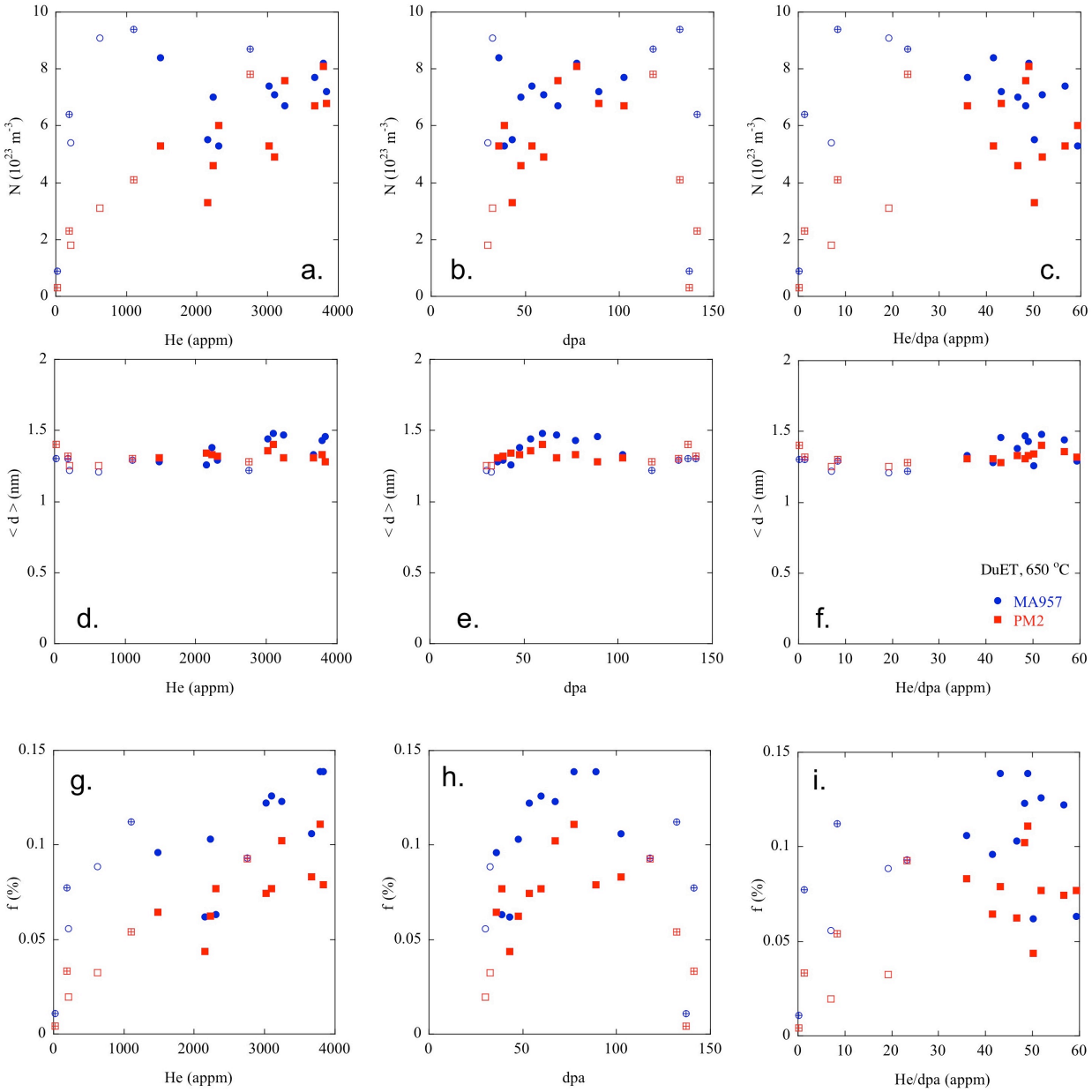

Figure 13. The N, <d> and f of cavities as a function of the He (a,d,g) and dpa (b,e,h). He/dpa (c,f,i) for depths between 100 and 1600 nm in MA957 and 14YWT(PM2) irradiated to nominal 48 dpa with 47 appm He/dpa. Filled symbols are for nominal He/dpa (≈ 50 ± 10 appm) condition, while open symbols are from the shallower, open symbols with cross are from deeper locations.

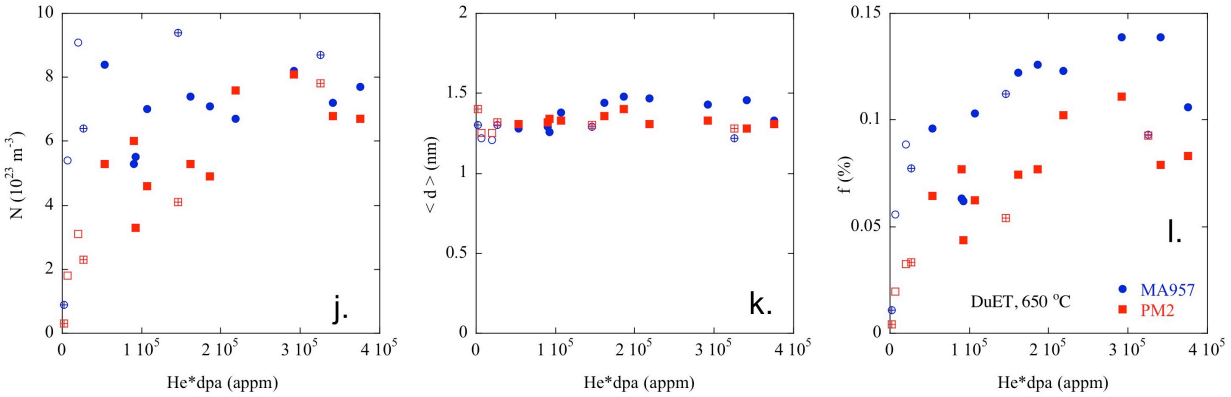

Figure 13j-l. The N, <d> and f of cavities as a function of the He*dpa for depths between 100 and 1600 nm in MA957 and 14YWT(PM2) irradiated to nominal 48 dpa with 47 appm He/dpa. Filled symbols are for nominal He/dpa (≈ 50 ± 10 appm) condition, while open symbols are from the shallower, open symbols with cross are from deeper locations.

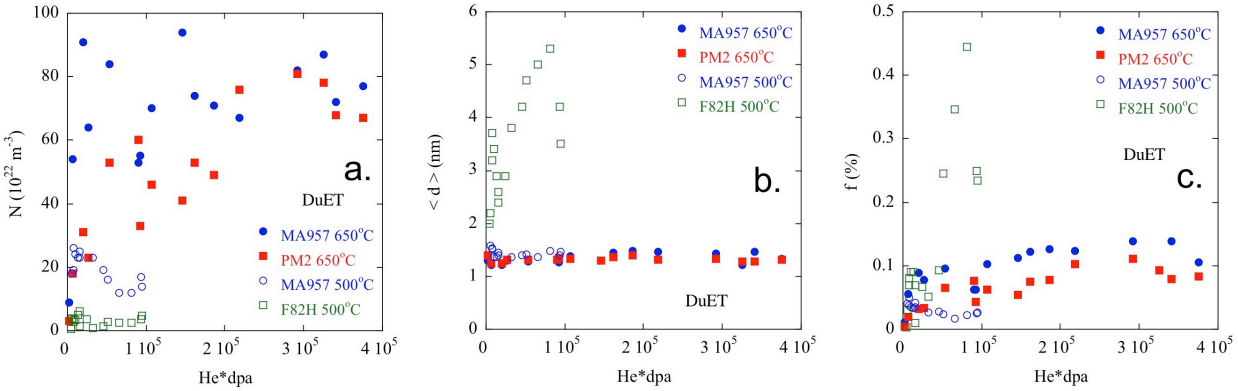

Figure 14. Comparison of all the DII results for N, <d> and f as a function of He*dpa.

ACKNOWLEDGEMENTS

The DII were conducted as a part of the TITAN program for US DOE- Japan MEXT collaboration for fusion energy research. The work performed at UCSB was supported by the U. S. Department of Energy, Office of Fusion Energy Sciences, under contract DE-FG03-94ER54275. We acknowledge the contributions of the NSF sponsored UCSB Microstructure and Microanalysis Facility. The ISHI results cited here were obtained as part of a collaboration with Drs. R. Kurtz and D. Edwards at PNNL and have been or will be discussed in detail in other publications.

REFERENCES

[1] Y. Dai, G. R. Odette, and T. Yamamoto, "*The Effects of helium on irradiated structural alloys," in Comprehensive Nuclear Materials, R. Konings, T. R. Allen, R. E. Stoller, and S. Yamanaka eds. (2012) Elsevier.*

[2] T. Yamamoto, G. R. Odette, and L. R. Greenwood, *Fusion Materials Semiannual Report 1/1 to 6/30/2005* DOE/ER-313/38 (2005) 95.

[3] T. Yamamoto, G. R. Odette, P. Miao, D. T. Hoelzer, J. Bentley, N. Hashimoto, H. Tanigawa, and R. J. Kurtz, *J. Nucl. Mater.* **367** (2007) 399.

[4] R. J. Kurtz, G. R. Odette, T. Yamamoto, D. S. Gelles, P. Miao, B. M. Oliver, *J. Nucl. Mater.* **367-370** (2007) 417.

[5] G. R. Odette, M. J. Alinger, and B. D. Wirth, *Annu. Rev. Mater. Res.* **38** (2008) 471.

[6] T. Yamamoto, G. R. Odette, P. Miao, D. J. Edwards, R. J. Kurtz, *J. Nucl. Mater.* **386-**388 (2009) 338.

[7] D. J. Edwards, R. J. Kurtz, G. R. Odette, and T. Yamamoto, *Fusion Materials Semiannual Report 12/31/2009* DOE/ER-313/47 (2010) 59.

[8] G. R. Odette, P. Miao, D. J. Edwards, T. Yamamoto, R. J. Kurtz, and Y. Tanigawa, *J. Nucl. Mat.* **417** (2011) 1001.

[9] E. H. Lee, J. D. Hunn, T. S. Byun and L. K. Mansur, *J. Nucl. Mater.* **280** (2000) 18.

[10] H. Kishimoto, K. Yutani, R. Kasada, and A. Kimura, *Fusion Eng. Des.* **81** (2006) 1045.

[11] R. Kasada, H. Takahashi, H. Kishimoto, K. Yutani, and A. Kimura, *Materials Science Forum **654-656*** (2010) 2791 (*doi:10.4028/www.scientific.net/MSF.654-656.2791).*

[12] T. Yamamoto, Y. Wu, G. R. Odette, K. Yabuchi, and A. Kimura, *Fusion Materials Semiannual Report 12/31/2010* DOE/ER-313/49 (2011) 1.

[13] K. Shiba, M. Enoeda, and S. Jitsukawa, *J. Nucl. Mater.* **329-333** (2004) 243.

[14] A. Kimura, R. Kasada, K. Morishita, R. Sugano, A. Hasegawa, K. Abe, T. Yamamoto, H. Matsui, N. Yoshida, B. D. Wirth and T. D. de la Rubia, *J. Nucl. Mater.* **307-311** (2002) 521-526.

[15] G. R. Odette, T. Yamamoto, H. J. Rathbun, M. Y. He, M. L. Hribernik, and J. W. Rensman, *J. Nucl. Mater.* **323** (2003) 313.

[16] T. Yamamoto, G. R. Odette, H. Kishimoto, J-W. Rensman, and P. Miao, *J. Nucl. Mater.* **356** (2006) 27.

[17] Z. Tong and Y. Dai, *J. Nucl. Mater.* **385** (2009) 258.

[18] M. L. Hamillton, D. S. Gelles, R. J. Lobsinger, M. M. Paxton, and W. F. Brown, "Fabrication Technology for ODS Alloy MA957", PNL-13165, Pacific Northwest Laboratory (2000).

[19] Y. Wu et al., to be published.

[20] A. Kohyama, Y. Katoh, M. Ando, and K. Jimbo, *Fusion Eng. Des.* **51-52** (2000) 789.

[21] G. R. Odette, T. Yamamoto, Y. Wu, E. Stergar, N. J. Cunningham, R. J. Kurtz, and D. J. Edwards, *Fusion Materials Semiannual Report 12/31/2011* DOE/ER-313/51 (2012) 91.

2.1 MICROSTRUCTURE CHARACTERIZATION OF NEUTRON IRRADIATED AND HELIUM INJECTED PM2000, 14YW, AND MODIFIED F82H ALLOYS — B. Yao, D. J. Edwards, R. J. Kurtz (Pacific Northwest National Laboratory), G. R. Odette, T. Yamamoto (University of California Santa Barbara)

OBJECTIVE

To characterize the microstructure of reduced activation ferritic/martensitic steel/oxide dispersion strengthened (RAFM/ODS) alloys irradiated to a helium concentration/neutron dose of 1230 appm He and 21.2 dpa at 500°C in the High Flux Isotope Reactor (HFIR) at Oak Ridge National Laboratory.

SUMMARY

Two ODS alloys and one RAFM steel (i.e., PM2000, 14YW, and modified F82H, respectively) with an adjacent 4.7 μm thick NiAl layer bond were neutron irradiated to a dose of 21.2 dpa at 500°C. An *in situ* ^{59}Ni(n, α) reaction in the NiAl layer produces high-energy He ions, which are implanted into the alloys. This report summaries initial TEM characterization results. The PM2000 contains a high density of small (< 2 nm) He bubbles in the matrix, while at the interface of Y-rich particles large voids are found. Both 14YW and modified F82H (F82H-mod) exhibit a large number of voids. The voids in the 14YW sample coexist with small Y_2O_3 particles typically less than 10 nm. Dislocation loops in all three samples were also quantified. A higher density of <100>{100} than that of ½<111>{111} loops was observed. The loop size in PM2000 is bigger than those in the other samples.

PROGRESS AND STATUS

Introduction

Due to their excellent high-temperature mechanical properties and high swelling-resistance, reduced activation ferritic/martensitic (RAFM) steels and oxide-dispersed strengthened (ODS) alloys are promising first-wall and blanket structural materials for future nuclear fusion reactors [1,2]. The extremely severe environment induced by the fusion reaction requires materials able to withstand high dose neutron irradiation, high concentrations of transmutation produced He, high temperatures, large stresses, and potentially corrosive coolants [3]. A high concentration of He can degrade material performance. As He has a negligible solubility in metals and alloys, it readily combines with irradiation-induced and thermal vacancies to form He-vacancy complexes and eventually He bubbles in both the matrix and on interfaces such as martensite lath boundaries, grain boundaries, and secondary-phase particle-matrix interfaces [4]. A high density of small bubbles may impede dislocation movement and contribute to irradiation hardening. Furthermore, He bubbles, if allowed to reach a critical size, can transition into unstable growing voids, which can cause significant swelling [5]. High concentrations of He, either in large cavities/voids or small He bubbles at grain boundaries are undesirable because high-temperature tensile and creep properties may be degraded along with fracture toughness. One strategy to control He is by introducing a high density of bubble nucleation sites (e.g. dislocations, nano-oxides) to trap the He gas atoms in the matrix, to some extent screening the grain boundaries [1]. Besides He bubbles and voids, the formation of dislocation loops is another concern. It has been reported that sessile <100> dislocation loops are strong obstacles

to dislocation movement [6]. Both small gas bubbles and dislocation loops are microstructural features contributing to irradiation hardening.

As fusion reactors are not available to test material performance, alternate approaches are needed to simulate the anticipated irradiation conditions. Recently, a novel approach, the *in situ* He injection (IHSI) technique, has been developed to examine the effects of simultaneous neutron irradiation and He injection on microstructural evolution of candidate alloys [7]. The IHSI technique has been described in detail elsewhere [7]. In this report, we present transmission electron microscopy (TEM) characterization results of neutron irradiated and He injected RAFM/ODS alloys. Two ODS alloys and one RAFM steel (i.e., PM2000, 14YW, and modified F82H, respectively) with 4.7 μm thick NiAl layer bonded or adjacent to a sample surface were neutron irradiated to a dose of 21.2 dpa at 500°C. The He concentration in regions near the NiAl coating is calculated to be about 1230 appm. Focused ion beam (FIB) methods were used to prepare cross-sectional foils for TEM study. Features such as He bubbles and voids, dislocation loops, secondary-phases, and nano-oxides were characterized.

Specimen Preparation and TEM Characterization Methods

The compositions of the RAFM/ODS alloys examined are listed in Table 1. Among them, samples PM2000 and 14YW are ODS alloys fabricated through powder metallurgical procedures. Details of the material fabrication were described in Ref. 7. Sample F82H-mod is a RAFM alloy processed by conventional steel metallurgy. Before the irradiation, a 20% cold work was applied to the F82H-mod specimen to generate a high dislocation density. All samples were neutron irradiated to a dose of 21.2 dpa at 500°C. The thickness of NiAl is 4.7 μm, which gives a He concentration of about 1230 appm in the alloy matrix extending to a depth of ~ 6 μm away from the NiAl coating.

Table 1. Composition of examined RAFM/ODS alloys

Alloy	Composition (wt.%) with Fe balance									
	Cr	Ti	$Y(Y_2O_3)$	C	Al	W	Mn	Si	Ni	V
PM2000	19.00	0.5	0.5	-	5.5		-	-	-	-
14YW	14.00	-	0.25	-	-	3.00	-	-	-	-
F82H-mod	8.16	<0.005	-	0.097	-	1.98	0.13	0.10	0.01	0.20

Cross-sectional TEM samples of irradiated specimens were prepared by a FIB (FEI Quanta 3D). Foils were roughly cleaned with 2 keV Ga^+ ion beam at ±4° tilt angles to remove artifacts. The final cleaning was conducted using low-energy Ar^+ ion milling (Fischione Model 1040 NanoMill). A reference specimen, well annealed unirradiated pure Fe (99.99%), was used to determine FIB/nanomilling procedures to give artifact-free TEM foils. It was found that the reference foil after cleaning with the parameters listed in Table 2 does not exhibit any visible bubbles at under-focused TEM imaging conditions, and there is no diffraction contrast similar to irradiated-induced clusters or dislocation loops under bright-field two-beam condition and weak-beam dark-field imaging conditions. All TEM specimens of irradiated alloys were cleaned using the same procedure.

The TEM characterization was performed using a JEOL 2010F microscope working at 200 keV. The thickness of TEM samples was determined through convergent-beam electron diffraction (CBED). Sample compositions were confirmed using Energy Dispersive X-ray Spectroscopy (EDXS). Bright-field TEM images of He bubbles and voids were acquired at an under-focus of 750 nm. The measured bubble size corresponds to the inner-diameter of the first dark Fresnel ring. Based on our previous TEM imaging simulations, this measured value is about 87% of the actual bubble size at a defocus of 750 nm [8]. The dislocation loop was imaged using multiple diffraction vectors at two-beam conditions. A novel approach based on both crystallographic projection and *g.b=0* contrast has been adopted for the loop analysis [9]. It is noted that loops smaller than 4 nm cannot be differentiated from nano-oxides based on diffraction contrast at two-beam conditions. These small loops were excluded during loop quantification, although the ODS samples do contain a high density of such ultrafine contrast.

Table 2. Nanomilling cleaning procedures for artifact-free TEM samples.

Step	High tension (eV)	Time (min)	Beam current (nA)	Milling size (μm)	Tilt angle (°)	Temperature (°C)
1	1800	45				
2	900	45	150	40 × 20	± 10	-165
3	500	30				

RESULTS AND DISCUSSION

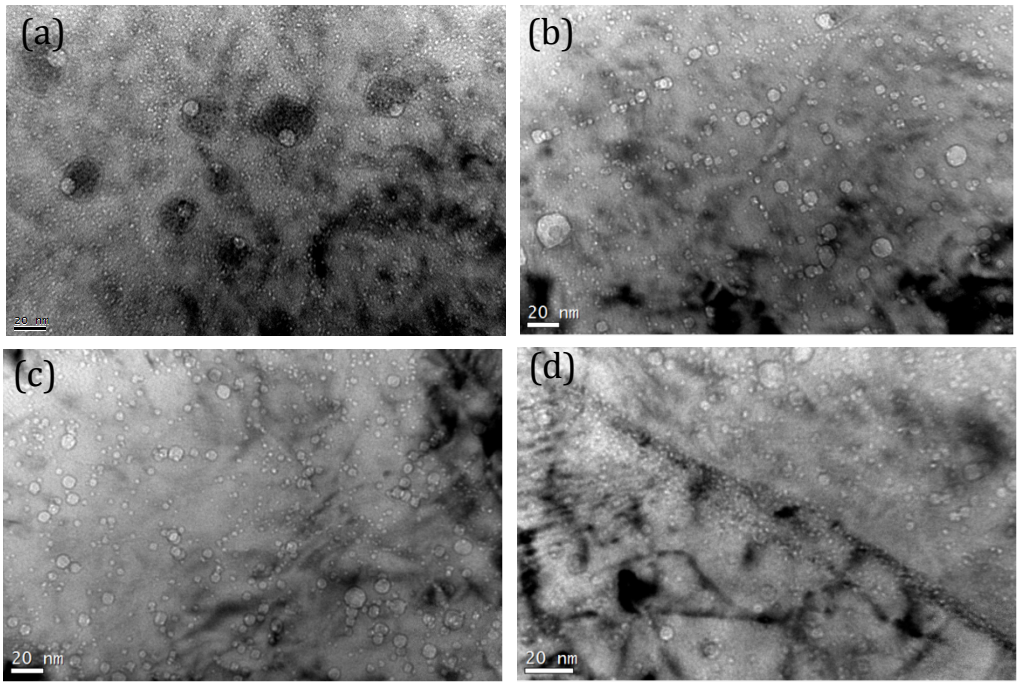

Fig. 1. TEM micrographs of He bubbles and voids in (a) PM2000, (b) 14YW, (c) F82H-mod, and (d) at a 14YW lath boundary.

Table 3. Size and density of He bubble/voids and dislocation loops in three alloys.

Alloy	He bubbles/voids		<100> dislocation loops		½<111> dislocation loops	
	size (nm)	density (m^{-3})	size (nm)	density (m^{-3})	size (nm)	density (m^{-3})
PM2000	Interface: 9.2 Matrix: 1.7	Interface: 9.3×10^{20} Matrix: 3.2×10^{23}	30.0±9.8	3.7×10^{21}	18.5±5.3	1.3×10^{21}
14YW	2.8	1.7×10^{23}	16.6±8.2	3.8×10^{21}	10.6±3.1	6.1×10^{20}
F82H-mod	3.7	6.9×10^{22}	18.6±5.3	3.0×10^{21}	Large: 38 Small: 13	1.6×10^{20}

Fig. 1 presents an overview of He bubble and voids distributed within three samples. The measured bubble sizes and densities are summarized in Table 3. The bubbles in the matrix of PM2000 (Fig. 1a) have an average size less than 2 nm, and the size distribution (not shown) is very narrow. At the interface of Y-rich particles, however, large voids up to 10 nm are found. Samples 14YW and F82H-mod contain both small He bubbles and large voids, as shown in Figs. 1b and 1c, respectively. The faceted planes of voids in both samples were identified to be mainly {100}. A few voids with {110} faceted planes were also observed. Despite a large fraction of voids distributed in the matrix, the lath boundaries were consistently decorated with a high density of small He bubbles less than 2 nm. One example of sample 14YW is shown in Fig. 1(d).

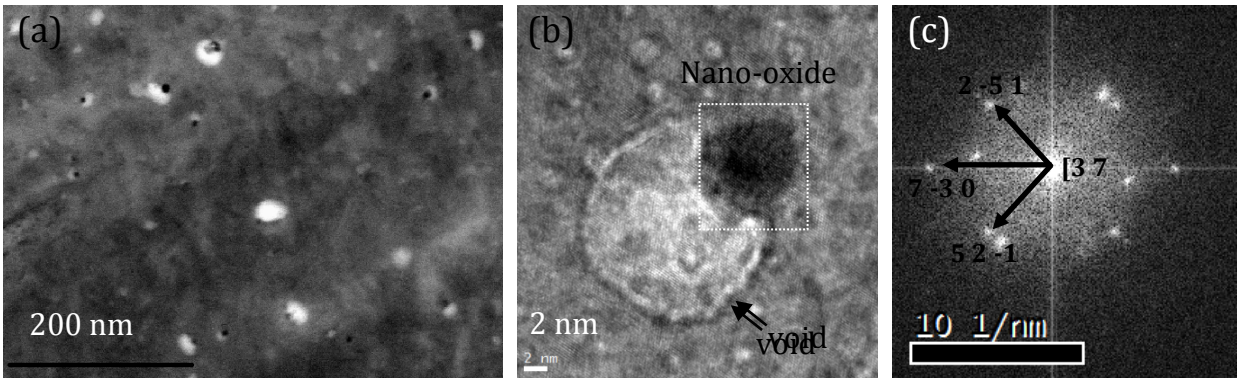

Fig. 2. TEM characterization of void-associated nano-particles in sample 14YW, (a) bright field image, (b) lattice image, and (c) FFT of the region in (b). The particle can be identified to be Y_2O_3.

The large voids distributed in F82H-mod are expected, while it is somewhat surprising to see similar voids in ODS alloys PM2000 and 14YW. It has been identified that sample F82H-mod exhibits large voids when irradiated to 380 appm He / 9 dpa at 500°C [10]. The ODS alloys, however, have a distinct microstructure from RAFM. It is anticipated that the high density of nano-oxides in ODS alloys should trap He in numerous subcritical size bubbles. The appearance of voids in the ODS alloys examined here may have three causes. First of all, the total available sites for He bubble nucleation is limited, which sets a threshold of He concentration that the alloy can contain. A He concentration above that limit may turn some He bubbles into voids. This limit is expected to be higher for ODS alloys than that for RAFM steels.

The other factor, which may be responsible for the void formation in the samples examined in this study, is related to secondary phases. It is clear in sample PM2000 (Fig. 1a) that large bubbles are associated with particles. These particles were identified to be a Y-rich amorphous phase. Similar void-particle association also exists in sample 14YW, as shown in Fig. 2a. Figs. 2(b) and 2(c) present the high-resolution lattice image and its Fast-Fourier-Transformation (FFT) of the particle. EDX cannot precisely measure the particle composition as the particle takes only about 5% of the excitation volume. However, the EDX quantification at the particle gives a Y concentration up to 3.1 wt.%, which is more than ten times higher than that in the bulk sample (0.25 wt.%). Further FFT identification confirms an Y_2O_3 phase. This is anticipated as other elements in this alloy (i.e., Fe, Cr, and W) have a much lower affinity for O than Y. The third reason is that the PM2000 and 4YW are not the same as the ODS variant, that we call nanostructured ferritic alloys (NFA), since the former contain fewer and coarser oxides of different character than the $Y_2Ti_2O_7$ complex oxide that are dominant for the latter class of ferritic stainless steels. These results are important since they demonstrate that the size, number density and character of the nanofeatures and secondary phases play a key role in irradiation tolerance. The existence of good and bad phases has been previously observed in austenitic stainless steels and is discussed in Reference 11.

In sample 14YW, regions with enhanced void formation were identified. The voids appear to be associated with secondary phases. One example is shown in Fig. 3. The phase shown in Fig. 3 was identified as a Cr-rich phase, and its selected-area diffraction pattern (SADP) was indexed to be Cr_5O_{12}. It should be noted that all the phase identification in this study should be considered preliminary as it is only based on one or two diffraction patterns. It is not uncommon that one pattern can be indexed to be multiple phases. Unambiguous phase identification will be conducted by examining more than one SADPs at different tilt orientations.

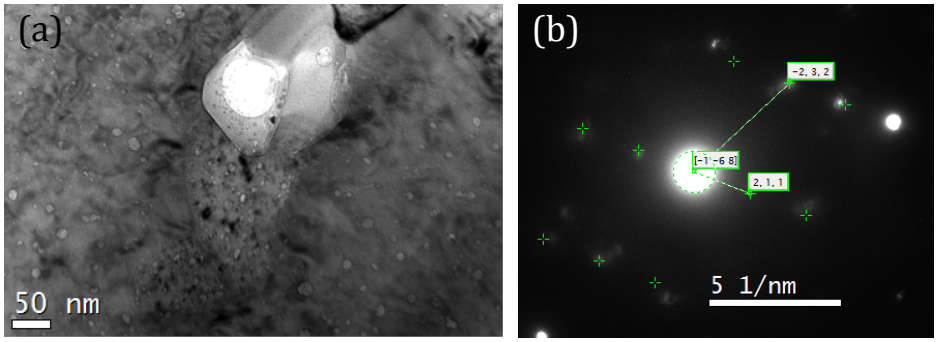

Fig. 3. (a) Bright-field TEM image of a Cr-rich secondary phase with large voids and bubbles, (b) SADP of the Cr-rich phase, which can be indexed to be Cr_5O_{12}. The SADP was overlapped with simulated diffraction patterns of Cr_5O_{12} phase under [-1 -6 8] zone axis.

Micrographs showing the dislocation loops seen in each alloy are shown in Fig. 4, and the measured loop size and density are summarized in Table 3. Note that only loops bigger than 4 nm were counted in this study. For each field of view, multiple micrographs at different two-beam conditions near the <100> zone axis are acquired, and a representative one is shown in Fig. 4. The diffraction vectors used to excite the loops are drawn in the micrograph. The rotation angle of the microscope is zero, indicating that the crystal orientation in the diffraction pattern and that in the micrograph are the same. Under the <100> zone axis, <100>{100} loops

exhibit edge-on double-line contrast perpendicular to <100> directions, while ½<111>{111} loops exhibit elliptical shapes with the major axis perpendicular to the <110> direction. Other types of dislocation loops were not observed, which is consistent with previous reports [9, 12]. The details of the method used for dislocation loop analysis can be found elsewhere [12].

Some interesting preliminary conclusions are obtained from this study. First, the high density of dislocation loops observed, and associated total line length, are much greater than expected for irradiations at 500°C. For example, in our previous study, the dislocation loop density of RAFM alloys irradiated to 9 dpa at 500°C with 380 appm He is much lower [13]. The loop density may increase at the higher dose, but this is inconsistent with the saturation of hardening at lower temperatures and the generally complete absence of hardening at higher temperatures around 500°C in ferritic alloys. The possible impact of high He levels on loop evolution remains to be determined. Secondly, a much higher density of <100>{100} than ½<111>{111} loops was found. This observation is consistent with other studies on RAFM/ODS alloys irradiated at high temperatures [12]. The different loop-density has been attributed to the higher mobility of ½<111>{111} loops, which might migrate to sinks such as grain boundaries, interfaces, and line dislocations. The <100>{100} loops, on the other hand, are less mobile and grow to form bigger loops. Although it has been reported that the <100>{100} loops at 500°C also have a significant mobility [14], the results from this study suggest otherwise. Lastly, the loops in PM2000 (30 nm for <100> loops) are larger than the two other alloys (16 nm and 19 nm). Note, that these observations are also preliminary and subject to future verification.

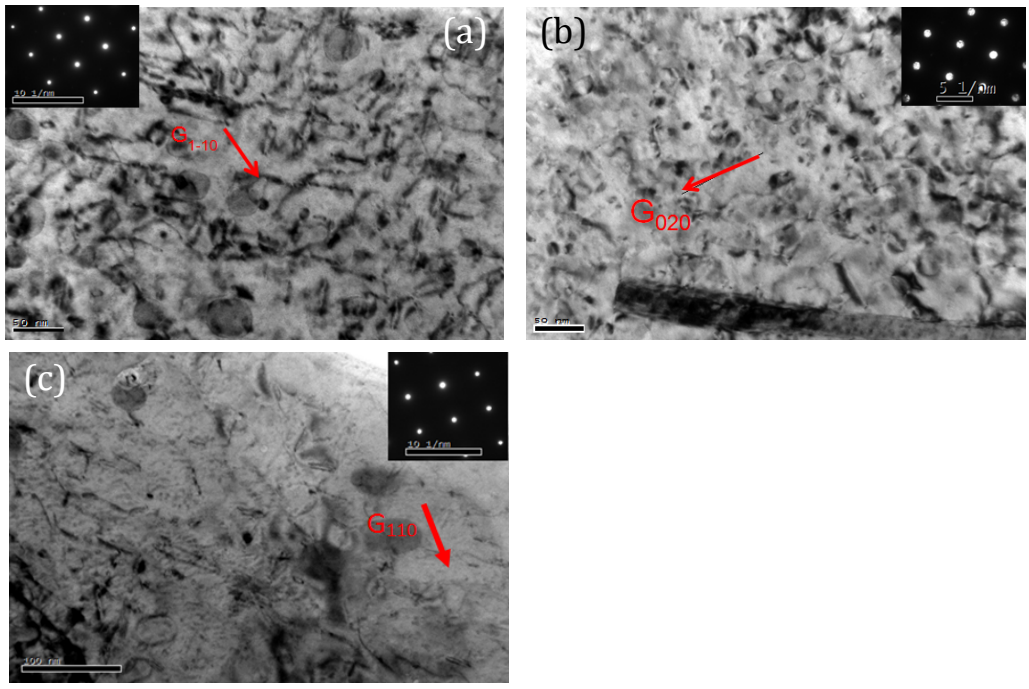

Fig. 4. TEM micrographs showing dislocation loops of samples (a) PM2000, (b)14YW, and (c) F82H-mod.

REFERENCES

[1] G. R. Odette, M. J. Alinger, and B. D. Wirth*, Annu. Rev. Mater. Res.* **38** (2008) 471.

[2] R. J. Kurtz, A. Alamo, E. Lucon, Q. Huang, S. Jitsukawa, A. Kimura, R. L. Klueh, G. R. Odette, C. Petersen, M. A. Sokolov, P. Spätig, and J. W. Rensman, *J. Nucl. Mater.* **386-388** (2009) 411.

[3] N. Baluc, K. Abe, J.L. Boutard, V.M. Chernov, E. Diegele, S. Jitsukawa, A. Kimura, R.L. Klueh, A. Kohyama, R.J. Kurtz, R. Lässer, H. Matsui, A. MÖslang, T. Muroga, G.R. Odette, M.Q. Tran, B. van der Schaaf, Y. Wu, J. Yu, and S.J. Zinkle, Nucl. Fusion 47 (2007) S696.

[4] H. Ullmaier, *Nucl. Fusion.* 24 (1984) 1039.

[5] R. E. Stoller and G. R. Odette, *J. Nucl. Mater.* **131** (1985) 118.

[6] R. Schäeublin and Y. L. Chiu, *J. Nucl. Mater.* **362** (2007) 152.

[7] G. R. Odette, P. Miao, D. J. Edwards, T. Yamamoto, R. J. Kurtz, and H. Tanigawa, *J. Nucl. Mater.* **417** (2011) 1001.

[8] B. Yao, D. J. Edwards, R. J. Kurtz, G. R. Odette, and T. Yamamoto, *Fusion Reactor Materials Program* **51** (2011), 85.

[9] B. Yao, D. J. Edwards, and R. J. Kurtz, G. R. Odette, T. Yamamoto, "Maps of Dislocation Loops in Irradiated bcc Fe–Based Steels." To be submitted.

[10] T. Yamamoto, G. R. Odette, P. Miao, D. J. Edwards, and R. J. Kurtz, *Fusion Reactor Materials Program* **44** (2008) 44.

[11] Y. Dai, G. R. Odette, and T. Yamamoto in: Konings R. J. M., (ed.) *Comprehensive Nuclear Materials*, Vol. 1 (2012) pp. 141-193 Amsterdam: Elsevier.

[12] J. Chen, P. Jung, W. Hoffelner, and H. Ullmaier, *Acta Materialia* **56** (2007) 250.

[13] D. J. Edwards, R. J. Kurtz, G. R. Odette, and T. Yamamoto, *Fusion Reactor Materials Program* **47** (2009) 59.

[14] R. Bullough and R. C. Perrin, *Proc. Roy. Soc. Lond. A* **305** (1968) 541.

2.2 Reference Characterization of the Advanced ODS 14YWT-SM12 Heat Used in HFIR JP30/31 Neutron Irradiation Experiment — D. T. Hoelzer, K. A. Unocic, E. T. Manneschmidt and M. A. Sokolov (Oak Ridge National Laboratory)

OBJECTIVE

Obtain results from characterization of the microstructures and mechanical properties of specimens produced from three heats of the advanced oxide dispersion strengthened (ODS) 14YWT-SM12 ferritic alloys with different extrusion temperatures to compare with irradiated specimens from the HFIR JP30/31 neutron irradiation experiment.

SUMMARY

Plate samples of ODS 14YWT-SM12 were produced from material extruded at 850, 1000 or 1150ºC followed by rolling parallel to the extrusion direction at 1000ºC to 50% reduction in thickness. Results from tensile tests conducted at 25ºC to 800ºC showed slightly lower strengths, but significantly better ductility in all the 14YWT-SM12 heats compared to results from previous 14YWT heats. The microstructural characteristics observed by SEM and TEM analyses showed that slightly larger grains with less uniformity in grain size had formed in the SM12 heats compared to previous 14YWT heats. The observed differences in the mechanical properties and grain structures of the SM12 heats compared to previous 14YWT heats were most likely due to the lower O, C and N levels achieved in producing the 14YWT-SM12 heats.

PROGRESS AND STATUS

Introduction

The advanced oxide dispersion strengthened (ODS) 14YWT ferritic alloy was developed for extreme neutron irradiation environments such as those encountered in plasma facing components of fusion reactors. The primary goal in development of the ODS 14YWT ferritic alloy was to obtain ultra-fine grains plus a high concentration of nano-size oxide particles, or Y-, Ti- and O-enriched nanoclusters (NC), that are responsible for the excellent strength and creep properties at elevated temperatures and good fracture toughness properties at low temperatures. In addition, the very high interfacial area associated with the ultra-fine grain structure and high concentration of NC provides high sink strength for trapping point defects that make 14YWT a very promising material for achieving high tolerance to neutron irradiation damage. However, there have only been a few studies conducted on 14YWT that consisted of neutron irradiations to relatively high doses. To date, SS-J3, DCT and TEM specimens from past 14YWT heats have only been included in two MATRIX collaborations that were conducted in the past between DOE (LANL)/ CEA, Saclay using the Phenix Reactor.

In 2011, the US Fusion Materials Program in collaboration with JAEA sponsored the construction of the JP30/31 neutron irradiation experiment at HFIR. This experiment was planned to irradiate specimens from several ferritic alloys in 3 sub-capsules at temperatures of 300ºC, 400ºC and 650ºC to a neutron dose of ~20 to 25 dpa depending on the final number of cycles. The specimen matrix included a variety of test specimens that were fabricated from the ODS 14YWT-SM12 ferritic alloy [1]. This alloy was developed in the NE Fuel Cycle Research and Development (FCRD) program and was produced by mechanical alloying to form three

heats differentiated by extruding the ball-milled powder at 1150ºC (SM12a), 1000ºC (SM12c) and 850ºC (SM12d). Plates were fabricated from the extruded bars by rolling either parallel or normal (cross) to the extrusion axis. The specimens fabricated from the plates consisted of SS-J3, APFIM, TEM, DCT, M5PCCVN and MMPC to provide for detailed PIE studies of the microstructure and mechanical properties in the future. The purpose of this report is to cover the preliminary results obtained from the reference characterization of the microstructures and mechanical properties of the 14YWT-SM12 heats to compare with irradiated specimens from the HFIR JP30/31 experiment.

Processing of 14YWT-SM12

The 14YWT-SM12 heat was produced by mechanical alloying (MA) using gas-atomized powder produced by Special Metals with nominal composition of Fe-14Cr-3W-0.4Ti (Fe pre-alloyed) and nano-size (17-31 nm) Y_2O_3 powder produced by Nanophase, Inc. The blended powder consisting of 99.7% Fe pre-alloyed and 0.3% Y_2O_3 powder (wt. %) was ball milled using the Zoz Simoloyer CM08 high kinetic energy mill for 40 h in an Ar atmosphere. Three 750 g batches of ball-milled powder were sealed in 2.9 inch diameter mild steel cans and degassed at 400ºC in vacuum before being hermetically sealed. The three sealed cans were annealed for 1 h at 850ºC and then 1 h at 1150ºC (SM12a heat), 1000ºC (SM12c heat) and 850ºC (SM12d heat) followed by extrusion. The cans were extruded through a rectangular shaped die to form bars. The extruded bars were annealed at 1000ºC for 1 h in vacuum and then cut into 3 sections of equal lengths for rolling. One section of each heat was rolled parallel (PR) to the extrusion direction at 1000ºC to ~50% reduction in thickness to form plates.

Chemical analysis was performed on ball milled powder and an extruded sample to correlate the interstitial O, C and N levels with processing of the ODS 14YWT-SM12 ferritic alloy. The results of the chemical analysis are shown in Table 1. The O and C levels were very similar between the ball milled powder and extruded sample. However, the results showed a very low N level in the ball-milled powder that increased significantly after extrusion. The reason for this increase is not apparent. Typically, poor ball milling conditions lead to significant contamination of both O and N due to the ingress of air into the chamber during ball milling. However, the O level was controlled very well using the ball milling conditions for the 14YWT-SM12 powder. Contamination of the ball-milled powder during degassing is not likely since the powder was degassed at 400ºC in vacuum. After degassing, the can was then sealed by crimping the tube connecting the can to the vacuum pump. Thus, to help understand the reason for the high N level after extrusion, a second sample will be prepared from 14YWT-SM12 and sent to DIRATS for independent chemical analysis.

Table 1. Comparison of the O, C and N levels of the ball milled powder and bulk extruded sample of 14YWT-SM12.

Condition	Composition (wppm)		
	O	C	N
Ball milled powder	1184	128	117
Extruded sample	1080	150	1740

Preparation of Specimens

Specimens were fabricated from plates of the three 14YWT-SM12 heats that were rolled parallel to the extrusion direction. The fabricated specimens consisted of miniature tensile (SSJ3; 5 x 1.4 x 0.75 mm gage), disk compact tension fracture toughness (DCT; ~Ø12.5 x 0.2 mm), TEM disk (Ø3 x 0.25 mm) and small angle neutron scattering coupon (SANS; 10.2 x 10.2 x 2.5 mm). The list showing the type, orientation and number of specimens prepared for the reference characterization studies is shown in Table 2. The DCT specimens were fabricated with the test load oriented parallel, or longitudinal (L), and the notch for pre-cracking oriented normal, or transverse (T), to the extrusion direction of the plates. Similarly, the SS-J3 tensile specimens were fabricated with the gage section lying parallel (L) or transverse (T) to the extrusion direction of the plates.

Table 2. Specimens fabricated from the plates of the three 14YWT-SM12 heats for the reference characterization studies.

Plate heat	Specimen Type	Orientation	Number
SM12a	DCT	L-T	13
	SS-J3	L	12
	SS-J3	T	5
	SANS	-	2
	TEM	-	3
SM12c	DCT	L-T	12
	SS-J3	L	19
	SS-J3	T	6
	SANS	-	2
	TEM	-	2
SM12d	DCT	L-T	16
	SS-J3	L	15
	SS-J3	T	12
	SANS	-	2
	TEM	-	1

Characterization Study

The purpose of the reference characterization study was to correlate the different processing conditions for producing the three 14YWT-SM12 heats with their microstructures and mechanical properties. The study focuses on microstructure analysis using SEM, TEM and possibly Atom Probe and on mechanical properties using hardness, tensile and fracture toughness tests. The results from this study will be compared later to those obtained from PIE of the irradiated specimens from JP30/31. The results of this comparison will help guide future development of the ODS 14YWT ferritic alloy for advanced nuclear energy systems including plasma facing components of fusion reactors.

Microstructural Analysis

The microstructures of the three 14YWT-SM12 heats were investigated using Transmission Electron Microscopy (TEM). The initial investigation was performed on electro-polished thin foil disk specimens that were prepared from each heat. The thin foil specimens were examined using the Philips CM200 FEG-TEM/STEM (Field Emission Gun-TEM/Scanning Transmission Electron Microscope) with XEDS, EELS/EFTEM (X-ray Energy Dispersive Spectroscopy, Electron Energy Loss Spectroscopy/Energy-Filtered TEM). The analysis of the grain structure was conducted using bright-field (BF) diffraction contrast imaging. Energy-Filtered TEM was used to investigate the oxide particles that formed in the 14YWT-SM12a heat. This heat was investigated first since the higher extrusion temperature (1150ºC) used to produce it most likely resulted in the largest oxide particle size compared to the oxide particles that formed in the two heats extruded at lower temperatures.

The microstructural characteristics of the three 14YWT-SM12 heats observed by BF imaging at low magnifications are shown in Figure 1. The analysis showed that all three heats contained grains that were similar in size, size distribution and morphology. The microstructures consisted of grains that were mostly less than 1 mm in size and wide distribution of sizes. The grains were slightly elongated in the extrusion and rolling directions. These results were consistent with those obtained from SEM analysis [1]. In addition, the dislocation analysis showed a relatively low dislocation density in the grains of the three heats.

The salient microstructural features of 14YWT-SM12 observed by BF imaging at high magnifications are shown in Figures 2, 3 and 4 for the SM12a, SM12c and SM12d heats, respectively. The results showed that the in matrix regions of the grains were mostly featureless. However, a low number density of visible particles larger than ~10 nm was observed in all the heats, but that these particles were non-uniformly distributed. Some of the grains in the heats showed the presence of a high density of very small particles. For example, the particles observed with dark contrast in the BF micrographs for the SM12d heat in Figure 4 were <4 nm in size. These small particles are most likely the Ti-, Y- and O-enriched nanoclusters, but this inference will need to be confirmed by EFTEM and atom probe in the future.

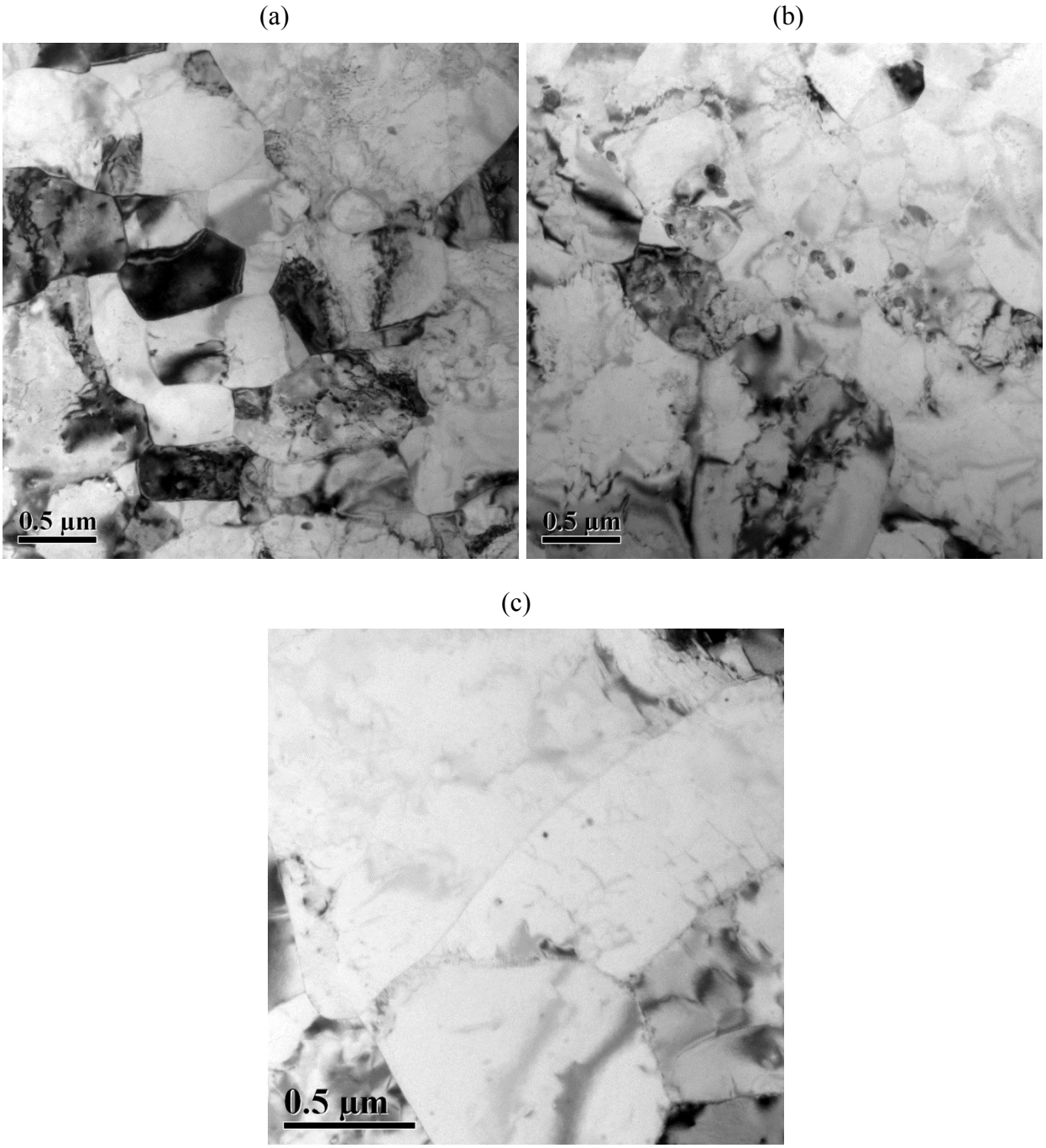

Figure 1. TEM BF micrographs showing the general microstructural characteristics of the (a) 14YWT-SM12a, (b) 14YWT-SM12c and (c) 14YWT-SM12d heats.

The results of the EFTEM analysis of the oxide particles that formed in the 14YWT-SM12a heat are shown in Figure 5. Several particles appearing with dark contrast near the edge of the thin foil specimen are observed in the Fe-M jump ratio map shown in Figure 5a. The dark contrast results from local displacement of Fe atoms by the particle that lowers the inelastic scattering

intensity in that region. There was one large particle that was ~50 nm in diameter and several particles <10 nm in size that were observed in the Fe M-jump ratio map. These particles along with several additional particles <10 nm in size are observed in the Ti L-composition map shown in Figure 5b. The bright contrast indicated that Ti atoms are associated with these particles, which is consistent with the small particles being Ti-, Y- and O-enriched nanoclusters.

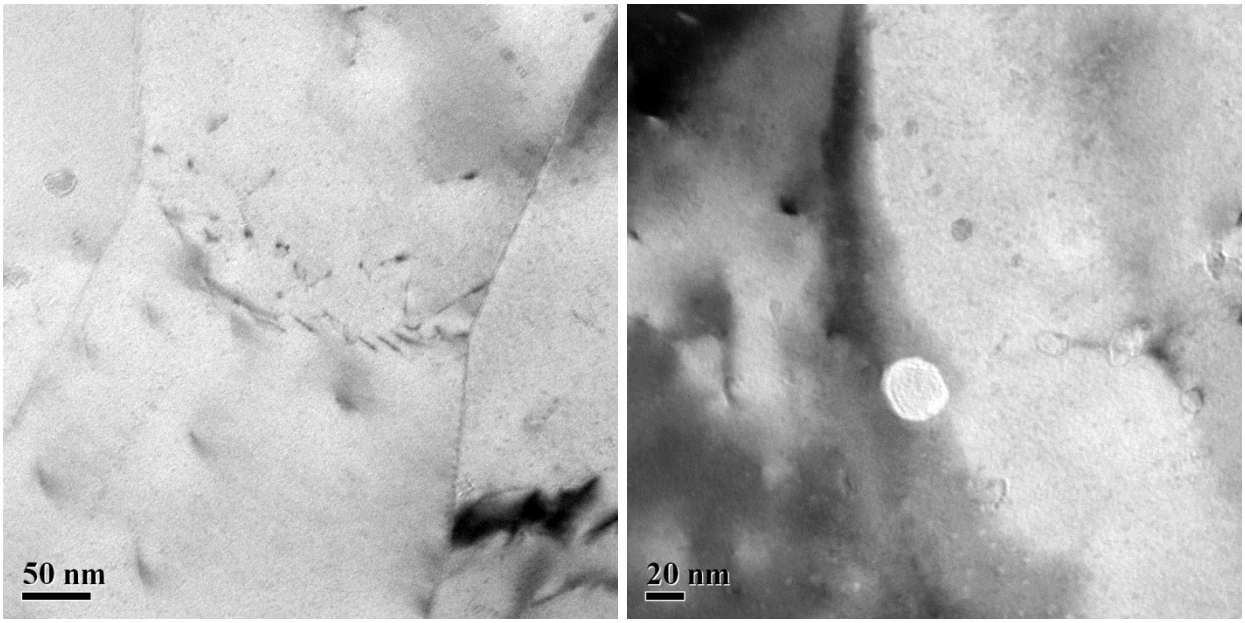

Figure 2. High magnification TEM BF micrographs showing the in-matrix regions of grains in the 14YWT-SM12a heat.

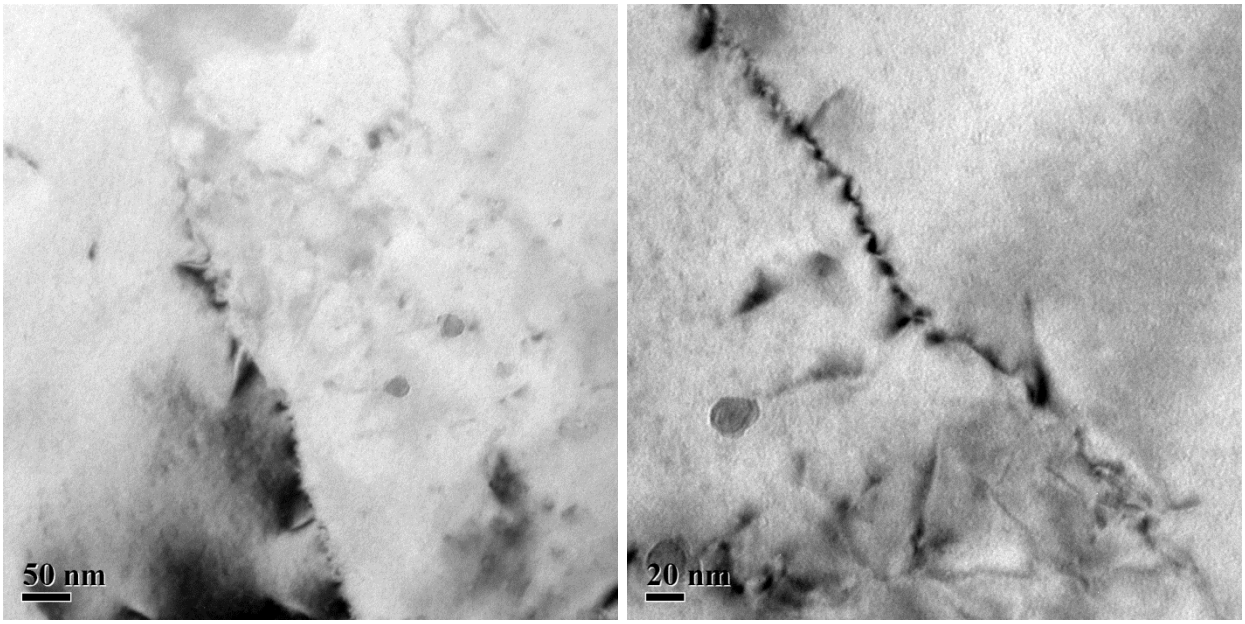

Figure 3. High magnification TEM BF micrographs showing the in-matrix regions of grains in the 14YWT-SM12c heat.

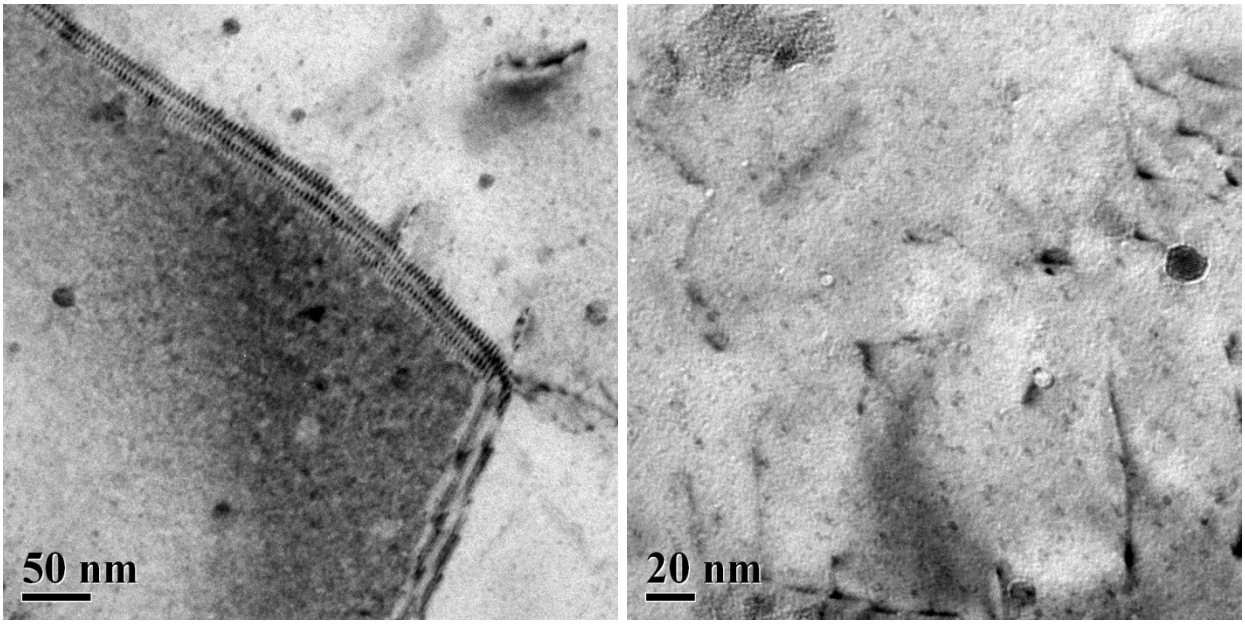

Figure 4. High magnification TEM BF micrographs showing the in-matrix regions of grains in the 14YWT-SM12d heat.

The EFTEM results were surprising since past research has shown that the Fe-M jump ratio method was very effective for producing reliable maps showing the size and distribution of oxide particles with resolution approaching 1 nm [2]. The Ti L-jump ratio and L-composition maps obtained from the same regions were typically noisier with lower resolution. However, the EFTEM results of this study showed that the Ti L-composition map resulted in better resolution for observing small particles. There may be several reasons for these differences in results. Results from the past investigations were obtained with the Philips CM30 TEM, which was a 300 kv instrument with a LaB_6 filament that produced a high probe current that achieved high-resolution EFTEM maps. The results for 14YWT-SM12a were obtained with the Philips CM200 FEG-TEM/STEM, which is a 200 kv instrument with an Schottky field emission gun that does not produce as high a probe current. The resolution of EFTEM maps is related to the incident electron energy and to signal-to-noise issues, which partly explains why EFTEM maps obtained from the CM30 showed better resolutions than those from the CM200. Another factor was that the Fe M post-edge and pre-edge maps used for producing the Fe M-jump ratio map showed low inelastic scattering intensity that contributed to poor signal-to-noise ratio. Also, the t/l image shown in Figure 5c indicated that the thin foil region was very thin. The t/l is obtained from:

$$t/l = \ln(\text{unfiltered image}/\text{zero-loss image})$$

where l is the inelastic scattering mean free path and is ~140 nm for the 14YWT composition. The diagonal line shown in Figure 5c is plotted in Figure 5d to show the variations in t/l with distance. The results indicated that most of the thin foil region where the EFTEM analysis was performed on had a thickness that was <30 nm. This resulted in low signal. Thus, the lower accelerating voltage and probe current of the CM200 and the thin thickness of the thin foil region contributed to the poor resolution of the Fe M-jump ratio map. Evidently, the method

used for removing the background near the Ti L ionization edge to calculate the Ti L-composition map was not as sensitive to the low signal-to-noise.

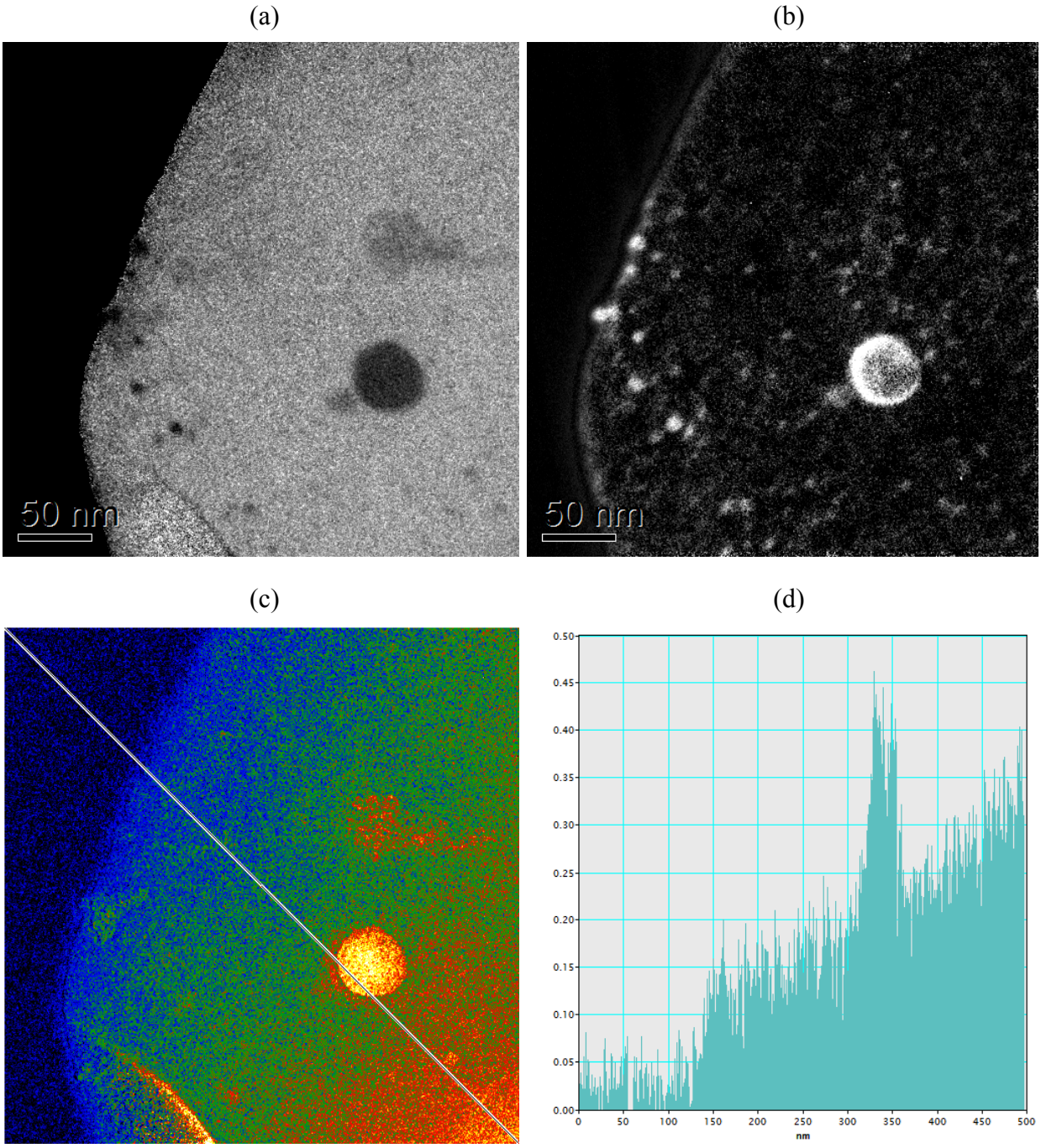

Figure 5. EFTEM analysis of 14YWT-SM12a near the thin foil edge showing (a) Fe M-jump ratio map, (b) Ti L composition map, (c) t/l thickness map and (d) thickness profile associated with line observed in the thickness map in (c).

Tensile Properties Analysis

Tensile tests were performed on SS-J3 specimens of the 14YWT-SM12 heats over the temperature range from room temperature (25ºC) to 800ºC using a strain rate of 1 x 10^{-3} s^{-1}. The results of the tensile tests are shown in Figure 6. The results indicated that values for the yield and ultimate tensile stresses and uniform and total elongations of the three heats were very similar over the temperature range. Compared to tensile properties of previous 14YWT heats, the 14YWT-SM12 heats showed generally lower strength and higher ductility properties. The yield stresses and ultimate tensile strengths of the SM12 heats were all near ~1050 MPa and ~1200 MPa, respectively, at room temperature and decreased with temperature to ~260 MPa and ~300 MPa, respectively, at 800ºC. The uniform and total elongations of the SM12 heats were ~9-10% and ~21-24%, respectively, at room temperature, which is significantly better than the 1 to 2% uniform elongation typically observed in previous 14YWT heats. The changes in uniform and total elongations with increasing temperatures showed similar trends for the SM12a and SM12c heats compared to the SM12d heat. For the SM12a and SM12c heats, the uniform elongation decreased slightly with temperatures while the total elongation remained nearly constant up to 400-500ºC and then increased to a peak value near 700ºC. The changes in uniform and total elongations with increasing temperatures were much less for the SM12d heat.

The comparison of stress-strain curves for the 14YWY-SM12 heats at room temperature is shown in Figure 7. The stress-strain curves of the three SM12 heats are remarkably similar. The stress increases to the yield point and then increases with strain to similar values of ultimate tensile strengths of ~1150-1200 MPa and uniform strains of ~9%. After plastic instability denoted by necking of the specimens, the deformation proceeded with decreasing stress with increasing strain until failure, which occurred at similar fracture stresses and total elongations.

The sets of stress-strain curves that have currently been obtained from tensile tests over the temperature range from 25ºC to 800ºC are shown in Figures 8, 9 and 10 for the SM12a, SM12c and SM12d heats, respectively. The analysis of the curves showed that gradual work hardening occurred in the specimens tested at temperatures up to 400ºC that resulted in higher values of uniform strain. Above 400ºC, the work hardening saturates quickly resulting in lower values of uniform strain. However, the stress tends to decrease very slowly with increasing strain, indicating that deformation may be following a pseudo-creep mechanism that is enhanced by the relatively small grain size of the SM12 heats. In most cases, this deformation behavior covers more than 10% strain before the stress begins to decrease more rapidly with increasing strain leading to ultimate failure of the specimen.

The results obtained from the reference characterization studies to date have revealed several interesting aspects of the effect that different processing conditions had on the microstructures and tensile properties of the three 14YWT-SM12 heats. One point is that the relatively lower strength and higher ductility properties of the SM12 heats compared to previous 14YWT heats could be attributed to the lower O, C and N levels. Another point is that the different extrusion

(a)

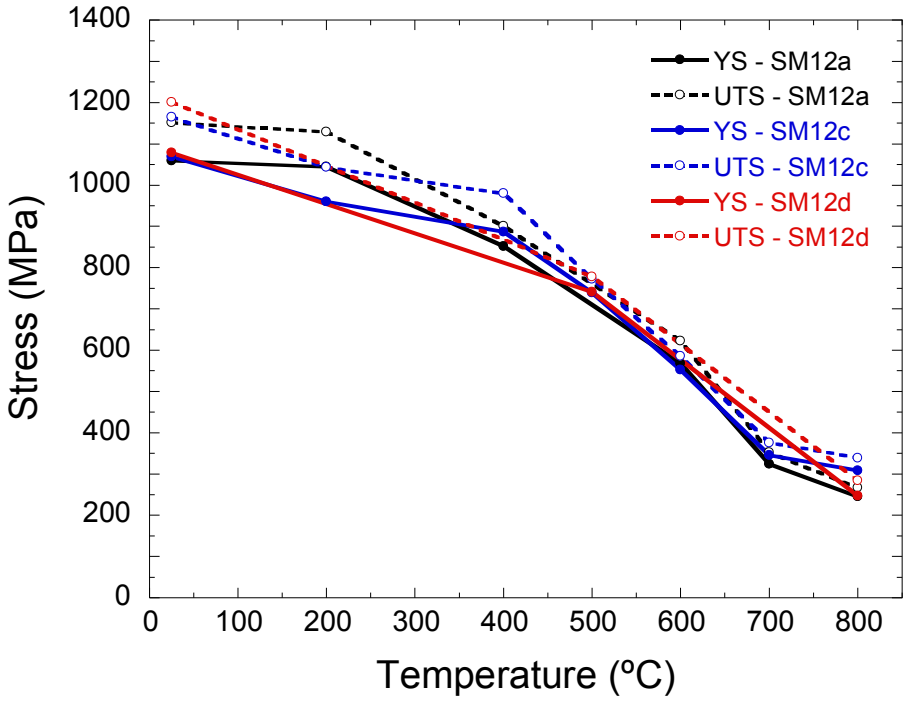

(b)

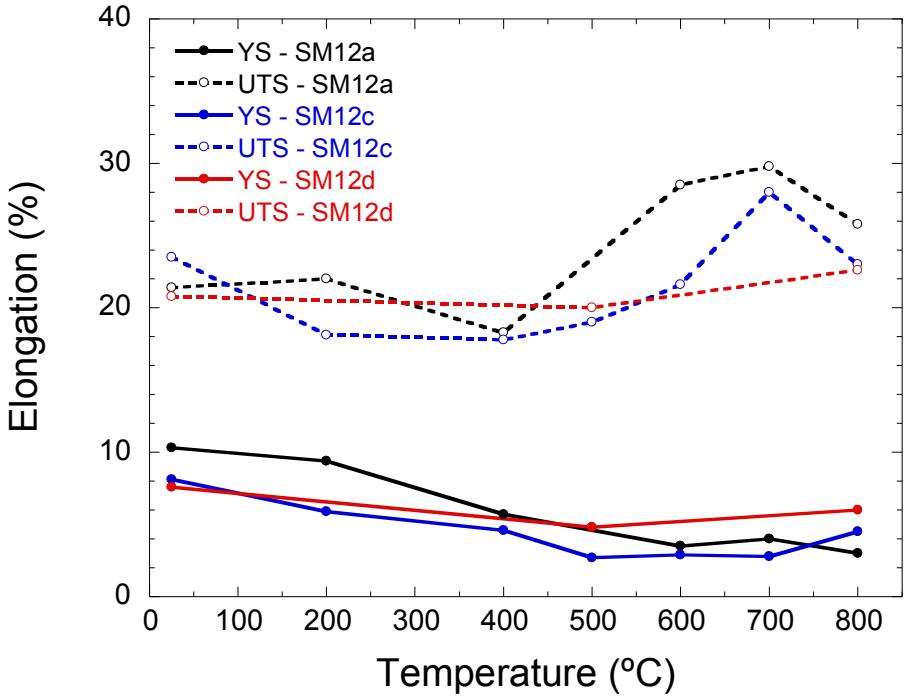

Figure 6. Results of the tensile tests conducted on specimens of the three 14YWT-SM12 heats over the temperature range from 25ºC to 800ºC. (a) Changes in yield and ultimate tensile stresses and (b) changes in uniform and total elongations as a function of temperatures.

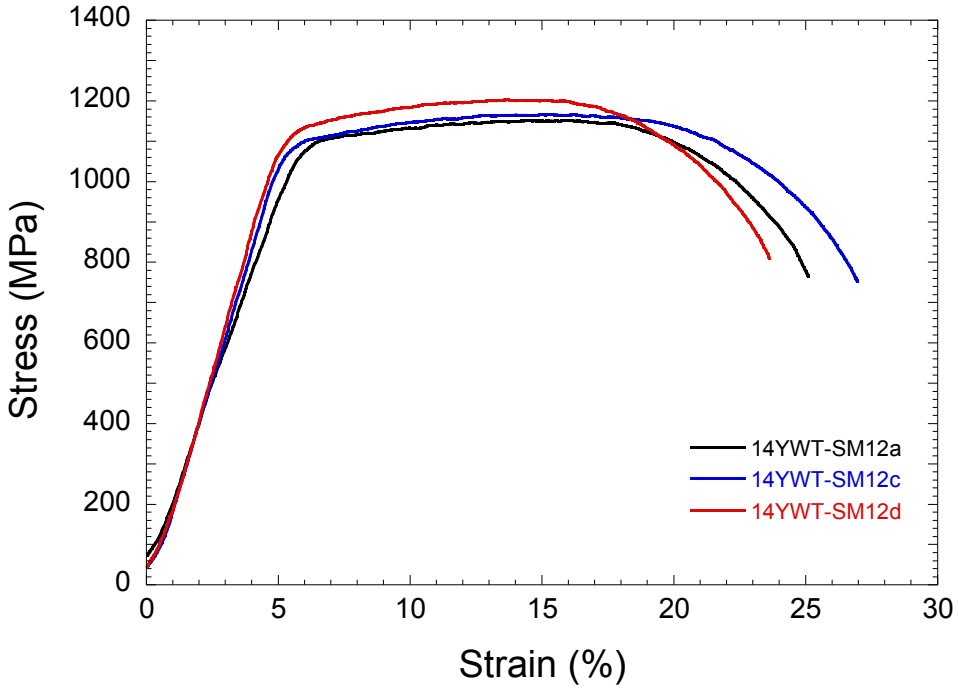

Figure 7. Comparison of stress strain curves from tensile tests at room temperature for the SM12a, SM12c and SM12d heats of 14YWT.

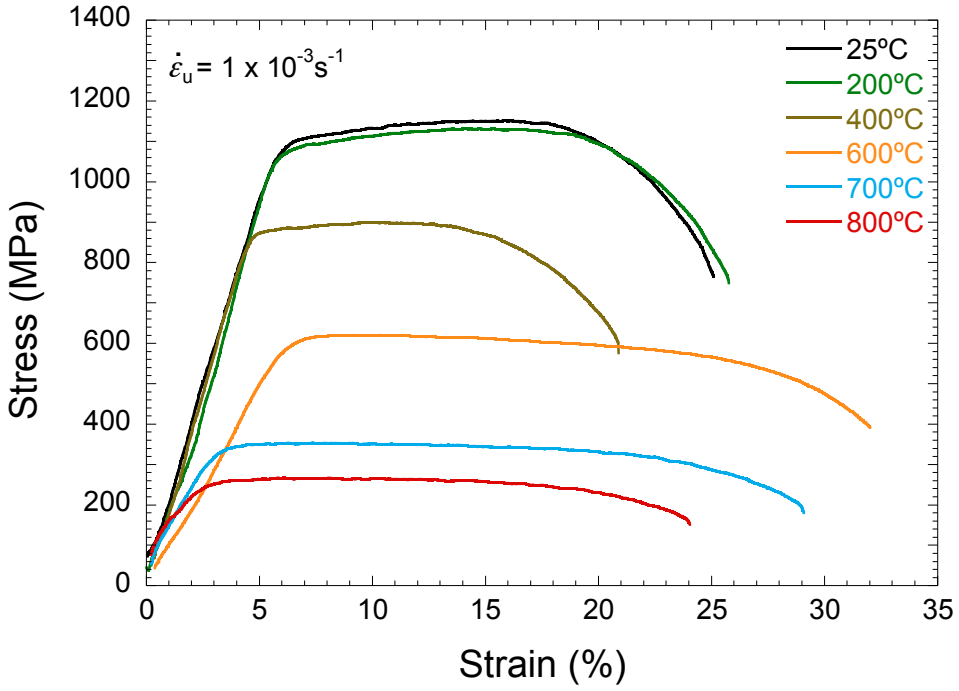

Figure 8. Stress strain curves from tensile tests ranging from 25ºC to 800ºC on 14YWT-SM12a.

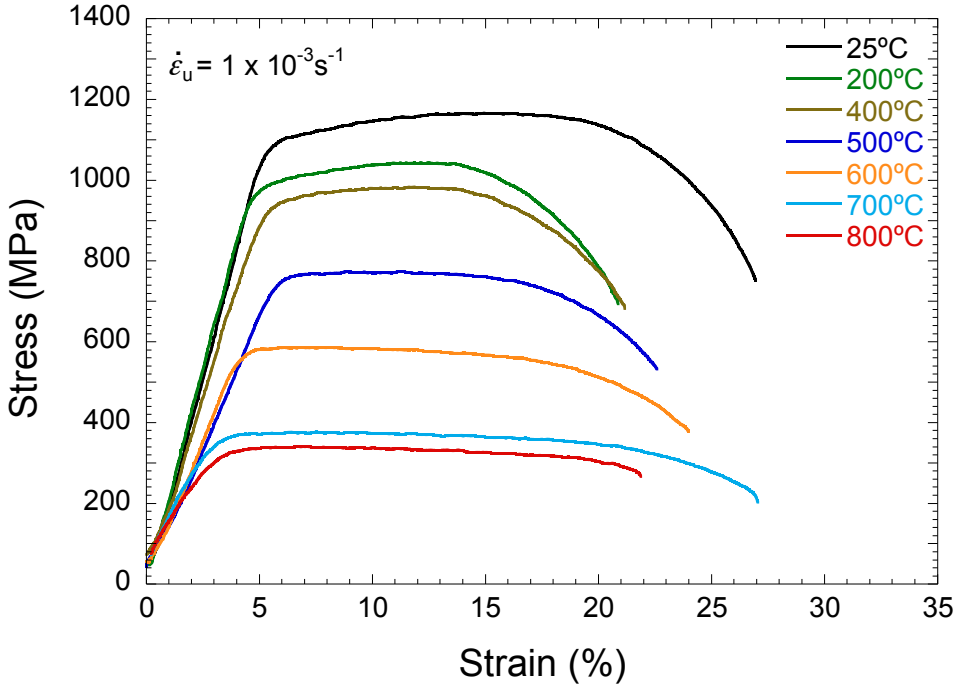

Figure 9. Stress strain curves from tensile tests ranging from 25ºC to 800ºC on 14YWT-SM12c.

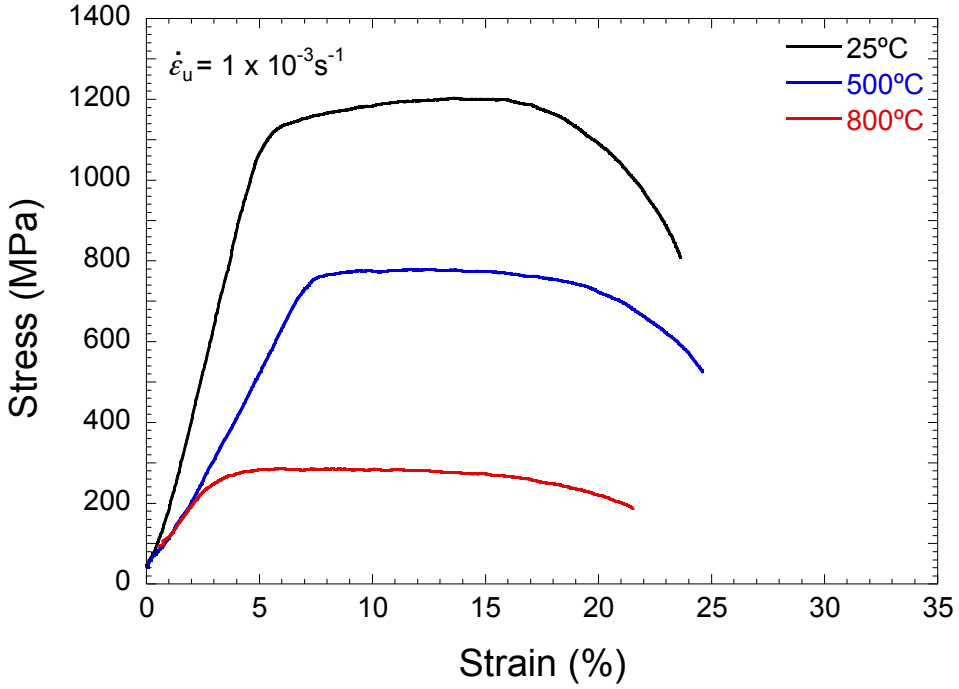

Figure 10. Stress strain curves from tensile tests ranging from 25ºC to 800ºC on 14YWT-SM12d.

temperatures had essentially no effect on the general microstructural features and tensile properties of the 14YWT-SM12 heats. The most likely reason for this result was due to the initial heat treatment that was performed on the cans containing the ball-milled powders used to produce the three heats. This heat treatment was for 1 h at 850ºC and was designed to form similar microstructures in the ball milled powders in each can before heat treating at the different temperatures for extruding the cans, which was for 1 h at 1150ºC for SM12a, 1000ºC for SM12c and 850ºC for SM12d. However, further microstructural characterization using advanced TEM techniques such as high angle annular dark field (HAADF) STEM imaging with the JEOL 2200FS-AC aberration-corrected STEM/TEM instrument and EFTEM analysis with the Philips CM200 TEM/STEM will be required to investigate more subtle differences in the nano-size oxide particle dispersions in the SM12 heats that will improve understanding the relationship between processing, mechanical properties and microstructure of the 14YWT-SM12 heats.

SUMMARY

Three heats of the advanced ODS 14YWT-SM12 ferritic alloy were produced by extrusion at different temperatures of 1150ºC (SM12a), 1000ºC (SM12c) and 850ºC (SM12d). Plate samples of the three heats were produced by rolling parallel to the extrusion direction at 1000ºC to 50% reduction in thickness. Results from tensile tests conducted over the temperature range from 25ºC to 800ºC showed lower strengths, but much better ductility in all the 14YWT-SM12 heats compared to results from previous 14YWT heats. The yield stresses and ultimate tensile strengths of the SM12 heats were ~1050 MPa and ~1200 MPa, respectively, at room temperature and decreased with temperature to ~260 MPa and ~300 MPa, respectively, at 800ºC. The uniform and total elongations of the SM12 heats were ~9-10% and ~21-24%, respectively, at room temperature. The TEM analysis of the 14YWT-SM12 heats showed that all three heats contained grains that were similar in size, size distribution and morphology. The microstructures consisted of grains that were mostly less than 1 mm in size with wide size distributions and slight elongated in the extrusion and rolling directions. The TEM results showed that the microstructures consisted of grains containing a low number density of particles larger than ~10 nm that were non-uniformly distributed. Both BF diffraction contrast imaging of the SM12 heats and initial EFTEM analysis of the SM12a heat revealed the presence of a high density of very small particles that were ~4-6 nm in size that were most likely the Ti-, Y- and O-enriched nanoclusters. However, this inference will need to be confirmed with additional EFTEM and atom probe analyses in the future.

FUTURE WORK

Detailed characterization of the microstructures and mechanical properties of the 14YWT-SM12 heats will continue. Since the ferromagnetic nature of the 3 mm dia. TEM disks prepared from the 14YWT-SM12 heats caused significant problems with alignment of the CM200 TEM/STEM, a set of new specimens will be prepared by lift-out of a small specimen (~10 mm x 8 mm x <1 mm thickness) from the polished section of the TEM disks and thinning by the Focused Ion Beam (FIB) method. These specimens will result in the achievement of better resolution with TEM imaging techniques. Several tensile tests will be conducted on specimens of the SM12a and SM12d heats to complete the high temperature tests. Fracture toughness (DCT) specimens were fabricated from the three heats and testing will focus on determining the fracture toughness transition temperature and possibly the fracture toughness at elevated temperatures.

ACKNOWLEDGEMENT

Research at Oak Ridge National Laboratory (ORNL) was sponsored by the Office of Fusion Energy Sciences, Office of Nuclear Energy, Science and Technology and research at the ORNL ShaRE Facility was supported in part by the Division of Scientific User Facilities, Office of Basic Energy Sciences, U.S. Department of Energy. ORNL is managed by UT-Battelle, LLC for the U.S. Department of Energy.

REFERENCE

1. D. T. Hoelzer, E. T. Manneschmidt, and M. A. Sokolov, Fusion Materials Semiannual Progress Report for the Period Ending December 31, 2011, DOE/ER-0313/51, Vol. 51, 2011, P. 22-31.
2. J. Bentley, D. T. Hoelzer, D. W. Coffey and K. A. Yarborough, *Microsc. Microanal.* **10**, Issue S02 (2004) 662-663.

2.3 Fabrication and Characterization of Oriented Fe-$Y_2Ti_2O_7$ Interfaces: Implications to the Development and Optimization of Nanostructured Ferritic Alloys — T. Stan, Y. Wu and G. R. Odette (University of California Santa Barbara), K. Sickafus (University of Tennessee), H. Dabkowska and B. Gaulin (McMaster University)

OBJECTIVE

The objective of this work is to better understand and characterize the interfaces between Y-Ti-O nano-features (NFs) and the bcc Fe-Cr ferrite matrix in nanostructured ferritic alloys (NFA).

SUMMARY

The smallest 2-3 nm features in NFA are $Y_2Ti_2O_7$ complex oxide cubic pyrochlore phase. The interface between the bcc Fe-Cr ferrite matrix and the fcc $Y_2Ti_2O_7$ plays a critical role in the stability, strength and damage tolerance of NFA. To complement other characterization studies of the actual embedded nano-features, a mesoscopic interface was created by electron beam deposition of a thin Fe layer on a {111} $Y_2Ti_2O_7$ bulk single crystal surface. We recognize that the mesoscopic interfaces may differ from those of the embedded NFs, but the former will facilitate characterization and investigations of the functionality of controlled interfaces, such as interactions with point defects and helium. The Fe-$Y_2Ti_2O_7$ interface was characterized using scanning electron microscopy (SEM), including electron back scattering diffraction (EBSD), atomic force microscopy (AFM), X-ray diffraction (XRD), and transmission electron microscopy (TEM). The polycrystalline Fe layer has two general orientation relationships (OR) that are close to: a) $(110)_{Fe}||(111)_{Y2Ti2O7}$ and $[001]_{Fe}||[1\text{-}10]_{Y2Ti2O7}$ [notably, this is a Nishiyama-Wasserman (NY) OR]; b) $(001)_{Fe}||(111)_{Y2Ti2O7}$ and $[100]_{Fe}||[1\text{-}10]_{Y2Ti2O7}$. High resolution TEM was used to characterize details of the interfaces, which ranged from being atomically sharp, with interface defects, to those with more diffuse interface zones that, in some cases, included a thin FeO_x layer.

PROGRESS AND STATUS

Background

Materials in fission and fusion reactor environments are subject to high temperatures, large time-varying stress, chemically reactive environments, and intense radiation fields [1]. Helium that is produced by transmutation reactions interacts with displacement damage to drive complex microstructural evolutions. Most notably, helium is insoluble in steels and precipitates as gas bubbles that act as formation sites for both growing voids and creep cavities, while helium also weakens grain boundaries over a wide range of temperatures. NFA have been found to be radiation tolerant since they contain an ultrahigh density of Y-Ti-O NFs that trap helium in harmless, fine-scale bubbles, suppressing void swelling and embrittlement. NFs also provide high stable sink densities for defect annihilation and high creep strength due to dislocation pinning [2].

Most previous TEM studies have indicated that the NFs are complex oxides, primarily fcc cubic pyrochlore $Y_2Ti_2O_7$. For example, scanning transmission electron microscopy (STEM) energy dispersive X-ray (EDX) measurements on NF extracted from NFA MA957, reported by

Sakasegawa et al., indicate that they are non-stiochiometric $Y_2Ti_2O_7$, with Y/Ti < 1.0 for precipitates in the larger size range up to 15 nm and Y/Ti ≈ 0.5 for the smallest pyrochlore features [3]. At largest sizes, from ≈ 15 to 35 nm, the oxides are closer to stiochiometric, with Y/Ti ≈ 1.0. Yamashita et al. also found non-stiochiometric $Y_2Ti_2O_7$, but generally with a range of Y/Ti slightly greater than 1 [4,5]. Klimiankou et al. found near stoichiometric $Y_2Ti_2O_7$ in a 9Cr NFA using electron energy loss spectroscopy, HRTEM-fast Fourier transform (FFT) power spectra indexing and energy filtered TEM (EFTEM) methods [6,7]. Early x-ray diffraction (XRD) studies by Okuda and Fujiwara also indicated the presence of $Y_2Ti_2O_7$ in a 14Cr model NFA [8]. This observation has been confirmed by Sasasegawa et al. based on XRD measurements of nanopore filtered oxides extracted from a 9 Cr martensitic alloy [8]. Recently, Yu et al. reported a comprehensive TEM characterization study of NFA MA957 in different conditions, using various techniques [9]. This work clearly showed that extracted NFs are structurally consistent with $Y_2Ti_2O_7$ and generally are near stoichiometric with Y/Ti ratios from 0.5 to 1. The dominant in-foil interface was found to be parallel to the {100} planes in Fe, although the oxide themselves could not be indexed. Note Yu also discusses some other recent work in the literature that did not find the pyrochlore yttrium titanate. Finally, a recent high resolution TEM (HRTEM) study by Cisten et al. confirmed that the in-foil NFs in the same friction stirred weld variant of MA957 are $Y_2Ti_2O_7$ [10]. The study on the TEAM 0.5 microscope at LBL showed that the dominant NF in-foil interface OR is $(100)_{Matrix}||(100)_{Y2Ti2O7}$ and $[001]_{matrix}||[1\text{-}10]_{Y2Ti2O7}$.

The high density of NFs trap He in fine bubbles [11] and pin dislocations. The NFs are also remarkably thermally stable [12,13]. However, the details of important processes (mechanisms and energies), such as helium trapping, are not well understood. Thus, while they may differ from those for embedded NFs, creating a variety of mesoscopic surrogates, with self-selected sets of ORs with bcc Fe, will facilitate developing a general understanding of such metal-oxide interfaces in NFA, especially with respect to their structures and functional properties.

Experimental Methods

A pure single crystal of $Y_2Ti_2O_7$ was acquired from McMaster University (Dabkowska and Gaulin). The crystal was grown using a two-mirror NEC floating zone image furnace. The starting materials for the polycrystalline rods were 99.999% pure Y_2O_3 and 99.995% pure TiO_2, both from Alfa Aesar. The feed rods were created in the same fashion as Gardner [14]. The final single crystal was grown using the floating zone technique at a speed 5 mm/hr in air [15]. A 1.8 mm wafer was cut with a diamond saw parallel to the $Y_2Ti_2O_7$ single crystal {111} surface. An Allied Multiprep system was used to polish the wafer using a sequence of 15 (for flattening), 9, 6, 3, 1, 0.5 and 0.1 μm papers for 10 minutes each at 75 rpm. The final 15 minute polishing step used a 0.02 μm non-crystallizing silica suspension.

An electron beam system was used to deposit Fe on the $Y_2Ti_2O_7$ crystal at $7x10^{-6}$ torr and 800°C. The deposition rate was 0.3 nm/s for 420 s, producing a total Fe layer thickness of ≈ 200 nm. The sample was then slowly cooled to room temperature at a rate of ≈ 0.16°C/s.

Results and Discussion

Deposits of Fe on a pyrex glass substrate were used to provide a naturally selected Fe grain OR for an amorphous control surface. AFM measurements show the deposit is characterized by many Fe polycrystals with average grain size of 1 μm and a surface roughness of about 40 nm (Figure 1a). XRD scans show that the grains have a {110} out-of-plane pole orientation.

The XRD <100>$_{Fe}$ pole figure forms a ring showing that, as expected, there is no in-plane orientation between the Fe polycrystals and the pyrex glass (Figure 1b). The same deposition conditions were used for the $Y_2Ti_2O_7$ {111} oriented substrate.

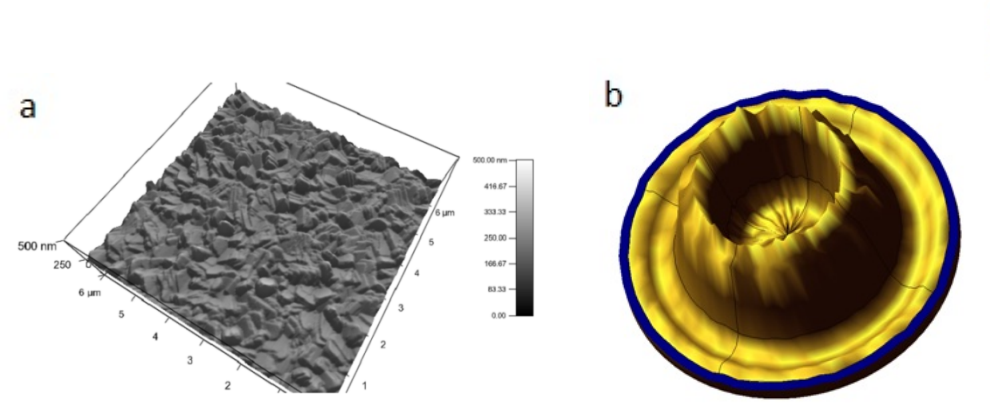

Figure 1. (a) AFM 3D reconstruction of the Fe grains on Pyrex. (b) Pole figure showing no in-plane OR between the Fe grains and the Pyrex.

The SEM image in Figure 2a shows a polycrystalline layer of Fe on the (111) $Y_2Ti_2O_7$ surface, with average grain size of about 1 µm, similar to that found in the pyrex control sample. The corresponding EBSD inverse pole map in Figure 2b and pole figures in Figure 2c show that the Fe grains have two orientations with the $\{111\}_{Y2Ti2O7}$ surface parallel to Fe grains with both $\{100\}_{Fe}$ and $\{110\}_{Fe}$. No $\{111\}_{Fe}$ grains were observed.

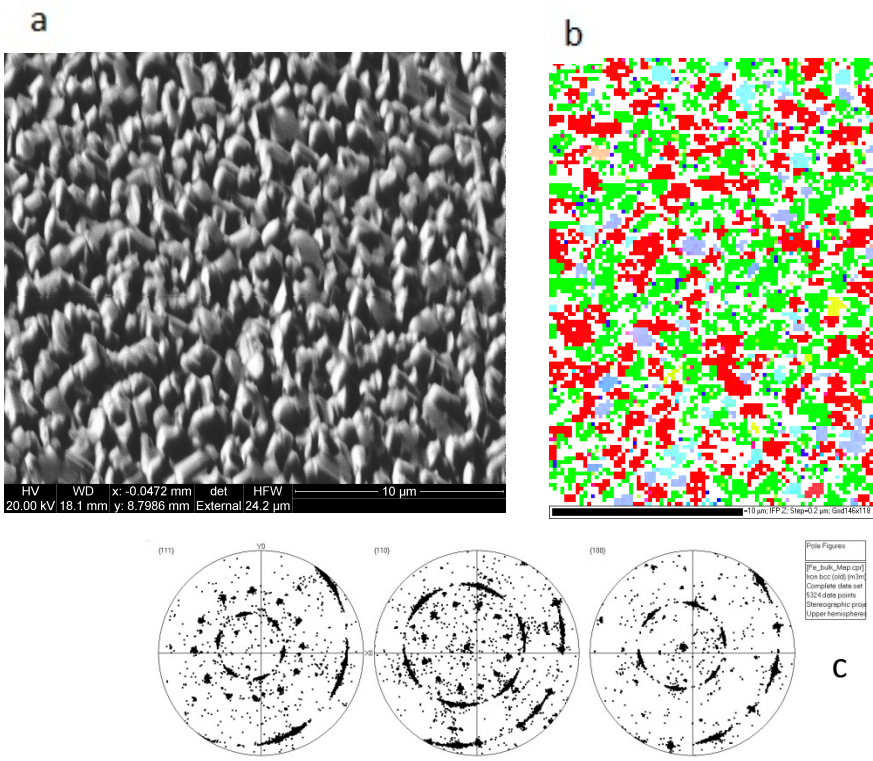

Figure 2. (a) EBSD of Fe grains on the $Y_2Ti_2O_7$ single crystal substrate. (b) Inverse pole figure map of the Fe grains. $\{100\}_{Fe}$ in red and $\{110\}_{Fe}$ in green. (c) Pole figures of Fe on $Y_2Ti_2O_7$. No $\{111\}_{Fe}$ grains, but many grains with $\{110\}_{Fe}$ and $\{100\}_{Fe}$.

The XRD scan in Figure 3 confirms the surface ORs observed with EBSD. T he $\{111\}_{Y2Ti2O7}$ is parallel to $\{110\}_{Fe}$ and to $\{100\}_{Fe}$.

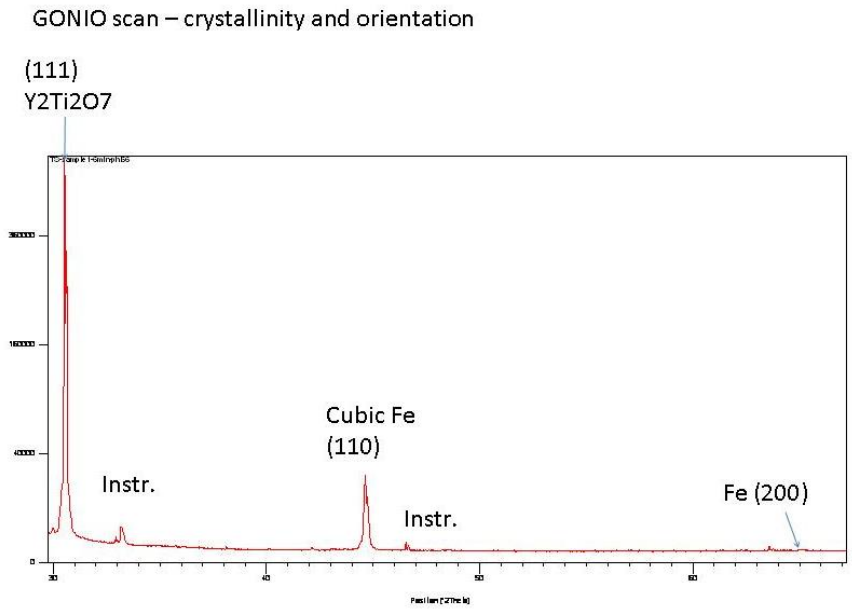

Figure 3. XRD of the Fe grains on the $Y_2Ti_2O_7$ substrate showing the $\{111\}_{Y2Ti2O7}$ reflection, the $\{110\}_{Fe}$ reflection, and a weak $\{200\}_{Fe}$ reflection. Signals are also seen from the XRD stage.

The XRD pole measurements in Figure 4 also show that there are two in-plane ORs: $<110>_{Y2Ti2O7}$ parallel to $<100>_{Fe}$ and to $<111>_{Fe}$. This further demonstrates that the $Y_2Ti_2O_7$ substrate affects the orientation of the Fe grains that grew during deposition.

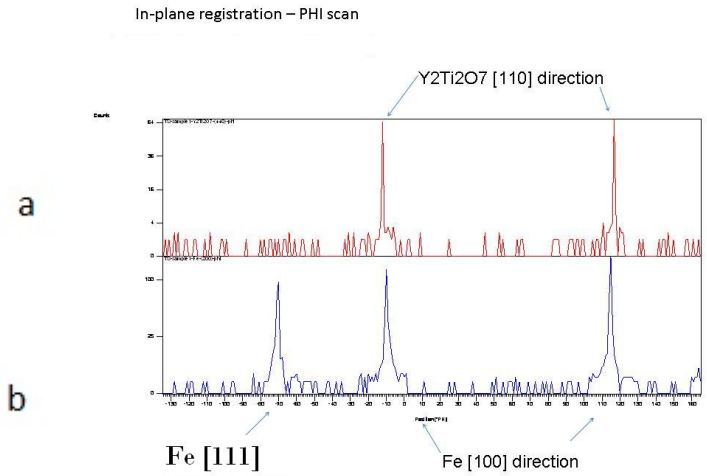

Figure 4. (a) The <110> in-plane direction of the $Y_2Ti_2O_7$ substrate. (b) The Fe in-plane directions. The Fe <100> peaks line up with the $Y_2Ti_2O_7$ <110> peaks. The $<111>_{Fe}$ reflection is also seen.

A FEI HELIOS Focused Ion Beam (FIB) tool was used to micro-machine < 20 nm thick electron transparent lift-outs of the interface as shown in Figure 6. The sample was cleaned by a low energy ion beam with 2 keV 5.5 pÅ. HRTEM, STEM and EDX were performed on the 300 keV FEI Titan TEM in the UCSB microstructure and microanalysis facility.

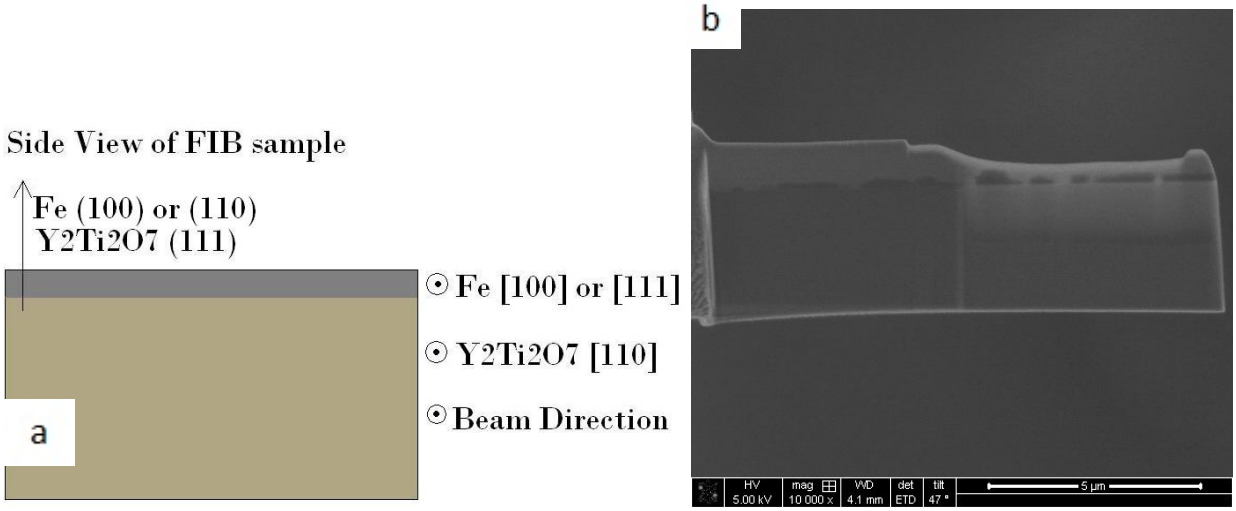

Figure 6. (a) Side view of FIB sample showing surface and direction ORs. (b) SEM image of the FIB sample used for TEM. The $<110>_{Y2Ti2O7}$ points out of the page.

TEM characterization

Figure 7 shows the low magnification TEM image of the cross-section of the lift out. A total of 13 grains were examined using TEM.

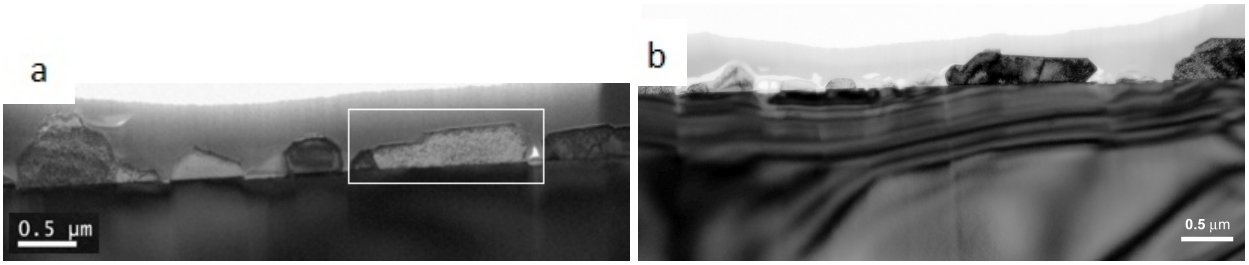

Figure 7. (a) and (b) are cross-section TEM images of Fe grains on the {111} $Y_2Ti_2O_7$ substrate. The white rectangle is enlarged for detail in Figure 8.

Six grains have an OR: $\{1\text{-}10\}_{Fe}||\{111\}_{Y2Ti2O7}$ and $<111>_{Fe}||<1\text{-}10>_{Y2Ti2O7}$ (off 5°-10°). Four grains have the OR: $\{001\}_{Fe}||\{111\}_{Y2Ti2O7}$ (off ~1°) and $<100>_{Fe}||<110>_{Y2Ti2O7}$; one grain has the OR: $\{110\}_{Fe}||\{111\}_{Y2Ti2O7}$ (off ~1°) and $<100>_{Fe}||<110>_{Y2Ti2O7}$; and 2 grains have no OR with the (111) $Y_2Ti_2O_7$ substrate. These results are summarized in Table 1.

Table 1. Summary of the OR found for the 13 grains observed with HRTEM.

Grain	Size	Orientation
No. 1	600 nm x 500 nm	$\{001\}_{Fe}$ ||$\{111\}_{Y2Ti2O7}$ <111>$_{Fe}$||<1-10>$_{Y2Ti2O7}$ (off 5°-10°)
No. 2	500 nm x 200 nm	No OR
No. 3	400 nm x 300 nm	$\{001\}_{Fe}$ ||$\{111\}_{Y2Ti2O7}$ (off ~1°) <100>$_{Fe}$ ||<1-10>$_{Y2Ti2O7}$
No. 4	250 nm x 200 nm	$\{001\}_{Fe}$ ||$\{111\}_{Y2Ti2O7}$ (off ~1°) <100>$_{Fe}$ ||<1-10>$_{Y2Ti2O7}$
No. 5	1000 nm x 300 nm	$\{1\text{-}10\}_{Fe}$ ||$\{111\}_{Y2Ti2O7}$ <111>$_{Fe}$||<1-10>$_{Y2Ti2O7}$ (off 5°-10°)
No. 6	1000 nm x 250 nm	$\{001\}_{Fe}$ ||$\{111\}_{Y2Ti2O7}$ (off ~1°) <100>$_{Fe}$ ||<110>$_{Y2Ti2O7}$
No. 7	1000 nm x 400 nm	$\{001\}_{Fe}$ ||$\{111\}_{Y2Ti2O7}$ <001>$_{Fe}$||<1-10>$_{Y2Ti2O7}$
No. 8	500 nm x 300 nm	$\{110\}_{Fe}$ ||$\{111\}_{Y2Ti2O7}$ <001>$_{Fe}$ ||<1-10>$_{Y2Ti2O7}$
No. 9	1000 nm x 500 nm	$\{1\text{-}10\}_{Fe}$ ||$\{111\}_{Y2Ti2O7}$ <111>$_{Fe}$ ||<1-10>$_{Y2Ti2O7}$ (off ~1°)
No. 10	1000 nm x 500 nm	$\{1\text{-}10\}_{Fe}$ ||$\{111\}_{Y2Ti2O7}$ <111>$_{Fe}$ ||<1-10>$_{Y2Ti2O7}$ (off 5°-10°)
No. 11	250 nm x 100 nm	$\{1\text{-}10\}_{Fe}$ ||$\{111\}_{Y2Ti2O7}$ <111>$_{Fe}$ ||<1-10>$_{Y2Ti2O7}$ (off 5°-10°)
No. 12	15 nm x 75 nm	$\{1\text{-}10\}_{Fe}$ ||$\{111\}_{Y2Ti2O7}$ <111>$_{Fe}$ ||<1-10>$_{Y2Ti2O7}$ (off 5°-10°)
No. 13	500 nm × 500 nm	No OR

The structure of the Fe-$Y_2Ti_2O_7$ Interface

The rectangular area in Figure 7 that is enlarged in Figure 8c shows two coalesced Fe grains with different orientations. Figure 8a shows the nano-diffraction pattern from the left grain, while Figure 8b shows the nano-diffraction pattern from the right grain. The left grain has an epitaxial relationship with the $Y_2Ti_2O_7$ substrate: $\{001\}_{Fe}$||$\{111\}_{Y2Ti2O7}$ and <100>$_{Fe}$||<1-10>$_{Y2Ti2O7}$. The right grain has the OR: $\{110\}_{Fe}$||$\{111\}_{Y2Ti2O7}$ and <111>$_{Fe}$||<1-10>$_{Y2Ti2O7}$ (off 5°-10°).

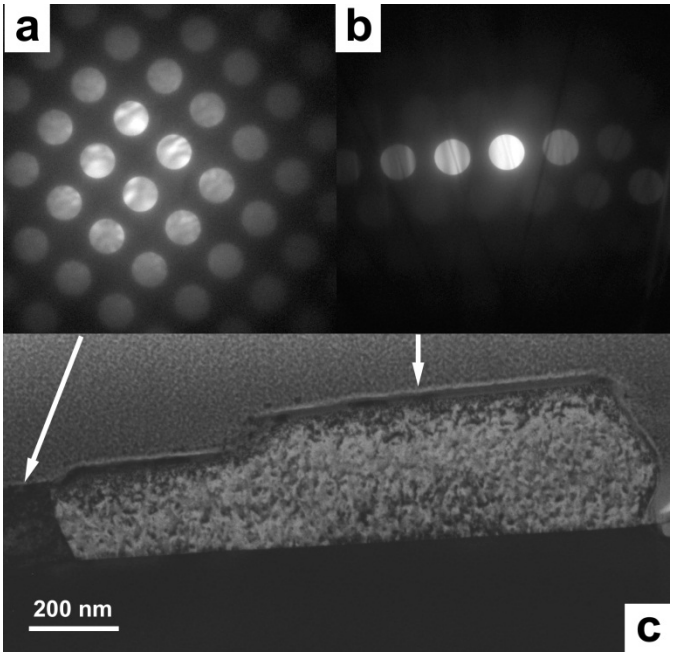

Figure 8. Nano diffraction patterns from the left grain and the right grain in (c) are shown in (a) and (b), respectively.

Figure 9 shows the interfacial structure of a grain with the OR: $\{1\text{-}10\}_{Fe}||\{111\}_{Y2Ti2O7}$ and $<111>||<1\text{-}10>_{Y2Ti2O7}$ (5°-10° off). This is close to the Kurdjamov-Sachs OR commonly found in fcc/bcc interfaces. The Fe-$Y_2Ti_2O_7$ interface has areas of dark and light patches spaced about 5 nm apart. The dark areas are stressed sections of the interface, which may be due to the miss cut of the $Y_2Ti_2O_7$ substrate.

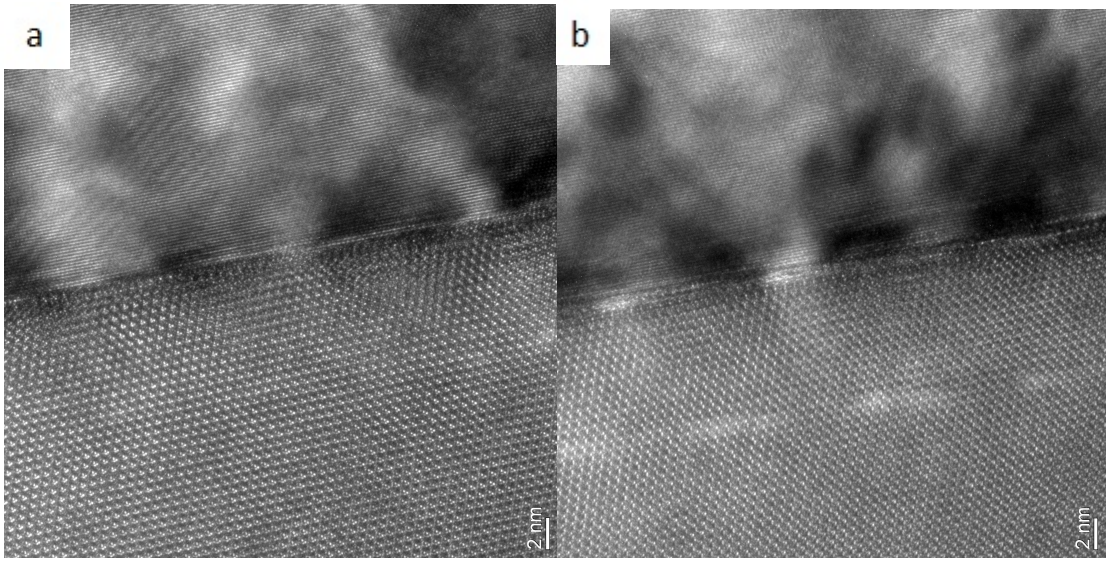

Figure 9. HRTEM images from a grain with $\{1\text{-}10\}_{Fe}$ $||\{111\}_{Y2Ti2O7}$ and $<111>||<1\text{-}10>_{Y2Ti2O7}$ (5°-15° off) OR.

Figure 10 shows the HRTEM images for a grain with the OR: $\{001\}_{Fe}||\{111\}_{Y2Ti2O7}$ (off ~1°) and $<100>_{Fe}||<110>_{Y2Ti2O7}$. Figure 11 shows that the grains with this orientation have a 2-3 nm thick transition layer; and STEM/EDX showed the transition layer is rich in Ti, O and Fe.

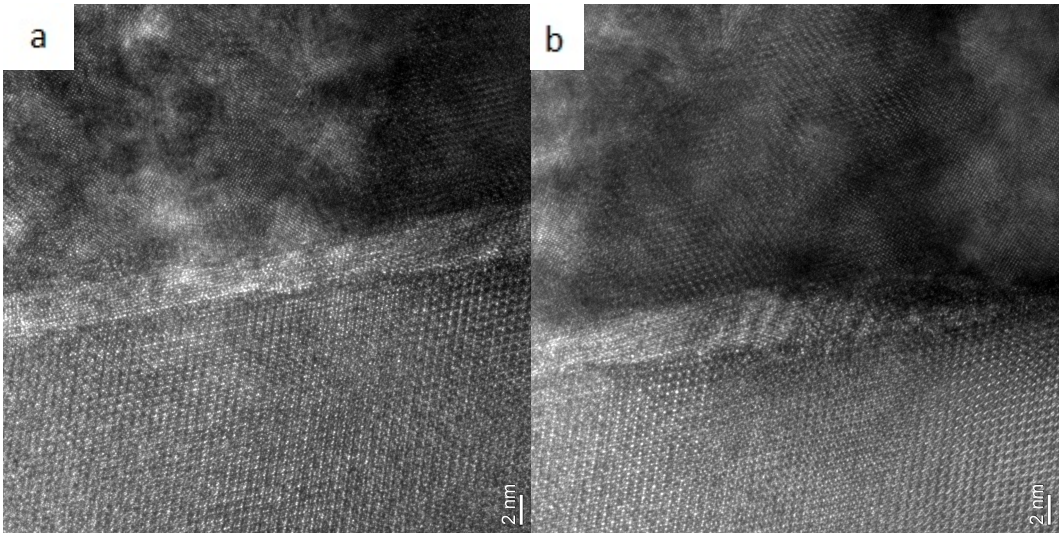

Figure 10. HRTEM images showing the light transitional layer found between Fe and $Y_2Ti_2O_7$ in the $\{001\}_{Fe}||\{111\}_{Y2Ti2O7}$ (off ~1°) and $<100>_{Fe}||<110>_{Y2Ti2O7}$ OR.

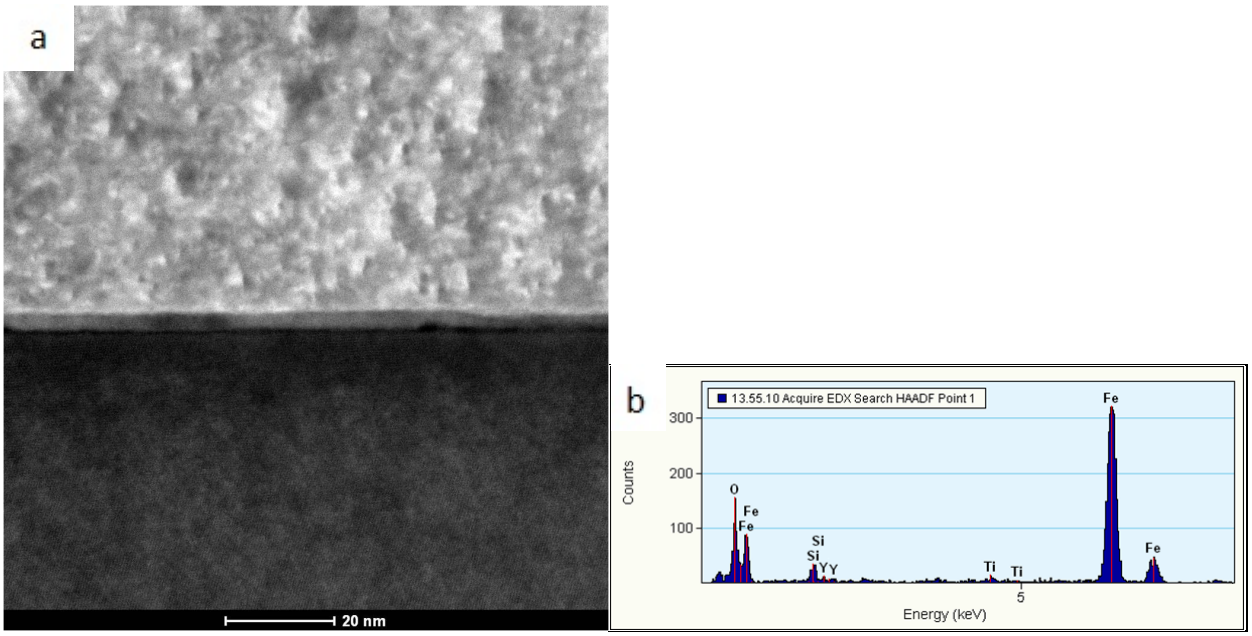

Figure 11. (a) STEM image of the $\{001\}_{Fe}||\{111\}_{Y2Ti2O7}$ (off ~1°) and $<100>_{Fe}||<110>_{Y2Ti2O7}$ OR. (b) an EDX spectra taken from the interfacial transition layer in image (a).

Figure 12a and 12b show a grain with no clear OR with the $Y_2Ti_2O_7$ substrate. The interface may be incoherent, and the dark area at the interface may again be a FeO_x transition layer.

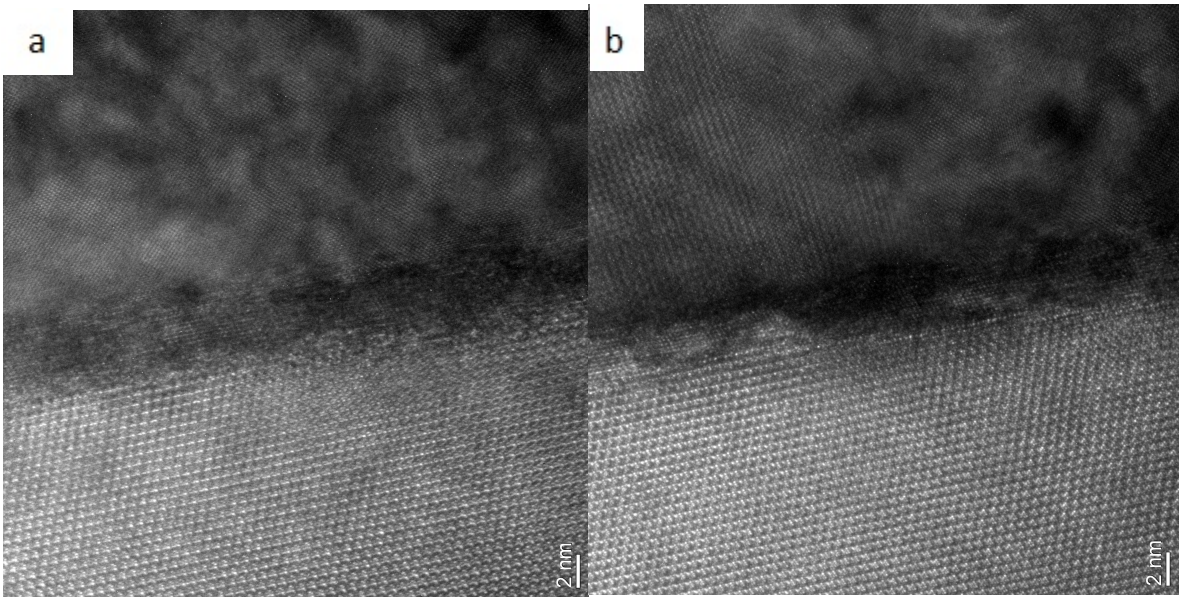

Figure 12. (a) and (b) show the interface of an Fe grain with no OR to the substrate.

CrystalMaker Studies of the Fe-$Y_2Ti_2O_7$ Interface

The $\{1\text{-}10\}_{Fe}||\{111\}_{Y2Ti2O7}$ and $<111>_{Fe}||<1\text{-}10>_{Y2Ti2O7}$ (off 5°-10°) OR was modeled with the CrystalMaker software (Figure 12a). The Kurdjumov-Sachs (KS) OR is obtained from the Nishiyama-Wasserman (NW) orientation by a 5.26˚ rotation about the interface normal [16]. The NW OR is $(110)_{Fe}||(111)_{Y2Ti2O7}$ and $[001]_{Fe}||[1\text{-}10]_{Y2Ti2O7}$. The $[001]_{Fe}$ and $[1\text{-}10]_{Y2Ti2O7}$ aligned direction mismatch is 2.5%. Note pattern of two well-matched Fe to substrate atoms (green) followed by a Fe defect location (purple) in Figure 12b. This calculation shows that there is a defect every 3 Fe <110> lengths, or 12.244 Å. Otherwise the interface is reasonably well matched. Note these calculations/images were made using the ideal unit cell parameters of the crystal.

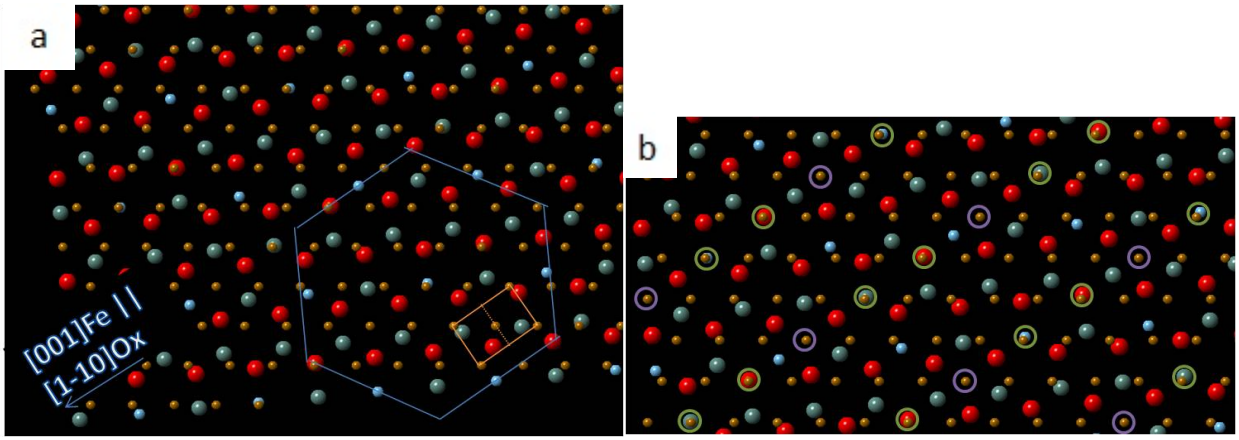

Figure 12. The orange, red, dark blue, and light blue circles are Fe, O, Y, and Ti, respectively. (a) The $\{1\text{-}10\}_{Fe}||\{111\}_{Y2Ti2O7}$ and $<001>_{Fe}||<1\text{-}10>_{Y2Ti2O7}$ OR. The blue hexagon in Figure 12a is the $\{111\}_{Y2Ti2O7}$ unit cell and the orange box is the $\{110\}_{Fe}$ unit cell. (b) Green circles show two well-matched Fe to substrate atoms and purple circles show Fe defect location.

Continuing and Future Research

This work is continuing and will be extended to other oxide surface orientations and different deposition conditions will also be explored. Another Fe deposition on $\{111\}_{Y2Ti2O7}$ was carried out with a deposition rate of 2 nm/s. Preliminary results show that there are Fe grains with one OR: $\{1\text{-}10\}_{Fe}||\{111\}_{Y2Ti2O7}$ and $<001>_{Fe}||<1\text{-}10>_{Y2Ti2O7}$. There were no Fe grains with {100} as seen in the sections above. The Fe grains had 3 in-plane orientations due to the 3-fold symmetry of the $Y_2Ti_2O_7$ {111} plane. This sample will be further characterized with AFM and HRTEM.

A Fe deposition was also done on a $\{001\}_{Y2Ti2O7}$ single crystal surface. The sample preparation and e-beam deposition conditions were kept the same as the previous deposits on $\{111\}_{Y2Ti2O7}$. XRD and EBSD scans show that only $\{110\}_{Fe}$ grains were seen and there was no in-plane OR with the substrate. This may be due to the non-stoichiometric termination of the $\{001\}_{Y2Ti2O7}$ plane, which made it difficult for the Fe grains to bond to the oxide surface. Further sample characterization will be carried out in the future.

There will also be studies of the interface interactions with irradiation induced defects and helium.

ACKNOWLEDGEMENTS

The authors thank Erin Haney, Gareth Seward, Mark Cornish, Deryck Stave, Youli Li, and Doug Klingensmith for help with various parts of the research. The work performed at UCSB was supported by the U. S. Department of Energy, Office of Fusion Energy Sciences, under grant DE-FG03-94ER54275. We also acknowledge the National Center for Electron Microscopy at LBL for the HRTEM on the TEAM 0.5 instrument in collaboration with Jim Cisten at LBL and Peter Hosemann at UC Berkeley.

REFERENCES

[1] G. R. Odette, M. J. Alinger, and B. D. Wirth, *Annu. Rev. Matter Res.* **38** (2008) 471
[2] Y. Dai, G. R. Odette, and T. Yamamoto, *Comp. Nucl. Mater.* **1** Chap. 6 (2012) 141
[3] H. Sakasegawa, L. Chaffron, F. Legendre, et al*., J. Nucl. Mater.* (2009) 384
[4] S. Yamashita, S. Ohtsuka, N. Akasaka, et al., *Phil. Mag. Lett.* (2004) 84
[5] S. Yamashita, N. Akasaka, and S. Ohnuki, *J. Nucl. Mater.* (2004) 329
[6] M. Klimiankou, R. Lindau, and A. Möslang, *J. Nucl Mater* (2004) 329
[7] M. Klimiankou, R. Lindau, and A. Möslang, *Micron* (2005) 36
[8] T. Okuda and M. Fujiwara, *J. Mater. Sci. Lett.* (1995) 14
[9] Y. Wu, E. M. Haney, N. J. Cunningham, et al., *Acta Mater.* **60** (2012) 3456
[10] J. Ciston, Y. Wu, G. R. Odette, et al., *Fus. Mat. Semiann. Prog. Rep.* (2012) DOE-ER-0313/51
[11] G. R. Odette, et al., *J. Nucl. Mater.* (2011)
[12] S. Y. Zhong, J. Ribis, V. Klosek, et al., *J. Nucl. Mater.* **12** (2012)
[13] M. J. Alinger, G. R. Odette, and D. T. Hoelzer, *J. Nucl. Mater.* (2004) 382
[14] J. S. Gardner, B. D. Gaulin, and D. M. Paul, *J. Cryst. Growth* **191** (1998) 740
[15] M. B. Johnson, H. A. Dabkowska, B. D. Gaulin, et al., *J. Solid State Chem.* **182** (2009) 725
[16] A. Hashibon, A. Y. Lozovoi, and P. Gumbsch, *Phys. Rev. B* **77** (2008) 094131

3.1 INTERLAMINAR SHEAR STRENGTH AND TRANS-THICKNESS TENSILE STRENGTH OF CVI AND NITE SIC/SIC COMPOSITES — C. Shih, Y. Katoh, K. Ozawa, and L. Snead (Oak Ridge National Laboratory)

OBJECTIVE

The main objective of this work is to determine the trans-plane properties (interlaminar shear strength and trans-thickness tensile strength) of three different types of SiC/SiC composites. These properties are in general lower than the in-plane properties and thus are the potentially design-limiting factors for the composites in fusion applications.

SUMMARY

The interlaminar shear strength and trans-thickness tensile strength of three different SiC fiber reinforced SiC matrix composites were evaluated by double-notched shear test and diametral compression test, respectively, in a non-irradiated condition. One composite showed weak interlaminar shear strength (~10 MPa) because of poorly densified interlaminar matrix. When the interlaminar matrix are adequately densified, dominating failure locations become intra-fiber bundle with fiber/matrix debond, resulting in a higher interlaminar shear strength (~30 MPa). Trans-thickness tensile loading caused crack propagation initiating from fiber/matrix debond. The crack can easily grow with the uni-directional woven composite, resulting in a lower trans-thickness tensile strength of ~20 MPa. The crack growth was obstructed by the weave pattern in the 2D woven composites, resulting in a higher trans-thickness tensile strength of ~35 MPa.

PROGRESS AND STATUS

Introduction

SiC fiber reinforced SiC matrix composites are promising materials for fusion applications due to their excellent thermal, chemical and mechanical stability, their high radiation stability and low activation properties upon neutron irradiation [1-4]. The thermal physical and mechanical properties of near-stoichiometric SiC fiber/SiC matrix (SiC/SiC) composites have been vastly studied [2, 4-8]. Mechanical properties integrity of SiC/SiC composites at high neutron dose of up to 40 displacement per atom (dpa) and high temperature of up to 800°C has been demonstrated [9].

It is well known that two-dimensionally fiber-reinforced ceramic matrix composites (2D CMCs) have improved fracture resistance and damage tolerance in the in-plane direction. However, the trans-plane properties of these composites are generally much lower and need to be addressed. In the development of SiC/SiC composites as fusion materials, there is a lack of trans-plane mechanical properties studies compared to the vastly studied in-plane properties. Moreover, the trans-plane mechanical properties are believed to be related with the initial matrix cracking and the crack propagation behavior of these composites under in-plane loading.

Several test methods have been developed to study interlaminar shear strength (ILSS) including shot-beam flexure test [10], and double-notched shear (DNS) test [11-14]. The double-notch shear test was used in this study because small specimens can be used. This is crucially important for neutron irradiation studies since volume in the irradiation capsules are limited and

often expensive. Furthermore, this method can be applied to high temperature test relatively easily. However, it should be noted that the notches make the shear stress distribution in the specimen non-uniform [11, 13, 15].

The tensile strength perpendicular to the 2D plane of the plains weave composites or perpendicular to the fiber direction of the uni-directional composites is called the trans-thickness tensile strength (TTS). It is typically much lower than the tensile strength of the in-plane direction since the load is not shared directly onto the fibers but results in tensile loading across the weak fiber-matrix interface. Therefore, TTS is a potential design-limiting factor for certain applications. The TTS of 2D CMCs can be evaluated per ASTM C1468-06 at room temperature by utilizing adhesively bonded extenders to transfer the load. However, the applicability of this test is limited by the strength and the operation temperatures of the adhesive. The diametral compression test can evaluate TTS of disk-shaped samples without using adhesive and thus eliminate the strength and temperature constrains imposed by the adhesive [16-20].

In this report, the ILSS and TTS of SiC fiber reinforced SiC matrix composites were investigated and discussed at non-irradiated conditions at room temperature. The fracture surfaces were examined by an SEM.

Experimental

Three types of composites were used in this study. Their properties are summarized in Table 1. These composites cover 2 types of commercially available near-stoichiometric SiC fibers (Tyranno™ SA3 fiber and Hi-Nicalon™ Type-S fiber), 2 types of SiC matrix densification methods (chemical vapor infiltration and NITE process [21, 22]), and 3 different fiber architectures. In the chemical vapor infiltration (CVI) process, SiC based matrix is deposited from gaseous reactants on a heated SiC fiber preforms. The NITE process incorporates a fiber coating and the infiltration of nano-phase SiC power based mixed slurry to the coated fiber preform. The slurry contains oxides sintering aids. This process is finished by a pressure sintering at temperatures above the melting point of the transient eutectic phase [23, 24].

The fiber/matrix interphase was coated with a layer of pyrolytic carbon (PyC) of nominally either 150 or 500 nm thickness. The interphase coating and the CVI matrix densification were provided by Hypertherm High-Temperature Composite, Inc. (Huntington Beach, CA) using an isothermal isobaric CVI process. It should be noted that the HNLS/PyC150 composite used finer weave fabrics of 24 × 24 thread-per-inch with 250 filament yarns instead of regular 16 × 16 thread-per-inch with 500 filament yarns. This resulted in a more homogeneous composite structure and increased interlaminar porosity.

Table I. Summary of composite materials studied.

Designator	Reinforcement	Interphase	Matrix	Porosity (%)	Density (g/cm^3)
TySA/PyC150	Tyranno™-SA3 (7.5um) 2D Plain Weave, 17 × 17 tpi, 800 filament yarns, 0°/90°	PyC (150 nm)	CVI-SiC	18	2.58
HNLS/PyC150	Hi-Nicalon™ Type-S, 900 denier 2D Plain Weave, 24 × 24 tpi, 250 filament yarns, 0°/90°	PyC (150 nm)	CVI-SiC	23	2.40
NITE/PyC500	Tyranno™-SA3 (7.5um) Uni-directional	PyC (500 nm)	SiC-NITE process	<2	N/A

Interlaminar shear strength of the composites was determined at room temperature by a double-notched shear (DNS) test per ASTM C1292-00. The dimensions of the specimen are 20 mm (length) × 4 mm (width) × 2 mm (thickness) with a notch separation of 6mm.

Trans-thickness tensile strength of the composite materials was determined by a diametral compression test at room temperature [17, 20]. In the test, a diametral compressive load applied to a truncated disc specimen is converted to tensile load in the perpendicular orientation leading to failure in trans-thickness tension. The maximum tensile stress is

$$\sigma_T = \frac{2P}{\pi dt} \tag{1}$$

where d is the disk diameter, t the thickness, and P the compressive load. The specimens are 4 mm in diameter and 3 mm thick. Details of the test method can be found elsewhere [16, 25].

For the SA3/PyC150 composite, the compressive load is along one of the fiber directions so that the tensile stress is perpendicular to the weave plane. For the NITE/PyC500 composite, the compressive load is also long the fiber direction, leading to a tensile stress perpendicular to the fiber direction.

Microstructures of the fracture surfaces were examined with Hitachi S4800 field emission scanning electron microscope.

RESULTS AND DISCUSSION

Interlaminar shear strength (DNS test)

The interlaminar shear strength (ILSS) of different composites is shown in Table II. The in-plane tensile strength for the same material is also listed for comparison. Typical shear

stress vs. displacement curves are shown in Figure 1. HNLS/PyC150 composite showed a much lower ILSS of 10.7 MPa. The TySA/PyC150 composite showed a higher ILSS of 30.1 MPa. NITE/PyC500 composite exhibited the highest interlaminar shear strength of 37.5 MPa.

ILSS of similar 2D SiC/SiC composites (TySA fiber, 80 nm PyC interphase, CVI SiC matrix, 40% fiber volume fraction, 13% porosity) has been studied by Riccardi et al. using a short beam shear test [30] and a ILSS of 54 MPa was reported. The higher ILSS by the short beam shear test can be explained by several reasons: firstly, there are no planer regions of constant maximum shear stress in this test method [31]. Moreover, the compressive stress from the load application points constrains the crack opening, resulting in an overestimate of the 'true' ILSS [31].

Table II. LSS and TTS of SiC/SiC composites. In plane tensile properties are also listed for comparison. Numbers in the parenthesis indicate one standard deviation

Material	ILSS (MPa)	# of tests	TTS (MPa)	# of tests	In plane PLS[1] (MPa)	In plane UTS[2] (MPa)
HNLS/PyC150	10.7 (5.7)	8	-	-	83 (12) [28]	318 (22) [28]
TySA/PyC150	30.1 (3.3)	6	34.1 (3.2)	4	113 (19) [28]	274 (29) [28]
NITE/PyC500	37.5 (1.63)	4	21.4 (3.3)	4	142 (26) [29]	344 (25) [29]

[1]proportional limit stress

[2]ultimate tensile stress

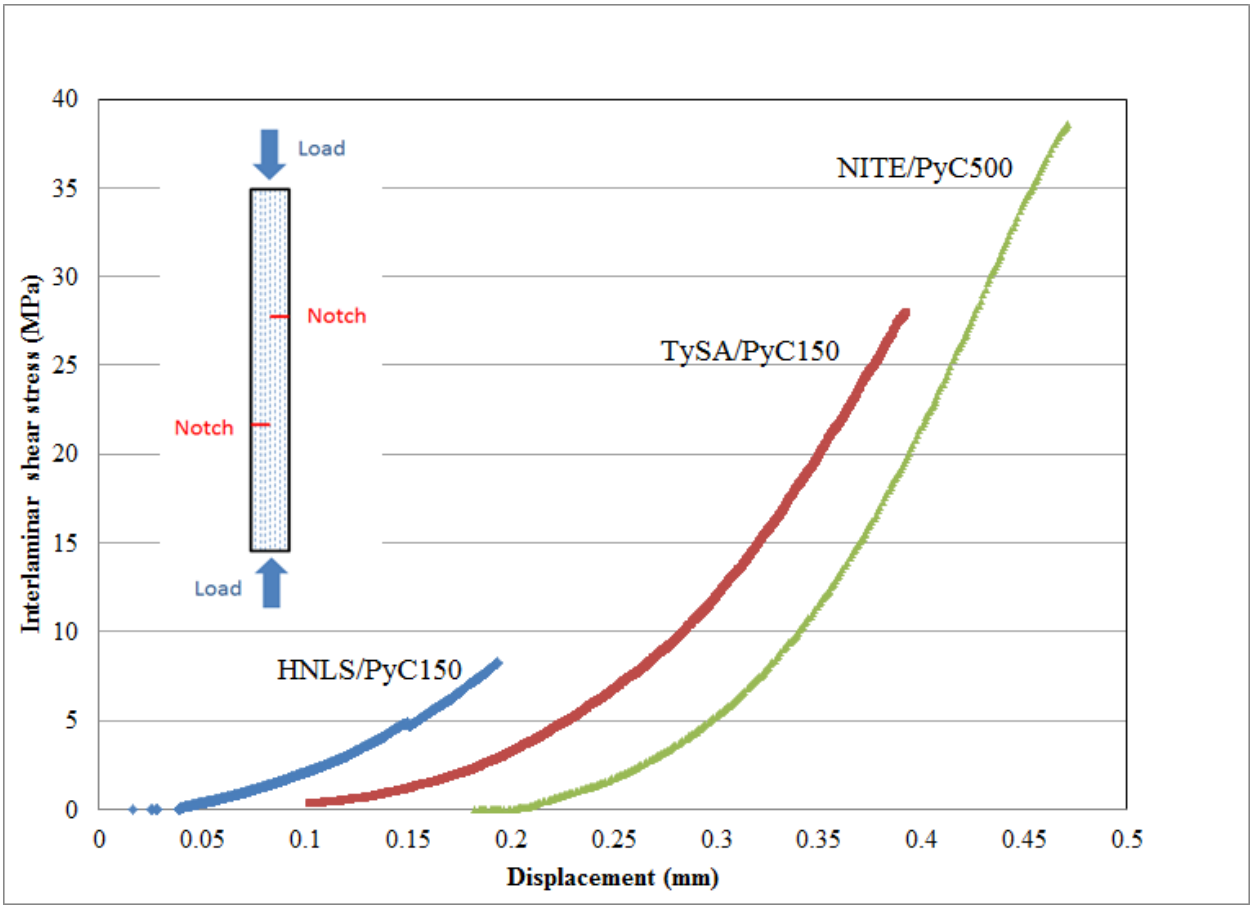

Figure 1. Tyrpical interlaminar shear stress vs. displacement curves in DNS tests. The horizontal positions are intentionally offset for better visibility.

SEM images of the fracture surface (Figures 2 and 3) of HNLS/PyC150 composites after DNS test showed a complete and an almost intact 2D interlaminar plane, indicating a failure between two fabric layers or true interlaminar failure. Apparently, the interlaminar layers are only connected by very limited areas, rendering very small interlaminar shear strength of 10.7 MPa. This is probably caused by the finer weave method that hinders the reactant gases from diffusing into the interlayer space. The areas where the inter layers were connected and broke by interlaminar shear can be clear seen in the SEM images (region 2 in Figure 2a and Figure 3).

Because of this failure mode, almost no fiber failures are involved with the composite failure. Further observations showed that the broken structures (region 2 in Figure 2a and Figure 3) are interlaminar matrices with fiber imprints. Some broken areas showed that the interlaminar matrices were pulled out, revealing the underneath bare fiber (Figure 3d). The blind or cavity regions between two adjacent tows can also be seen very clearly in Figure 2a (region 1). These blind regions didn't contribute directly to the low ILSS of the HNLS/PyC150 composite. Debond occurred between the SiC fiber and the PyC interphase coating (Figure 2d, e and f), leaving the PyC interphase attached with the matrix.

SEM images of a side of the HNLS/PyC150 composites after DNS test are shown in Figure 4. The interlaminar pores between plies can be seen very clearly. Two types of pores were observed. Region 1 in Figure 4a showed typical pores in 2D CVI SiC/SiC composites. Region 2 showed inter ply pores that were connected. This suggests an unusually poor bonding between fabric layers. The fracture occurred in the matrix between two adjacent plies, leaving a smooth fracture surface in the lateral images. This observation agrees with the fracture mode determined from the fracture surface image in Figure 2. Figure 4 also shows that the connected inter ply pores appear randomly in the HNLS/PyC150 composites, resulting in a larger scattering of composite ILSS with a coefficient of variation of 53%, as calculated from Table 2.

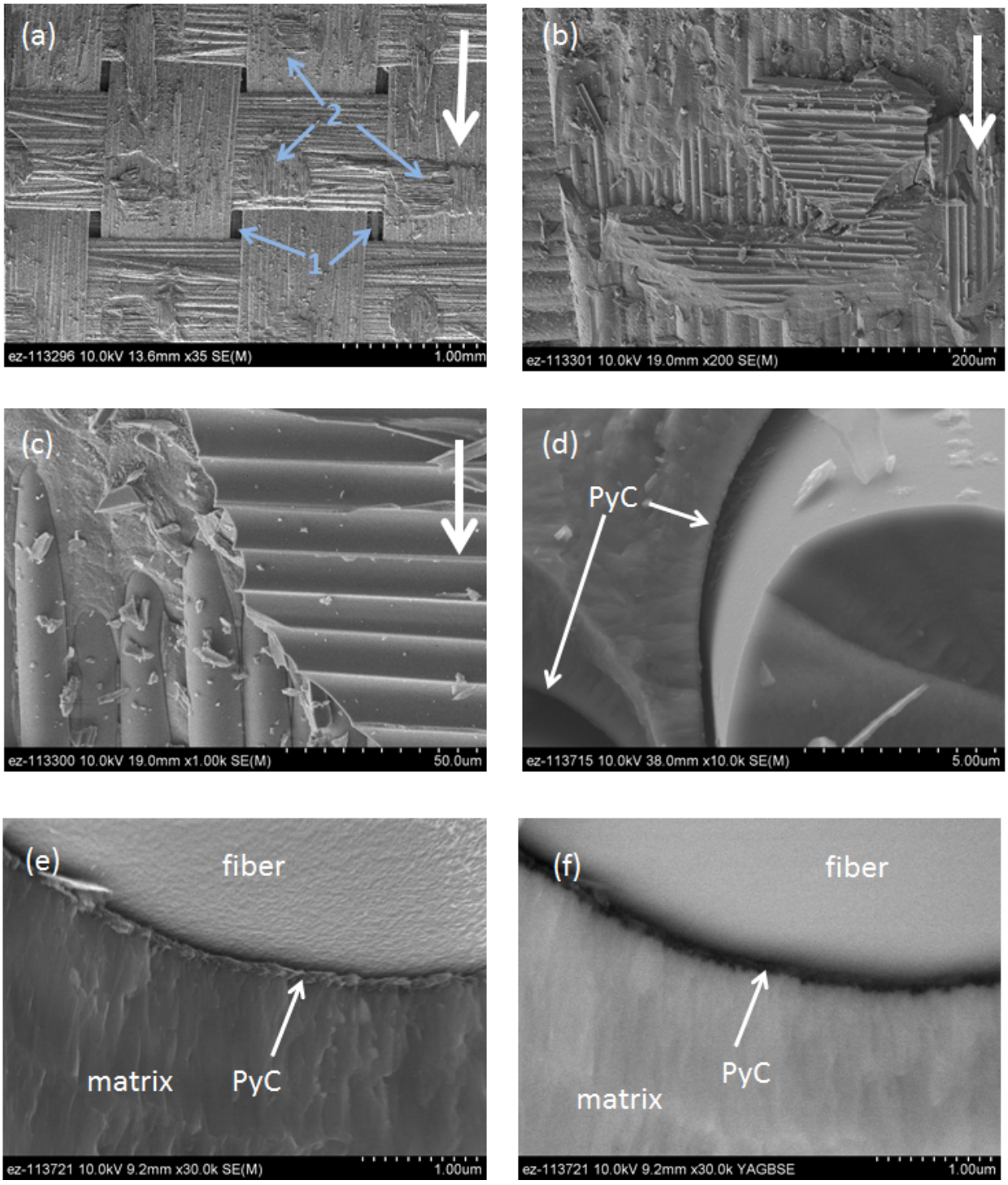

Figure 2. SEM Images of fracture surface of HNLS/PyC150 composites after double-notched shear test. Arrow represents the shear direction. Image (f) is the back scattered electron image of (e).

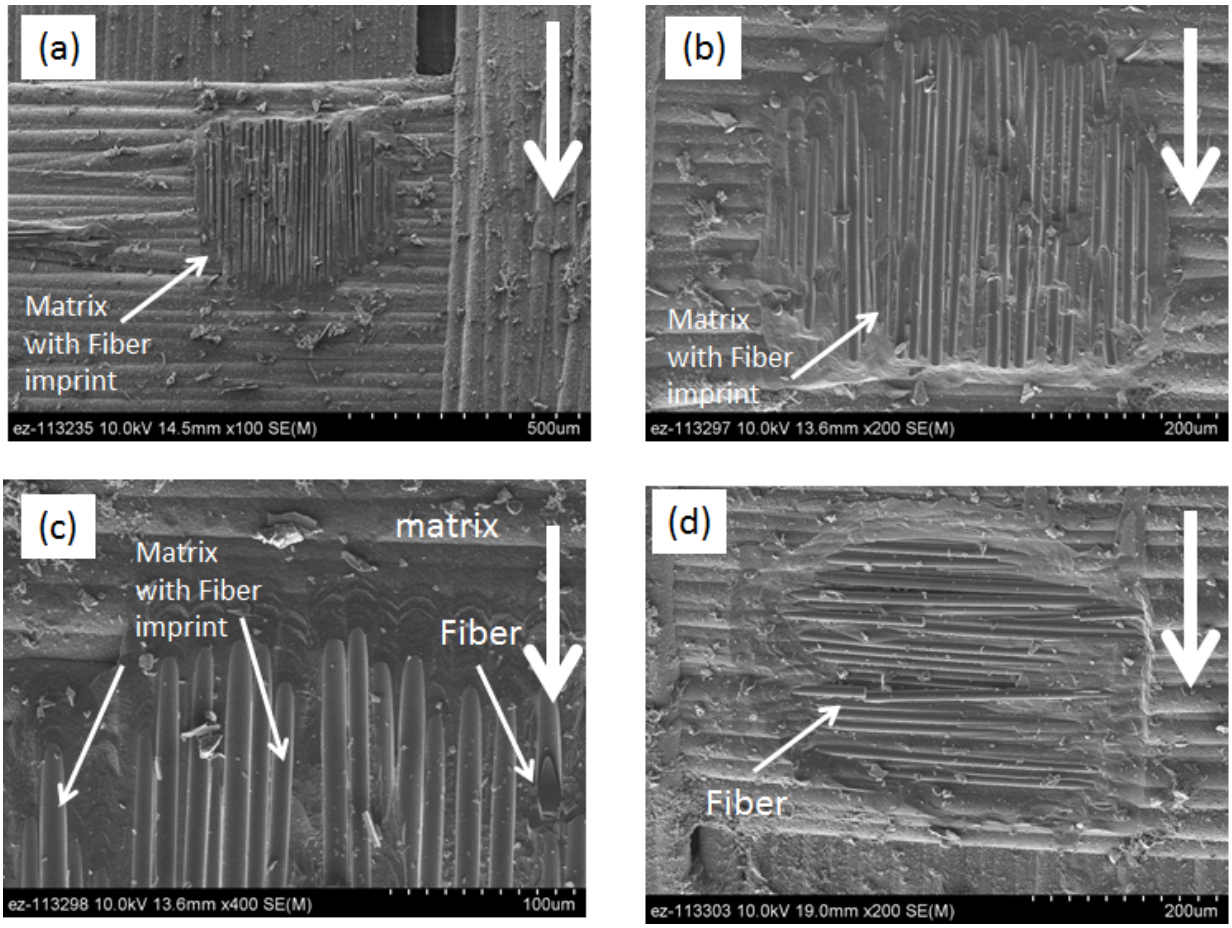

Figure 3. SEM Images of fracture surface of HNLS/PyC150 composites after double-notched shear test showing the matrix with fiber imprint (a, b, and c) and the revealed bare fibers (d). Arrow represents the shear direction.

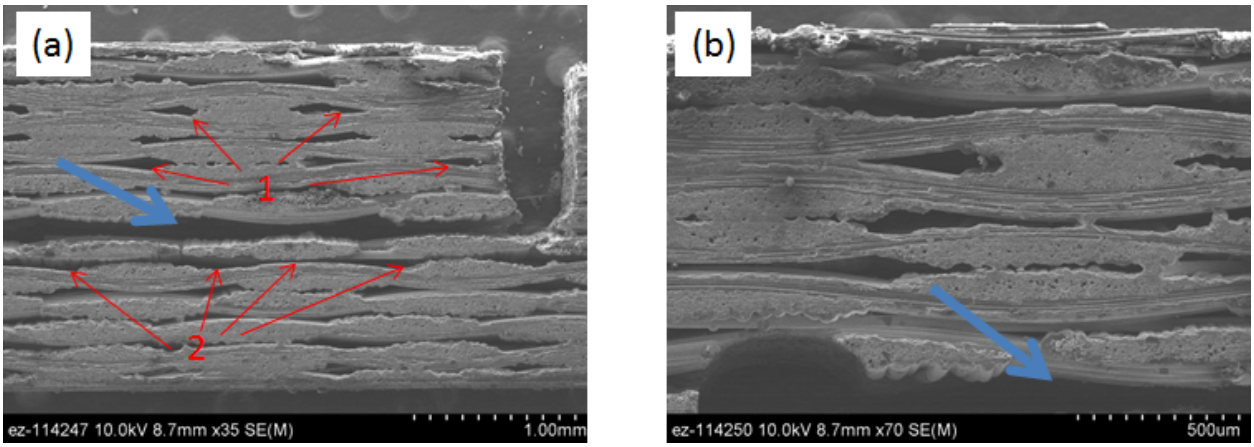

Figure 4. Lateral SEM Images of HNLS/PyC150 composites after double-notched shear test. Arrow indicates the fracture surface.

SEM images of TySA/PyC150 composites fracture surface (Figures 5 and 6) after DNS test show a 2D weave plane with damaged fiber tows. The lateral SEM images in Figure 7 show that the interlaminar layers are better densified by the CVI process as compared to the HNLS/PyC150 composites. Nonetheless, the images still show typical inter ply pores for 2D CVI SiC/SiC composites, i.e., the blind regions between fiber tows (inter-tow pores, region 1 in Figure 5a) and the non-densified space between adjacent layers (interlaminar pores, region 2 in Figure 5a). Since the interlayers are better densified, trans-thickness shear caused intra-bundle failure, revealing the intra-bundle SiC matrix and broken bare fibers (Figure 5a and Figure 7b). Some intra-bundle crack near the fracture surface can also be seen in Figure 7b (region 1). The intra-bundle SiC matrix is characterized by the small bumps. Failure inside the fiber tows rather than the interlaminar matrix rich regions suggests that the shear stress bearing capacity of the tows was lower than the interlaminar matrix rich regions when the interlaminar layers are adequately densified [30, 31]. This type of composite failure involves lots of fiber fracture and fiber/matrix debond and sliding, thus achieving higher interlaminar shear strength of 30.1 MPa. This intra-bundle failure mode results in a much lower scattering of ILSS with a variation coefficient of 11%. The inhomogeneity of the intra-bundle structure in the TySA/PyC150 composites appears to be much less than the structure inhomogeneity of the inter ply pores in the HNLS/Py150 composites. The broken tows appeared very rough, suggesting that slow crack growth alone the fiber matrix interphase is not predominating [30]. Debond occurred between the fiber and the PyC coating, leaving a thin layer of PyC coating on the matrix (Figure 6).

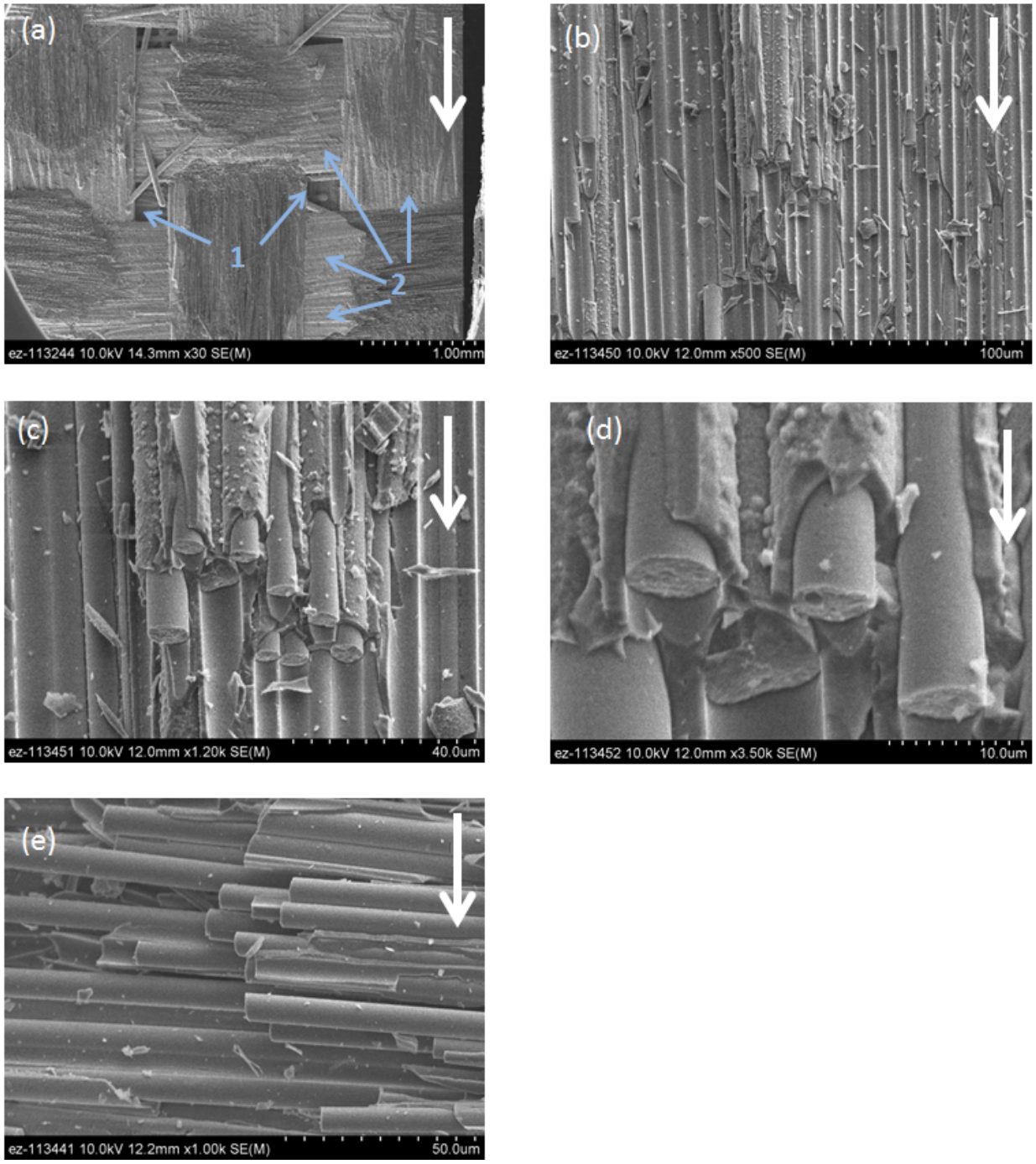

Figure 5. SEM Images of fracture surface of TySA/PyC150 composites after double-notched shear test. Arrow represents the shear direction.

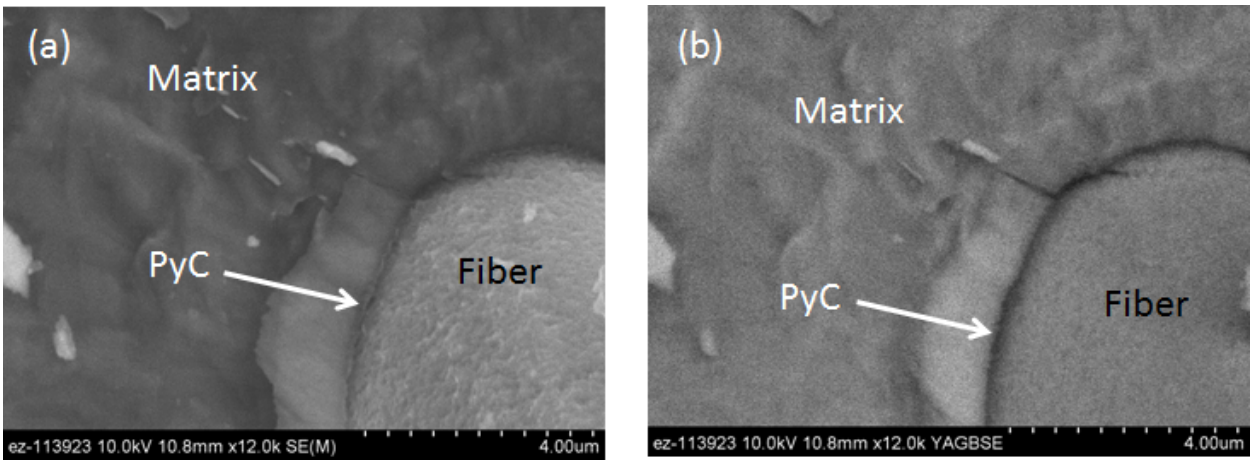

Figure 6. SEM Images of TySA/PyC150 composites after double-notched shear test that show the fiber, PyC interphase and the matrix. Image (b) is the back-scattered electron image of (a).

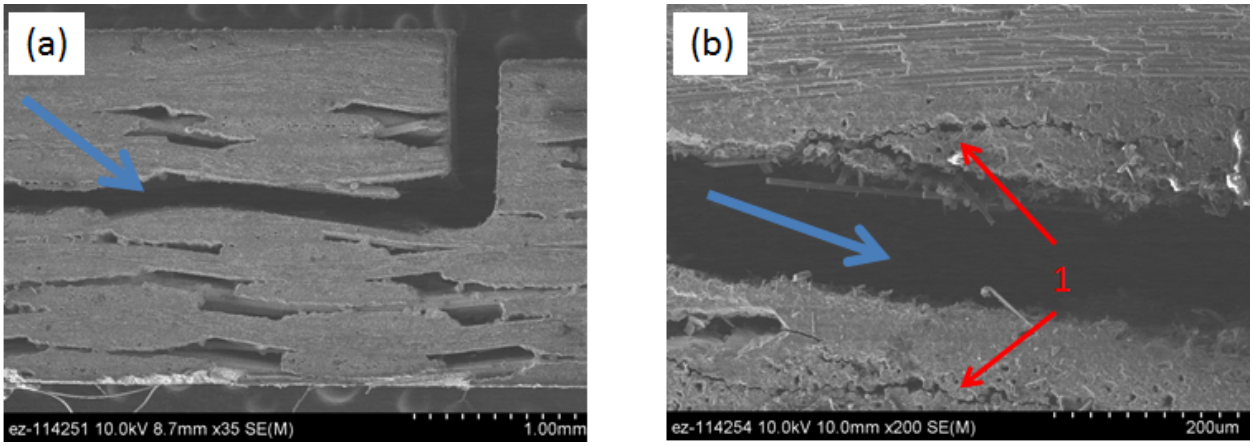

Figure 7. Lateral SEM Images of TySA/PyC150 composites after double-notched shear test. Arrow indicates the fracture surface.

Figure 8 shows the fracture surface of the NITE/PyC150 composite after DNS test. The sintering additives (white phase), the SiC matrix (grey phase) and the fiber with PyC coating (dark phase) can be readily distinguished from the back-scattered images. The NITE processed unidirectional composite appears to be relatively dense without large pores compared to the 2D weaved HNLS/PyC150 or TySA/PyC150 composites. The NITE/PyC500 composites have higher interlaminar shear strength because it didn't suffer from poor interlaminar densification like the 2D plain weaved CVI densified composites. The low porosity also results in very low ILSS scattering among the NITE/PyC500 samples, which have a variation coefficient of 4%.

Debond of NITE/PyC500 occurred between the PyC coating and the matrix, leaving most of the fibers still coated with the PyC interphase.

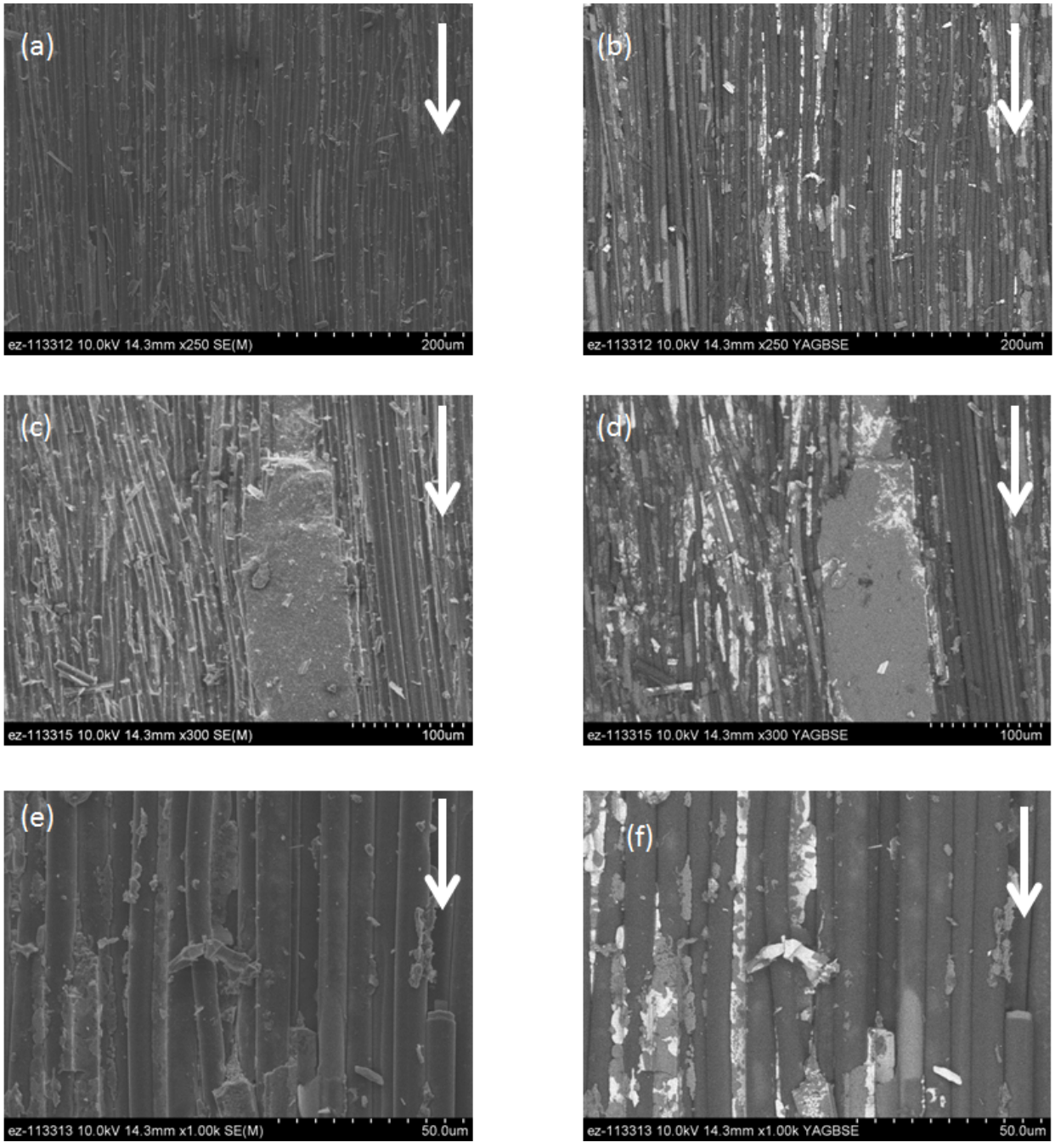

Figure 8. SEM Images of fracture surface of NITE/PyC50 composites after Double-notched shear test. (a), (c) and (e): secondary electron images, (b), (d) and (f): back scattered images. The arrow represents the shear direction.

Trans-thickness tensile strength (diametral compression test)

The Trans-thickness tensile strength of the composites is summarized in Table 2. SEM images of the fracture surface are shown in Figures 9 and 10 for TySA/PyC150 and NITE/PyC500 composites, respectively. TySA/PyC150 composite has a higher trans-thickness tensile strength than NITE/PyC500 in spite of the higher porosity of TySA/PyC150.

Nozawa et al. reported that without using a strain gauge, the diametral compression test would overestimate the TTS of SiC/SiC composites because a main crack initiated before the maximum load was reached [32]. Therefore, the "true" stress when the first major crack initiated in the specimens is smaller than the value reported here. TTS of similar 2D SiC/SiC composites has been reported by Riccardi et al. [26] by the adhesively bonded extender method and the reported TTS was only 7.6 MPa. The higher value obtained by the diametral compression method in this study might be partially caused by the overestimate of TTS by the diametral compression test. Another reason is that the effective volume of the diametral compression test is smaller than the effective volume of the adhesively bonded extender method, resulting in inherent higher measured TTS by the diametral compression test.

The fracture surface of TySA/PyC150 composite after diametral compression test showed a very uneven fracture plane (Figure 9). Failure appears to be intra-bundle and inter-ply with lots of fiber/matrix debond and fiber fracture. The intra-bundle fracture mode suggests that the trans-thickness tensile load bearing capacity of the intra-bundle matrix is lower than the inter-bundle matrix. This finding agrees with the low interlaminar shear load bearing capacity of the intra-bundle matrix discussed previously the 2D weave pattern prevented composite failure from just one direction of crack growth since tows form the other direction can still bear the trans-thickness tensile load. The final composite failure was caused by intra-bundle failure of fiber tows from both directions. Debond occurred between the fiber and the PyC, as shown in Figure 9d, reflecting stronger bonding between CVD SiC matrix and the PyC layer, as discussed previously for the same composite with interlaminar shear loading.

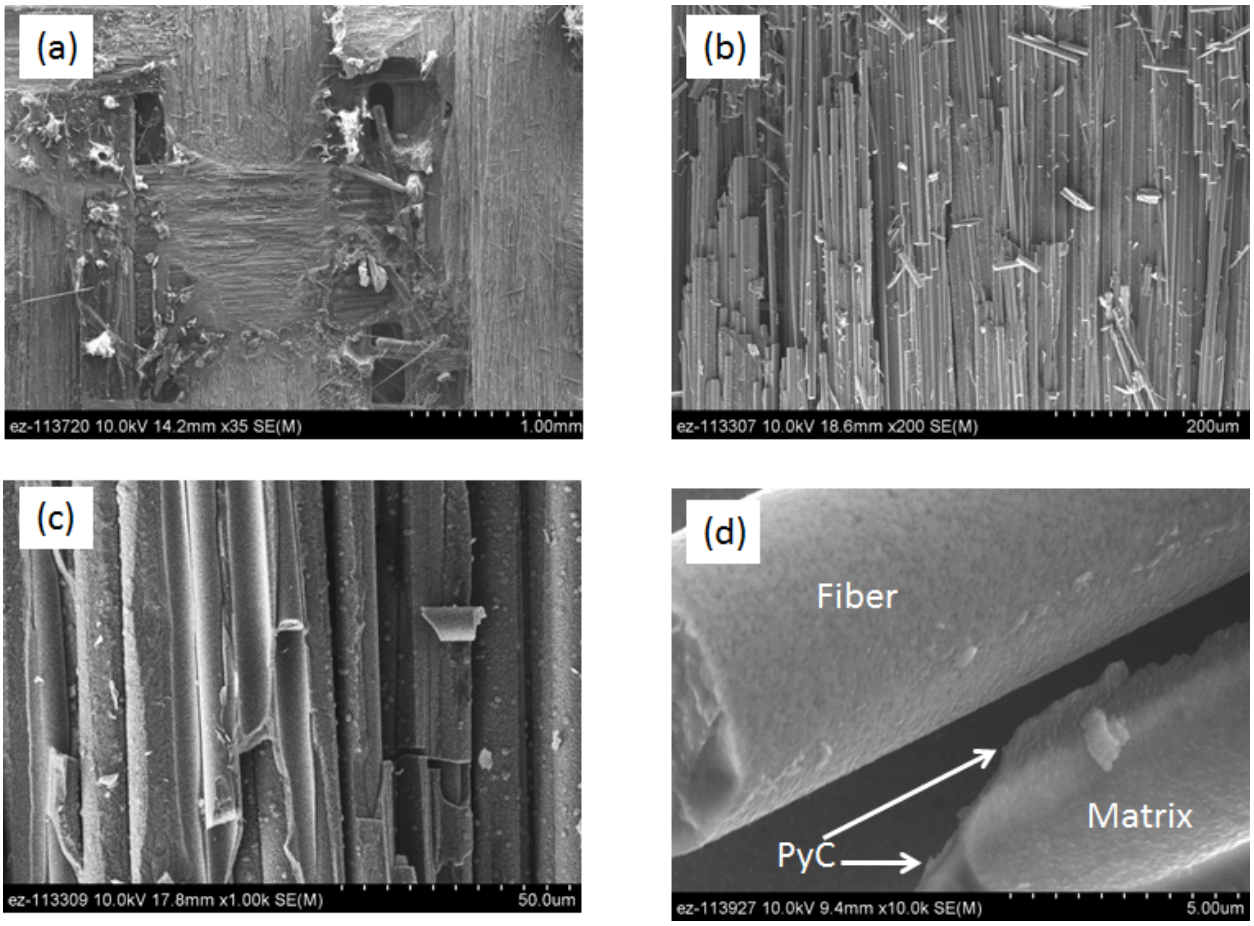

Figure 9. SEM Images of fracture surface of TySA/PyC150 composites after diametral compression test.

Fracture surface of NITE/PyC500 composite after diametral compression test (Figure 10) is flatter than the TySA/PyC150 composite because of the uni-directional weave architecture. Less fiber fracture is observed. On the contrary, it is observed that fibers are lifted by the trans-thickness tensile stress, revealing the matrix (with fiber imprint) underneath the fiber. Failure occurs mostly between the PyC coating and Matrix interphase so most of the fibers in the fracture surface still have a PyC coating. Even though the NITE/PyC500 composites have less porosity, the crack can grow along the PyC coating and the SiC matrix without much interference while subject to a trans-thickness tensile load, resulting in a smaller tensile strength (21.4 MPa).

Debond occurs mostly between the PyC coating and Matrix interphase so most of the fibers in the fracture surface still have a PyC coating. This agrees with the previous finding for the same composite under interlaminar shear loading.

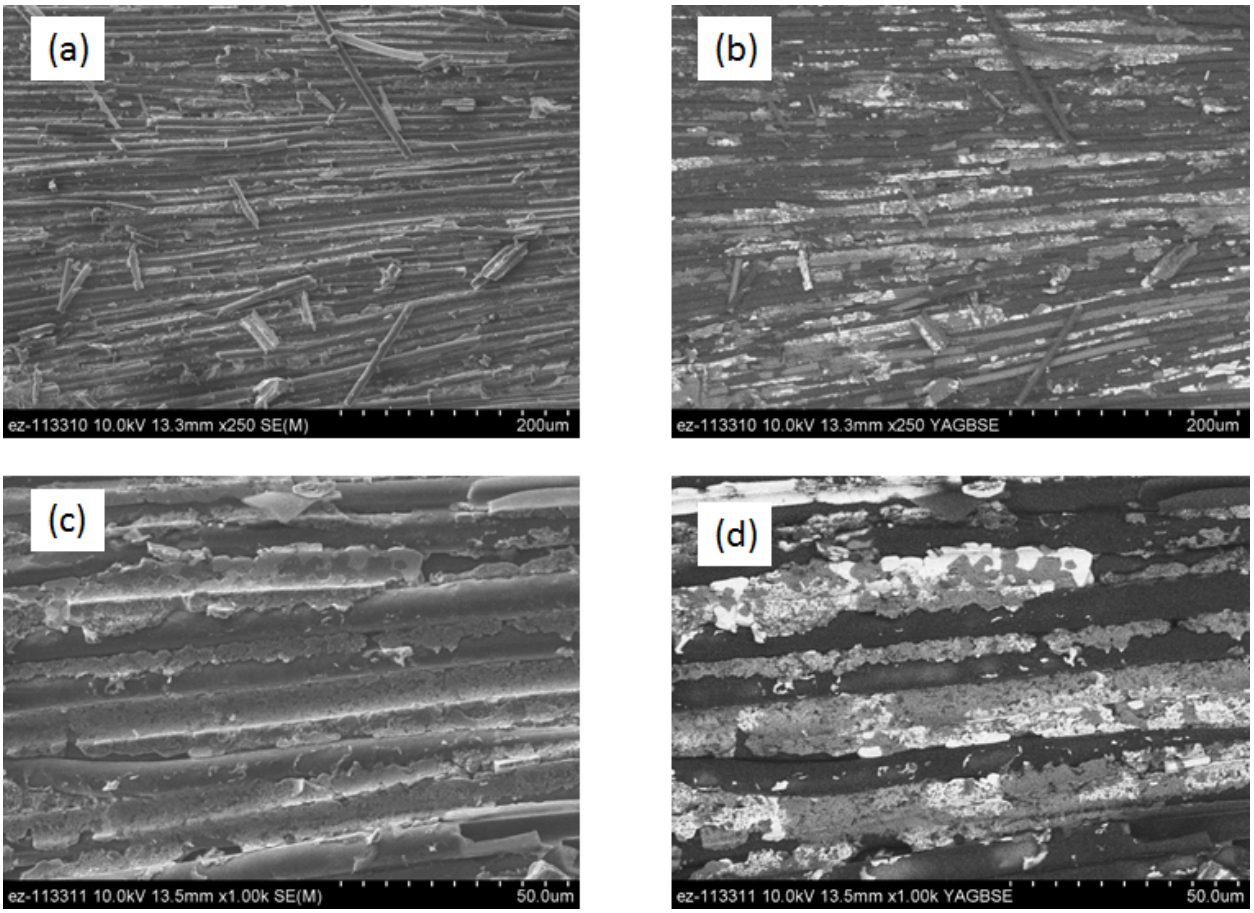

Figure 10. SEM images of fracture surface of NITE/PyC500 composites after diametral compression test. (a) and (c), secondary electron image; (b) and (d), back scattered electron image.

CONCLUSIONS

Interlaminar shear strength and trans-thickness tensile strength of different type of SiC fiber reinforced SiC matrix composites have been successfully evaluated with doubled notched shear test and diametral compression test respectively. HNLS/PyC150 composite has a low ILSS (10.7 MPa) because of poorly densified interlaminar matrix, resulting in interlaminar failure. TySA/PyC150 composite has a better densified interlaminar matrix, thus showing intra-bundle failure upon DNS test and a higher ILSS (30.1 MPa). The NITE/PyC500 composite showed the highest ILSS (37.5 MPa) because of its high density and the lack of interlaminar structure.

Upon diametral compression test, HNLS/PyC150 composites showed an intra-bundle fracture pattern with a TTS of 34.1 MPa. For the NITE/PyC500 composites, trans-thickness tensile stress caused the crack to grow along the PyC coating and the SiC matrix without much interference, resulting in a smaller TTS of 21.4 MPa. Debond occurred between the PyC coating and SiC fiber for the two CVI densified composites. For NITE densified composites, debond occurred between the PyC coating and the SiC matrix.

For 2D weave composites, both shear and tensile stress bearing capacities of the tows were lower than the interlaminar matrix, assuming the interlaminar matrix is adequately densified. The interlaminar mechanical properties of these SiC/SiC composites are much weaker than their in-plane properties. Whether the interlaminar properties will be the design limit of these materials need to be addressed for individual application.

REFERENCE

[1] R. J. Price and G. R. Hopkins, *J. Nucl. Mater.* **108** (1982) 732-738
[2] Y. Katoh and L. L. Snead, *J. ASTM Int.* **2** (2005) 12377
[3] G. Newsome, L. L. Snead, T. Hinoki, Y. Katoh and D. Peters, *J. Nucl. Mater.* **371** (2007) 76-89
[4] L. L. Snead, T. Nozawa, Y. Katoh, T. S. Byun, S. Kondo and D. A. Petti, *J. Nucl. Mater.* **371** (2007) 329-377
[5] L. L. Snead and S. J. Zinkle, *Nucl. Instrum. Methods Phys. Res. Sect. B-Beam Interact. Mater. Atoms* **191** (2002) 497-503
[6] Y. Katoh, L. L. Snead, C. H. Henager Jr., A. Hasegawa, A. Kohyama, B. Riccardi and H. Hegeman, *J. Nucl. Mater.* **367-370, Part A** (2007) 659-671
[7] T. Nozawa, Y. Katoh and L. L. Snead, *J. Nucl. Mater.* **367** (2007) 685-691
[8] Y. Katoh, L. L. Snead, T. Nozawa, S. Kondo and J. T. Busby, *J. Nucl. Mater.* **403** (2010) 48-61
[9] Y. Katoh, T. Nozawa, L. L. Snead, K. Ozawa and H. Tanigawa, *J. Nucl. Mater.* **417** (2011) 400-405
[10] K. T. Kedward, *Fibre Sci. Technol.* **5** (1972) 85–95
[11] O. Unal and N. P. Bansal, *Ceram. Int.* **28** (2002) 527-540
[12] O. Unal and N. P. Bansal, *Interlaminar shear strength of a unidirectional fiber-reinforced celsian composite by short-beam and double-notched shear tests*, in *25th Annual Conference on Composites, Advanced Ceramics, Materials, and Structures: A*. M. Singh and T. Jessen, Editors (2001) p. 585-595.
[13] M. M. Shokrieh and L. B. Lessard, *Appl. Compos. Mater.* **5** (1998) 49-64
[14] F. Sugiyama, K. Ogawa and T. Nishida, *J. Ceram. Soc. Jpn.* **104** (1996) 978-983
[15] N. J. J. Fang and T. W. Chou, *J. Am. Ceram. Soc.* **76** (1993) 2539-2548
[16] T. Hinoki, E. Lara-Curzio and L. L. Snead, *Evaluation of transthickness tensile strength of sic/sic composites*, in *27th International Cocoa Beach Conference on Advanced Ceramics and Composites: B*, W. M. Kriven and H. T. Lin, Editors (2003) p. 401-406.
[17] T. Hinoki, E. Lara-Curzio and L. L. Snead, *Fusion Science and Technology* **44** (2003) 211-218
[18] A. BrucknerFoit, T. Fett, D. Munz and K. Schirmer, *J. Eur. Ceram. Soc.* **17** (1997) 689-696
[19] M. K. Fahad, *J. Mater. Sci.* **31** (1996) 3723-3729
[20] M. Mellor and I. Hawkes, *Engineering Geology* **5** (1971) 173-&
[21] J. S. Park, A. Kohyama, T. Hinoki, K. Shimoda and Y. H. Park, *J. Nucl. Mater.* **367** (2007) 719-724
[22] Y. Katoh, S. M. Dong and A. Kohyama, *Fusion Eng. Des.* **61–62** (2002) 723-731
[23] Y. Katoh, A. Kohyama, T. Nozawa and M. Sato, *J. Nucl. Mater.* **329** (2004) 587-591
[24] S. M. Dong, Y. Katoh and A. Kohyama, *J. Am. Ceram. Soc.* **86** (2003) 26-32
[25] T. Hinoki, Y. Maki, A. Kohyama, E. Lara-Curzio and L. L. Snead, *Ceramic Engineering and Science Proceedings* **25** (2004) 65-70
[26] B. Riccardi, E. Trentini, M. Labanti, M. Leuchs, S. Roccella and E. Visca, *J. Nucl. Mater.* **367** (2007) 672-676
[27] S. T. Peters, *Handbook of Composites, 2nd edition*. 1998, Chapman & Hall, p. 790-791.

[28] Y. Katoh, K. Ozawa, T. Hinoki, Y. Choi, L. L. Snead and A. Hasegawa, *J. Nucl. Mater.* **417** (2011) 416-420
[29] Y. Katoh, *Unpublished data*
[30] S. R. Choi, R. W. Kowalik, D. J. Alexander and N. P. Bansal, *Compos. Sci. Technol.* **69** (2009) 890-897
[31] P. Brondsted, F. E. Heredia and A. G. Evans, *J. Am. Ceram. Soc.* **77** (1994) 2569-2574
[32] T. Nozawa, Y. Choi, T. Hinoki, H. Kishimoto, A. Kohyama and H. Tanigawa, *IOP Conference Series: Mater. Sci. Eng.* **18** (2011) 162011

4.1 HIGH-HEAT FLUX TESTING USING PLASMA ARC LAMPS OF LOW-LEVEL IRRADIATED MATERIALS — A. S. Sabau, E. Ohriner, Y. Katoh, and L. Snead (Oak Ridge National Laboratory)

OBJECTIVE

The objective of this work is testing of irradiated materials that are candidates for use in divertor components and mock-up divertor components under high-heat flux using Plasma Arc Lamps (PAL).

SUMMARY

The high-heat flux testing facility using Plasma Arc Lamps was demonstrated at ORNL for W samples. The test sections were designed by taking into account safety and materials compatibility requirements in order to handle the testing of low level irradiated tungsten articles. An enclosure was designed and fabricated. Test sections for the high-heat flux testing using PAL of low-level radioactive sample were designed and fabricated. The test sections were assembled and proof-of-principle testing was conducted, demonstrating the readiness of the new facility for irradiated samples.

PROGRESS AND STATUS

Introduction

Developing plasma-facing materials is a key challenge to the realization of the steady state high power fusion that will be required in DEMO and future fusion power plants. Based primarily on high temperature performance and plasma poisoning issues the two candidate materials for PFC armor have been tungsten and carbon. However, for the case of ITER, and likely the next generation of deuterium-tritium fueled machines, tungsten appears the material of choice. In order to demonstrate the performance of these new materials and structures, the Plasma-arc-lamp facility at ORNL will be used with minor modification to provide fusion-prototypical steady state heat flux conditions.

This work specifically addresses (1) coupling of the material design effort with material testing, and (2) cost-effective testing, as specifically identified in the Fusion ReNeW roadmap as follows:

- thrust area 11 “Careful *coupling of the material design effort with material testing* will be required to advance a science-based development approach.” and “Such testing will need to proceed in a timely and *cost-effective* manner to ensure that the results are incorporated into improved material designs that will enhance the performance of the developed materials.”
- *thrust area 14* high heat flux testing will be aimed at “Basic materials property information and models of materials behavior in the harsh fusion environment.”

There are several high heat flux (HHF) test facilities that provide thermal loads with power densities ranging from the MW/m^2 to several GW/m^2, and pulse durations ranging from a few hundred microseconds to almost continuous (Hirai et al., 2005; Coenen et al. 2011). For the static high heat flux testing, tests in electron beam facilities, particle beam facilities, IR heater and in-pile tests have been performed (Hirai et al., 2005). In this effort, only high heat flux (HHF) testing will be considered and the primary facility utilized will be the plasma arc lamp facility, a high-intensity infrared lamp. This technology has been successfully demonstrated for this purpose in the past for

the High Average Power Laser inertial fusion program. Static heat loads corresponding to cycling loads during normal operation, are estimated to be up to 20 MW/m^2 in the divertor targets in ITER. Tungsten coatings bonded to F82H steel have been successfully tested to greater than 10 MW/m^2 for one thousand cycles using the plasma arc lamp facility at ORNL (Romanoski, et al., 2005; Figure 5).

EXPERIMENTAL PROCEDURE

In this project, as part of the material characterization of divertor armor the testing is undertaken of actively cooled components under fusion specific (a) thermal loading conditions and (b) operational temperatures. The high heat flux testing at ORNL using the plasma arc lamp will aim at obtaining (1) basic materials property information and (2) formulating constitutive equations for models of materials behavior in the harsh fusion environment.

PAL Facility

ORNL has two Plasma-arc lamps available, as illustrated in Figure 1 and described in Table 1.

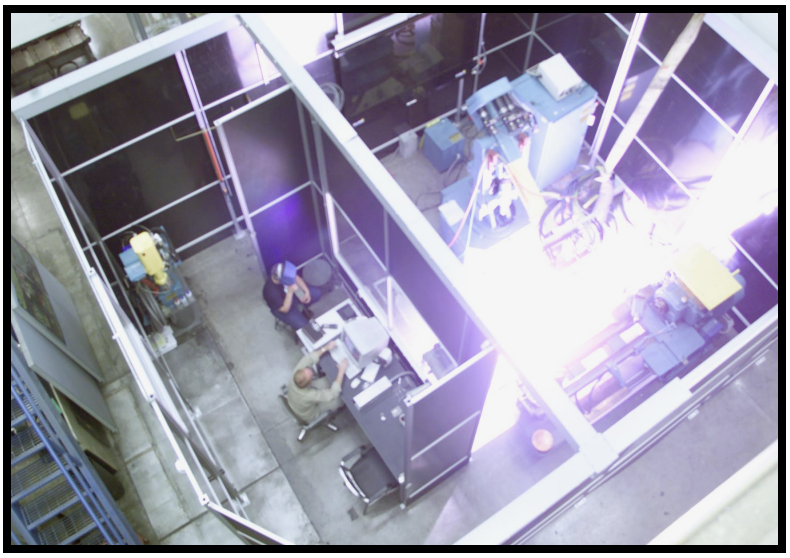

Figure 1. Plasma Arc Lamp available at ORNL for high heat flux testing.

Table 1. Incident and absorbed heat fluxes in tungsten at current ORNL PAL Capabilities.

Plasma Arc Lamp System	Min. Pulse Time [s]	Max. Pulse Time [s]	Incident Max. Heat Flux [MW/m^2]	*Absorbed Max. Heat Flux in W [MW/m^2] at 1,100 K	Process Area [cm^2]	Size of Max Heat flux [cmxcm]
Vortek 300	0.01	50-400	27	12.7	41	1x10
Vortek 500	0.02	50-400	4.2	2	320	18x18

*Based on W emissivity of 0.47.

Test Section Design

The test sections were designed by taking into account safety and materials compatibility requirements in order to handle the testing of low levels irradiated tungsten articles (Table 2). An enclosure was designed and fabricated (Figure 2). Test sections for the high-heat flux testing using PAL of low-level radioactive sample were designed and fabricated (Figure 3). The test section was instrumented with thermocouples as shown in Figure 3b. I order to handle RAD materials, the facility relies on two levels of containment: (1) a quartz cylinder that contains the sample holder, (2) the Al test enclosure that is vacuum tight including a high-temperature o-ring to support the large quartz window and vacuum-tight thermocouple feedthroughs, (3) Ar evacuation using HEPA vacuum filters.

Table 2. Design considerations and solution adopted for the testing of low-level irradiated tungsten articles.

Design Considerations	Solutions
IR heating	Quartz window
Quartz window seal	High temperature o-ring
Enclosure overheating	Enclosure size larger than area of peak power, water cooled
W testing: No O_2 at high temp.	Evacuation of air in enclosure and backfill with Ar
Quartz window integrity during air evacuation	Secondary chamber for equalizing pressure on both sides of window
Liftoff of quartz window	Vent & Pressure gauge
Avoid overheating & cracking of Q-window during high-heat flux	Air knife to cool the quartz
High-heat flux	Impingement water cooling
Containment of RAD volatilization compounds	1. HEPA filter vacuum 2. Testing section enclosed in quartz cylinder 3. Vacuum tight thermocouple feedthroughs 4. No water connections within the enclosure
Temperature measurements	K, S, R thermocouples; pyrometer

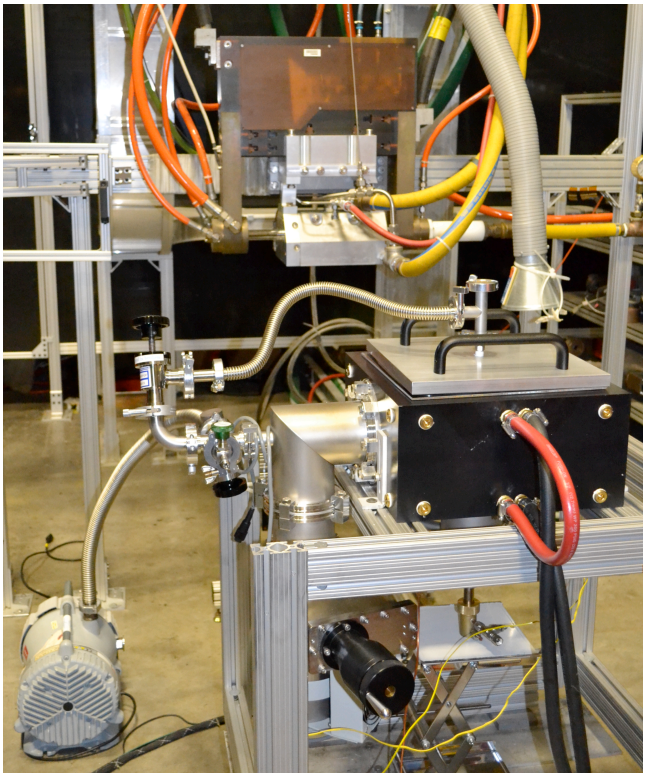

Figure 2. Aluminum enclosure (black anodized) as prepared for the evacuation procedure, showing vacuum pump and top chamber.

(a) 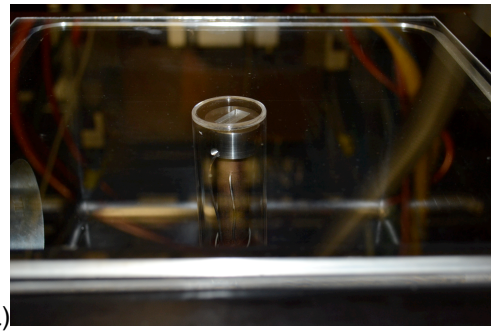 (b) 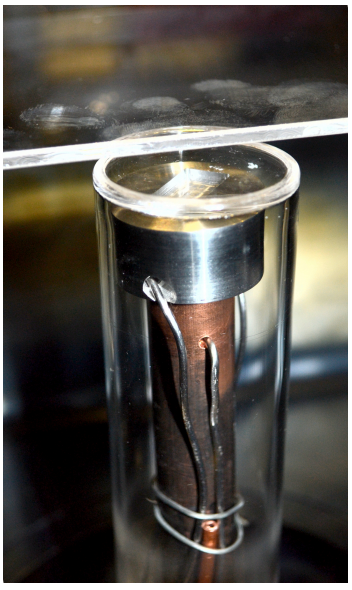

Figure 3. Test section (a) panoramic top view and (b) test stand composed of quartz cylinder for containment of volatile RAD gases, water cooled rod, Mo sample holder, and thermocouples.

RESULTS

The test sections were assembled and proof-of-principle high-heat flux testing was conducted, demonstrating the readiness of the new facility. The locations of the thermocouples are shown in Figure 4. The temperature data during demonstration test was obtained using the uniform reflector of the 750kW PAL at an estimated heat flux of 2 MW/m^2 at an offset distance of 3.2cm. The heat flux measured at 2cm offset was 2.35 MW/m^2. It is estimated that the incident heat flux into the sample was approximately 1 MW/m^2. A typical temperature evolution during a demonstration test is shown in Figure 5. The test duration was 30 s.

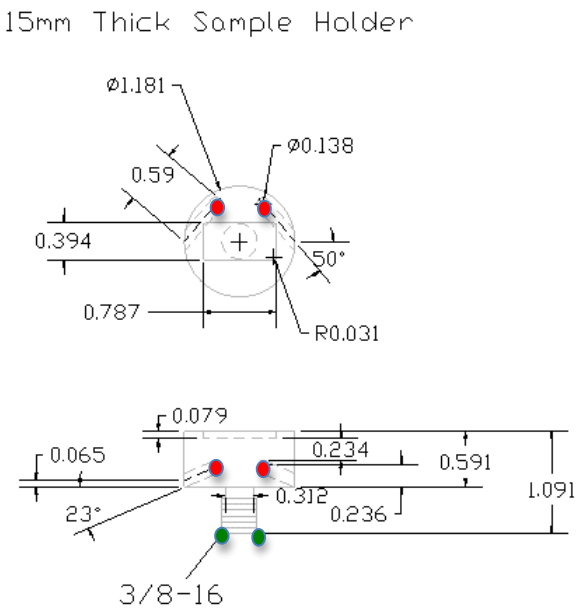

Figure 4. Location of thermocouples in the sample holder (red dots) and cooled rod (green dots).

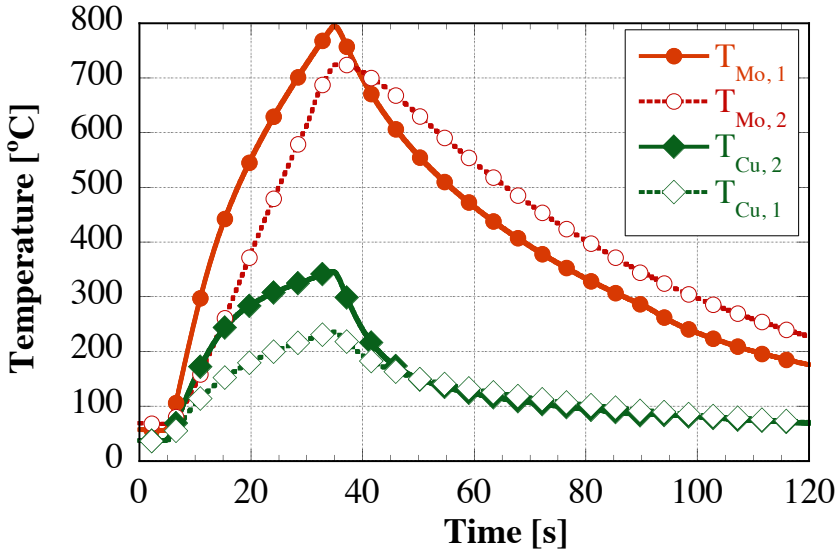

Figure 5. Typical temperature evolution during a demonstration test showing temperatures in the Mo sample holder (circle symbols) and in the Cu water-cooled rod (diamond symbols).

ACKNOWLEDGMENTS

The authors would like to thank Charles Ross (Chuck) Schaich for assisting with CAD design, fabrication specifications, and assembly; Jim Kiggans for design and fabrication of the Al enclosure, Marie Alta Williams for RAD safety considerations, and David Harper for operating the PAL.

REFERENCES

[1] T. Hirai, K. Ezato, and P. Majerus, "ITER Relevant High Heat Flux Testing on Plasmas Facing Surfaces," *Mater. Trans.* **46**, 3 (2005) 412.

[2] J. W. Coenen, V. Philipps, S. Brezinsek, B. Bazylev, A. Kreter, T. Hirai, M. Laengner, T. Tanabe, Y. Ueda, U. Samm, and the TEXTOR Team, "Analysis of Tungsten Melt-Layer Motion and Splashing Under Tokamak Conditions at TEXTOR," *Nucl. Fusion* **51**, 083008 (11pp) 2011.

[3] G. Romanoski, L. Snead, A. Sabau, J. Kelly, and S. Zinkle, "Bonding Tungsten to Low Activation Ferritic Steel, *HAPL Workshop*, LLNL, June 20-21, 2005.

4.2 GRAIN BOUNDARY STRENGTHENING PROPERTIES OF TUNGSTEN ALLOYS — W. Setyawan and R. J. Kurtz (Pacific Northwest National Laboratory)

OBJECTIVE

The objective of this research is to support the search for tungsten alloys with increased grain boundary cohesion using first-principles methods.

SUMMARY

Density functional theory was employed to investigate grain boundary (GB) properties of W alloys. A range of substitutional solutes across the Periodic Table was investigated to understand the behavior of different electronic orbitals in changing the GB cleavage energy in the Σ27a[110]{525} GB. A number of transition metals were predicted to enhance the GB cohesion. This includes Ru, Re, Os, Ir, V, Cr, Mn, Fe, Co, Ti, Hf, Ta and Nb. While lanthanides, *s* and *p* elements were tended to cause GB embrittlement.

PROGRESS AND STATUS

Introduction

The development of novel W-based materials that are suitable for future fusion reactors is likely to involve synergistic advancements in intrinsic W alloys [1, 2], grain boundary (GB) engineering [3, 4] and W-based composites [5, 6]. In all of these areas, understanding and controlling the characteristics of materials at intergranular regions are important. Using first-principles methods, we have recently started to study the strengthening properties of substitutional solutes on the GB cohesion of tungsten. In our previous studies [7], the effects of the fifth- and sixth-row transition metals (TM) were investigated in three GB structures, Σ27a[110]{525}, Σ11[110]{323} and Σ3[110]{112}. GB strengthening was found for Hf, Ta, Nb, Ru, Re, Os and Ir for the Σ27a GB and to a lesser degree for the Σ11 GB. Lower valence solutes, with respect to W, strengthen the GB at certain substitutional sites, while higher valence elements enhance it at other positions. For the Σ3 GB, the Ru, Re, and Os slightly increased the cleavage energies. Hence, alloying with these TMs increases the cohesion more effectively for large-angle GBs whose cleavage energy, in general, is lower than the low-angle ones. Electron density plots elucidates the mechanism of charge addition or depletion of the GB bonding region upon alloying leading to stronger or weaker intergranular cohesion, respectively.

In this report, we extended the study to include a more complete list of solutes spanning the different characters of electronic valence across the Periodic Table. The fourth-row TMs (Sc to Zn), lanthanides, alkalis, alkaline earth metals, and *p*-electron solutes from Groups 3A-5A were investigated. Knowledge of how different types of valency and atomic volume differences affect the GB would provide a reference in designing tungsten-based materials with improved fracture resistance.

Formalism

In this study, the Σ27a[110]{525} tilt GB was used as a model. The GB structure was initially relaxed using conventional molecular dynamics (MD). We used the interatomic potential developed by Ackland and Thetford [8]. Systematic interfacial shifts and atoms relaxations were

done to achieve the most stable configurations. The structures obtained from the MD were further optimized via the ab initio method. VASP software was used to perform the quantum mechanical calculations based on the density functional theory (DFT). Accurate projector-augmented-wave pseudopotentials with Perdew-Burke-Ernzerhof exchange-correlation functionals were employed [9–11]. Plane-wave energy cutoffs and k-point sampling of the Brillouin zone were carefully checked for convergence. Spin-polarized calculations were performed. Structures were fully relaxed with a tolerance of 1 meV. For non-slab configurations, a force tolerance of 10 meV/A was used. At the end of volume-nonconserving relaxations, an additional static calculation was performed to avoid numerical errors due to basis incompleteness. The necessary slab thickness for the DFT calculations was determined from the convergence tests of the {525} surface energy. A total of 62 layers including one GB interface and two free surfaces were required for the Σ27a GB. A 1x2x1 supercell containing 124 atoms was used throughout the simulations.

RESULTS

Figure 1 shows the structure of the Σ27a GB as viewed from the <110> direction. An electron density plot reveals the alternating atomic layers along [110]. The unit cell contains four such layers. The slab thickness was carefully determined to include atoms with a "bulk-like" atomic environment (site O). The details of the convergence study of the slab thickness can be found in Ref [12]. The cube of the bcc with site O as the center is shown. The dashed lines represent the edges of the cube. Site O is eight-coordinated with nearest-neighbor (nn) distance of 2.73 Å. As the cube is viewed from [110] projection, only six nn atoms are visible. We introduce three types of coordination as follows:

nc: Site B is eight-coordinated with 8 nearest neighbors: A (2.73 Å), C (2.73 Å), F (2.79 Å) and H (2.66 Å), two atoms each. Even though the angular position of the neighbors deviates from the perfect bcc structure, the nn distances are similar to that of a single crystal. For this reason, site B is referred as "normally-coordinated" (*nc*).

oc: Site A represents an "over-coordinated" (*oc*) position with 10 nearest neighbors: G (2.46 Å), B (2.73 Å), E (2.56 Å), two atoms each and F (2.89 Å) four atoms.

uc: Site D is an "under-coordinated" (*uc*) position with 6 nearest neighbors: C (2.72 Å) two atoms and E (2.90 Å) four atoms.

The electron density plot (Fig. 1) reveals the bonding of atoms A, B and D with their visible neighbors. The charge distribution corroborates the coordination types of those sites. From this point of view, these three sites are good representatives to elucidate the important response of various orbital types to different atomic environments in the GB.

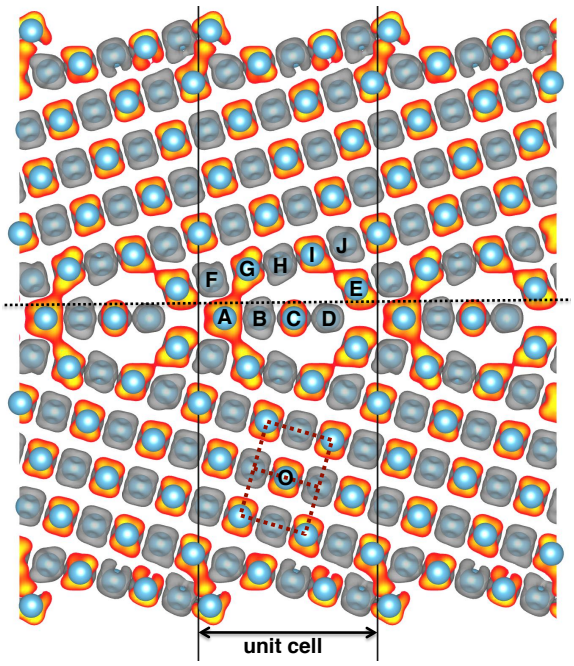

Figure 1. Structure and electron density of the W Σ27a[110]{525} tilt GB viewed along the <110> direction. The relative strength of the GB bonds is revealed (higher electron density indicates stronger bond).

Grain Boundary Strengthening

The GB strengthening property of a solute was studied by substituting one atom at sites A, B or D. This corresponds to ~ 2.6 at.% in bulk. The horizontal dashed line (Fig. 1) denotes the cleavage plane for calculating the cleavage energy (E_{cv}). Figure 2 shows the evolution of the cleavage energy as a function of atomic number of the solute at different substitutional positions. The line at 4.16 J/m^2 marks the cleavage energy of the pure GB. Systematic trends are evident and can be summarized as follows:

(i) *s*-valence: embrittlement at all sites, fewer electrons → lower E_{cv}. Substitution at *oc* site promotes lower cleavage energy.

(ii) *p*-valence: embrittlement at all sites, more electrons → lower E_{cv}. Substitution at *oc* site promotes lower cleavage energy.

(iii) *d*-valence: strengthening at *oc* site (maximum with 7B-8B elements) and *uc* site (maximum with 3B-4B solutes), but embrittlement at *nc* site.

(iv) *f*-valence: embrittlement at all sites except Lu and Tm at *uc* site, fewer electrons → lower E_{cv}. Substitution at *oc* site promotes lower cleavage energy. Note that La and Lu may also be assigned to the *d*-valence group since their *f*-orbitals are well screened.

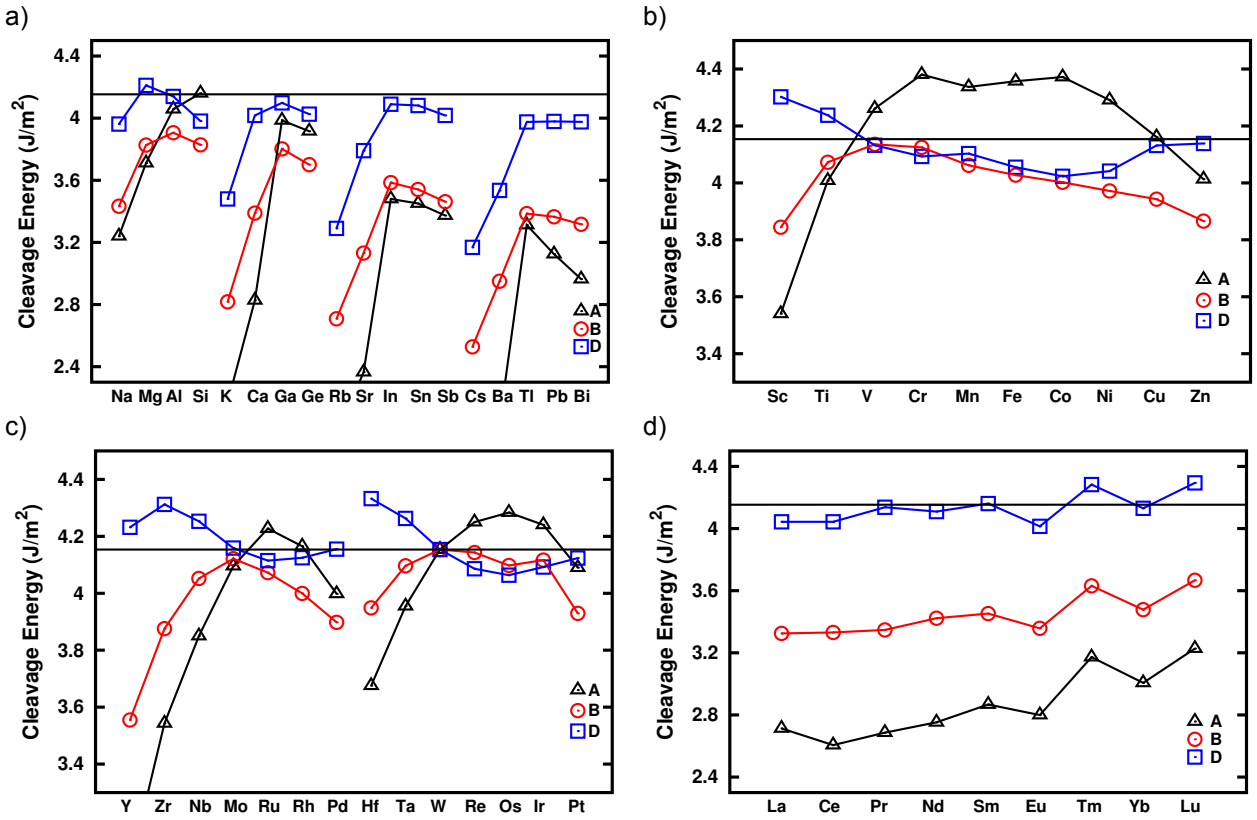

Figure 2. Cleavage energy of W Σ27a GB as a function of solutes substituted at positions A, B and D in Fig. 1. The elements are arranged with increasing atomic number. a) *sp*-valence elements, b) transition metals row-4, c) transition metals row-5 and row-6, and d) lanthanides. The line at 4.16 J/m^2 marks the cleavage energy of the pure GB.

These results indicate that strengthening can be achieved by using solutes near the middle region of the Periodic Table. Towards the edges of the Periodic Table, embrittlement is enhanced. The behavior of lanthanides is in between that of Ba and Hf.

Among the strengthening solutes, those with a smaller valency than W strengthen at *uc* site. The mechanism is that these solutes give off some electrons to the nearby *oc* site governing the most GB bonding, hence increasing the cohesion. On the other hand, higher-valence metals increase the cohesion at *oc* site by providing more electrons to be available for bonding. The bonding is mediated by the *d*-orbitals. At the *oc* site, the maximum strengthening is produced by Os, Ru, and near Fe, which is due to the fact that these atoms, with six electrons, complement tungsten's four electrons to fully occupy the *d*-orbitals. At the *nc site,* all solutes decrease the cleavage energy. This is caused by the redistribution of the electrons between the solute at this site and W at the *oc* site, which results in a net decrease of in GB bonding. A list of the potential strengthening solutes is presented in Table 1 along with their maximum solubility at several temperatures.

Table 1. Solubility limit [atomic %] of potential alloying elements in W at several temperatures T. Solutes that increase the grain boundary cohesion when substituted at over- or under-coordinated site are grouped in the top or bottom panel, respectively [13, 14]. Several data are not available (N/A).

T [°C]	V	Cr	Mn	Fe	Co	Ni	Ru	Re	Os	Ir
0	100	<4.8	N/A	2.1	7.2	1.2	6.3	19.7	5	<1.7
500	100	4.8	N/A	2.1	7.2	4.8	6.3	22.6	5	<1.7
1000	100	11.2	N/A	2.4	7.3	6.2	6.3	25.7	5.7	1.7
1500	100	26.5	N/A	2.7	8.8	4.6	8.2	27.8	6.9	2.4
	Mg	Sc	Ti	Y	Zr	Nb	Hf	Ta	Lu	
0	N/A	~0	<11.1	N/A	0.7	100	<3.4	100	~0	
500	N/A	~0	11.1	N/A	0.7	100	<3.4	100	~0	
1000	N/A	~0	44	N/A	0.8	100	3.4	100	~0	
1500	N/A	~0	100	N/A	1.3	100	6.2	100	~0	

Substitutional Solute Stability

Figure 3 shows the segregation energy of a substitutional solute relative to the configuration when the solute is at the “bulk-like” site O in the same simulation cell. A negative value of segregation energy indicates that the solute is more stable at the GB site than in the bulk. For any solute, the most stable configuration results in the highest cohesion. The most important finding is that solutes that potentially increase the cleavage energy are stable at their corresponding GB site. Therefore, energetically, their strengthening properties as predicted in this study can be realized.

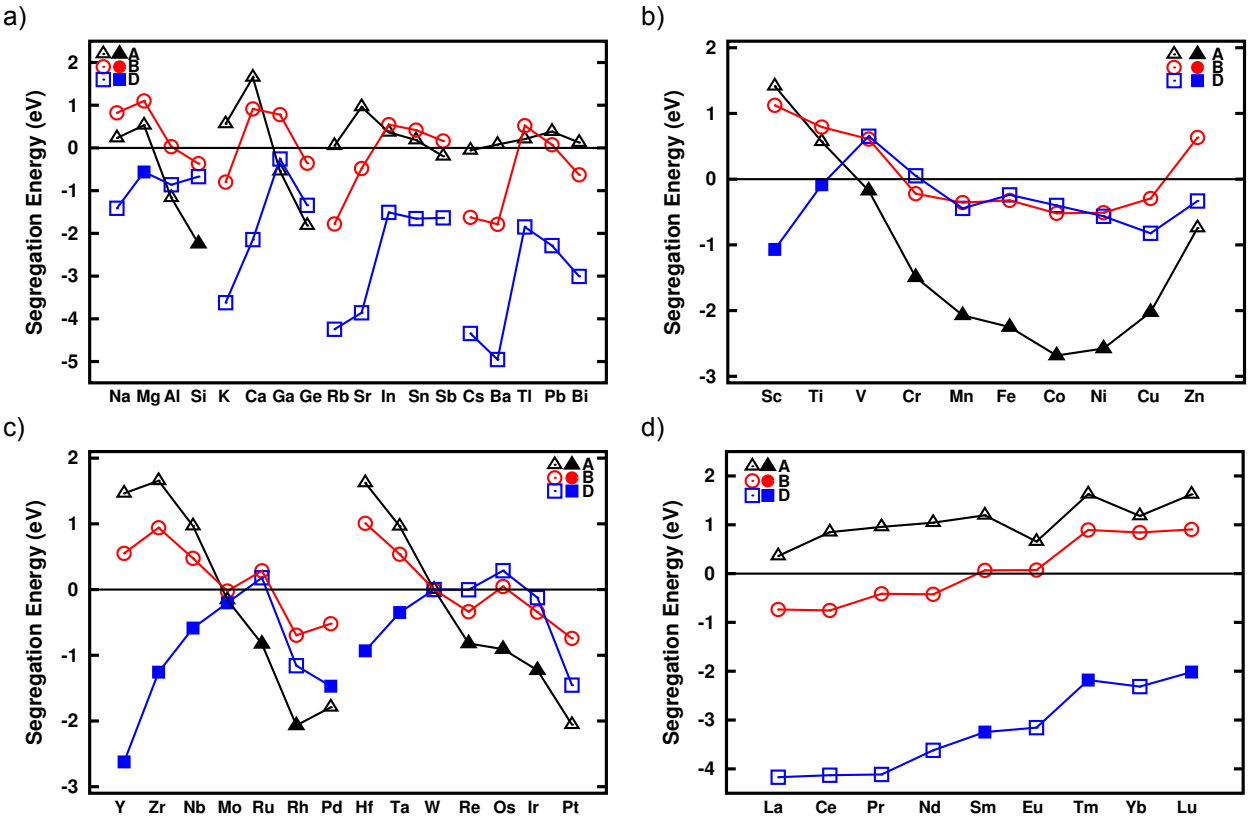

Figure 3. Segregation energy of substitutional solutes in W Σ27a GB relative to "bulk-like" site in the same simulation cell. The more negative the segregation energy the more stable it is at that site. The combinations of atom and position that increase or decrease the GB cohesion are plotted in filled or open marks, respectively.

Computations were performed partly on Chinook supercomputer (EMSL-45390) at Pacific Northwest National Laboratory (sponsored by the DOE's Office of Biological and Environmental Research).

REFERENCES

[1] Y. Mutoh, et al., *J. Mater. Sci.* **30** (1995) 770.
[2] S. Wurster, et al., *J. Nuc. Mater.* **413** (2011) 166.
[3] L. J. Kecskes, et al., *Mater. Sci. Eng. A* **467** (2007) 33.
[4] M. Faleschini, et al., *J. Nucl. Mater.* **367** (2007) 800.
[5] E. Lassner and W. -D. Schubert, "Tungsten", Springer (1995).
[6] Y. Ishiyama, et al., *Mater. Sci. Eng. A* **473** (2008) 7.
[7] W. Setyawan and R. J. Kurtz, Semiannual Report period ending December (2011).
[8] G. J. Ackland and R. Thetford, *Phil. Mag. A* **56** (1987) 15.
[9] P. E. Blöchl, *Phys. Rev. B* **50** (1994) 17953.
[10] G. Kresse and D. Joubert, *Phys. Rev. B* **59** (1999) 1758.
[11] J. P. Perdew, K. Burke and M. Ernzerhof, *Phys. Rev. Lett.* **77** (1996) 3865.
[12] W. Setyawan and R. J. Kurtz, *Scrip. Mat.* **66** (2012) 558.

[13] Alloy Phase Diagram, in ASM Handbook Online Vol. III (2012).
[14] T. B. Massalski, et al., Binary Alloy Phase Diagram, ASM International, Metals Park (1986).

4.3 W-ALLOY AND COMPOSITE FRACTURE TEST METHOD DEVELOPMENT AND INITIAL EXPLORATION OF DUCTILE PHASE TOUGHENING — G. R. Odette, E. Stergar[1], D. Gragg, K. Fields, and J. Heathcote[2] (University of California, Santa Barbara), C. H. Henager and R. J. Kurtz (Pacific Northwest National Laboratory)

OBJECTIVES

The objectives of this work include to: a) develop and apply methods to measure the fracture toughness of brittle W and brittle W matrix composites; and b) carry out an initial study of ductile phase toughening in a W-Cu model composite.

SUMMARY

There are many claims in the literature regarding various approaches to *"ductilizing"* W that are difficult to assess, in part because different tests have been used to *"characterize"* the various alloys. Thus one objective of this work is to demonstrate the application of accepted fracture mechanics test methods, so as to provide a common toughness-based metric for comparing different W alloys and composites. A major challenge to testing monolithic W is pre-cracking a very brittle material. A variety of approaches to pre-cracking an elemental W plate were attempted. The most successful method was compression fatigue applied in the axial direction of a small, initially notched bend bar, with the crack in the (T-L) orientation. The linear elastic toughness was measured in 3-point bend tests and averaged K_{Ic} = 8.34±0.43 MPa√m.

A second testing challenge is associated with ductile phase toughened composites. In this case it is necessary to measure the toughness resistance curve associated with extensive stable crack growth. The resistance curve is expressed in terms of J_r/K_r-da curves. Ductile phase toughening (DPT) is largely due to the formation an intact bridging zone behind the tip of crack, which results in a increase in the remote load stress intensity needed for continued crack growth with increasing crack length, da. The main challenge in this case was measuring da as a function of the load (P) and load point displacement (δ). We successfully characterized a K_r-da curve for a W-25%Cu heavy metal composite by combining load P-δ curves with digital image correlation (DIC) measurements of crack growth on the specimen surfaces that could not be observed by normal optical methods. The W-Cu system also served as a model system for an initial exploration of DPT of W composites. The results showed that DPT increased the maximum load toughness of the composite to an average of 24.9±3.5 MPa√m, or a maximum load capacity of ≈ 3 times higher than for monolithic W. The detectible initiation toughness of the composite, marking persistent crack growth, was also increased to ≈ 45 MPa√m compared to 8.34 MPa√m for the monolithic W. More importantly, extensive stable crack growth in the composite provided a major increment of effective post-peak load plastic ductility that is completely absent in linear elastic, monolithic W.

[1] Current address SCK Laboratory, Belgium
[2] Current Address Readly College, Readly, CA

PROGRESS AND STATUS

Introduction

This extended background section and associated references were extracted from a successful proposal to OFES entitled *Ductile-Phase Toughened and Fiber-Reinforced Tungsten for Plasma Facing Materials*. This section is included here because we believe that it provides a concise summary of ductile phase toughening of brittle matrix composites, which holds the promise of transforming W to an effective structural material for fusion applications. Tungsten (W) and W-alloys are the leading candidates for the plasma facing components (PFCs) of future fusion power systems because of their high melting point, strength at high temperatures, high thermal conductivity and low sputtering yield [1-5]. In fact, W and W-alloys (hereafter referred to as W-alloys) are almost certainly the material of choice for this extreme service application. However, W-alloys exhibit low fracture toughness and high brittle to ductile transition temperatures (DBTT) that will require them to be treated as fully elastic fracture brittle material in ITER or for DEMO reactor design and operation [1, 3, 6]. The poor starting mechanical properties of W-alloys will be further degraded by radiation damage even at elevated temperatures [7, 8]. The DBTT for unirradiated W-alloys typically ranges from 300 to 400˚C up to ~1000°C, and as noted above, radiation hardening would further elevate the DBTT [3, 9, 10]. Operation of W-alloys at even higher temperatures is limited by re-crystallization of fine grain structures that also degrades toughness [6, 11-13].

Metallurgical approaches to toughen W-alloys, including alloying with Re at concentrations up to 26% [10] and severe plastic deformation (SPD) [14], result in modest to significant toughness increases, and corresponding decreases in the unirradiated DBTT [14]. However, to date, there is no common basis to compare the various W-alloys, since the mechanical characterization methods used to declare an alloy to be “ductilized” have ranged from tensile tests, to smooth bar bend tests [14] to, in only a few cases, actual fracture toughness tests [14]. Thus one objective of this work is to develop and demonstrate a common protocol for testing W-alloys and measuring their fracture toughness.

Ductilizing W is a grand challenge. For example, severe deformation would be very difficult to implement in processing alloys and fabricating structures. Perhaps the most promising toughness increase was observed for the W-26%Re alloy [10]. However, this alloying approach suffers both from high costs and the potential for irradiation-induced precipitation (RIP) of Re-W intermetallic phases, which would produce significant hardening and embrittlement even at low dpa. Transmutation product Re is generated in W and the total concentration when RIP becomes a concern is not precisely known, but is probably less than 10% [15-17]. Claims of significant toughening by fine particle stabilized grains remain largely unproven, in part because of the ambiguous testing methods noted above.

The principles of DPT are illustrated in Figure 1 [18-23]. Figure 1b schematically shows ductile bridging ligaments being stretched in the wake of an open crack in a brittle matrix [22], such as W. A highly effective resistance curve toughening mechanism develops as a crack extends in a brittle matrix containing a suitable volume fraction of the ductile phase. Specifically, as a crack grows in the brittle matrix, it leaves behind a bridging zone of ductile ligaments over a length *L* behind the crack-tip. As cracks continue to

extend, L increases. For small scale bridging (SSB), when the ductile phase bridging zone is much smaller than the crack length, L reaches a steady state length, L_{SSB}. The ligaments produce crack face closure tractions acting in opposition to the applied loading stress intensity factor (SIF), $K_{Applied}$, thus reducing (shielding) the net crack tip SIF, $K_{Tip} < K_{Applied}$. Crack growth occurs when $K_{Tip} = K_{Matrix}$, the toughness of the brittle matrix. The closure stresses are determined by a ductile ligament stress-crack opening displacement function, $\sigma(u)$. The crack opening, u, increases with distance behind the crack-tip, and the reinforcement breaks at a critical u^* where $\sigma(u^*) = 0$ and a maximum L_{SSB} and steady-state K_{SSB}. Thus, an initially un-bridged crack begins to grow when $K_{Applied} = K_{Matrix}$. But as the crack grows L and $K_{Applied}$ needed for $K_{Tip} = K_{Matrix,}$ increase, producing a resistance curve, $K_r(da) > K_{Matrix}$, up to a maximum steady state, K_{SSB} at $da = L = L_{SSB}$. Energy principles can determine K_{SSB}, which depends only on K_{Matrix}, the $\sigma(u)$ work of the ductile phase rupture (in a non-dimensional form, χ) and the elastic modulus (E, see below) [19, 22].

While the concept of DPT is quite simple, the mechanics are more complex [22, 27]. Even for SSB it is necessary to model $K_r(da)$ based on self-consistent solutions for the $\sigma(u)$, $u(L)$ and $\sigma(L)$ functions [22]. Details of $K_r(da)$ are important because, for example, the strength of a composite in the presence of microcracks is primarily determined by the initial $K_r(da)$ slope, while for large cracks, the $K_r(da)$ closer to K_{SSB} controls fracture. Thus it is necessary to know the composite constituent properties from careful analysis and measurements, including for the ductile phases in the composite environment [22, 23, 28].

If DPT occurs under large-scale bridging (LSB) conditions, when L is not very small compared to the crack length, the entire $K_r(da)$ resistance curve behavior depends in a complicated way on the length scales and geometries of the reinforcement and the cracked body. In this case, as Figure 2a shows, very large increases in K_r are possible [22]. Application to composite structures requires that the $K_r(da)$ information be converted to remote applied load (P) and load-displacement (δ) functions, $P(\delta)$, for the cracked body. Figure 2b shows that $K_r(da)$ can be modeled based on the $\sigma(u)$, E and K_{Matrix} properties that can be both independently measured and modeled (see below). Figure 2c shows that DPT provides composite ductility as well as large strengthening factors compared to the brittle matrix. The most important composite constituent property is the $\sigma(u)$ function, which also depends in a complicated way on both intrinsic material properties of the ductile phase and extrinsic factors such as the reinforcement size, geometry, and other effects such as de-bonding from the brittle matrix. Thus the mechanics controlling $\sigma(u)$ is critical, and must be modeled using finite element methods [29, 30]. The most important take away point is that this complexity is a real advantage because: 1) it can be modeled and analyzed to predict the behavior of a structure; and 2) the variety of mechanisms and mechanics can be used to tailor and optimize DPT composite design for particular applications. It is our opinion that purely empirical efforts to develop W-composites that are not guided by proper understanding of the mechanisms and mechanics are likely to be expensive failures.

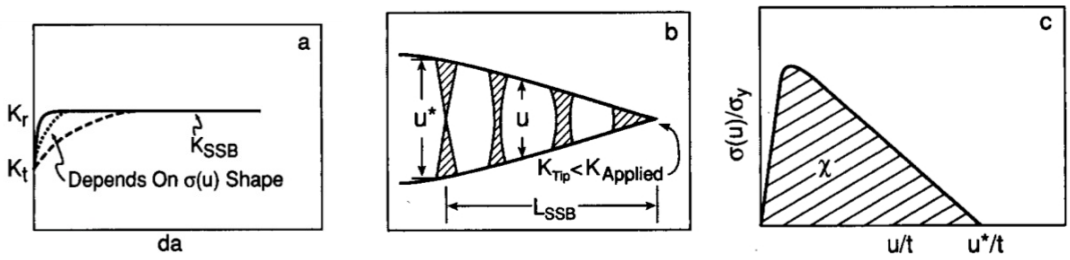

(a) (b) (c)

Figure 1. Schematic representation of ductile phase toughening: (a) Crack growth resistance curve behavior and steady-state toughness; (b) a steady-state bridge zone shown schematically in 2D; and (c) a typical normalized stress-displacement function and work of rupture, *c* for a DPT composite [22]. Symbols and terms are defined in the text above.

It is useful to provide more detail on one specific example of a DPT composite shown in Figure 2, Odette et al. fabricated a γ-TiAl/TiNb laminate by hot pressing and forging TiNb foils with TiAl powders to produce 105-μm layers of TiNb separated by about 500-μm of γ-TiAl matrix plus a thin α_2 reaction layer [22]. Chevron-notched three point bend specimens were machined from the starting material, which contained about 22% TiNb as the ductile phase reinforcement. Crack growth resistance curve, $K_r(da)$, tests were carried out under displacement control as a function of incremental crack length. The results were compared to the predicted SSB DPT toughening. For SSB the maximum net K_{SSB} is given by

$$K_{SSB} = \left(K_\chi^2 + K_{Matrix}^2\right)^{1/2}$$
$$K_\chi = \left(E\,\sigma_y\,t\,f\,\chi\right)^{1/2} \qquad (1)$$
$$\chi = f\int_0^{u^*}\left(\frac{\sigma(u)}{\sigma_y}\right)\frac{du}{t}$$

The $\sigma(u)$ is the absolute ductile phase ligament stress-displacement function. The non-dimensional χ is defined in terms of the corresponding crack face ductile phase area fraction (f), ligament thickness (t), yield stress (σ_y), and rupture displacement (u^*). Here E is the composite elastic modulus needed to relate K to the corresponding plastic work (J) as $K = [EJ]^{1/2}$. Normally K_c is much greater than K_{Matrix}, so the former has the dominant effect on the toughness, while the latter, along with E, has relatively less effect. Thus, from the perspective of gross mechanical failure, even if matrix toughness is low and further degraded in service by radiation damage, the consequence to composite behavior is greatly mitigated. Further, as discussed below, under LSB, when the bridging zone is not small compared to crack dimensions, the composite toughness is much greater than for SSB.

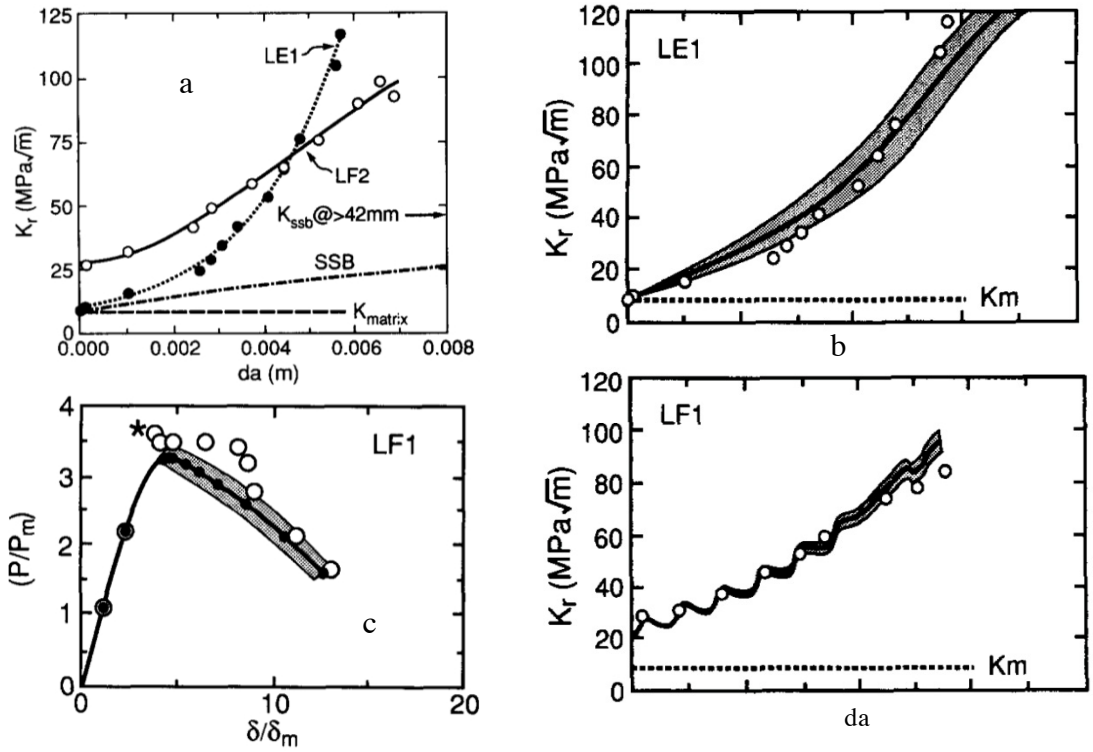

Figure 2. (a) Crack growth resistance curves in the LSB regime for a TiAl-TiNb composite showing large increases in toughness; (b) the corresponding normalized predicted and measured $K_r(da)$ curves showing enormous increases in toughness; and c) a corresponding $P(\delta)$ curve showing both large strengthening (≈ x3.5) and ductility increases (≥ x13) provided by DPT [22].

In the previous research of Odette and co-workers [22], the $\sigma(u)$ function was independently measured under constrained deformation conditions using sandwich TiAl/TiNb/TiAl specimens containing pre-cracks [31]. These independent measurements are critical since residual stresses and constraints affect the $\sigma(u)$ function relative to tensile test measurements. Rigorous modeling of LSB was carried out based on the independent $\sigma(u)$ function by calculating self-consistent solutions for the crack opening profile $u(x)$ and the corresponding crack face distribution $\sigma(x)$, where x is the distance from the crack tip, for a specified set of $\sigma(u)$, E, and K_{tip} composite properties [22]. Figure 2b shows the resistance curves from the model (lines) and the experimental measurements (symbols), for edge and face (E and F) orientations, where the crack intersects the edges and faces of the ductile layers, respectively. Figure 2a shows that: i) enormous DPT occurs under LSB that greatly exceeds that found for either the monolithic TiAl (which has a K_{Ic} similar to that of W at room temperature) and SSB conditions; ii) the F orientation initially provides an extra increment of K_r since cracks arrested at one face of a ductile layer must be re-nucleated on the back face to continue propagating; iii) the model is in good agreement with experiment; iv) extensive stable crack growth occurs for the LSB conditions; and v) the corresponding slope of the resistance, dK_r/da, curve is low. Figure 2c shows the benefits of DPT on the effective composite strength and ductility. Here, the P-δ curves (that are akin to the engineering

stress and strain curves) have been normalized by the corresponding fracture loads and displacements of the brittle matrix (subscript m). Again the model predictions are in good agreement with experimental measurements. The load and displacement capacity of the composite exceeds that of the matrix by factors of more than 3 and 10, respectively. The results indicate that: i) DPT under LSB conditions can produce enormous increases in resistance curve toughness; ii) resistance curve toughening can be rigorously modeled in terms of the properties of the composite constituents; and iii) the toughening can be modified by choices in the reinforcement material and architecture. The models can also be used to assess component failure limits including the effects of compliance.

For example, if the objective is to increase the strength of a composite in the presence of micro-cracks, then micron scale reinforcements (much smaller t) are better, since the initial slope of the K_r *(da)* curve is larger in this case [32-37]. The DPT principles and models described above are also applicable to measuring and modeling enhanced composite strength and ductility. Indeed, a general design approach to optimizing the composite architecture tailored to a specific application has been developed based on the SSB and LSB bridging mechanics combined with finite element method (FEM) models of $\sigma(u)$ functions and the various factors that individually and in combination control them [32, 34, 36, 37].

Heathcote and Odette have used combinations of SSB/LSB and FE $\sigma(u)$ models to develop a set of quantitative design tools that permit the optimization of a DPT composite strength for a particular application [32-34, 36, 37]. An example is shown in Figure 3a as a map of the strengthening for a specified combination of crack length and ductile layer thickness in both non-dimensional and absolute values for LSB conditions for a baseline $\sigma(u)$ function. The dashed line shows the optimal layer thickness. Similar maps are available for different $\sigma(u)$ functions. Figure 3b shows the effect of layer thickness on the composite strength as a function of layer thickness for the base function and two variants related to internal stresses and constraint loss due to de-bonding for a 40-μm microcrack. The increases in peak strength correspond to increases in the slope of the initial $K_r(da)$ resistance curve. This work also developed a method to derive critical composite $\sigma(u)$ curves directly from $K_r(da)$ resistance curves and confocal microscopy-fracture reconstruction (CM-FR) characterization of the three dimensional topology of ruptured or fractured ductile ligaments [32-34, 36, 37]. In addition to the macro- and micro-laminates, research of Odette and co-workers also includes composites reinforced with discrete ductile phase particles [23, 38-40].

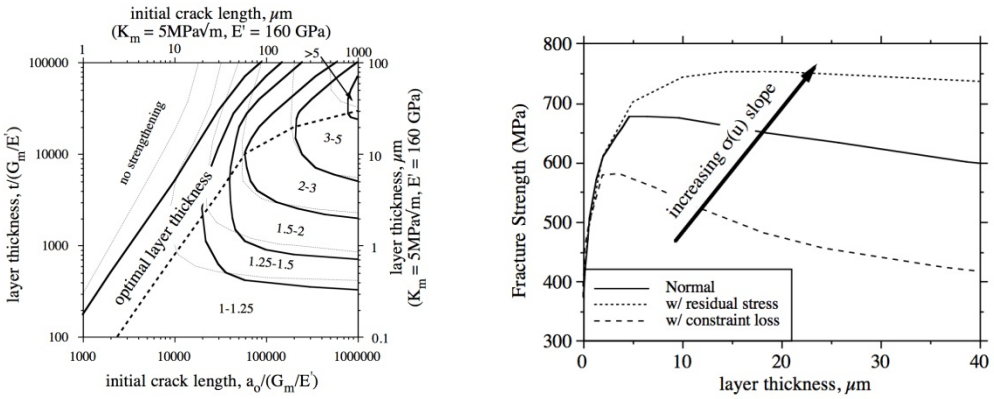

Figure 3. (a) A strength map showing the effect of constraint loss (curves for fully constrained deformation are shown as dashed lines for reference). The various solid curves correspond to ranges of strengthening ratios. The curve for the optimal layer thickness for strengthening is shown as the dashed line. (b) Fracture strength as a function of layer thickness for a composite with a plane strain elastic modulus of 160 GPa, a matrix toughness, G_m, of 100 J/m^2 (K_m = 4 MPa√m), and an initial crack size of 40 μm. Increasing the slope of the *σ(u)* curve (through either deformation constraint or residual stresses) causes an increase in the strength for layer thicknesses above a few microns, especially at the optimal layer thickness, and decreases the sensitivity of the fracture strength on the layer thickness for 10 < *t* < 40 μm.

Several other issues that have been addressed in previous work, but that will require additional study, include the role and mechanics of de-bonding [33, 34, 36, 37, 41, 42], composite behavior under fatigue loading conditions [23, 38, 43] and dynamic (high rate) loading conditions [43]. However, the examples shown here clearly demonstrate that there is a rigorous quantitative scientific foundation of experimental methods and analysis to design and test DPT W-composites that are optimized for plasma facing component service.

Experimental Methods

A 4.0 mm thick plate of unalloyed W, initially produced by Plansee, was obtained from Michael Reith at KIT. The W was fabricated by de-oxidizing and then HIPing powders to nearly full consolidation. The resulting consolidated W was then rolled to the plate thickness. Further details on the material and processing path will be supplied elsewhere. But it is sufficient here to say that this unalloyed, monolithic W can be considered a baseline *"garden variety"* material for comparison to other W alloys and composites.

Fracture tests were carried out on 3.2mm x 1.575mm x 18mm bend bars. To date testing has been confined to the T-L orientation as shown in Figure 4a, with the crack propagating in the rolling direction; T-L is generally considered to be the most brittle orientation. Two bars were EDM notched to a depth (a_n) over width (W) ratio of a_n/W = 0.3 and four bars were EDM notched to a depth (a_n) over width (W) ratio of a_n/W = 0.5.

The bars were then pre-cracked by cyclic axial compression loading as illustrated schematically in Figure 4b [44]. Sharp pre-cracks were then grown from the notch to a small increment of extension with a typical pre-crack extension of ≈ 0.4 mm for the specimens with $a_n/W = 0.3$ and pre-crack extension of ≈ 0.135 mm for the specimens with $a_n/W = 0.5$. Six pre-cracked specimens were then tested at ambient temperature in three-point bending on a hydraulic load frame at a displacement rate of 0.1 mm/min. All fractures were linear elastic, and the K_{Ic} were evaluated based on the ASTM E399 test method [45].

The W-25wt%Cu heavy metal composite, Copelmet ®, was purchased from Goodfellow Co in the form of a rectangular bar with a 25mm x 25mm cross section. Although Goodfellow does not specify hoe the material is manufactured, we believe that the composite bar was initially processed by the standard route by making a porous pre-form out of the W-powders that was then pressure infiltrated with molten Cu and sintered. The volume fraction of Cu is about 50%. Hardness, SEM fractography and confocal microscopy-fracture reconstruction measurements were carried out as well as fracture testing. Further details of the material, processing path and experimental methods will be provided elsewhere.

The small bend bar specimens used for the composite were the same as those for the monolithic W testing and were fabricated from the bar as illustrated in Figure 4c. The bend bars were also notched and fatigue pre-cracked in 3-point bending. The subsequent resistance curve tests were also carried in 3-point bending, in some cases with unloading cycles. A resistance K_r-da curve is characterized by an initiation K_{Ic} marking the nominal onset of crack extension (da) followed by an increasing $K_r(da)$ with increasing crack length, a. In order to determine $K_r(da)$, the da must be combined with the P-d curve to determine increments of DK_r with da. Note this can be done either using the J-integral method [46] or computing the nominal stress intensity factor K_I for the remote loads and instantaneous crack length, a_o + da. The resistance curve da is typically measured by unloading compliance or, in some cases, electro-potential drop methods. However, these techniques do not work in cases where there is a bridging zone behind the crack tip. It is sometimes possible to optically measure da on the specimen surface; and this approach is reasonably valid for brittle matrix composites. However, the surface of the W-Cu composite is too complex (mottled and irregular) and cannot be sufficiently polished to permit accurate measurements of the da for fine cracks. Thus we used a digital image correlation (DIC) method instead. DIC provides a very high-resolution map of 2-D (in this case) displacement fields by comparing the sequential positions of small surface features over an increment of loading, or in this case, crack extension. The displacement fields can also be converted to strain fields. The fields can readily show crack the extension, da, on painted (white) and speckled (black) surface. An example is shown in Figure 5.

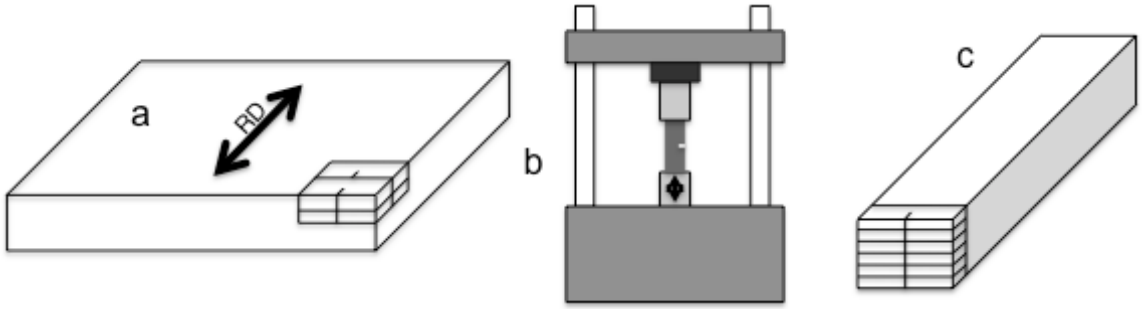

Figure 4. a) T-L orientation of the fracture specimens in the W plate; b) schematic of the compression fatigue method or unalloyed W; c) layout of the fracture specimens in the W-Cu compsite.

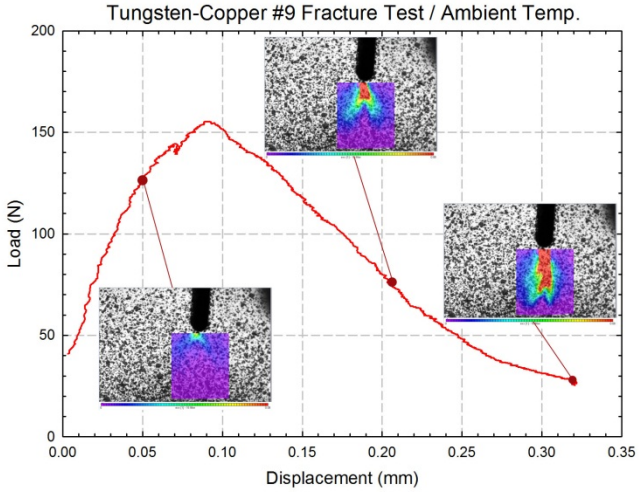

Figure 5. A typical load displacement curve for the W-composite and the corresponding assessment of the crack extension, da, using the DIC method.

Table 2 summarizes the K_{Ic} data for the monolithic W plate. The Vickers microhardness of the composite was measured at 204 kg/mm^2.

Figure 6 compares the P-δ curves for the monolithic W plate and the W-Cu composite for specimens with the same a_o/W. The increase in the maximum P and much larger δ are clear. The average maximum load K_{Jcm} for 8 tests is 24.9 MPa√m ≈ 3 times and the average δ_c ≈ 7.5 times the K_{Ic} and δ_c for the monolithic W. The P versus a curve measured by the DIC method is shown in Figure 7. There is some chatter in near da ≈ 0 that is likely associated with cracking before actual propagation begins, and P decreases approximately linearly with da after that. Figure 8 shows the corresponding J_r-da curve where the equivalent K_r is given by √JE' where E' is the effective plain strain elastic

modulus of the composite taken as E' = xxx GPa. This data suggest that the initiation toughness is ≈ 45 MPa√m and the maximum K_r in the test is ≈ 75 MPa m.

Table 2. Summary of the K_{Ic} measured in the W Plate

K_{Ic} MPA√m
7.8
8.35
8.99
8.6
7.8
8.35

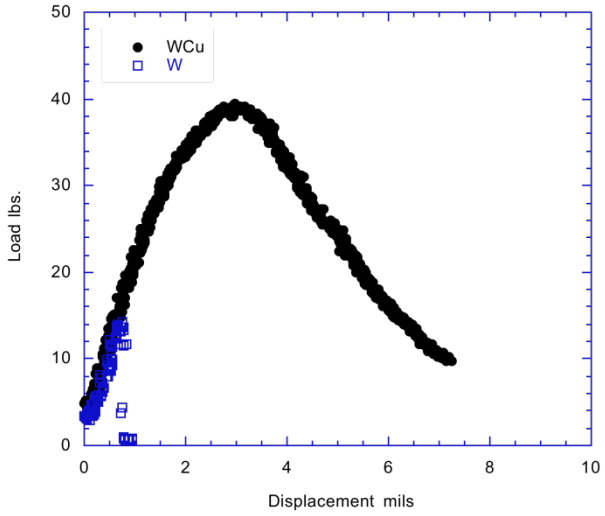

Figure 6. A typical load-displacement curve for the linear elastic W plate and the W-Cu composite manifesting extensive stable crack growth and resistance curve behavior.

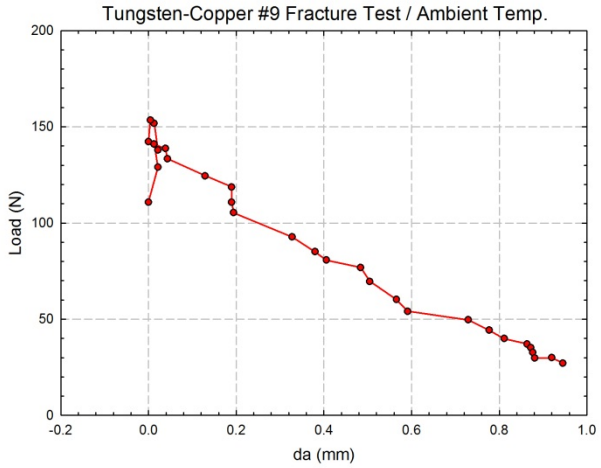

Figure 7. Load versus crack extension in the W-Cu composite measured by the DIC method.

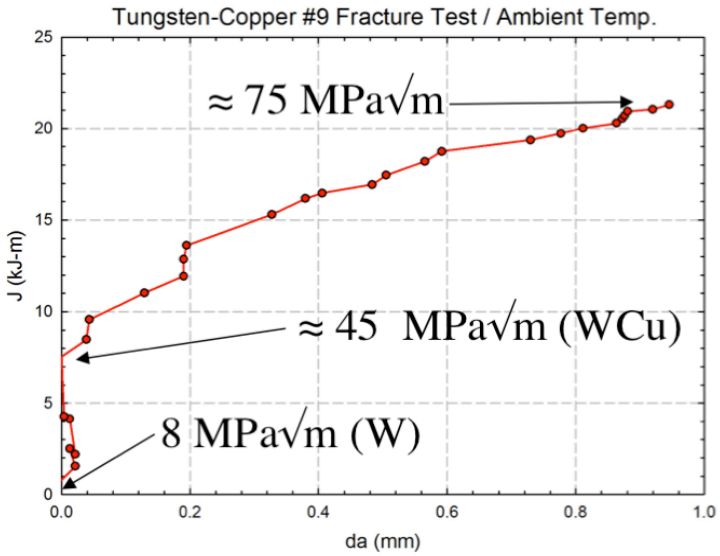

Figure 8. A J_r-da resistance curve for the W-Cu composite.

Figure 9 shows facture surface of the composite with a mixture of brittle cleavage in W and ductile ligament fracture in the Cu. Figure 10 shows a confocal microscopy-fracture reconstruction (CM-FR) 3D map of a region of the fracture surface. These techniques, and others, will be used to develop a fully quantitative model of DPT in the W-Cu system that will serve as a template for future research on developing W-composite based divertor components.

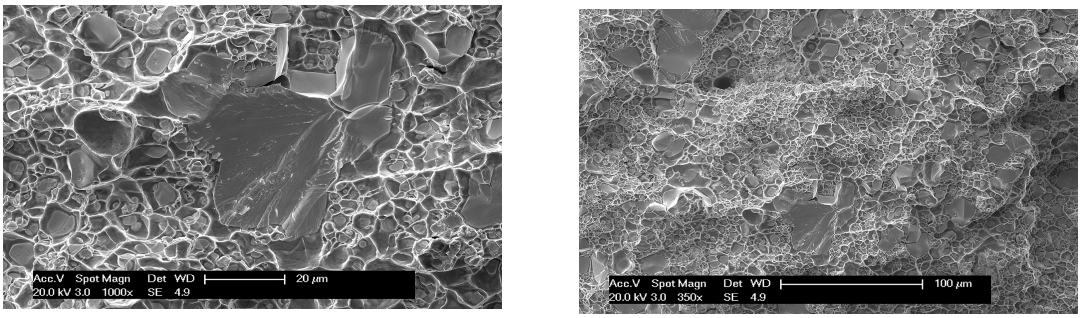

Figure 9. The fracture surface of the W-Cu composite showing a mixture of cleavage (W) and ductile fracture (Cu).

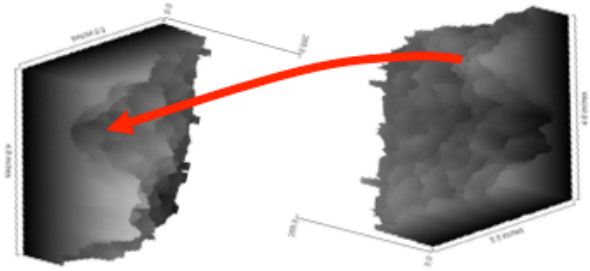

Figure 10. CM-FR images of conjugate fracture surfaces in the W-Cu composite sowing the ductile behavior of the Cu reinforcement phase.

SUMMARY AND FUTURE WORK

A reasonable value for the room temperature toughness of unalloyed rolled W plate in the T-L orientation is $K_{Ic} \approx 8$ MPa$\sqrt{m}$. Thus similar tests on so-called ductilized W will be needed to compare to this benchmark value. Efforts will continue to develop mechanical testing protocols for W alloys (and composites), including improved pre-cracking methods and extension of the measurements to high temperature. These test methods will be applied to improved W-alloys and composites as they become available.

An exploratory study of a model W-composite yielded very encouraging results. A commercial W-25%Cu heavy metal composite showed a much a higher effective toughness compared to the monolithic plate. The improved fracture resistance is manifested by a higher initiation toughness followed and extensive stable crack growth that is controlled by a significant resistance K_r-da curve. The much higher composite toughness is due to DPT associated with LSB mechanics. The composite has an approximately 3 times higher maximum load capacity compared to the W plate and more that 7 times the deflection capacity that is akin to plastic ductility. Future work on the W-Cu composite will focus on extracting the critical ductile phase constituent σ(u) function

based on a combination of 3-D fractography (CM-FR), inverse LSB modeling of the test observables and finite element simulations. This work is providing an important foundation for a new initiative that UCSB will be undertaking in collaboration with PNNL to develop structural W composites.

REFERENCES

1. M. Rieth, J. L. Boutard, S. L. Dudarev, et al., *J. Nucl. Mater.* **417** (2011) 463.
2. R. A. Pitts, A. Kukushkin, A. Loarte, et al., *Phys. Scrip.* **T138** (2009) 014001.
3. P. Mertens, T. Hirai, M. Knaup, et al., *Fus. Eng. Design* **84** (2009) 1289.
4. A. Gervash, R. Giniyatulin, T. Ihli, et al., *J. Nucl. Mater. B* (2007) 1472.
5. M. Merola, W. Danner, M. Pick, *Fus. Eng. Design* (2005) 325.
6. P. Mertens, V. Philipps, G. Pintsuk, et al., *Phys. Scrip.* **T138** (2009) 014032.
7. A. Moslang, E. Diegele, M. Klimiankou, et al., *Nucl. Fus.* **45** (2005) 649.
8. M. A. Abdou, A. Ying, N. Morley, et al., *Fus. Eng. Design* **54** (2001) 181.
9. S. J. Zinkle, N. M. Ghoniem, *Fus. Eng. Design* **51** (2000) 55.
10. B. Gludovatz, S. Wurster, A. Hoffmann, et al., *Int. J. Refrac. Met.* **28** (2010) 674.
11. S. Wurster, B. Gludovatz, R. Pippan, *Int. J. Refrac. Met.* **28** (2010) 692.
12. Z. Zhangjian, L. Jochen, G. Pintsuk, et al., *J. Nucl. Mater.* (2009) 733.
13. T. Tanabe, V. Philipps, K. Nakamura, et al., *J. Nucl. Mater.* (1997) 1164.
14. M. Faleschini, H. Kreuzer, D. Kiener, et al., *J. Nucl. Mater.* (2007) 800.
15. T. Tanno, A. Hasegawa, J. C. He, et al., *J. Nucl. Mater.* (2009) 218.
16. T. Tanno, A. Hasegawa, M. Fujiwara, et al., *Mater. Trans.* **49** (2008) 2259.
17. T. Tanno, A. Hasegawa, H. Jian-Chao, et al., *Mater. Trans.* **48** (2007) 2399.
18. V. D. Krstic, M. Komac, *Phil. Mag. A* **51** (1985) 191.
19. A. G. Evans, *Mater. Sci. Eng. A* **105** (1988) 65.
20. L. S. Sigl, P. A. Mataga, B. J. Dalgleish, et al., *Acta Metall.* **36** (1988) 945.
21. T. C. Lu, A. G. Evans, R. J. Hecht, et al., *Acta Metall. Mater.* **39** (1991) 1853.
22. G. R. Odette, B. L. Chao, J. W. Sheckherd, et al., *Acta Metall. Mater.* **40** (1992) 2381.
23. K. T. Venkateswara Rao, G. R. Odette, R. O. Ritchie, *Acta Metall. Mater.* **42** (1994) 893.
24. R. J. Zhang, Y. Q. Yang, W. T. Shen, et al., *J. Cryst. Grow.* **313** (2010) 56.
25. R. J. Zhang, Y. Q. Yang, W. T. Shen, et al., *Thin Solid Films* **519** (2010) 1367.
26. C. Guo, C. Zhang, L. He, et al., *J. Mater. Sci. Technol.* 23 (2007) 677.
27. A. G. Evans, F. W. Zok, *Solid State Phys.* **47** (1994) 177.
28. D. M. Shah, D. L. Anton, D. P. Pope, et al., *Mater. Sci. Eng.* **A192** (1995) 658.
29. L. S. Sigl, S. Schmauder, *Inter. J. Fract.* **36** (1988) 305.
30. H. F. Fischmeister, S. Schmauder, L. S. Sigl, *Mater. Sci. Eng.* ***A105*** (1988) 305.
31. H. C. Cao, B. J. Dalgleish, H. E. Deve, et al., *Acta Met.* **37** (1989) 2969.
32. J. R. Heathcote, University of California, Santa Barbara (1996).
33. J. Heathcote, G. R. Odette, G. E. Lucas, et al., *Acta Mater.* **44** (1996) 4289.
34. J. Heathcote, G. R. Odette, G. E. Lucas. Symposium, (1996) PA, USA: *Mater. Res. Soc.*
35. R. G. Rowe, D. W. Skelly, M. Larsen, et al., *Scr. Metall. Mater.* **31** (1994) 1487.
36. J. A. Heathcote, G. R. Odette, to be published.
37. J. A. Heathcote, G. R. Odette, to be published.
38. K. T. Venkateswara, G. R. Odette, R. O. Ritchie, *Acta Metall. Mater.* **40** (1992) 353.
39. G. R. Odette, H. E. Dève, C. K. Elliott, et al., Symposium (1990) TMS.
40. C. K. Elliott, G. R. Odette, G. E. Lucas, et al., *Mater. Res. Soc.* (1988). Boston, MA: MRS.

41. H. E. Deve, A. G. Evans, G. R. Odette, et al., *Acta Metall. Mater.* **38** (1990) 1491.
42. J. A. Heathcote, G. R. Odette, G. E. Lucas, et al., Symposium (1996) MRS.
43. J. A. Heathcote, G. R. Odette, to be published.
44. R. Pippan, *Fatigue Fract. Eng. Mater. Struct.* **9** (1987) 319.
45. Standard Test Method for Linear-Elastic Plane-Strain Fracture Toughness K_{Ic} of Metallic Materials, ASTM E399 - 09E2, ASTM Book of Standards 3.01 (2011).
46. Standard Test Method for Measuring Fracture Toughness, ASTM E1820-08, ASTM Book of Standards 3.01 (2011).

5.1 EXAMINATION OF THE IRRADIATED SUPERCONDUCTING PROPERTIES OF NANOPARTICLE-DOPED $YBA_2CU_3O_{7-X}$ COATED CONDUCTORS FOR FUSION ENERGY APPLICATIONS

— Keith J. Leonard, Tolga Aytug, Lance Snead (Oak Ridge National Laboratory), Albert Gapud (University of South Alabama), and William J. Weber (University of Tennessee)

OBJECTIVE

The goal of this work is to evaluate the irradiation response of the newest generation of $YBa_2Cu_3O_{7-x}$ (YBCO) high temperature superconducting (HTS) materials. The task will include the effects of different processing conditions (method of deposition, type of buffers, use of dopants, etc.) on the initial defect structure prior to irradiation and the defect structure changes during irradiation.

SUMMARY

A program is in place to examine the effects of room temperature ion irradiation on the superconducting properties of several YBCO HTS materials that utilize different flux pinning strategies. This will provide a first investigation into both the radiation-induced flux pinning and changes to pre-existing pinning centers. The work will then be expanded to low temperature irradiation testing that will include *in situ* measurement of self-field superconducting properties as a function of dose, with a further analysis into defect annihilation and effects of temperature excursions on conductor properties.

PROGRESS AND STATUS

Background

In an effort to reduce reactor complexity and costs, the ORNL Fusion Materials Program is evaluating the irradiation response of the newest generation of $YBa_2Cu_3O_{7-x}$ (YBCO) high temperature superconducting (HTS) materials for possible qualification in future magnetic confinement reactor designs. In addition to the higher critical temperature over currently used Nb_3Sn (T_c = 92 K versus 18 K for Nb_3Sn), YBCO conductors offer higher critical current density (J_c) values, a smaller flux pinning coherency length that can produce J_c increases on exposure to neutron irradiation up to $1x10^{22}$ n/m^2 (E>0.1 MeV) [1-10] and a smaller effective neutron capture cross section.

Since the appearance of HTS materials and their fabrication into long-length wires, they have been limited to self-field applications such as power transmission due to their low characteristic irreversibility field [11]. The newest generation of YBCO conductors incorporate the use of engineered textured substrates and nanoparticle additions to the conductor to produce correlated defect structures in the YBCO lattice that increase J_c values with reduced dependence on magnetic field. These defect structures can be tailored to specific field applications and have demonstrated increases in J_c by a factor of 6 or more under high magnetic fields [12].

The majority of irradiation studies to date on YBCO have been centered on examining the development of radiation-induced flux pinning defect structures at low irradiation fluences. Little systematic examination of the overall behavior of the material under irradiation exists, or on the effect of different processing conditions (method of

deposition, type of buffers, use of dopants, etc.) on the initial defect structure prior to irradiation and its changes during irradiation. Typically, the YBCO irradiation database consists of testing at or slightly above room temperature and is dominated by materials that are processed by melt-textured or powder processing techniques producing poly- and single-crystal samples, rather than coated conductor wires. For the latter however, ion-irradiated testing has primarily involved swift heavy ions (100 MeV to several GeV) in order to generate long columnar defect structures similar to those created by the incorporation of nanoparticles into the YBCO films [013-17]. The use of low energy ions (0.5 to 25 MeV) is more representative of the defect cascades produced by neutron irradiation [18-20].

The goal of this work to evaluate the irradiation response of several types of the latest generation of YBCO coated conductors that incorporate nanoparticle additions into their microstructure for enhanced flux pinning and improved performance in externally applied magnetic fields. The samples chosen will represent different methods for flux pinning related to the defect structures produced in the YBCO and will examine the HTS materials response to irradiation damage. Ion beam irradiation will be used to simulate neutron damage cascades in the YBCO and buffer layers, allowing for simplified post-irradiation characterization.

In the first year we plan on investigating the effect of room temperature irradiation on both the radiation-induced flux pinning response as well as examining the induced changes to pre-existing pinning centers. This will allow the establishment of the overall response of the materials to different ion energies and fluence. This work will continue to low temperature ion-irradiation tests over specific energy ranges and fluence including *in situ* measurements of self-field superconducting properties as a function of dose. The low temperature irradiations will also allow for studies on defect annihilation as well the effects of temperature excursions on conductor properties.

Materials

The YBCO films to be examined are based on the highest J_c performing coated conductor technologies. Table 1 lists the materials selected for testing. The coated conductors consist of biaxial textured YBCO films (1.0-1.5 μm thick) deposited by metalorganic chemical vapor deposition (MOCVD) onto buffered Ni-alloy tapes. The biaxial texturing of the YBCO needed for the flow of current along the length of the tape is generated from either the rolling assisted bi-axial textured metallic substrate or developed within the buffer layer. Examples of the two tape architectures used in this study are illustrated in Figure 1. The addition of different dopants to the MOCVD films result in the development of nanoparticles, sometimes referred to as nanodots, that improved angular and field dependent J_c values resulting from the alignment of these nanodots, the defect structures generated by them or the combined effect of defect and particle. Addition of Zr in the MOCVD processing of YBCO forms self-assembled $BaZrO_3$ nanodots that are aligned in a columnar fashion along the c-axis direction, producing superior performance over baseline films primarily at orientations corresponding to the magnetic field parallel to the c-planes, or H//c. The addition of Dy aids in the development of $(Dy,Y)_2O_3$ particles as well as promotes $YBa_2Cu_4O_8$ intergrowths (additional Cu-O layers in the YBCO stacking) that increase H//ab pinning. Enhanced pinning in both the H//c and H//ab conditions is produced in Nb-doped YBCO through the development of a three-dimension defect structure of c-axis aligned YBa_2NbO_6 particles and faulted defect structures in a- and b-directions. Comparison of

the enhanced pinning YBCO films to plain YBCO on SuperPower substrate will be examined.

Table 1. List of the YBCO and substrate conditions to be tested, the type of pinning features created, and the status of the work to date.

YBCO additive	Substrate	Pinning Effects	Status
Zr	SuperPower	$BaZrO_3$ nanodots aligned along the c-axis direction, producing enhanced H//c pinning.	Material undergoing pre-irradiation characterization.
Dy	American Superconductor	$(Dy,Y)_2O_3$ nanoparticles, enhanced H//ab pinning from increased $YBa_2Cu_4O_8$ intergrowths.	Material undergoing pre-irradiation characterization.
Nb	SuperPower	YBa_2NbO_6 nanoparticle alignment in c-axis direction, for enhanced H//c pinning, in addition to increased H//ab pinning from defects generated.	Material to be fabricated.
None	SuperPower	No additional pinning defects, other than those generated at buffer interface creating stacking faults within the YBCO.	Materials to be fabricated.

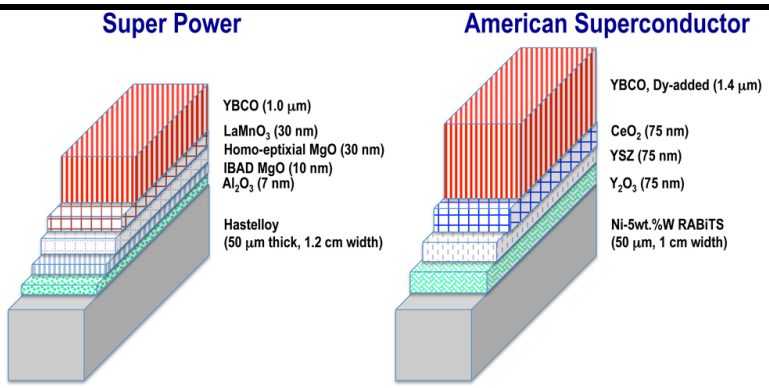

Figure 1. Illustration of the two types of coated conductor tape architectures used in this work.

Pre-Irradiation Characterization

Characterization of the pre-irradiated electrical properties of the Zr-YBCO and Dy-YBCO samples has begun. The Zr-YBCO tape was purchased directly from SuperPower Incorporated, while American Superconductor Corporation provided the Dy-YBCO for this work. Un-doped YBCO and Nb-YBCO tapes will be fabricated at ORNL at a later date on the SuperPower buffered tape architecture. The long-length Zr- and Dy-YBCO conductors showed critical current, I_c, values in self-field of approximately 239 A/cm-width and 525 A/cm-width, respectively. The tapes have been cut down into smaller test samples and for the case of the Zr-YBCO material, the Ag overlay coating was removed through etching. Patterned current bridges were laser scribed into the YBCO for electrical characterization tests. Silver was deposited at specific sites for the pad positions of the four-probe voltage and current contacts. Following this, the samples

were given a thermal anneal in oxygen at 500°C for 1 hour. The initial bridge pattern, version 1 shown in Figure 2, which was selected for electrical characterization, was found to be susceptible to shorting caused by Ag not removed from the edges of the sample following etching in addition to tolerance related issues associated with the laser scribe. The version 1 shown in pattern is a standard bridge design that eliminates the effects of stress and localized heating in the YBCO at the probe positions. A simplified bridge pattern, version 2, was employed to avoid the problems related with the more complex pattern.

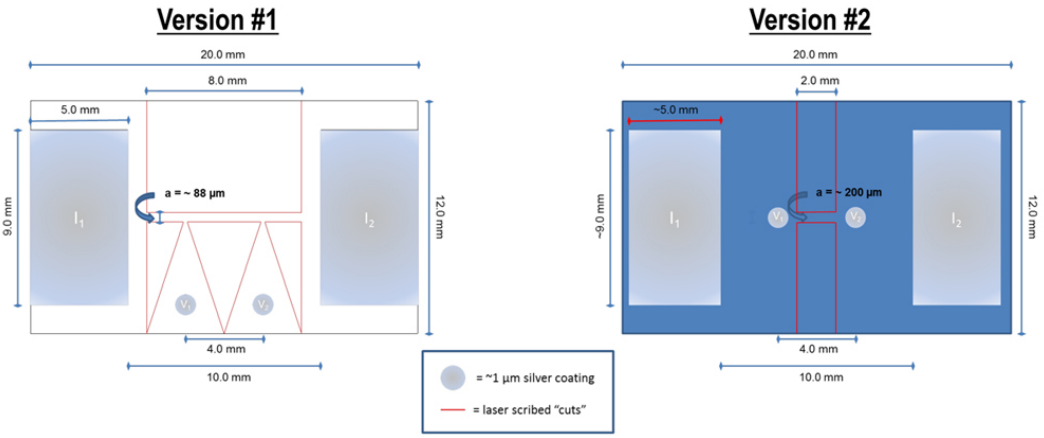

Figure 2. Versions of the bridge design for testing the high I_c doped-YBCO samples. Version 1 was found to be problematic due to electrical shorting and replaced with the simplified version 2.

Field dependence characterizations of J_c as a function of applied magnetic field strength, and resistance versus temperature are now being performed on both the Zr-YBCO and Dy-YBCO series of samples at the University of South Alabama. Angular dependence of I_c with field is being measured at ORNL. An example of the data being collected is shown in Figure 3, for a sample of the Zr-YBCO film on SuperPower tape architecture. Pre-irradiation characterization will allow for the precise assessment of each samples response to irradiation. Further detailed information on sample testing, tape performance and microstructural characterization in the pre-irradiated condition will be provided at a later date.

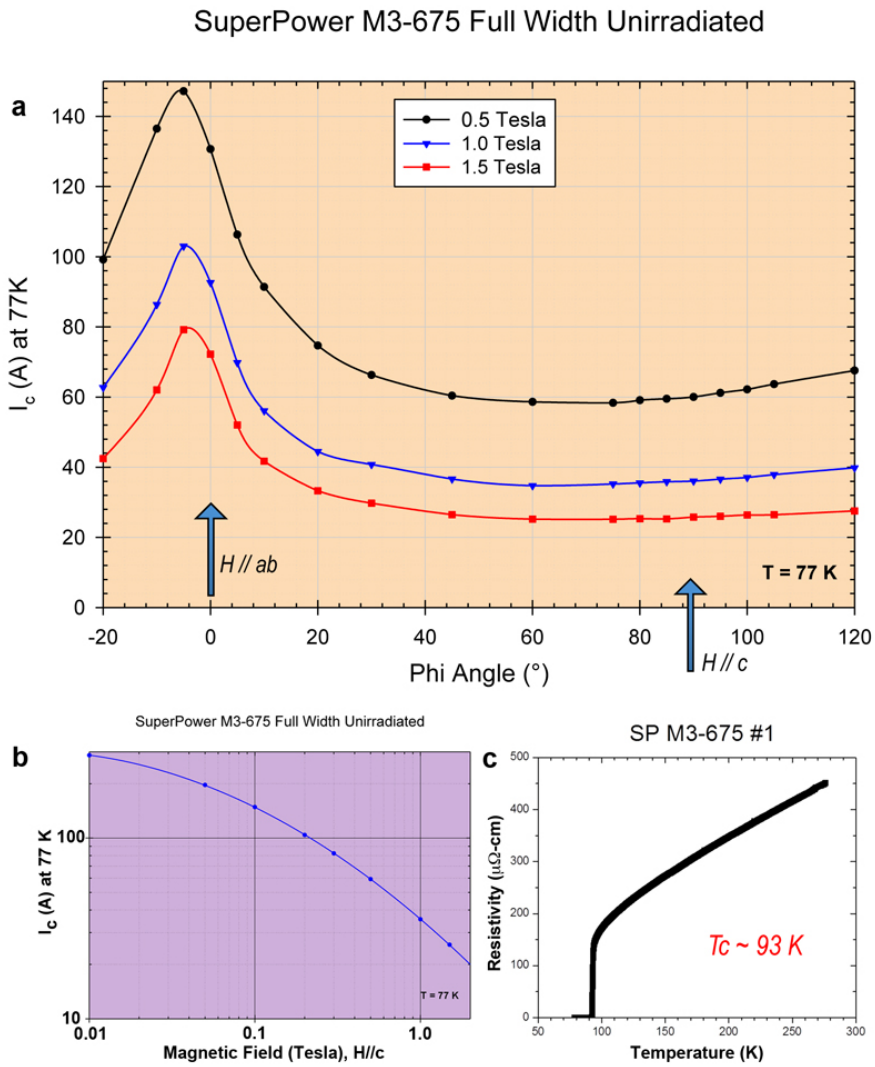

Figure 3. Preliminary data for Zr-YBCO film on SuperPower buffered tape architecture. (a) Angular dependence of critical current on the applied field at different field strengths, (b) critical current as a function of applied field at H//c, and (c) the resistivity versus temperature curve showing the transition temperature, T_c = 93 K.

Ion Irradiation Testing

Ion irradiation will be used as effective approach to evaluate materials performance in neutron irradiation environments. Irradiation of the short segments of coated conductor tapes will be performed at the University of Tennessee Ion Materials Laboratory (UT-IML). The facility, which is operational but completing final construction, will be equipped with two ion sources, three beam lines and three end stations providing the capability irradiation of ions from H to Au with energies ranging from a few keV to ~25 MeV, depending on ion and current required.

Ion irradiation of the MOCVD YBCO conductors will be performed at lower energy levels typical of simulating cascade damage to avoid columnar defect formation that is typically observed by higher energy heavy ion irradiations (in the hundreds of MeV region). In order to produce defect cascades similar to that observed in neutron irradiations, the electronic energy loss of the irradiating ions will need to be less than that of 20 keV/nm based on previous work [18, 21, 22].

To examine physical property changes over the unirradiated materials, irradiation by ions in the high keV - low MeV energy range, fluences between 10^{11} to 10^{14} ions/cm^2 will be likely [21]. Computational analysis of energy loss profiles through the HTS tapes was performed using TRIM calculations to evaluate the optimum dose rate, fluence, ion energies and penetration depth. Three ion energies that are being considered for this study are 10 MeV oxygen, 25 MeV copper, and 25 MeV gold, with examples of the ion ranges, energy loss and collision profiles as a function of depth into the sample are shown in Figure 4. Ion penetration depths will be into the Ni-alloy substrates to avoid the introduction of impurities that may create the introduction of unintentional artifacts measured in the conductor properties.

SUMMARY

The ion-irradiation examination of these films follows a significant multi-decade development of both optimized buffered tape technology and research into increased flux pinning response of HTS films. This latest generation of HTS conductors offers improved in-field properties that can be tailored to suite specific magnetic field conditions. It is the objective of this study to investigate radiation effects on these materials and assess their suitability for potential applications in fusion environments. This investigation will be one of the first irradiation experiments on nano-doped YBCO coated conductors. The objective of this work is to examine the effect of room temperature ion irradiation on the superconducting properties of several HTS materials utilizing different flux pinning strategies in YBCO. To provide a first investigation into both the radiation-induced flux pinning and changes to pre-existing pinning centers. This will then be expanded to low temperature irradiation testing that will include *in situ* measurement of self-field superconducting properties as a function of dose, with a further analysis into defect annihilation and effects of temperature excursions on conductor properties.

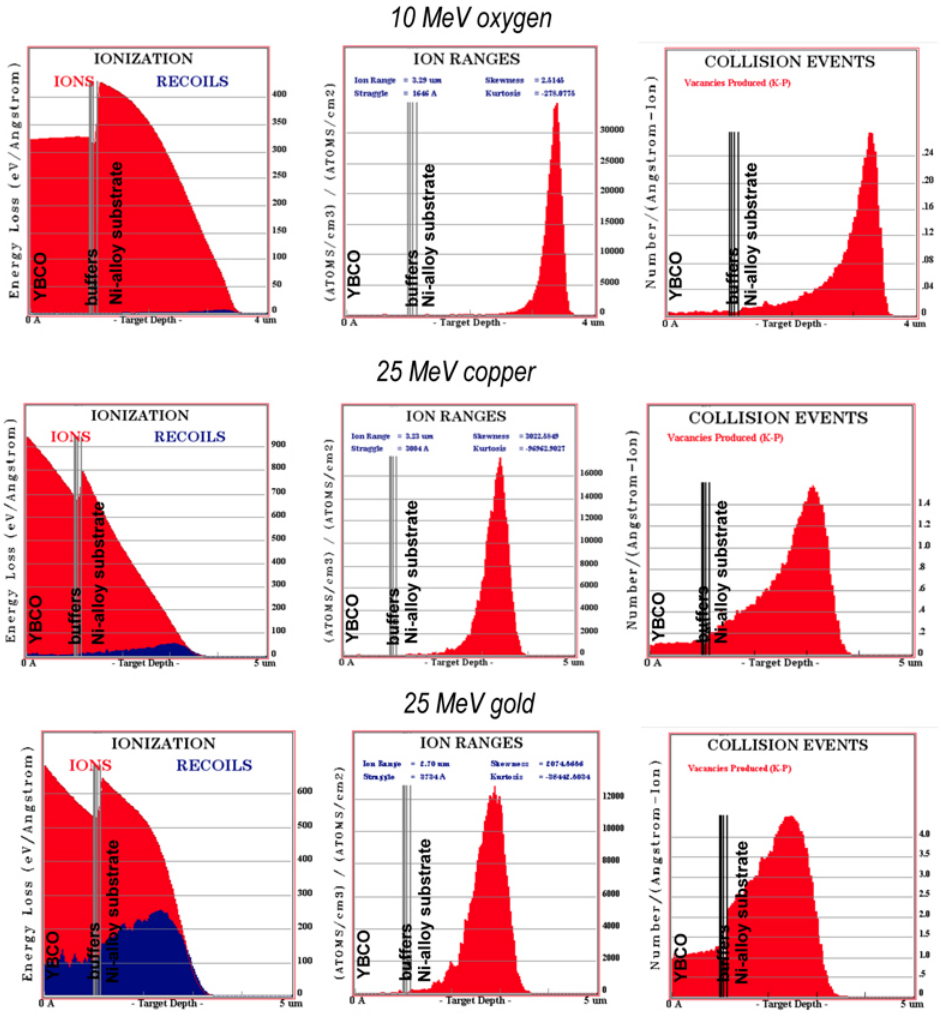

Figure 4. Examples of the energy loss, ion ranges and collision events as a function of target depth produced from TRIM calculations for 10 MeV oxygen, 25 MeV copper and 25 MeV gold ion irradiations of YBCO conductors on SuperPower substrates.

REFERENCES

1. H. W. Weber, *Physica C* **185-189** (1991) 309-314.
2. P. X. Zhang, et al., *Physica C* **282-287** (1997) 1607-1608.
3. F. Vasiliu, V. Sandu, P. Nita, S. Popa, E. Cimpoiasu, and M. C. Bunescu, *Physica C* **303** (1998) 209-219.
4. D. V. Kulikov, Y. V. Trushin, F. M. Sauerzopf, M. Zehetmayer and H. W. Weber, Physica C, 355 (2001) 245-250.
5. U. Topal, H. Sozeri, and H. Yavuz, *Physica C* **408-410** (2004) 636-637.
6. U. Topal, L. Dorosinskii and H. Sozeri, *Physica C* **407** (2004) 49-54.

7. S. Shojaei, R. Khoda-Bakhsh and H. Sedgi, *J. Supercond. Nov. Magn,* **24** (2008) 387-390.
8. R. Fuger, M. Esterer, and H. W. Weber, *IEEE Trans. on Appl. Supercond.* **19**, 3 (2009) 1532-1535.
9. M. Chudy, R. Fuger, M. Eisterer and H. W. Weber, *IEEE Trans. on Appl. Supercond.* **21**, 3 (2011) 3162-3165.
10. A. Nishimura, T. Takeuchi, S. Nishijima, G. Nishijima, T. Shikama, K. Ochiai, and N. Koizumi, *Fusion Eng. and Design* **84** (2009) 1425-1428.
11. D. Larbalestier, A. Gurevich, D. M. Feldmann and A. Polyanski, *Nature* **414** (2001) 368-377.
12. A. Goyal, et al., *Supercond. Sci. Techn*. **18** (2005) 1533-1538.
13. L. Civale, *Superconductor Sci. and Techn*. **10**, 7A (1997) A11-A28.
14. J. Veternikova, M. Chudy, V. Slugen, M. Eisterer, H. W. Weber, S. Sojak, M. Petriska, R. Hinca, J. Degmova, and V. Sabelova, *J. Fusion Energ*., published on-line June 9, 2011.
15. M. Kaur Marhas, K. Balakrishnan, P. Saravanan, V. Ganesan, R. Srinivasan, D. Kanjilal, G. K. Mehta, M. Vedwyas, S. B. Ogale, S. P. Pai, M. S. Ramachandra Rao, R. Pinto, G. Mohan Rao, S. Senthilnathan, and S. Mohan, *Nucl. Inst. Meth. Phys. Res. B* **156** (1999) 21-29.
16. T. Sueyoshi, S. Inada, T. Ueno, N. Jyodai, T. Fujiyoshi, K. Miyahara, T. Ikegami, K. Ebihara, R. Miyagawa, Y. Chimi, and N. Ishikawa, *Physica C* **424** (2005) 153-158.
17. R. Biswal, J. John, P. Mallick, B. N.Dash, P. K. Kulriya, D. K. Avasthi, D. Kanjilal, D. Behera, T. Mohanty, P. Raychaudhuri, and N. C. Mishra, *J. of Appl. Phys*. **106** (2009) 053912.
18. N. M. Stickland, N. J. Long, J. Xia, J. Kennedy, A. Markwitz, A. Zondervan, M. W. Rupich, W. Zhang, X. Li, T. Kodenkandath and Y. Huang, *IEEE Trans. on Appl. Supercond.* **17**, 2 (2007) 3306-3309.
19. J. C. Barbour, E. L. Venturini, D. S. Ginley and J. F. Kwak, *Nucl. Instr. Methods Phys. Res. B* **65** (1992) 531-538.
20. M. A. Kirk and Y. Yan, *Micron* **30** (1999) 507-526.
21. B. Hensel, B. Roas, S. Henke, R. Hopfengartner, M. Lippert, J. P. Strobel, M. Vildic and G. Seaman-Ischenko, *Phys. Rev. B* **42**, 7 (1990) 4135-4142.
22. R. Wheeler, M. A. Kirk, A. D. Marwick, L. Civale, and F. H. Holtzberg, *Appl. Phys. Lett.* **63**, 11 (1993) 1573-1575.

6.1 ADDITIONAL CHARACTERIZATION OF V-4Cr-4Ti AND MHD COATINGS EXPOSED TO FLOWING Li – B. A. Pint and K. A. Unocic (Oak Ridge National Laboratory)

OBJECTIVE

A flowing Li thermal convection loop was operated with V-4Cr-4Ti specimens and multi-layer electrically-insulating coatings needed to reduce the magneto hydrodynamic (MHD) force in the first wall of a lithium cooled blanket. Both types of specimens are now being characterized to examine the effect of exposure in flowing Li.

SUMMARY

Additional results are presented on the characterization of V-4Cr-4Ti tensile specimens and MHD coatings exposed to flowing Li. For the alloy specimens, anneals were performed at 400° and 550°C on tensile specimens to determine the effect of the thermal exposure without Li. The 550°C anneal resulted in a higher yield stress and lower serration amplitude for the dynamic strain aging at 500°C. For the MHD specimens, the higher temperature exposures showed a degradation in the high temperature resistivity after exposure. Metallographic cross-sections indicated the formation of a second phase at the alloy-coating interface. While $YLiO_2$ is suspected, this phase has not been identified by EELS (electron energy loss spectroscopy) or EPMA (electron microprobe analysis).

PROGRESS AND STATUS

Introduction

Previous reports[1-4] presented 500°C tensile behavior of V-4Cr-4Ti after various exposures including flowing Li in a thermal convection loop with a peak temperature of 700°C for 2,355h.[5] The results were unusual and more characterization was warranted along with additional thermal anneals to separate the effects of time at temperature from the flowing Li. Also, the dual layer (Y_2O_3/V) MHD coatings deposited by physical vapor deposition that were exposed in the same loop [5] were not fully characterized because a method was not apparent to evaluate the electrical resistivity without damaging the coatings. A micro-milling technique has been used to cut specimens suitable for resistivity measurements out of the original coated coupons. A vacuum rig for measuring resistance at high temperature has been reassembled and each of the coatings measured and then metallographic cross-sections made for characterization. Focused ion beam (FIB) milling is being used to prepare specimens for transmission electron microscopy (TEM).

Experimental Procedure

Details of the thermal convection loop exposure have been presented previously.[5] The specimens consisted of miniature tensile specimens (type SS-3: 25 x 4 x 0.9mm), tab specimens and specimens with a dual layer MHD coating linked in a chain held together with V-4Cr-4Ti wire. The tensile specimens were annealed for 1h at 1050°C prior to exposure in Li. The exposure temperature for each specimen is estimated by using a linear extrapolation of the temperatures measured at the top and bottom of the each leg.[5] Tensile specimens from the same batch of specimens were annealed in Ar-filled quartz ampoules at 400° and 550°C for 2,355h to simulate the loop temperature exposure. Previously, a 700°C anneal was conducted [5]. Tensile testing was conducted at 500°C in a vacuum with a base pressure of 10^{-6}Pa (10^{-8}Torr) and a strain rate of $10^{-3}s^{-1}$. After tensile testing, the specimens were sectioned and metallographically polished to measure the grain size and hardness. TEM specimens were prepared to further examine the microstructure. For the MHD coated specimens, electrical resistance across the coating was measured in vacuum (~10^{-5}-10^{-6} Pa) at 100° increments from 25°-700°C on sub-specimens

(4mm x 4mm) cut from the original coated specimens in order to electrically isolate the outer vanadium layer from the V-4Cr-4Ti substrate. The remaining pieces were characterized by scanning electron microscopy (SEM), EPMA, x-ray photoelectron spectroscopy (XPS), and scanning transmission microscopy (STEM), including energy x-ray dispersive spectroscopy (EDS) and EELS with specimens prepared by focused ion beam milling.

Results and Discussion

Figure 1 shows the stress-strain behavior of several specimens during tensile testing at 500°C. The recently completed anneal at 550°C exhibited similar DSA behavior as the 459°C specimen from the bottom of the hot leg in the loop. At higher temperatures, there was very little effect on the DSA behavior. Figure 2 shows the amplitude of the DSA serrations measured during tensile testing at 500°C as a function of the measured yield stress at 500°C. The new 550°C data point fits along the same curve including an 800°C isothermal Li exposure for 1000h and two previous studies [6,7]. A similar relationship was observed with the ultimate tensile strength. A previous explanation was that the lower temperature exposures showed a lower amplitude because O was depleted in the presence of Li but little C and N update occurred. However, with a similar amplitude observed in the 550°C anneal, this explanation does not seem to be applicable. It appears more likely that the Li exposure had little effect on the properties and instead the thermal aging dominated the observed changes.

Figure 3 shows additional nanohardness measurements made on these specimens after sectioning. The specimens exposed in the loop show increased surface hardness that may be attributed to C and N uptake near the surface. The higher temperature loop and 800°C Li exposures show reduced hardness away from the surface, perhaps due to O depletion. These measurements are generally consistent with the bulk hardness measurements that were lowest after the highest temperature exposures [4]. TEM characterization is continuing for these specimens but does not appear to be resolving the effect of interstitials.

For the V/Y_2O_3 MHD coatings, Figure 4 shows the resistivity as a function of temperature for the coatings exposed at various temperatures in the loop and one annealed at 700°C for the same exposure time [8].

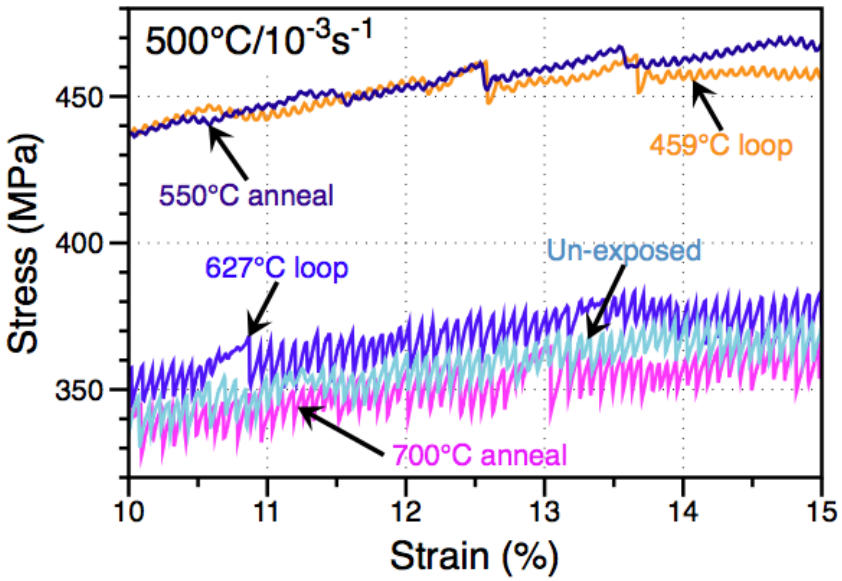

Figure 1. Stress-strain behavior of V-4Cr-4Ti specimens exposed for 2,355h either in a Li loop or in an Ar-filled ampoule. The values were narrowed to illustrate the DSA serrations.

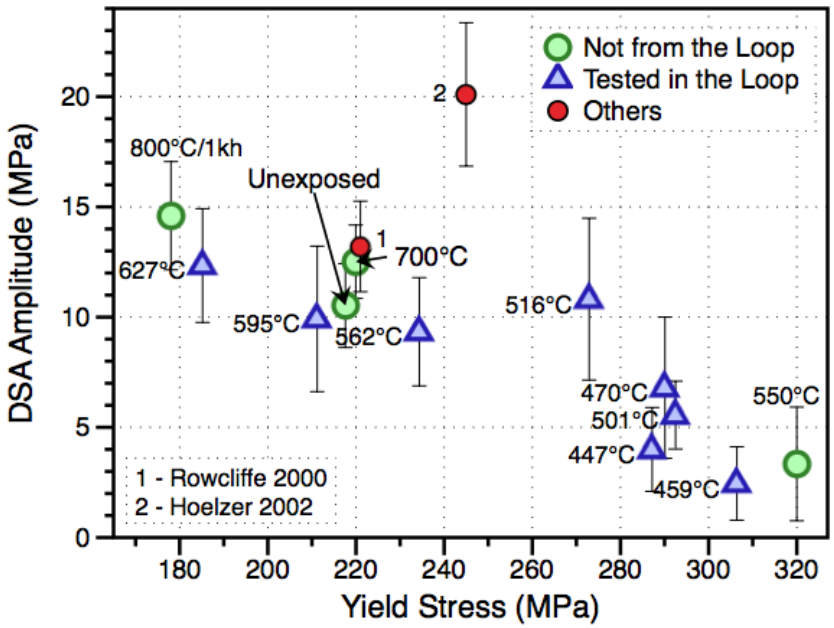

Figure 2. Amplitude of the dynamic strain aging observed at 500°C as a function of 500°C yield stress for V-4Cr-4Ti specimens exposed in the Li loop, other exposures and other reports [6,7] from the literature. The bars note the standard deviation of the measurements.

Above ~504°C in the loop, the coatings were strongly degraded and the resistivity was below the established metric for effectiveness [9]. Based on the cross-sections, this decrease is not surprising because the coatings exposed at higher temperature appeared to form a second phase at the Y_2O_3-V-4Cr-4Ti substrate, Figure 5. The layer did not form during the 700°C thermal anneal, Figure 5a, and got

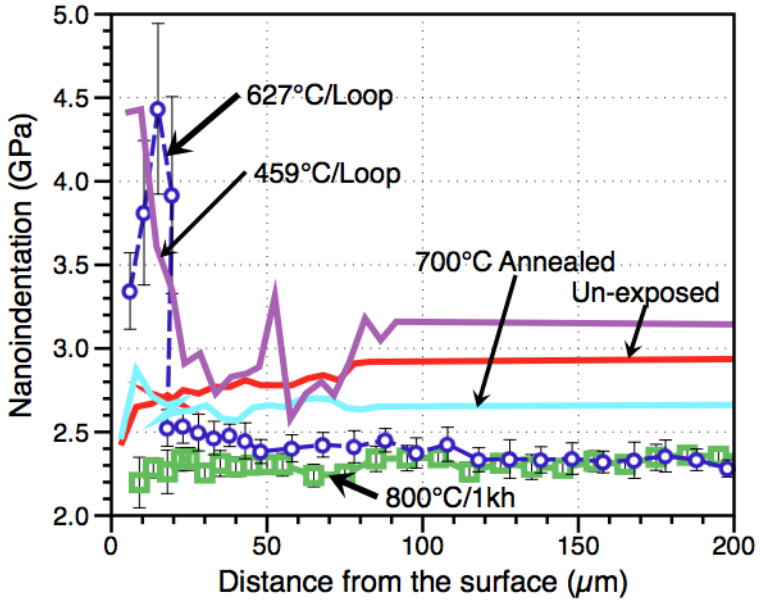

Figure 3. Nanoindentation hardness as a function of depth for various V-4Cr-4Ti specimens. The bars mark standard deviations for the measurements.

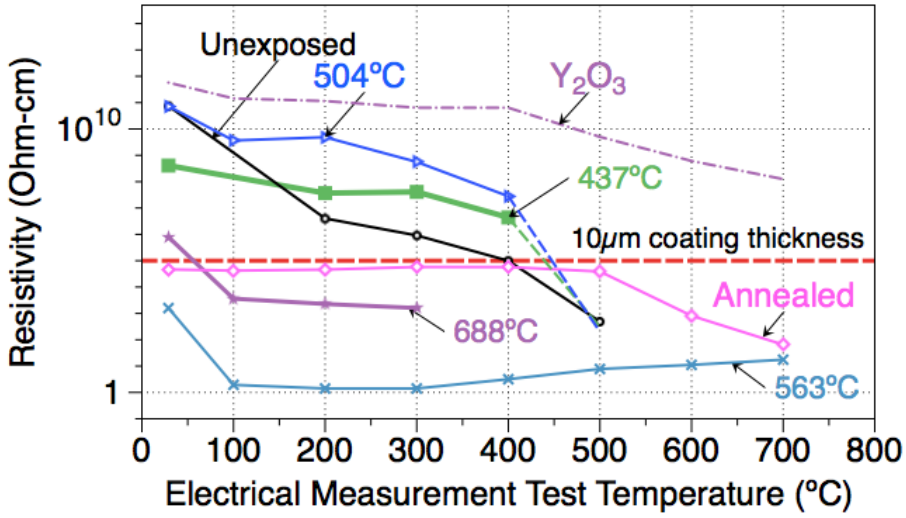

Figure 4. Resistivity of the MHD coatings exposed at different temperature in the loop as a function of measurement temperature. For reference, values for bulk Y_2O_3 and the MHD coating metric are shown.

progressive larger at higher loop exposure temperatures. Furthermore, no other elements could be detected in the layer besides Y and O using EPMA, Figure 6. Therefore, it does not involve a reaction between the coating and substrate. The most likely conclusion is that the V over coating was not sound and Li leaked along the V-alloy interface resulting in $LiYO_2$ formation [10,11]. However, XPS and EELS

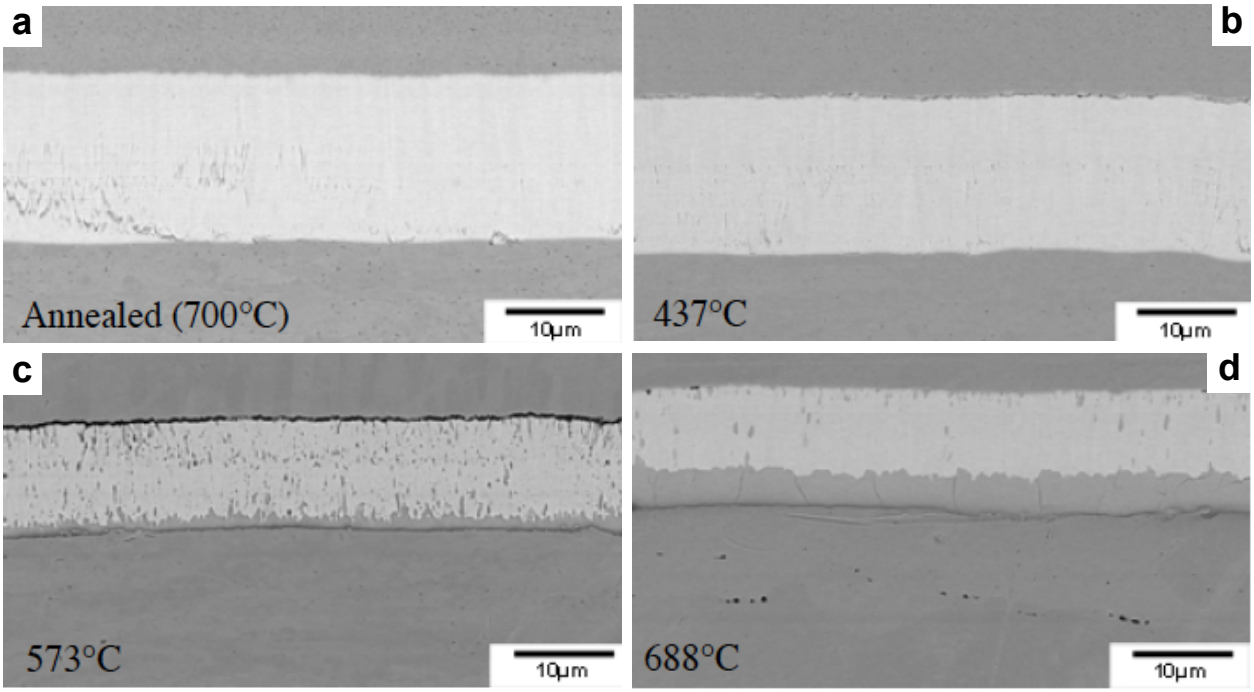

Figure 5. SEM backscattered electron images of polished sections of MHD coatings (a) after 700°C anneal and after loop exposures at (b) 437°C, (c) 573°C and (d) 688°C.

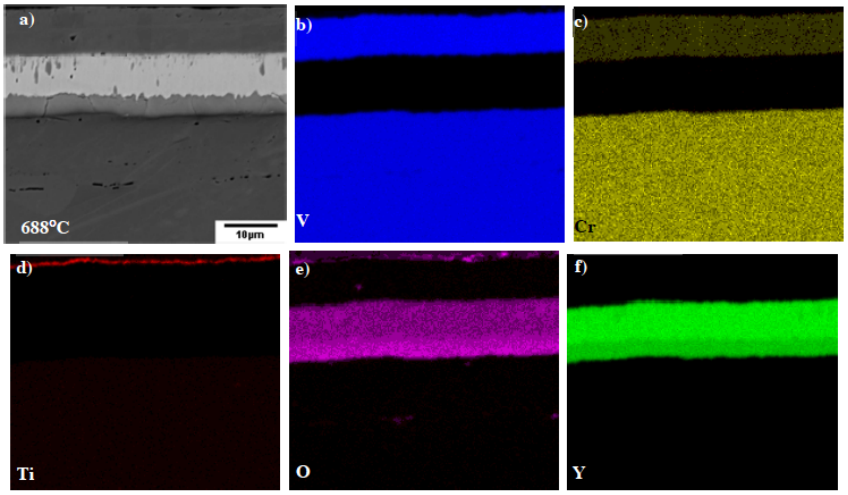

Figure 6. a) BSE image of the area used for EPMA analysis from the coating exposed to Li at 688°C and EPMA maps (b) V, (c) Cr, (d) Ti, (e) O and (f) Y.

have not been able to detect Li in this new phase. Additional TEM work is in progress to attempt to use selected area diffraction to identify the phase.

References

[1] B. A. Pint, DOE/ER-0313/45 (2008) 11.
[2] B. A. Pint, DOE/ER-0313/46 (2009) 1.
[3] K. A. Unocic, M. Lance and B. A. Pint, submitted to J. Nucl. Mater.
[4] B. A. Pint and K. A. Unocic, DOE/ER-0313/51 (2011) 67.
[5] B. A. Pint, et al., J. Nucl. Mater. 386-388 (2009) 712.
[6] A. F. Rowcliffe, S. J. Zinkle and D. T. Hoelzer, J. Nucl. Mater. 283-287 (2000) 508.
[7] D. T. Hoelzer and A. F. Rowcliffe, J. Nucl. Mater. 307-311 (2002) 596.
[8] K. A. Unocic, D. N. Leonard, H. M. Meyer, M. J. Lance and B. A. Pint, in Proc.8th Int. Symp. High Temperature Corr. Protection of Materials, Les Embiez, France, May 2012, Paper#176.
[9] Y. Y. Liu and D. L. Smith, J. Nucl. Mat. 141-143 (1986) 38.
[10] T. Terai, et al., J. Nucl. Mater. 233-237 (1996) 1421.
[11] B. A. Pint, K. L. More, H. M. Meyer and J. R. DiStefano, Fusion Sci. Technol. 47 (2005) 851.

7.1 ON NANOFEATURE COARSENING KINETICS IN MA957: FITTED LATTICE AND DISLOCATION PIPE DIFFUSION MODELS — N. J. Cunningham, M. J. Alinger, G. R. Odette, and D. Klingensmith (University of California, Santa Barbara)

OBJECTIVES

The objective of this work is to derive a coarsening model for the nanofeatures in nanostructured ferritic alloys.

SUMMARY

The development of advanced structural and functional materials with unprecedented properties that are enabled by a controlled distribution of nanoscale features (NF) presents enormous opportunities and challenges. One significant challenge is to develop an understanding of and control over the stability of the NF under far from equilibrium, interface dominated, high temperature conditions. Indeed, in the context of the classical near equilibrium materials theory, stable NF might seem an oxymoron. Here we explore the long-term thermal stability of a class of potentially transformational alloys for high temperature energy applications, that we call nanostructured ferritic alloys (NFA). Ultra high densities of Y-Ti-O NF endow NFA with outstanding strength and irradiation tolerance. We have previously reported the results of long-term thermal aging (LTTA) studies of NF and NFA between 800ºC and 1000ºC for times up to 32.4 kh using a toolkit of characterization techniques [1-3]. The NFA are stable at 900°C and below, while experiencing slow, but systematic NF coarsening at 950 and 1000°C, that is accompanied by small reductions in strength and modest grain growth. In the present work we use our experimental observations and data in the literature to derive a quantitative semi-empirical NF coarsening model for aging between 950 and 1300°C. The model predicts negligible coarsening rates below 900°C.

PROGRESS AND STATUS

Background

NFA have a unique combination of high temperature strength and radiation damage tolerance. These important attributes are primarily due to an ultrahigh density of oxide NF with average diameters in the range of 2-3 nm. Thus a critical issue is the high temperature long-term thermal and radiation stability of the NF and the balance of the NFA microstructures. We have previously reported on LTTA studies of NFA MA957. Here we describe the development of a quantitative, semi-empirical model of the coarsening kinetics of the NF based on the LTTA results and other data from the literature.

Analysis Methods

The NF coarsening data analyzed in this work includes:

- LTTA up to 31.2 kh at 950 and 1000°C in MA957 (this study).
- Short to intermediate times up to 480 h at 1200 and 1250ºC in MA957 taken from the work of Alinger et al. [4].

- Short time up to 24 h at 1300°C for MA957 from Miller et al. [5].
- Short to intermediate time up to 100 h at 1200°C for a 14YWT NFA from Williams et al. [6].

These data were analyzed using classical coarsening models as summarized by Ardell [7]. The models can generally be represented by

$$[d(t)^p - d_o^p] = k_p(T)t \quad (1)$$

Here d_o and d are the average initial and coarsened NF diameters and k_p is a material property-temperature dependent rate coefficient. The values of p and parameters in k_p depend on the coarsening mechanism. The power p varies from 2, for interface controlled coarsening, to 5 for a dislocation pipe diffusion mechanism. The p for lattice diffusion controlled coarsening is 3. Using this model, non-linear least square fits (LSF) were used to estimate, p, the rate coefficients, k_p or k_{po} (see below), and the activation energy, Q_p. One approach was the fit all the data simultaneously as

$$[d(t)^p - d_o^p] = k_{po}[\exp(-Q_p/RT)]t \quad (2)$$

to determine p, k_{op} and Q_p. Here R is the universal gas constant and T is the aging temperature in °K. Another method used data set at each temperature to individually determine p and $k_p(T)$. The latter approach yielded a range of p values. In order to establish a unified model the third approach was to fit $k_p(T)$ with fixed values of p = 3 and 5. Then $\ln[k_p]$ vs. 1/T data were then used to fit Q_p.

RESULTS

The data analyzed is shown in Table 1. A high degree of scatter is present in the 1000ºC and 950ºC LTTA data, but it can be reasonably represented by the model with either p=3 or p=5, as shown in Figure 1. Further details on the materials and aging conditions are given in the references [1-6]. Table 1 indicates the technique [small angle neutron scattering (SANS) or atom probe tomography (APT)] used to measure changes in d as a function of time and temperature for the NFA MA957 and a model 14YWT NFA.

Table 1. Analyzed aging data.

Anneal Time (h)	Diameter (nm)	LSF
Miller 1300ºC (MA957 – APT)		
0	2.4	$p_{unconst}$ = 2.7
1	3.4	k_3 = 3.15
24	9.2	k_5 = 4.52
Alinger 1250ºC (MA957 – SANS)		
0	2.64	$p_{unconst}$ = 6.8±0.8
0.33	3.18	k_3 = 1.74±0.17
1	3.58	k_5 = 3.31±0.16
3	5.30	
9	6.30	
27	6.44	
81	7.44	
243	9.18	
Alinger 1200ºC (MA957 – SANS)		
0	2.64	$p_{unconst}$ = 5.2±0.4
3	3.26	k_3 = 1.06±0.07
9	3.68	k_5 = 2.21±0.03
27	4.32	
81	5.12	
243	6.86	
480	7.44	
Williams 1200ºC (14YWT – APT)		
0	5.0	$p_{unconst}$ = 19.3±4.3
1	5.44	k_3 = 1.46±0.27
4	5.70	k_5 = 2.95±0.33
24	5.94	
100	6.8	
Cunningham 1000ºC (MA957 – SANS)		
0	2.68	$p_{unconst}$ = 7.7±14.5
3000	3.26	k_3 = 0.103±0.015
4000	2.82	k_5 = 0.440±0.043
8000	2.82	
11000	3.47	
19500	3.87	
21900	2.94	
Cunningham 950ºC (MA957 – SANS)		
0	2.68	No fit but
3000	2.73	$p_{unconst}$ < 2
6600	2.64	k_3 = 0.054±0.018
9600	2.65	k_5 = 0.235±0.088
17700	2.85	
31200	3.46	

The simultaneous fit of all the data yielded p = 5.55±0.49 and Q_p = 673±41 kJ/mole. The predicted d minus measured d standard deviation is ≈ ±0.5 nm. However, this fit is dominated by the higher temperature data. The unconstrained fit to the individual data sets yielded p values ranging from < 2 to 19.3, as given in Table 1. At 1300ºC (Miller) p ≈ 2.7, but this fit is for only two data points; the p for the 950°C (Cunningham) is < 2, but this data is highly scattered, since the changes in d are small. The other p values

were all > 5, averaging 6.63. After constraining p to values ≤ 6, the fit of p for the other 3 datasets, including at 1000°C, averaged 5.8 in reasonable agreement with the p = 5 pipe diffusion mechanism. Again, these results are summarized in Table 1. Fits of k_p to the individual datasets for fixed p = 3 and 5 yielded Q_3 and Q_5 values and standard errors of 551±10.5 and 665±12.8 kJ/mole, respectively. The corresponding k_{po} are also found from these fits and used to predict coarsening d values for any aging time and temperature condition. The estimated Q values and standard deviations for the predicted minus measured d for each analysis is summarized in Table 2.

Table 2. Fit Q values with standard error and measured d – predicted d standard deviation (SD).

	Non-linear LSF	**p = 3**	**p = 5**
Activation Energy (kJ/mole)	Q_p = 673±41	Q_3 = 551±10.5	Q_5 = 665±12.8
SD of $d_{meas.} - d_{predicted}$ (nm)	SD = 0.51	SD = 0.83	SD = 0.51

Figure 1 shows the $[d^p - d_o^p]^{1/p} = kt^{1/p}$ fits for p = 3 (1a) and 5 (1b). For the 950ºC data the standard error in the slope, k, is in excess of 30% for both p values. The 1000ºC data has a standard error of ≈14% for p = 3 and 10% for p = 5. The Alinger 1200ºC data is best represented with p = 5 with a standard error of 1.5%. The Williams 1200ºC data is less well represented by the model, but the best fit occurs with p = 5. The Alinger 1250ºC data is also best represented by p = 5 with a standard error of 4.7% compared with 9.8% for p = 3. As stated above the Miller 1300ºC is best represented by p = 3, but this fit only includes two data points.

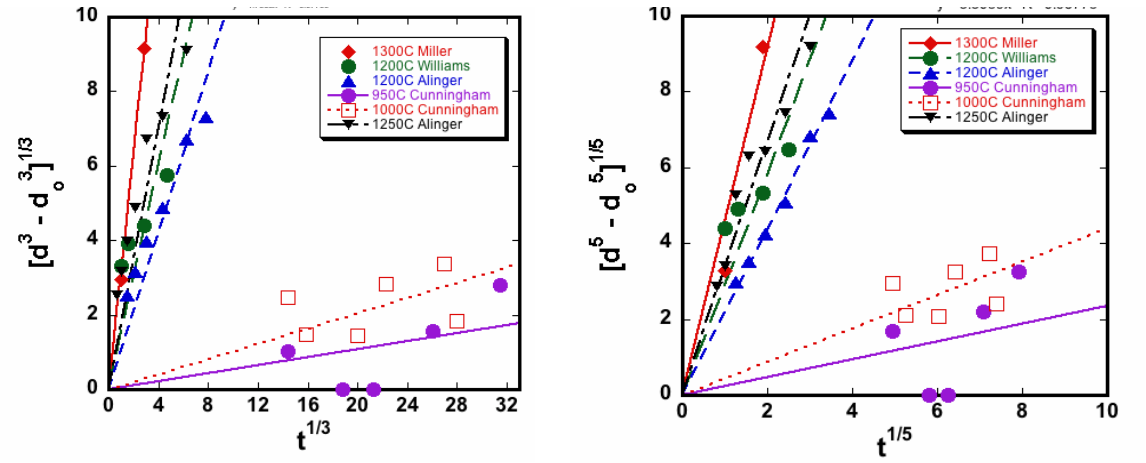

Figure 1. $[d^p - d_o^p]^{1/p} = kt^{1/p}$ fits for a) p = 3 and b) p = 5.

Figure 2 shows the corresponding ln(k) vs 1/T plots that were fit to derive Q_p, which is given by R*p*m, where m is the slope of the LSF and R is the gas constant. For p = 5 the Q_5 ≈ 665 kJ/mole with the overall NF coarsening rate in MA957 for p = 5 can be expressed as

$$d(t,T) = [2.4x10^{25}\exp(-665{,}000/RT)t + d_o^5]^{1/5} \text{ (nm)}$$

For p =3 the $Q_5 \approx 551$ kJ/mole

$$d(t,T) = [5.0x10^{19}exp(-551{,}000/RT)t + d_o^3]^{1/3} \text{ (nm)}$$

Note the Williams data was not used in the $\ln[k_p(T)]$ vs. 1/T fits, but is shown for comparison.

Figure 3 shows the predictions of these models for 50,000 to 150,000 h as a function of temperature. The prediction is based on a d_o = 2.68 nm. The model using p = 3 gives higher coarsening rates compared to p = 5, and is a more conservative value. However, the data is significantly more consistent with a p = 5 value. In either case it is clear that the NF coarsening rates are negligible below 900°C.

DISCUSSION AND FUTURE STUDIES

The results reported here is only one part of a larger effort to understand the thermal stability of NFA. Other aspects of this research include developing models of strength and other property changes in NFA under LTTA conditions, including the effects of evolutions in the balance of grain, dislocation and precipitate microstructures. In addition, experimental and modeling studies are being carried out to better understand the detailed (and complex) physics of NF coarsening and the evolution in NFA under far from equilibrium conditions.

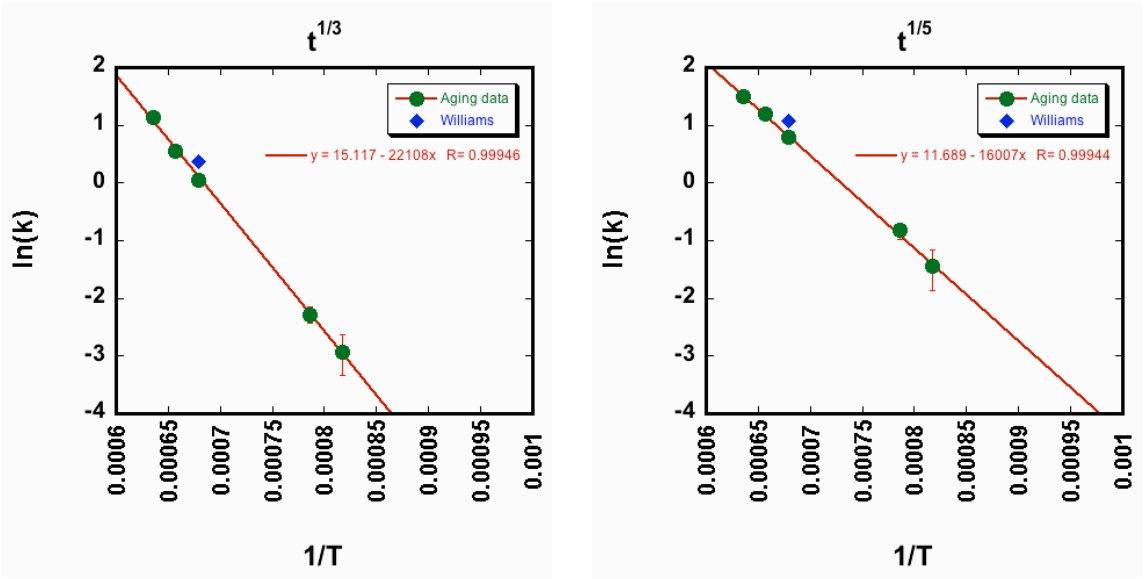

Figure 2. ln(k) vs 1/T plots for a) p = 3 and b) p = 5.

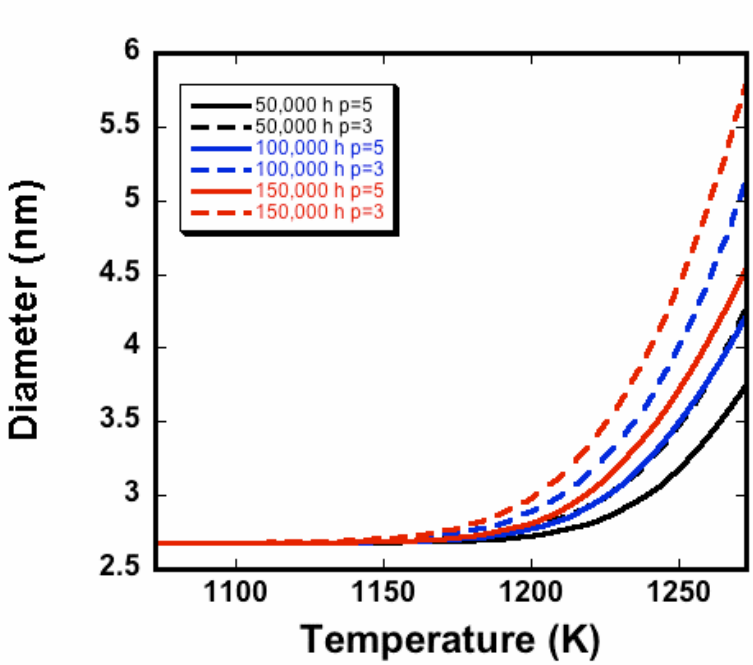

Figure 3. Predicted coarsening based on p = 3 and p = 5 models.

REFERENCES

1. N. J. Cunningham, A. Etienne, Y. Wu, E. M. Haney, and G. R. Odette, "On the Oxide Nanofeatures and Precipitates in the Nano-Structured Ferritic Alloy MA957: A Multiple Technique Study of Heat to Heat Variations and the Effects of Friction Stir Welding and Long Term Thermal Aging," Fusion materials semiannual progress report for period ending June 30, 2010, 60-75, DOE-ER-0313/48.
2. N. J. Cunningham, est. August 2012, "Study of the Structure, Composition, and Stability of Y-Ti-O nm-Scale Features in Nano-Structured Ferritic Alloys," Ph.D. Dissertation, University of California, Santa Barbara.
3. N. J. Cunningham, Y. Wu, D. Klingensmith, and G. R. Odette, "On the Remarkable Thermal Stability of Nanostructured Ferritic Alloys," paper in preparation.
4. M. J. Alinger, September 2004, "On the Formation and Stability of Nanometer Scale Precipitates in Ferritic Alloys during Processing and High Temperature Service," Ph.D. Dissertation, University of California, Santa Barbara.
5. M. K. Miller, D. T. Hoelzer, E. A. Kenik, and K. F. Russell, "Stability of Ferritic MA/ODS Alloys at High Temperatures," *Intermetallics* **13** 2005, 387-392.
6. C. A. Williams, G. D. W. Smith, and E. A. Marquis, "The Effect of Ti on the Coarsening Behavior of Oxygen-Rich Nanoparticles in Oxide-Dispersion-Strengthened Steels after Annealing at 1200ºC," *Sripta Materialia* **67** (2012) 108-111.
7. A. J. Ardell, "On the Coarsening of Grain Boundary Precipitates", *Acta Metallurgica* **20** (1972) 601-609.

8.1 MOLECULAR DYNAMICS MODELING OF 10 AND 50 keV ATOMIC DISPLACEMENT CASCADES IN 3C-SiC — G. D. Samolyuk, Y. N. Osetskiy and R. E. Stoller (Oak Ridge National Laboratory)

OBJECTIVE

The objective of this research is to investigate the damage in 3C-SiC induced under fusion irradiation conditions and describe microscopic origin of such experimentally observed phenomena as amorphization [1-6] and swelling [7-9].

SUMMARY

Molecular dynamics (MD) simulations of atomic displacement cascades in 3C-SiC were carried out at a range of temperatures and two energies. A new code for post processing the MD results was developed to analyze the results. We simulated cascades produced by 10 and 50 keV primary knock-on atoms (PKA) at temperatures of 300, 600, 900, 1200 and 1500 K. Similar to previous results [10, 11] it was observed that the main defects produced in 3C-SiC are carbon interstitials (C(I)) and carbon vacancies (C(V)). The temperature dependence of number of defects is weak. 30 % of defects are accumulated into clusters of size ~20 defects, which are often, interpreted [11] as amorphous domains. Many pair clusters of C(I)-C(V) were observed. The stability of these objects is a result of specific crystal structure of 3C-SiC. The 3C-SiC lattice has “empty space” in the unit cell positions (3/4, 3/4, 3/4) and (1/2, 1/2, 1/2).

PROGRESS AND STATUS

Introduction

3C-SiC subjected to fusion conditions is changing their microstructure and hence mechanical properties. Understanding the details of this process is necessary for predicting changes, estimation of material lifetime. Experimental studies have demonstrated that depending on the structural material composition and particular conditions such phenomena as amortization [1-6], swelling [7-9] were observed.

Formalism

The LAMMPS (Large-scale Atomic/Molecular Massively Parallel Simulator, see http://lammps.sandia.gov) code was used for atomistic molecular dynamics simulations [12]. The interactions between atoms were described by a hybrid Tersoff/ZBL potential [13-15]. The simulation cell contains from 80x80x80 unit cells (409600 atoms) for 10 keV the PKA kinetic energy, 100x100x100 unit cells (8000000 atoms) for 50 keV PKA kinetic energy at temperature 600 K and 120x120x120 unit cells (13824000 atoms) for 50 keV PKA kinetic energy at temperature 1200 K. The initial system was equilibrated for 2 picoseconds with time step 0.1 femtosecond. Each cascade was initiated by giving a Si atom kinetic energy of 10 or 50 keV keeping zero total momentum. The cascade evolves for ~20 ps and the time step is modified such that the distance covered by the fastest particle in the system is less than 0.014 A. We apply constant volume through the iteration and the lattice parameter is chosen from the condition of zero pressure of system in equilibrium at particular temperature. The Wigner-Seitz cell analysis method was used to determine defects in the modeling system. The defects separated by distance less than a lattice parameter are interpreted as a defect clusters.

RESULTS

The number of point defects as a function of time for different temperatures and 10 or 50 keV PKA kinetic energy are presented in Figures 1-7. On this figures the notations Si(V) and C(V) correspond to silicon/carbon vacancies, Si(I) and C(I) – interstitials, Si_C and C_{Si} – aniticites and Si_{Si} and C_C – replacement atoms (Si atoms in Si lattice site came from other position).

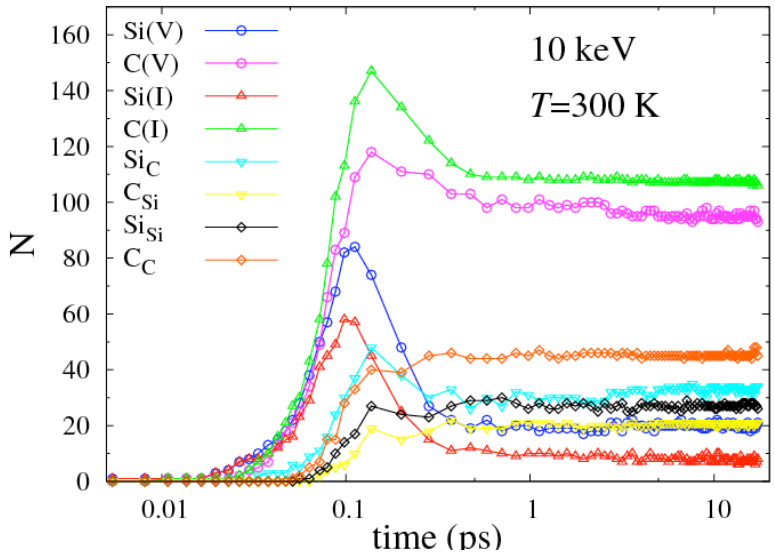

Figure 1. Plot of defect count for 300 K and 10 keV Si displacement cascade.

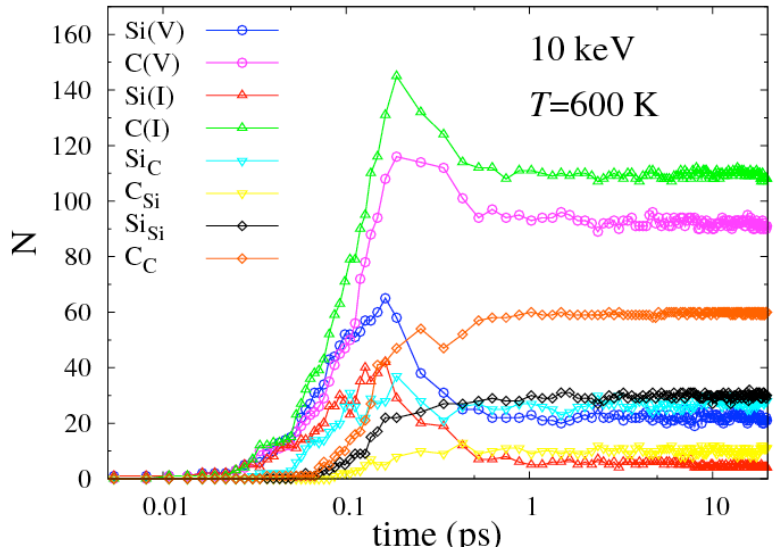

Figure 2. Plot of defect count for 600 K and 10 keV Si displacement cascade.

Analysis of cascade evolution in SiC indicates that by 0.2 picoseconds the PKA has lost most of its kinetic energy and by 1 picosecond its kinetic energy is close to background energy. After this time the velocity of cascade evolution is significantly reduced. The number of defects doesn't demonstrate significant dependency of the temperature. Carbon vacancies and interstitials are the main type of defects observed. They number 2.5 times more than Si defects. At ~1.5 picosecond the number of defects reaches a maximum value and is reduced by ~30% for carbon vacancies/interstitials and by 60 % for silicon defects. The time evolution of carbon (C_{Si}) and replacement atoms does not exhibit this maximum. The number of these type of defects monotonically increases with time until it reaches saturation at a time of ~2 picoseconds. This difference in the behavior could be related to the fact that formation energy for replacement atoms is equal to zero and is very low for C_{Si} defects. The largest formation energy corresponds to Si(I) and Si(V) defects and this fact reflects the larger (3 times increase at 1.5 picoseconds) spike in time dependence.

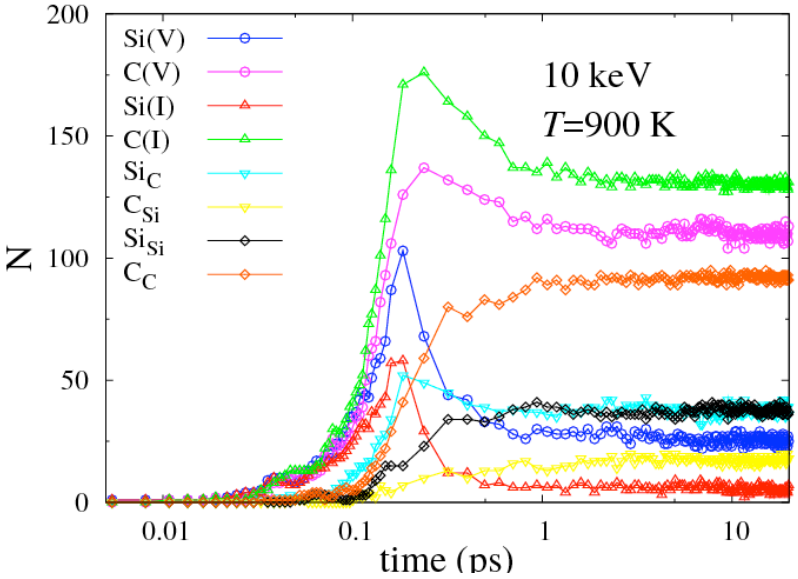

Figure 3. Plot of defect count for 900 K and 10 keV Si displacement cascade.

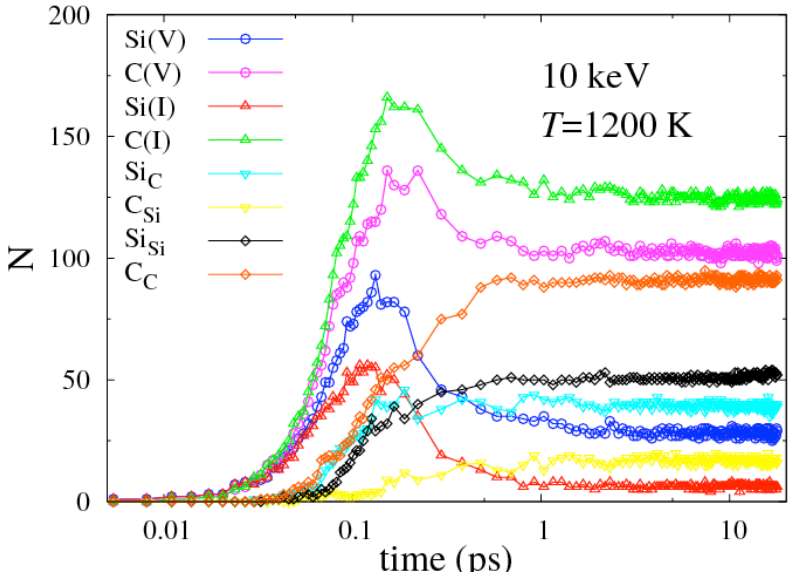

Figure 4. Plot of defect count for 900 K and 10 keV Si displacement cascade.

The defects cluster distribution calculated from the 10 keV PKA cascade at temperature 300K and time 20 picoseconds is presented in Figure 8. Single point defects comprise 15 % of the surviving defects. Almost the same fraction of defects is contained in clusters of size two. Most of these size two clusters consist of C(I)-C(V) defects. The stability of these objects is a result of low formation energy caused by specific crystal structure of 3C-SiC. The 3C-SiC lattice has an “empty space” in relative position (3/4, 3/4, 3/4) and (1/2, 1/2, 1/2). The energy to shift a C atom from its “perfect” position to the “empty space” is comparable to formation energy of single C defects. The three clusters of size ~20 defects can be interpreted as amorphous domains.

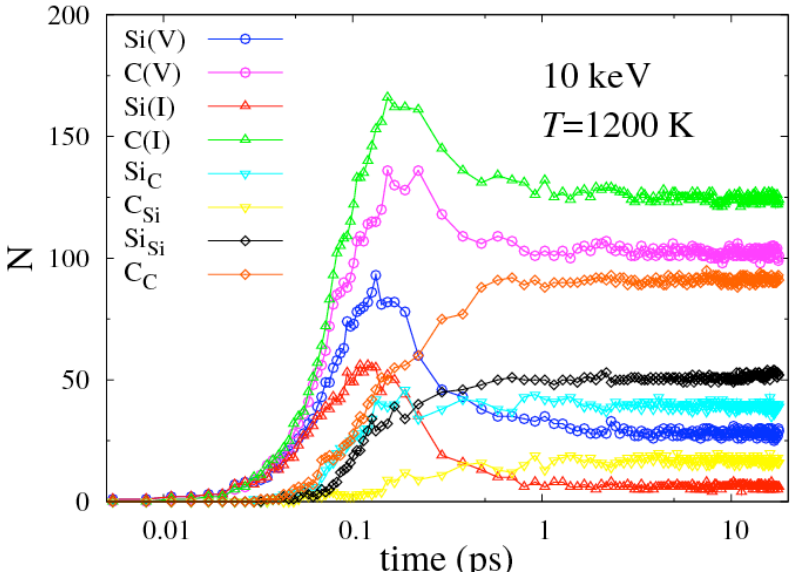

Figure 5. Plot of defect count for 1200 K and 10 keV Si displacement cascade.

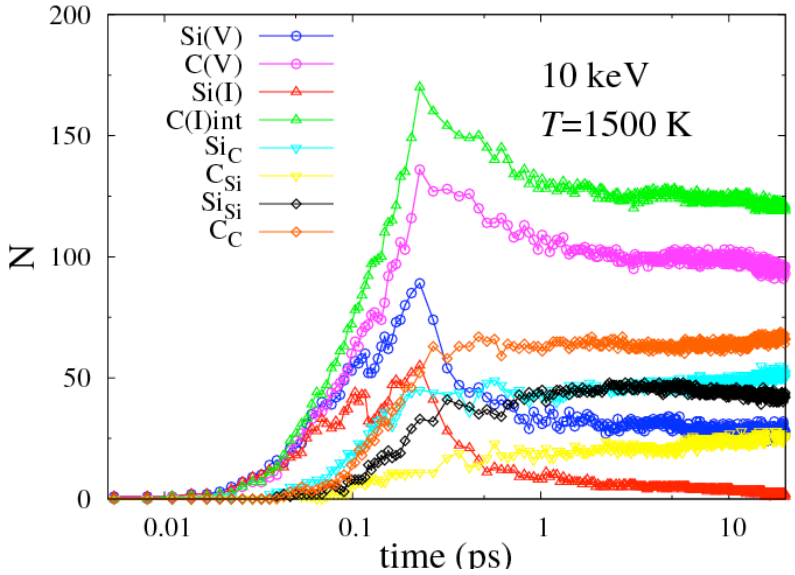

Figure 6. Plot of defect count for 1500 K and 10 keV Si displacement cascade.

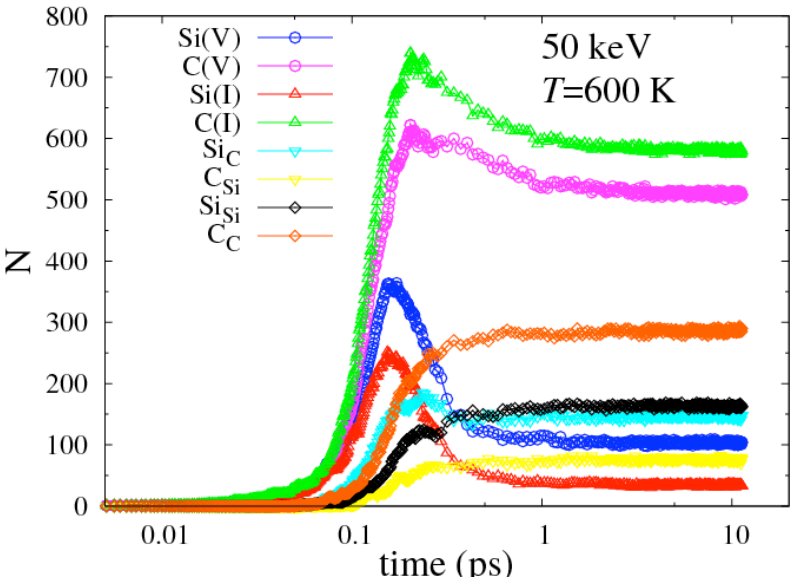

Figure 7. Plot of defect count for 1200 K and 50 keV Si displacement cascade.

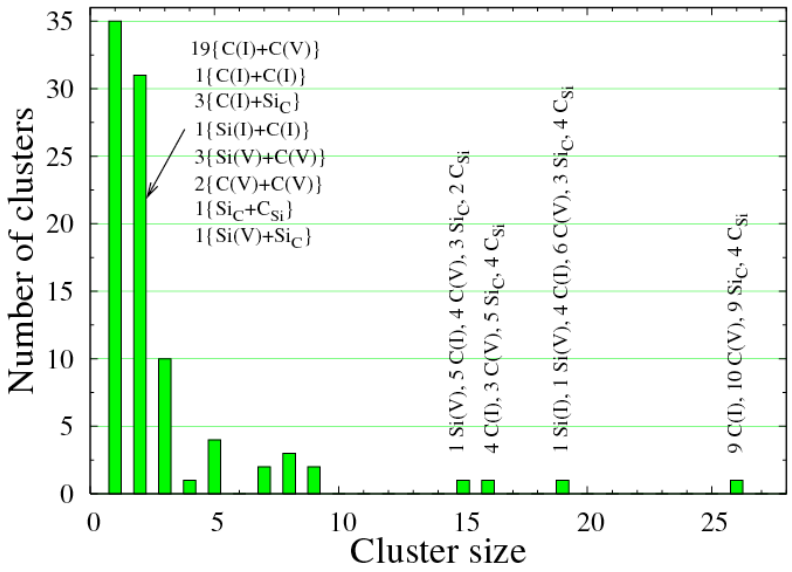

Figure 8. Defect cluster distribution in 10 keV cascade after 20 ps at temperature 300 K.

FUTURE WORK

Simulations are underway at additional temperatures at 50 keV to provide direct comparisons with the 10 keV results. Additional simulations will also provide further information on statistical variations. More detailed analysis of the structure of defect clusters is planned to determine whether or not they are consistent with an amorphous structure. Finally, MD simulations of defect mobility are underway to characterize diffusion in SiC.

REFERENCES

1. H. Inui, H. Mori, and H. Fujita, "Electron-irradiation-induced crystalline to amorphous transition in a-SiC single crystals," *Philos. Mag. B* **61**, 107 (1990).
2. H. Inui, H. Mori, T. Sakata, and H. Fujita, "Electron-irradiation induced crystalline-to-amorphous transition in b-SiC single crystals," *Philos. Mag*. B **65**, 1 (1992).
3. E. Wendler, A. Heft, and W. Wesch, "Ion-beam induced damage and annealing behavior in SiC," *Nucl. Instrum. Methods Phys. Res*. Sect. B **141**, 105 (1998).
4. Y. Zhang, F. Gao, W. Jiang, D. E. McCready, and W. J. Weber, "Damage accumulation and defect relaxation in 4H–SiC," *Phys. Rev*. B **70**, 125203 (2004).
5. W. Jiang, H. Wang, I. Kim, I-T. Bae, G. Li, P. Nachimuthu, Z. Zhu, Y. Zhang, and W. J. Weber, "Response of nanocrystalline 3C silicon carbide to heavy-ion irradiation," *Phys. Rev. B* **80**, 161301 (2009).
6. L. L. Snead and J. C. Hay, "Neutron irradiation induced amorphization of silicon carbide," *J. Nucl. Mater*. **273**, 213 (1999).
7. R. Blackstone and E. H. Voice, *J. Nucl. Mater*. **39** (1971).
8. J. E. Palentine, *J. Nucl. Mater*. **61**, 243 (1976).
9. A. I. Ryazanov, A. V. Klaptsov, A. Kohyama, and H. Kishimoto, *J. Nucl. Mater*. **307– 311**, 1107 (2002).
10. D. E. Farrell, N. Bernstein and W. K. Liu, "Thermal effects in 10 keV Si PKA cascades in 3C-SiC," *J. Nucl. Mater*. **385**, 572 (2009).

11. W. J. Weber and F. Gao, “Irradiation-induced defect clustering and amorphization in silicon carbide,” *J. Mater. Res*., **25**, 2349 (2010).
12. S. J. Plimpton, *J. Comp. Phys*. **117**, 1 (1995).
13. J. Tersoff, *Phys. Rev*. B 39 (1989).
14. R. Devanathan, T. Diaz de la Rubia, and W. J. Weber, *J. Nucl. Mater*. 253 (1998) 47.
15. J. F. Ziegler, J. P. Biersack, and U. Littmark, “The stopping and ranges of ions in solids,” Vol. 1, Pergamon (1985).

8.2 NUCLEATION OF HE BUBBLES AT A LOW-ANGLE GRAIN BOUNDARY IN α-FE —

L. Yang, F. Gao, H. L. Heinisch and R. J. Kurtz (Pacific Northwest National Laboratory)

OBJECTIVE

To study the nucleation of He bubbles at the Σ73b low-angle grain boundary in α-Fe using the newly developed Fe-He potential and to compare the results with those previously obtained for the Σ3 GB.

SUMMARY

In a fusion reactor environment He is produced at high rates in steels by nuclear (n, α) transmutation reactions. Understanding the deleterious effects of He, especially the nucleation of He bubbles at GBs in steels, is one of the most important issues in nuclear fusion technology. The accumulation of He atoms and nucleation of He bubbles in the Σ3 <110> {112} GB in α-Fe have been previously studied [1] using molecular dynamics with our newly developed Fe-He potential [2]. It was found that the accumulation of He atoms, the formation of He bubbles, and the evolution of the GB structure all depend on the local He concentration and temperature. In order to broaden understanding of the effects of GB structure on the accumulation of He atoms and the nucleation of He bubbles in α-Fe the interaction of He with the ∑73b<110>{661} GB in α-Fe is currently being investigated using the same methodology as that used for our earlier studies of He in the Σ3 GB. It is found that in the ∑73b GB at low He concentrations most He atoms migrate to the GB dislocations in a very short time, and they can move along the GB dislocation lines at high temperatures. He atoms seldom congregate to form clusters in the ∑73b GB, even at 800 K, compared to clustering in the Σ3 GB. Emission of an Fe self-interstitial atom (SIA) caused by a single He is observed at 300 K, while it occurs for the clusters containing at least four He atoms at 600 K in the Σ3 GB and higher temperatures. At a local He concentration of 5 % (as defined within 20 Å from the GB), a large number of He clusters are formed. The nucleation of He bubbles is more significant at higher temperatures in the ∑73b GB, while it depends only slightly on the temperature in the Σ3 GB. Most of the He clusters are distributed along the GB dislocation lines in the ∑73b GB at low temperatures, forming platelet like configurations. At a 10 % local He concentration, a large number of SIAs are created, which results in the propagation of GB dislocations along the <112-1> direction.

PROGRESS AND STATUS

Introduction

The effect of helium on first wall structural materials has been widely recognized as one of the most crucial material issues in nuclear fusion reactors, because the synergistic interaction of large amounts of helium with the existing and radiation-induced defects and microstructures in materials can significantly degrade their mechanical properties. Multi-scale modeling, especially including the atomic scale, provides a basis to obtain insight into general understanding of the complex radiation damage process. As an important part of this modeling, molecular dynamics (MD) methods, including improved interatomic potentials, have been widely employed to study the atomic-level processes of defects controlling microstructural evolution in advanced ferritic steels.

The new interatomic potential for Fe-He interactions [2] used in the present studies is based on the electronic hybridization between Fe *d*-electrons and He *s*-electrons. This potential was used previously to investigate the nucleation of He clusters and bubbles, the emission of SIAs from the He clusters, and the formation of dislocation loops in bulk α-Fe, as well as to study the effects of these phenomena on microstructural changes at 800 K [3]. That investigation found that a cluster of four He atoms is able to push an iron atom into an interstitial position, creating a He_4V cluster and a SIA. Small He clusters and SIA can migrate in the matrix, but He-vacancy (He-V) clusters are immobile on accessible molecular dynamics time scales. At low He concentrations SIA clusters (or loops) are attached to He-V clusters, while at high He concentrations He-V cluster-loop complexes with more than one He-V cluster are formed. Also, the accumulation of He atoms and nucleation of He bubbles in Σ3 <110> {112} GB of α-Fe have been previously studied using molecular dynamics [1], which provides a good reference to compare with the current study of the accumulation of He atoms and the nucleation of He bubbles in the ∑73b<110>{661} GB.

Simulation Methods

In the present simulations we investigate the nucleation and formation of He clusters in the ∑73b <110> {661} low angle GB in α-Fe, which contains intrinsic GB dislocations. The model consists of 48,000 Fe atoms in a block of size 103.50 Å × 70.00 Å × 80.76 Å. Periodic boundary conditions are imposed along the *x* and *z* directions, but fixed boundary conditions are applied along the *y* direction, where the x, y and z represent the <112-1>, <-616> and <101> directions in the GB model, respectively, as indicated in Figure 1. The interatomic potentials for Fe-Fe, Fe-He and He-He interactions are the same as those used in Ref. 2

The NVT (constant number of atoms, volume and temperature) ensemble is chosen in the present simulations with a time step of 1 fs. Initially the simulation cell is quenched to 0 K at constant pressure with the molecular statics (MS) approach, and then the stress field of the Σ73b GB is determined. It is found that the stress is distributed within about 20 Å of the GB core, with a maximum value of about 10 GPa. He atoms are inserted at random positions within the stressed region near the GB at local He concentrations of 1 % (72 He atoms), 5 % (359 He atoms) and 10 % (718 He atoms), which are the ratios of the number of He atoms to those Fe atoms within the considered stressed region. After He insertion, the cell was again quenched to 0 K to obtain a minimum energy configuration, followed by a temperature rescaling to the required temperature and relaxation for 1 ns. Three temperatures of 300 K, 600K and 800 K are considered.

RESULTS AND DISCUSSION

After randomly inserting 1 % He into the region within 20 Å of the ∑73b GB core, a simulation was performed at 300 K. Within a very short time almost all the He atoms aggregate at the ∑73b GB dislocations, but few He clusters are formed in the GB, especially as compared to He clustering in the Σ3 GB. Some He atoms can move along the ∑73b GB dislocation lines at high temperatures, and clustering of He up to only He_3 is observed to form even at 800 K. In contrast, a few He_6 clusters are formed in the Σ3 GB, as shown in Figure 1, where the upper image shows a view parallel to the tilt axis and the lower image shows a view normal to the GB plane. This suggests that the probability of forming He clusters may be limited in the GBs with higher excess volumes: these calculations are in progress. Emission of a SIA by a single He replacing an Fe atom is observed at 300 K, but this is a rare event, while it occurs for the clusters with four He atoms at 600 K and higher temperatures in the Σ3 GB.

MD simulations of the Σ73b GB with a 5 % He concentration were performed for 1 ns. The final atomic configurations at 300 K and 800 K are shown in Figure 2, from which it is clearly seen that some large He clusers are formed, especially at the higher temperature. It is of interest to note that at 300 K almost all the He atoms are distributed along the GB dislocation lines and all He clusters exhibit longitudinal platelet like shapes along the dislocation lines. However, at 800 K more large He clusters are formed near the GB plane, and most of them have spherical shapes. During the simulations at 800 K, it is clearly seen that the He atoms in clusters accumulate into spherical shapes to minimize the surface energy of the clusters at high temperatures. A number of SIAs are emitted from the clusters, and they collect near the GB dislocation cores.

When the He concentration increases to10 %, He atoms rapidly diffuse to the GB plane at all temperatures considered, and they form many large He clusters with platelet-like structures. The sizes of the He clusters obviously increase with increasing temperature. Helium clusters are distributed almost uniformly near the GB at 600 K and higher temperatures, as shown in Figure 3. It is clear that most He clusters do not have spherical shapes, which is different from the clustering at the He concentration of 5 % (see Figure 2b), which may be associated with the smaller size of the clusters at low concentrations. A large number of SIAs are created by the nucleation of He bubbles. It is of interest to note that those SIAs prefer to aggregate at the dislocation cores in the GB, causing these dislocations to climb along the <112-1> direction (see insets I and II in Figure 3), and that the propagation is more significant at higher temperatures. This phenomenon is different from that in the Σ3 GB for the same He concentration, where the SIAs reconstruct to form an extra atomic layer above the original GB plane, leading to GB climb along the <-112> direction.

CONCLUSION

He accumulation and the nucleation of He clusters (bubbles) in S73b GBs in α-Fe are studied using molecular dynamics, and the results are compared with results previously obtained for the S3 GB. It is clear that the evolution of the GB configurations, the accumulation of He atoms and the nucleation of He bubbles all depend on the He concentration, temperatures and the GB configurations. At a 1% He concentration, most He atoms migrate to the GB dislocation lines in a very short time, but in the Σ73b GB they seldom congregate to form clusters, even at 800 K, especially as compared to those in Σ3 GB. At higher He concentrations a large number of He clusters are formed, and the nucleation of He bubble is more significant at higher temperatures in $\sum$73b GBs, while it slightly depends on the temperature in Σ3 GBs. Most of the He clusters are distributed along the GB dislocation lines in the $\sum$73b GB at low temperatures, forming platelet like structures. It is also observed that a large number of SIAs are emitted from the clusters at a 10 % He concentration, which results in the climb of the GB dislocations along the <112-1> direction.

REFERENCES

[1] L. Yang, F. Gao, H. L. Heinisch, and R. J. Kurtz, In *DOE/ER-0313/50-Volume 51 Semiannual Progress Report December 31, 2011*.
[2] L. Yang, H. Q. Deng, F. Gao, H. L. Heinisch, R. J. Kurtz, S. Y. Hu, Y. L. Li, and X. T. Zu, submitted to *Nuclear Instruments and Methods B.*
[3] F. Gao, H. Q. Deng, H. L. Heinisch, and R. J. Kurtz, *J. Nucl. Mater.* **418** (2011) 115.

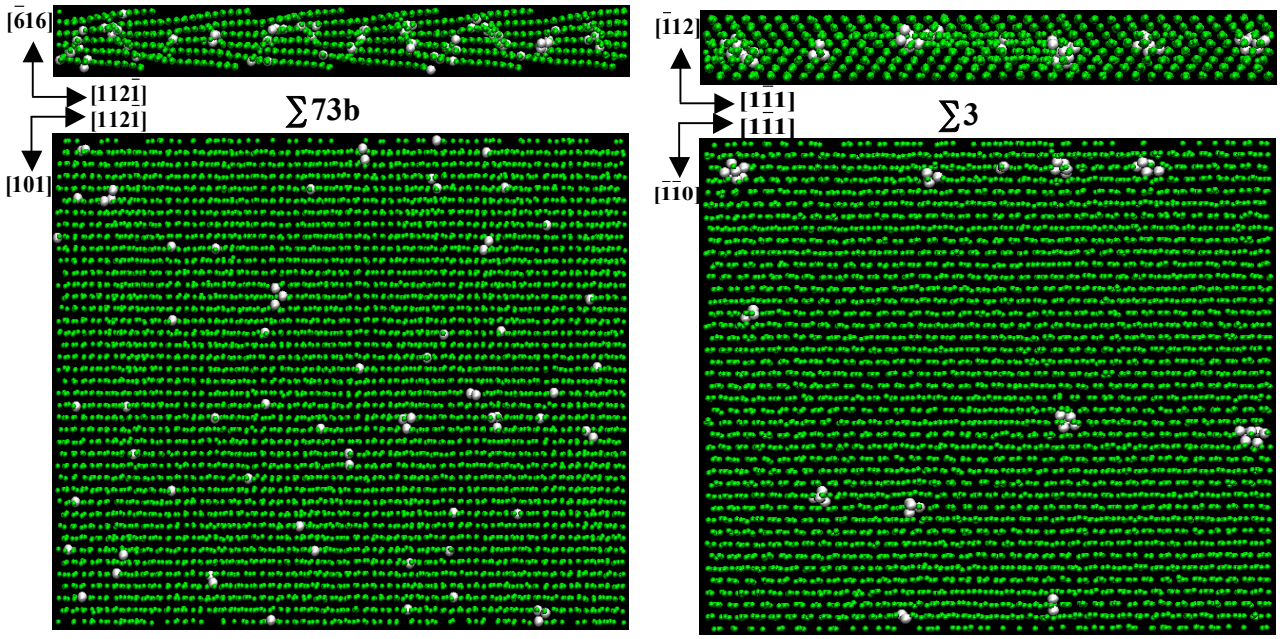

Figure 1. Final atomic configurations with a 1 % He concentration at 800 K in α-Fe: (a) Σ73b GB and (b)Σ3 GB.

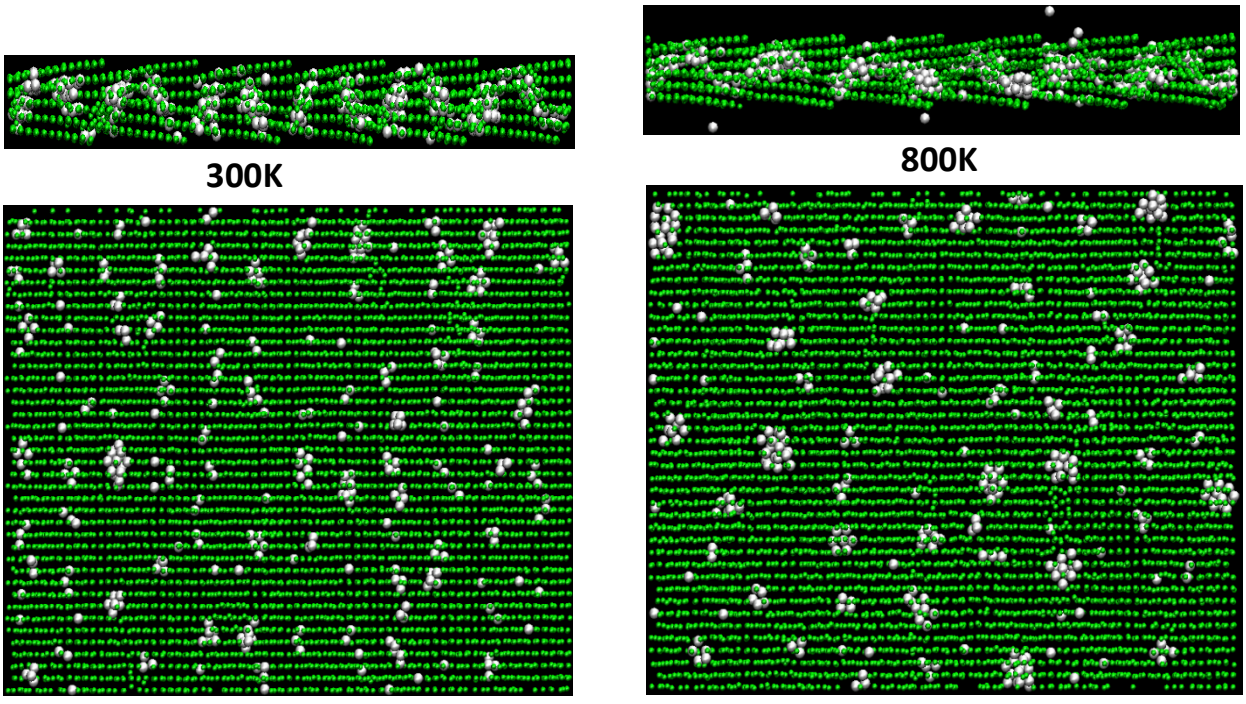

Figure 2. Final atomic configurations of Σ73b GB with a 5 % He concentration in α-Fe at: (a) 300 K and (b) 800 K.

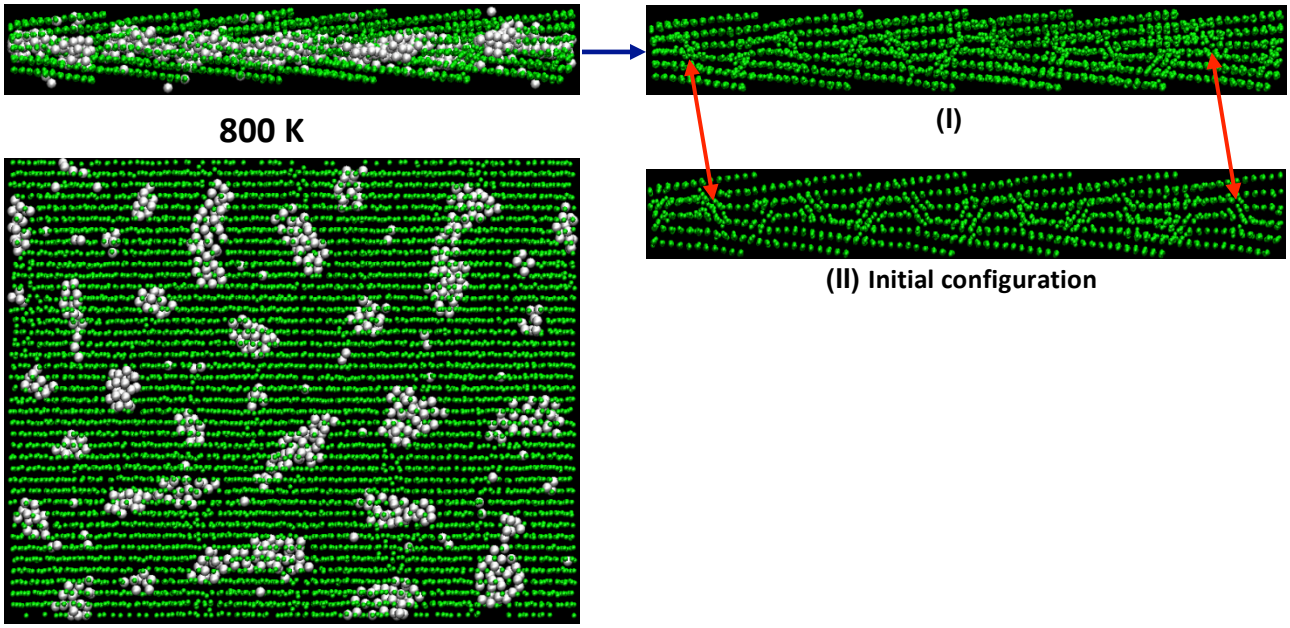

Figure 3. Final atomic configurations of Σ73b GB with a 10 % He concentration at 800 K in α-Fe. The He atoms are omitted from the inset figures I and II.

8.3 DEVELOPMENT OF A NEW EQUATION OF STATE FOR HELIUM IN IRON —

R. E. Stoller and Y. N. Osetskiy (Oak Ridge National Laboratory)

OBJECTIVE

The objective of this research is to develop the modeling and simulation tools necessary to improve our understanding of how helium interacts with other defects in iron-based alloys to produce changes in the microstructure and mechanical properties.

SUMMARY

A large series of molecular dynamics simulations are underway to provide the detailed atomistic data, which will enable final fitting of a new equation of state for helium in iron. This potential will be based on the behavior of helium as described by the three-body Fe-He potential developed at ORNL under the fusion program.

PROGRESS AND STATUS

Introduction

Because of the high helium levels generated by nuclear transmutation reactions, predictions of structural material performance under DT fusion conditions must account for how the helium influences microstructural evolution and the related mechanical properties. One of the primary issues that must be addressed is the behavior of He-vacancy clusters, which evolve, into finite-sized bubbles with the potential for growing into voids. In this case, a 'bubble' is defined as a cavity, which is stabilized by the helium pressure it contains. If helium is removed a bubble will shrink. In contrast, a 'void' is a cavity, which has grown large enough that growth can be maintained by the absorption of a net vacancy flux. The gas pressure plays essentially no role in voids stability. The properties of small He-vacancy clusters, such as the helium and vacancy binding energy are critical to predicting bubble stability. These processes can only be accurately described by atomistic simulations such as molecular dynamics (MD), which requires an interatomic potential to describe the behavior of both the metal and helium atoms. In order to improve our predictive capability for the Fe-based materials of most interest to fusion structural applications, a new Fe-He interatomic potential was developed based on ab initio calculations of the interactions between He and point defects in Fe [1-2]. Additional work using this potential as characterized the properties of small He-vacancy clusters and parameters such as the He-to-vacancy ratio as a function if cluster/bubble size and temperature [3-4]. The observations of that work is being extended to develop an atomistic equation of state for helium in iron which can then be applied in a broad range of mesoscale to predict microstructural evolution.

Current Progress

In order to provide a basis for fitting the pressure-temperature relationship required for the equation of state (EOS), a series of MD simulations has been initiated. The primary conditions are described in Table 1. The temperature range was chosen to cover a range, which includes much lower and higher temperatures than the expected applications of the EOS. The bubble sizes encompass those of interest to fusion reactor materials, and an accurate extrapolation to larger sizes will be verified. If needed, larger sizes may be included, although the expectation

is that the pressure will be sufficiently low at large sizes that a more simple equation of state will be appropriate. For each of the bubble sizes, the pressure will be obtained for a broad range of He/vacancy ratios, from highly over-pressurized to a void-like under-pressurized state. The pressure at mechanical equilibrium will also be determined.

The primary issue in fitting the EOS is to choose an appropriate function to describe the compressibility of the gas. We will first adopt the hard-sphere model of Brearley and MacInnes [5] for testing and evaluation. One difference between the atomistic results and the assumptions typically applied in developing an EOS is illustrated in Fig. 1. The general thought is that the gas atoms occupy the complete bubble volume. However, MD simulations using the ORNL Fe-He potential in concert with the Fe potential of Ackland, et al. [6] indicate that the Fe-He interaction leads to a small exclusion volume near the bubble surface. This is demonstrated in Fig. 1a in which the time-averaged positions of the iron surface atoms (green) and helium atoms (gold) are shown. Fig. 1b shows the corresponding radial distribution of He atoms graphically. The result of this standoff distance is that the effective volume of the bubble used to compute the pressure is smaller and the pressure is higher.

Table 1. Conditions for MD simulations

Temperature (K)	Bubble radius (nm)
200	0.25, 0.5, 1.0, 2.0, 5.0
300	same as above
400	same as above
500	same as above
600	same as above
700	same as above
800	same as above
900	same as above
1000	same as above
1100	same as above

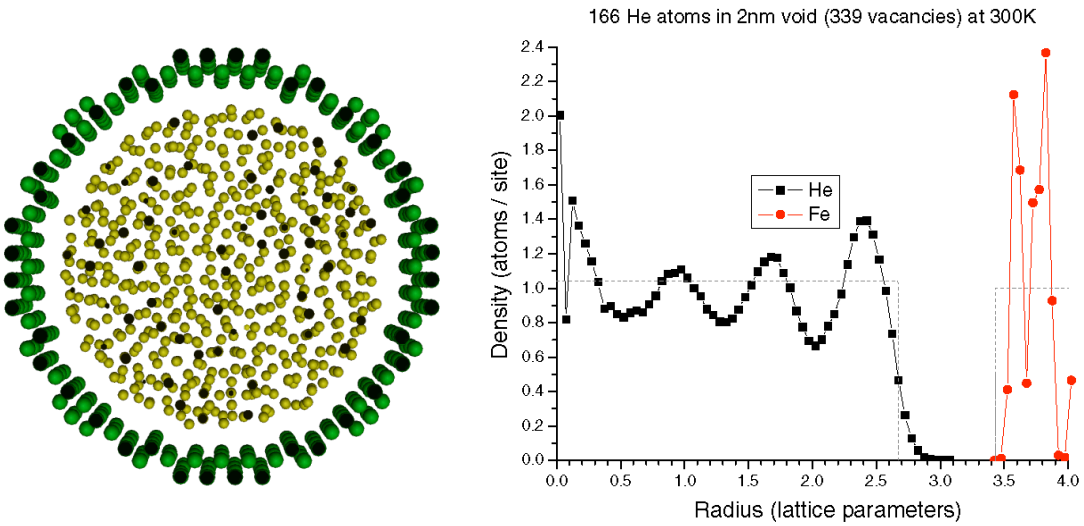

Fig. 1. Illustration of how Fe-He interaction leads to the formation of a gas-free region near the bubble surface for a 2 nm diameter bubble [4].

REFERENCES

1. T. Seletskaia, Yu. N. Osetsky, R. E. Stoller, and G. M. Stocks, "Development of a Fe–He Interatomic Potential Based on Electronic Structure Calculations," *J. Nucl. Mater.* **367-370** (2007) 355-360.
2. R. E. Stoller, S. I. Golubov, P. J. Kamenski, T. Seletskaia, and Yu. N. Osetsky, "Implementation of A New Fe-He Three-body Interatomic Potential for Molecular Dynamics Simulations," *Phil. Mag.* **90** (2010) 923-934.
3. D. M. Stewart, Yu. N. Osetsky, R. E. Stoller, S. I. Golubov, T. Seletskaia, and P. J. Kamenski, "Atomistic Studies of Helium Defects Properties in BCC Iron: Comparison of He–Fe Potentials, *Philos. Mag*. **90** (2010) 923.
4. D. M. Stewart, Yu. N. Osetskiy and R. E. Stoller, "Atomistic Studies of Formation and Diffusion of Helium Clusters and Bubbles in BCC Iron," *J. Nucl. Mater.* **147** (2011) 1110-1114.
5. I. R. Brearley and D. A. MacInnes, "An Improved Equation of State for Inert Gases at High Pressures," *J. Nucl. Mater.* **95** (1980) 239-252.
6. G. J. Ackland, D. J. Bacon, A. F. Calder, and T. Harry, "Computer Simulation of Point Defect Properties in Dilute Fe-Cu Alloy Using a Many-body Interatomic Potential," *Phil. Mag.* **A75** (1997) 713-732.

8.4 MODELING FAST NEUTRON IRRADIATION DAMAGE ACCUMULATION IN TUNGSTEN — J. Marian (Lawrence Livermore National Laboratory) and T. Hoang (University of California, Berkeley)

OBJECTIVE

The objective of this work is to simulate neutron damage in pure W and understand He effects and dislocation loop accumulation under fast and fusion reactor conditions.

SUMMARY

Due to its advantageous physical properties, tungsten (W) is being considered as a candidate structural material in fusion applications. In this paper, we perform stochastic cluster dynamics calculations of irradiation damage accumulation in pure W under fast neutron spectra up to doses of 1.5 dpa in the 400–600°C interval. Our calculations suggest that He bubbles and dislocation loops accumulate under fusion conditions, but not under fast fission spectra. We study the temperature dependence of swelling and find that it is maximum in the 550–590°C temperature range, falling precipitously above 600°C. Swelling levels are very low, never surpassing a fraction of a percentage point. We also provide hardening estimates based on the accumulation of sessile dislocation loops under fusion conditions and show that they are moderate, ranging between 70 and 137 MPa at 400°C.

PROGRESS AND STATUS

Introduction

Tungsten (W) is being considered as a leading candidate for plasma-facing applications in magnetic fusion energy (MFE) devices. The most attractive properties of W for MFE are its high melting point and thermal conductivity, low sputtering yield and low long-term disposal radioactive footprint. These advantages are accompanied unfortunately with very low fracture toughness characterized by brittle trans- and inter-granular failure, which severely restrict the useful operating temperature window [1]. W is typically alloyed with 5–26 at.% Re to increase low temperature ductility and improve high temperature strength and plasticity [2]. However, Re is an undesired impurity in MFE neutron environments due to its high transmutation rate into Os [3] and the possible formation of brittle r phases [4]. Even in pure W, Re is the main transmutation product under fast neutron conditions and so understanding the irradiation behavior of the W–Re system is paramount to component performance predictions. Indeed, irradiations in EBR-II up to 9 dpa have revealed the absence of swelling in W–25%Re [5] and W–10%Re [6] compared to values of close to 2% in pure W. Matolich measured the temperature at which peak swelling occurs in pure W at approximately 750°C [5]. In a series of recent papers, Hasegawa and collaborators have shown that Re precipitation suppresses void and dislocation loop density accumulation and size growth [7–9], although they observe that subsaturated Re precipitation above 1 dpa gives rise to very dramatic hardening increases. This precipitation of soluble Re under irradiation was observed by Williams et al. during EBR-II experiments in 1983 [10]. By comparison, the effect of transmutant He on W under fast neutron irradiation has been less studied. Gilbert and Sublet [3] report relatively low He transmutation rates under ITER first-wall conditions (≈1 appm per dpa). However, Kornelsen [11,12] studied He accumulation in pure W crystals previously irradiated with heavy ions and observed the formation of He bubbles.

Computer simulations can provide insight into the fundamental mechanisms of damage accumulation and associated detrimental effects. At the atomistic scale, the treatment of W–Re alloys is limited to a few hundred atoms using electronic structure calculations due to the absence of suitable empirical potentials. By contrast, W-He potentials have been developed and used to assess the effect of He on Frenkel pair production in displacement cascades [13]. In addition, ion implantation studies in W have been published recently using energetics from electronic structure calculations [14]. In this work we conduct simulations of void swelling and hardening in pure W including the effect of transmutant He in the temperature range of fusion materials. We analyze the nature of the vacancy and self-interstitial atom (SIA) type defects and discuss the implications for material degradation. We consider two distinct neutron environments. The first is that found in the fast-fission JOYO reactor, following the irradiations by Hasegawa et al. [9]. The second corresponds to ITER fusion neutron conditions, such as those considered by Gilbert and Sublet [3].

Computational Methods

The Stochastic Cluster Dynamics Method

Here we use the stochastic cluster dynamics method (SCD) [15] to perform all simulations. SCD is a stochastic variant of the mean-field rate theory technique, alternative to the standard ODE-based implementations that eliminates the need to solve exceedingly large sets of ODEs and relies instead on sparse stochastic sampling from the underlying kinetic master equation. Rather than dealing with continuously varying defect concentrations in an infinite volume, SCD evolves an integer-valued defect population N_i in a finite material volume V, thus avoiding combinatorial explosion in the number of ODEs. This makes SCD ideal to treat problems where the dimensionality of the cluster size space is high, e.g., when multispecies simulations — for example involving energetic particles, He, H, etc., simultaneously — are of interest. SCD recasts the standard ODE system into stochastic equations of the form:

$$\frac{dN_i}{dt} = \tilde{g}_i - \sum_i \tilde{s}_{ij} N_i + \sum_j \tilde{s}_{ji} N_j - \sum_{i,j} \tilde{k}_{ij} N_i N_j + \sum_{j,k} \tilde{k}_{jk} N_j N_k,$$

where the set $\{\tilde{g}, \tilde{s}, \tilde{k}\}$ represents the reaction rates of 0th (insertion), 1st (thermal dissociation, annihilation at sinks), and 2nd (binary reactions) order kinetic processes taking place inside V. In this work we use V = 10^{19} m^3 in all the simulations.

Method Parameterization

The neutron spectra used for the JOYO and ITER reactors are given in Figure 1 (left panel).

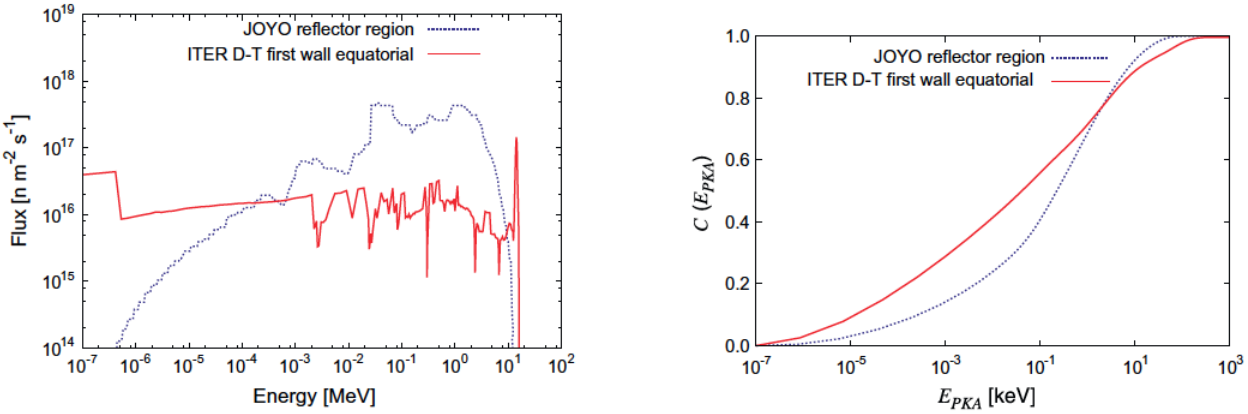

Fig. 1. (Left panel) Neutron flux spectra for the two locations considered in this work. The peak at 14 MeV for the ITER flux can be clearly appreciated. (Right panel) Recoil cumulative distribution function in W corresponding to the neutron spectra given in the left panel.

The spectral-averaged recoil energy distributions are shown in Fig. 1 (right panel), while the He production is given in Table 1. The recoil spectra are given as cumulative distribution functions, which are then used to obtain random samples of the primary knock-on atom (PKA) energies. The production of He in JOYO can be considered negligible, consistent with a threshold of 0.3 MeV for the 184W(n,α)181Hf channel [19]. As we shall show, this has a large effect on the ensuing microstructural evolution under irradiation. The complete characterization of the damage source term requires that the PKA energies be expressed in terms of the number and classification of the point defects produced. This has been the subject of very recent molecular dynamics studies in pure W [22,20,21], which we use here. After Fikar and Schäublin [22], we assume that the fraction of SIAs and vacancies in clusters is, on average, 0.5 and 0.2. In accordance with these authors, we consider a cluster to be formed when two or more defects aggregate together.

The calculations described here involve three distinct species, namely, SIAs, vacancies and He atoms, and any kind of reaction among them and their clusters is allowed. The energetics to enable these reactions have been obtained by Becquart and Domain using electronic structure calculations and published in a series of recent papers [23,24]. In these works, migration parameters for all single species objects are provided for all cluster sizes—i.e. all pure vacancy, SIA, and He clusters are considered mobile — which is the approach used here as well. Conversely, He bubbles are sessile. In addition, we have enabled SIA and SIA cluster reactions with He atoms in the same manner as done in our previous study in Fe [15], i.e. any collision between He and SIA clusters results in a SIA-He sessile structure that is thermally stable. In fact, this becomes the sole mechanisms of SIA loop accumulation in our calculations. Similarly, He bubbles are considered immobile.

Table I: Irradiation parameters and description of simulations performed.

	JOYO irradiations		
Dose rate (dpa s^{-1})	3.5×10^{-7}		
He production (appm dpa^{-1})	2.5×10^{-11}		
Temperature (°C)	400	538	583
Dose (dpa)	0.17	0.40	0.96
	ITER irradiations		
Dose rate (dpa s^{-1})	5.8×10^{-8}		
He production (appm dpa^{-1})	1.1		
Temperature (°C)	400	500	550
Dose (dpa)	0.10	0.44	1.54
Hardening (MPa)	68.5 ~ 136.9	23.1 ~ 46.2	8.4 ~ 16.8

RESULTS

Swelling as a Function of Temperature

The energetics at hand dictates that vacancy mobility in W is relatively low in the temperature range explored here. This allows small V clusters; either generated directly in displacement cascades or formed upon the subsequent time evolution, to accumulate at first. However, in the absence of stabilizing He atoms, the long-term fate of these clusters, especially those containing five or less vacancies, is questionable. In addition, fast-diffusing SIAs and small SIA clusters probe the configurationally space in 3D, leading to recombination and mutual annihilation. However, a critical population of clusters does survive and grows to become thermally stable. This is a temperature-dependent process, set by the timescale. The accumulated tally of these (stable) V clusters gives the total swelling of the material. The percentage swelling in the 400-600°C range for both the JOYO and ITER scenarios is plotted in Fig. 2. The labels assigned to each data point indicate the dose at which the swelling tally was obtained. Owing to their relatively high mobility, single vacancies are not included in the swelling calculation. Similarly, di-vacancies are not considered stable due to their negative binding energy and are also not tallied unless they are found in the form of 2V–*n*He complexes for any $n > 0$. Calculations performed at and above 600°C show negligible swelling in both cases. As the figure shows, the ITER environment results in approximately 30% higher swelling than JOYO at 400°C. However, the values converge as the temperature increases.

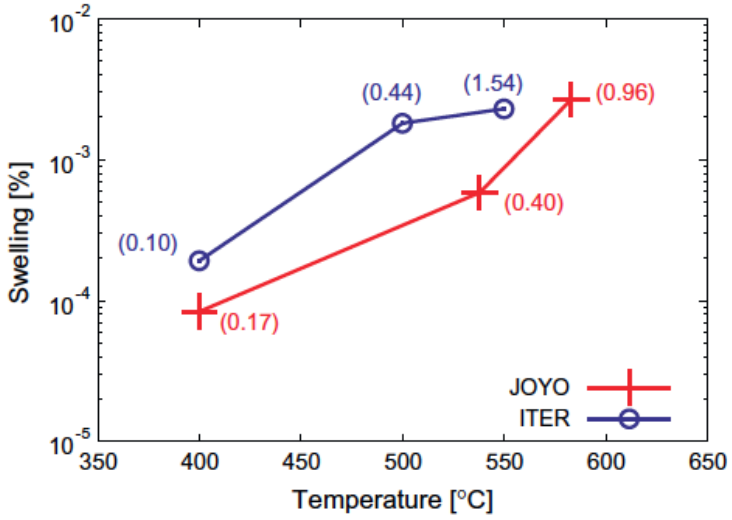

Fig. 2. Temperature dependence of swelling in pure W under JOYO and ITER irradiation conditions. The numbers in parentheses correspond to the accumulated dose expressed in dpa for each case.

By itself, the information plotted in Fig. 2 does not expose the differences in temperature and dose in full detail. For that, it is useful to look at the size partition of the void subpopulation. Fig. 3 shows a composite histogram including all cases simulated here. For size calculations, it is assumed that vacancy clusters adopt spherical shapes and SIA loops are arranged as circular loops. 'Size' refers to their respective diameters. Here the distinctions are clearer. In both the JOYO and ITER cases, a clear shift in the size distribution is observed as a function of temperature. For example, at 400°C — for which the swelling is highest — voids appear mostly in the form of small clusters less than 2 nm in diameter. The average void size at the higher temperatures, on the contrary, shifts to approximately 3 and 5 nm, with no voids observed below 1.5 nm. With respect to neutron spectrum effects, both the number and average void size for each temperature are higher for the ITER irradiations. A first-order explanation for this behavior resides in the role of He (again, present in ITER, absent in JOYO). To illustrate this, superposed with the total vacancy cluster size distribution in Fig. 4, we have plotted the fraction of clusters containing He atoms. In view of the results, we can conclude that He has two main effects, namely, to increase the population of total clusters (likely by the enhanced production of stable void nuclei), and to play an increasingly more important role the higher the temperature (all the voids at 550°C contained He atoms). The buildup of He bubbles in ITER is shown in Fig. 4.

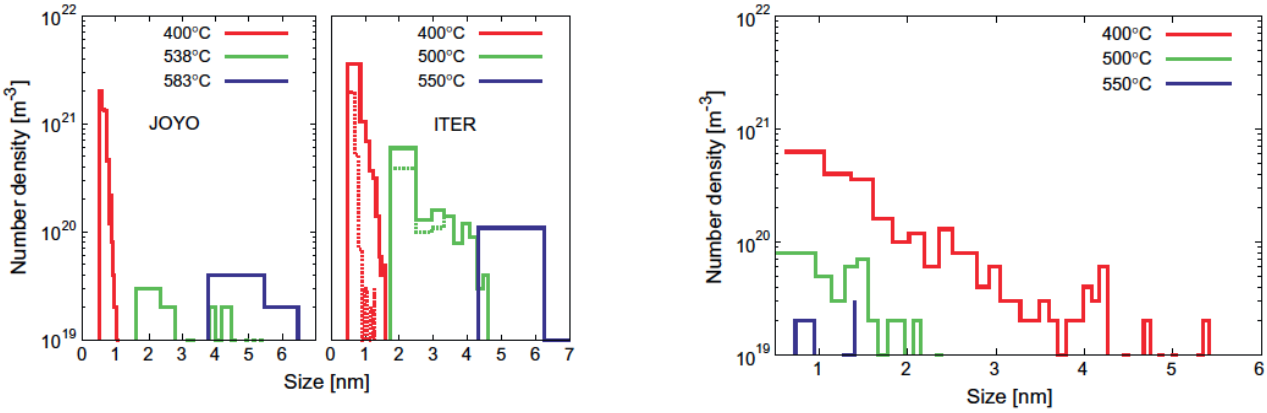

Fig. 3. (Left panel) Vacancy cluster size histogram at the point of maximum dose for JOYO and ITER irradiations. The dashed line in the ITER case represents the fraction of voids containing He. (Right panel) SIA cluster size histogram at the point of maximum dose (cf. Fig. 3) for the ITER irradiations.

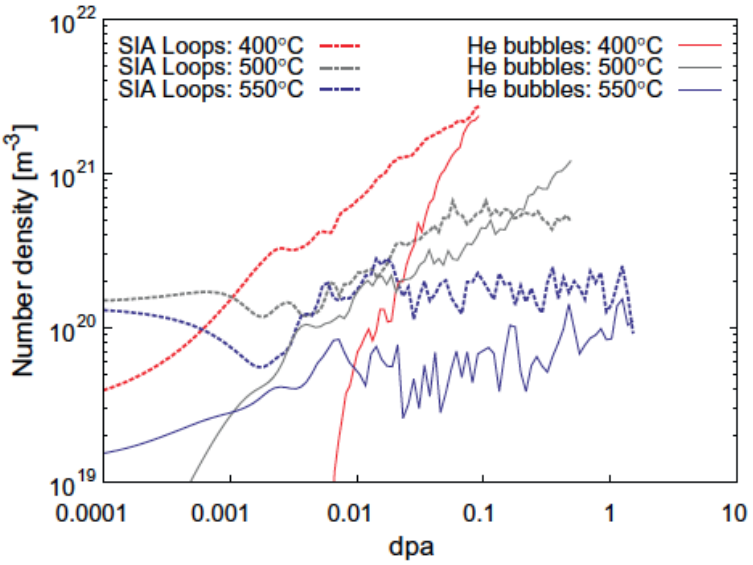

Fig. 4. Accumulation of visible (>1.0 nm) SIA loops and He bubbles as a function of dose and temperature for the ITER irradiations.

Another important effect induced by He-atom production is the accumulation of SIA loops. Evidently, no density of loops builds up in the JOYO scenario. By contrast, in the ITER case, a gradual buildup occurs at 400°C, while at 500 and 550°C saturation tendencies can be appreciated after 0.1 and 0.03 dpa, respectively. Whether this will be the eventual outcome also at 400°C is unclear at this point. What is clear is the strong inverse temperature dependence of SIA loop accumulation, also in agreement with the established understanding about irradiation hardening in bcc metals. As for swelling, no appreciable accumulation of SIA loops occurred above the

temperatures studied here. Once more, it is informative to plot the SIA loop subpopulation in terms of the size of the equivalent circular disc corresponding to the number of constituent defects. This is done in Fig. 3 (right panel).

SIA Loop Hardening

The equivalent integrated quantity associated to the SIA loop size histogram is hardening, expressed in our context as:

$$\Delta\sigma = M\alpha\frac{\mu b}{4\pi l}$$

where *M* is the Taylor factor, α is a strength coefficient, μ the shear modulus; *b* is the Burgers vector, and *l* the distance between obstacles. *l* can be computed as $(\overline{D}\rho_t)^{-1/2}$, where:

$$\overline{D}\rho_t = \int_v D(n)\rho(n)dn$$

is the product of the effective loop diameter and the total loop density. Here *D*(*n*). is the diameter of a loop (not to be confused with the diffusivity) of *n* SIAs and *ρ*(*n*) the corresponding number density. The integral can be approximated by a sum of discrete bins describing the histogram of loop sizes such as that shown in Fig. 3 (right panel). For values of *M* = 2.75 (for bcc crystals) [27], and α = 0.25–0.50 we obtain increases in yield stress that range between 137 MPa at 600°C and 8 MPa at 550°C. The actual range of hardening values for each temperature is given in Table 1. It is worth mentioning that voids and He bubbles are likely to have their own non-negligible contribution to hardening. However, having multiple strengthening mechanisms introduces a new set of complications, particularly associated with which rule of mixtures to use.

REFERENCES

[1] S. J. Zinkle and N. M. Ghoniem, *J. Nucl. Mater.* **417** (2011) 2.
[2] E. Lassner and W. F. Schubert, "Tungsten: Properties, Chemistry, Technology of the Element, Alloys, and Chemical Compounds," Kluwer Academic/Plenum Publishers, New York, NY, 1999.
[3] M. R. Gilbert and J. C. Sublet, *Nucl. Fusion* **51** (2011) 043005.
[4] G. A. Cottrell, *J. Nucl. Mater.* **334** (2004) 166.
[5] J. Matolich, H. Nahm, and J. Moteff, *Scripta Metall.* **8** (1974) 837.
[6] R. Herschitz and D.N. Seidman, *Acta Metall.* **32** (1984) 1141.
[7] J. C. He, A. Hasegawa, and K. Abe, *J. Nucl. Mater.* **377** (2008) 348.
[8] T. Tanno, A. Hasegawa, J. C. He, M. Fujiwara, M. Satou, S. Nogami, K. Abe, and T. Shishido, *J. Nucl. Mater.* **386–388** (2009) 218.
[9] A. Hasegawa, T. Tanno, S. Nogami, and M. Satou, *J. Nucl. Mater.* **417** (2011) 491.
[10] R. K. Williams and F.W. Wiffen, J. Bentley, J.O. Stiegler, Metall. Trans. A 14A (1983) 655.
[11] E. V. Kornelsen, *Can. J. Phys.* **48** (1970) 2812.
[12] E. V. Kornelsen, *Radiation Effect* **13** (1972) 227.
[13] N. Juslin, V. Jansson, and K. Nordlund, *Phil. Mag.* **90** (2010) 3581.
[14] C. S. Becquart, M. F. Barthe, and A. De Backer, *Phys. Scripta* **T145** (2011) 014048.

[15] J. Marian and V. V. Bulatov, *J. Nucl. Mater.* **415** (2011) 84.
[16] http://www.jaea.go.jp/04/o-arai/joyousersguide/joyomk3/spectrum/main.html.
[17] D. N. Seidman, R. S. Averback, and K. Benedek, *Phys. Satus Solidi (B)* **144** (1987) 85.
[18] L. R. Greenwood and R. K. Smither, SPECTER: Neutron Damage Calculations for Materials Irradiations, ANK/FPP/TM-197.
[19] http://www.nndc.bnl.gov/exfor/endf02.jsp.
[20] J. Fikar and R. Schäublin, *J. Nucl. Mater.* **386–388** (2009) 97.
[21] T. Troev, N. Nankov, and T. Yoshiie, *Nucl. Inst. Meth. Phys. Res. B* **269** (2011) 566.
[22] J. Fikar and R. Schäublin, *Nucl. Inst. Meth. Phys. Res. B* **255** (2007) 27.
[23] C. S. Becquart and C. Domain, *J. Nucl. Mater.* **385** (2009) 223.
[24] C .S. Becquart, C. Domain, U. Sarkar, A. DeBacker, and M. Hou, *J. Nucl. Mater.* **403** (2010) 75.
[25] D. Terentyev, N. Juslin, K. Nordlund, and N. Sandberg, *J. Appl. Phys.* **105** (2009) 103509.
[26] W. Knauss, Plansee Corp., Private Communication.
[27] Yu. M. Platov, V. M. Lazorenko, V. I. Tovtin, and F. A. Khasanov, *Inorg. Mater. Appl. Res.* **2** (2011) 37.

9.1 HFIR IRRADIATION EXPERIMENTS – July 31, 2012

Summary of Recent, Current and Planned Fusion Materials Program Experiments

Experiment Designation	Primary Materials	Specimen Types*	Irradiation Temperature (°C)	Max Exposure (dpa)	Number of Reactor Cycles	Irradiation Period (month/year)		
Beryllium reflector (RB) irradiation positions								
RB-15J	F82H	T, F, FT	300, 400	6	10	6/08	–	12/09
Target zone full-length capsules								
JP-25	F82H	T, FT	300, 500	20	10	2/99	–	1/01
JP-26	F82H	T, FT	300,400,500	9	5	12/03	–	11/04
JP-27	F82H	T, FT	300, 400	21	13	12/03	–	1/08
JP-28	F82H	T, FT	300,400,500	80	~50	4/05	–	
JP-29	F82H	T, FT	300,400,500	80	~50	1/05	–	
12-DCT	F82H	DCT	50	1.6	1	8/11	–	8/11
JP-30	F82H	T, FT	300,400,650	20	~10	11/11	–	
JP-31	F82H	T, FT	300,400,650	20	~10	11/11	–	
Target zone rabbit capsules (DOE-JAEA)								
F8A1	F82H	T, FT	300	50	28	2/09	–	
F8A2	"	"	"	"	"	"	–	
F8B1	"	"	"	"	"	"	–	
F8B2	"	"	"	"	"	"	–	
JCR-1	SiC/SiC	Bend bars	800	30	15	10/04	–	1/09
JCR-2	"	"	"	"	"	"	–	"
JCR-3	"	"	"	"	"	"	–	"
JCR-4	"	"	"	"	"	"	–	"
JCR-5	"	"	"	>50	>25	10/04	–	
JCR-6	"	"	"	"	"	"	–	
JCR-7	"	"	"	"	"	"	–	
JCR-8	"	"	"	"	"	"	–	
JCR-9	"	"	500	30	15	10/04	–	1/09
JCR-10	"	"	"	"	"	"	–	"
JCR-11	"	"	"	"	"	"	–	"
JCR-12	"	"	"	"	"	"	–	"
F11A3	F82H	T, FT	300	20	12	5/11	–	
F11A4	"	"	"	"	"	"	–	
F11B3	"	"	"	"	"	"	–	
M4-TEN	F82H	DCT	50	1.6	1	8/11	–	8/11

Target zone rabbit capsules (TITAN)								
T8A1	SiC	BSR	300	0.01	HT**	10/09	–	10/09
T8A2	SiC	BSR	300	0.1	HT	10/09	–	10/09
T8B1	SiC	BSR	500	0.01	HT	10/09	–	10/09
T8B2	SiC	BSR	500	0.1	HT	10/09	–	10/09
T8C1	SiC	BSR	500	~1	1	5/09	–	6/09
T8D1	SiC	BSR	800	0.1	HT	3/11	–	10/09
T8E1	SiC	BSR	800	~1	1	8/09	–	8/09
T8F1	SiC	BSR	1200	~1	1	8/09	–	8/09
T9A1	W, Ni	Discs	90	0.1	HT	1/09	–	10/09
T9A2	W, Ni	Discs	90	1.2	1	1/09	–	1/09
T9C1	Steels	T, MC	500	5.5	3	11/09	–	2/10
T9C2	Steels	T, MC	500	9.6	5	11/09	–	6/10
T9G1	Steels	T, MC	300	1.2	1	6/09	–	8/09
T9G2	Steels	T, MC	300	9.6	8	6/09	–	8/11
MTTN01	Steels	T, MC	300	4.8	4	1/12	–	
300-LD-1	Steels	SSJ, MC	300	2	1	5/12	–	6/12
300-HD-1	Steels	SSJ, MC	300	12	6	5/12	–	
500-LD-1	Steels	SSJ, MC	500	2	1	5/12	–	6/12
500-HD-1	Steels	SSJ, MC	500	12	6	5/12	–	
500-HD-2	Steels	SSJ, MC	500	12	6	5/12	–	
500-HD-3	Steels	SSJ, MC	500	12	6	5/12	–	
650-LD-1	Steels	SSJ, MC	650	2	1	5/12	–	6/12
650-LD-2	Steels	SSJ, MC	650	2	1	5/12	–	6/12
650-HD-1	Steels	SSJ, MC	650	12	6	5/12	–	
650-HD-2	Steels	SSJ, MC	650	12	6	5/12	–	
300-LD-2	Steels, W	SSJ, MC	300	2	2	7/12	–	
300-LD-4	W	Disc 6D	300	2	2	TBD	–	
300-MD-1	Steels, W	SSJ, MC	300	7	4	7/12	–	
300-MD-2	W	Disc 6D	300	7	4	TBD	–	
500-LD-2	Steels, W	SSJ, MC	500	2	2	10/12	–	
500-LD-4	W	Disc 6D	500	2	2	TBD	–	
300-LD-3	Steels, W	SSJ, MC	300	2	2	7/12	–	
300-HD-2	Steels, W	SSJ, MC	300	12	8	7/12	–	
500-LD-3	Steels, W	SSJ, MC	500	2	1	7/12	–	8/12
500-HD-4	Steels, W	SSJ, MC	500	12	6	7/12	–	
650-LD-3	Steels, W	SSJ, MC	650	2	2	10/12	–	
650-HD-3	Steels, W	SSJ, MC	650	12	8	7/12	–	
PC1	Various	SSJ, MC	80/100	0.02	HT	6/12	–	
PC1A	Various	SSJ, MC	80/100	0.02	HT	6/12	–	
PC2	Various	SSJ, MC	80/100	0.1	HT	6/12	–	
PC2A	Various	SSJ, MC	80/100	0.1	HT	6/12	–	
PC3	Various	SSJ, MC	80/100	0.5	HT	6/12	–	
PC3A	Various	SSJ, MC	80/100	0.5	HT	6/12	–	

PC4	Various	SSJ, MC	80/100	2	1	6/12	–	7/12
PC4A	Various	SSJ, MC	80/100	2	1	6/12	–	7/12
PC5	Various	SSJ, MC	80/100	20	9	6/12	–	
TB-300-1	Steels, W	SSJ, MC	300	0.02	HT	8/12	–	
TB-300-2	Steels, W	SSJ, MC	300	0.1	HT	8/12	–	
TB-300-3	Steels, W	SSJ, MC	300	0.5	HT	8/12	–	
TB-300-4	Steels, W	SSJ, MC	300	7	5	7/12	–	
TB-500-1	Steels, W	SSJ, MC	500	0.1	HT	8/12	–	
TB-500-2	Steels, W	SSJ, MC	500	0.5	HT	8/12	–	
TB-500-3	Steels, W	SSJ, MC	500	7	4	7/12	–	
TB-650-1	Steels, W	SSJ, MC	650	0.1	HT	8/12	–	
TB-650-2	Steels, W	SSJ, MC	650	0.5	HT	8/12	–	
TB-650-3	Steels, W	SSJ, MC	650	7	5	7/12	–	
TB-650-4	Steels, W	SSJ, MC	650	20	11	7/12	–	
TTN09	SiC	Joint	500	3.4	2	8/11	–	11/11
TTN10	SiC	Joint	500	4.1	2	8/11	–	11/11
TTN11	SiC	Joint	800	4	2	3/12	–	5/12
TTN01	SiC	BSR	300	1	1	2/11	–	3/11
TTN02	SiC	BSR	300	10	6	2/11	–	12/11
TTN03	SiC	BSR	300	20	11	2/11	–	
TTN04	SiC	BSR	500	10	6	5/11	–	4/12
TTN05	SiC	BSR	500	20	11	5/11	–	
TTN06	SiC	BSR	800	10	6	5/11	–	4/12
TTN07	SiC	BSR	800	20	11	5/11	–	
TTN08	SiC	BSR	1200	10	6	5/11	–	8/12
TTN16	SiC	Fiber BSR	500	1	1	11/11	–	12/11
TTN17	SiC	Fiber BSR	500	10	6	8/11	–	6/12
TTN18	SiC	Fiber BSR	500	20	11	8/11	–	
TTN19	SiC	Fiber BSR	1200	1	1	3/12	–	4/12
TTN20	SiC	Fiber BSR	1200	10	6	3/12	–	

*T = Tensile, F = Fatigue, FT = Fracture Toughness, MC = Multipurpose Coupon, BSR = Bend Stress Relaxation Creep, DCT = Disc Compact Tension. Most experiments also contain TEM disks, other special purpose specimens, and monitors occupying small spaces.
**Hydraulic tube – fractional cycle exposures.